DR Argillite Disposal R&D at LBNL

Fuel Cycle Technology

Prepared for
U.S. Department of Energy
Used Fuel Disposition Campaign

Liange Zheng, Kunhwi Kim, Hao Xu, Jonny Rutqvist
Lawrence Berkeley National Laboratory

August 2016

FCRD-UFD-2016-000437
LBNL-1006013

Revision 2
12/20/2012

APPENDIX E
FCT DOCUMENT COVER SHEET [1]

Name/Title of Deliverable/Milestone/Revision No.	Investigation of Coupled Processes and Impact of High Temperature Limits in Argillite Rock
Work Package Title and Number	DR Argillite Disposal R&D - LBNL FT-16LB08030203
Work Package WBS Number	1.02.08.03.02
Responsible Work Package Manager	Liange Zheng (signature on file) (Name/Signature)

Date Submitted 08/12/2016

Quality Rigor Level for Deliverable/Milestone[2]	☒ QRL-3	☐ QRL-2	QRL-1 ☐ Nuclear Data	☐ Lab/Participant QA Program (no additional FCT QA requirements)

This deliverable was prepared in accordance with Lawrence Berkeley National Laboratory
(Participant/National Laboratory Name)

QA program which meets the requirements of
☒ DOE Order 414.1 ☐ NQA-1-2000 ☐ Other

This Deliverable was subjected to:

☒ Technical Review ☐ Peer Review

Technical Review (TR)

Review Documentation Provided

☐ Signed TR Report or,
☐ Signed TR Concurrence Sheet or,
☒ Signature of TR Reviewer(s) below

Peer Review (PR)

Review Documentation Provided

☐ Signed PR Report or,
☐ Signed PR Concurrence Sheet or,
☐ Signature of PR Reviewer(s) below

Name and Signature of Reviewers

Patrick Dobson (signature on file)
Pierre Jeanne (signature on file)
Yiwei Cheng (signature on file)

NOTE 1: *Appendix E should be filled out and submitted with the deliverable. Or, if the PICS:NE system permits, completely enter all applicable information in the PICS:NE Deliverable Form. The requirement is to ensure that all applicable information is entered either in the PICS:NE system or by using the FCT Document Cover Sheet.*

NOTE 2: *In some cases there may be a milestone where an item is being fabricated, maintenance is being performed on a facility, or a document is being issued through a formal document control process where it specifically calls out a formal review of the document. In these cases, documentation (e.g., inspection report, maintenance request, work planning package documentation or the documented review of the issued document through the document control process) of the completion of the activity along with the Document Cover Sheet is sufficient to demonstrate achieving the milestone. If QRL 1, 2, or 3 is not assigned, then the Lab/Participant QA Program (no additional FCT QA requirements box must be checked, and the work is understood to be performed, and any deliverable developed, in conformance with the respective National Laboratory/Participant, DOE- or NNSA-approved QA Program.*

\

TABLE OF CONTENTS

LIST OF FIGURES

LIST OF TABLES

ACRONYMS

ABM	Alternative Buffer Materials
BBM	Barcelona Basic Model
BExM	Barcelona Expansive Model
CIEMAT	Centre for Energy, Environment and Technology
DECOVALEX	Development of Coupled Models and their Validation against Experiments
DFN	Discrete Fracture Network
DMS	Document Management System
DOE	Department of Energy
DRZ	Disturbed Rock Zone
EBS	Engineered Barrier System
EBS-NS	Engineered Barrier System-Natural System
EDZ	Excavation Damaged Zone
FE	Full-Scale Emplacement Experiment
FEBEX	Full-Scale Engineered Barrier Experiment
FEBEX-DP	Full-Scale Engineered Barrier Experiment-Dismantling Project
FEPs	Features, Events and Processes
HLW	High-Level Radioactive Waste
HPLC	High Pressure Liquid Chromatograph
JAEA	Japan Atomic Energy Agency
LBNL	Lawrence Berkeley National Laboratory
MCC	Modified Cam Clay
NBS	Natural Barrier System
PWR	Pressurized Water Reactor
R&D	Research and Development
RBSN	Rigid Body Spring Network
SXR-μCT	Synchrotron X-ray microCT
TH	Thermal and Hydrogeological
THM	Thermal-Hydrological-Mechanical
THC	Thermo-Hydro-Chemical
THMC	Thermal-Hydrological-Mechanical-Chemical
TPHM	Two-Parts Hooke's Model
UDM	User Defined constitutive Model
UFD	Used Fuel Disposition
UFDC	Used Fuel Disposition Campaign
URL	Underground Research Laboratory

DEEP BOREHOLE FIELD TEST RESEARCH ACTIVITIES AT LBNL

1. INTRODUCTION

Shale and clay-rich geological formations have been considered as potential host rock for geological disposal of high-level radioactive waste throughout the world because of their low permeability, low diffusion coefficient, high retention capacity for radionuclides, and capability to self-seal fractures. The low permeability of clay and shale rock are well-known in the hydrogeology community where these rock types represent aquitards that severely limit groundwater movement, and in petroleum geology, where they act as caprocks limiting the rise of buoyant petroleum fluids. While fractures can occur, clay and shale often demonstrate the tendency to self-seal fractures, which reduces the effects of fractures on bulk permeability. Other favorable characteristics of clay/shale rock are the strong sorptive behavior for many radionuclides, reducing conditions because of the lack of oxygen transport from the surface, and chemical buffering of introduced materials.

Engineered barrier system (EBS) with bentonite backfilled is also a critical component in most repository concepts. A large body of information concerning the behavior of clay/shale geologic environments using bentonite backfill/buffers for nuclear waste disposal has been developed through the repository programs with underground research laboratories in Switzerland, France, Belgium, and Japan. In this report we document modeling of tests conducted at Mont Terri underground rock laboratory and Grimsel underground rock laboratory in Switzerland, and the Horonobe underground research laboratory in Japan. The focus of research within the Used Fuel Disposal (UFD) Campaign is on repository-induced interactions that may affect the key safety characteristics of EBS bentonite and an argillaceous rock. These include thermal-hydrological-mechanical-chemical (THMC) process interactions that occur as a result of repository construction and waste emplacement. Some of the key questions addressed in this report include the development of fracturing in the excavation damaged zone (EDZ) and THMC effects on the near-field argillaceous rock and buffer materials and petrophysical characteristics, particularly the impacts of induced temperature rise caused by waste heat.

Within the Natural Barrier System (NBS) group of the Used Fuel Disposition (UFD) Campaign at the Department of Energy's (DOE) Office of Nuclear Energy LBNL's research activities have focused on understanding and modeling EDZ evolution and the associated coupled processes and impacts of high temperature on parameters and processes relevant to performance of a clay repository to establish the technical base for the maximum allowable temperature. This report documents results from some of these activities. These activities address key Features, Events, and Processes (FEPs), which have been ranked in importance from medium to high, as listed in Table 7 of the Used Fuel Disposition Campaign Disposal Research and Development Roadmap (FCR&D-USED-2011-000065 REV0) (Nutt, 2011). Specifically, they address FEP 2.2.01, Excavation Disturbed Zone, for clay/shale, by investigating how coupled processes affect EDZ evolution; FEP 2.2.05, Flow and Transport Pathways; and FEP 2.2.08, Hydrologic Processes, and FEP 2.2.07, Mechanical Processes, and FEP 2.2.09, Chemical Process—Transport, by studying near-field coupled THMC processes in clay/shale repositories. The activities documented in this report also address a number of research topics identified in Research & Development (R&D) Plan for Used Fuel Disposition Campaign (UFDC) Natural System Evaluation and Tool Development (Wang 2011), including Topics S3, Disposal system modeling – Natural System; P1, Development of discrete fracture network (DFN) model; P14, Technical basis for thermal loading limits; and P15 Modeling of disturbed rock zone (DRZ) evolution (clay repository).

This report documents the following research activities:

- Section 2 presents THM modeling of underground heater experiments in clay formations, including studies related to the Development of Coupled Models and their Validation against Experiments (DECOVALEX)-2015 project and the Mont Terri FE (Full-scale Emplacement) Experiment. The FE Experiment is undertaken as an ultimate test for the performance of geologic disposal in Opalinus Clay; it will be one of the largest and longest running heater tests worldwide. Coupled THM model for FE test was developed using TOUGH-FLAC, which provides a unique opportunity to validate and test the models at realistic, large-scale, in-situ conditions, including the interactions between the host rock and EBS.
- Section 3 presents the development and application of thermal-hydrological-mechanical-chemical (THMC) modeling to evaluate bentonite EBS and clay rock NS responses under higher temperatures (200 °C). Model results are presented to help to understand the impact of high temperatures on the properties and behavior of bentonite and clay rock.
- Section 4 presents coupled THMC modeling for an *in situ* test conducted at Grimsel underground laboratory in Switzerland in the FEBEX-DP project. The data collected in the test after almost two decades of heating and two dismantling events provide a unique opportunity of validating coupled THMC models and enhancing our understanding of coupled THMC process in EBS bentonite.
- Section 5 presents development, testing, and applications of a discrete fracture network (DFN) approach for modeling THM induced damage and fracturing in argillaceous rocks. The modeling work was conducted using TOUGH-RBSN, a simulation code combines TOUGH2 with the rigid-body-spring network (RBSN) model. The code is validated against the laboratory experiments for hydraulic fracture propagation in rock-analogue samples and used to model anisotropic failure characteristics of a uniaxial compression tests and a tunnel excavation process in the presence of discrete faults. In addition, the ongoing work on the dynamic simulation code development is presented.
- Section 6 summarizes the main research accomplishments for FY, 2016 and proposes future work activities.

2. THM MODELING: FE HEATER TEST AND DECOVALEX

In this section, we present LBNL's activities related to THM modeling of underground heater experiments in clay formations, including studies related to the Development of Coupled Models and their Validation against Experiments (DECOVALEX)-2015 project and the Mont Terri FE (Full-scale Emplacement) Experiment. DECOVALEX-2015 is an acronym for the sixth phase of the "Development of Coupled Models and their Validation against Experiments" project, from 2012 through 2015. Thus, the DECOVALEX-2015 was completed in December 2015, although some reporting was done during the spring of 2016 and some joint journal papers are still being prepared summarizing the results. In DECOVALEX-2015, LBNL participated in a modeling task denoted Task B, which included:

Subtask B1—Mont Terri HE-E Experiment: A heating experiment to evaluate sealing and clay-barrier performance, in a micro-tunnel at the Mont Terri URL in Switzerland; and,

Subtask B2—Horonobe Engineered Barrier System (EBS) Experiment: A heating experiment to study the thermo-hydro-mechanical-chemical (THMC) behavior of the EBS and its interaction with the mudstone host rock, in a vertical emplacement hole at the Horonobe URL in Japan.

In addition to the modeling work in these two DECOVALEX tasks, LBNL participates in the Mont Terri FE Experiment as one of the participating modeling teams. The FE Experiment is undertaken as an ultimate test for the performance of geologic disposal in Opalinus Clay, focusing on both the EBS components and the host-rock behavior; it will be one of the largest and longest running heater tests worldwide.

UFD objectives for participating in these international activities are to develop expertise and test advanced models of coupled processes in clay-based backfill in interaction with clay host rock. Through participation in modeling these field experiments, the models will be developed and experience will be gained for a range of different backfill materials (e.g., bentonite pellets and sand/bentonite mixture), as well as different host rocks (e.g., Opalinus clay and mudstone). The main software developed and used for these simulations is the numerical simulator TOUGH-FLAC (Rutqvist et al. 2002; 2011; 2014b). For nuclear waste isolation, TOUGH-FLAC provides UFD with a model framework for modeling coupled THM processes in the EBS and host rock and their interactions using state-of-the-art macroscopic constitutive models for bentonite, crushed rock salt backfill, clay, salt and crystalline host rocks. For rigorous modeling of the THM behavior of bentonite-based (swelling) buffer and back-fill materials, the BBM (Barcelona Basic Model) and BExM (Barcelona Expansive Model) have been implemented into TOUGH-FLAC (Rutqvist et al., 2011; 2014b; Vilarrasa et al., 2015). Modeling of the in situ heater experiments provides a unique opportunity to validate and test the models at realistic, large-scale, in-situ conditions, including the interactions between the host rock and EBS. Finally, through the numerical modeling of these experiments and being at the forefront of modeling coupled THMC processes our goal is also to advance the state-of-the-science internationally in the field of coupled processes modeling of clay barriers.

In the following Subsection 2.1, the modeling approach and the status of model development will be summarized, and in Subsection 2.2 the work related to improvement and validation of the BExM implementation in TOUGH-FLAC will be presented. Then the modeling work conducted associated with field experiments is presented in Subsections 2.3 through 2.5. Finally, in Subsection 2.6, the current status and future plans for THM modeling are summarized.

2.1 MODELING APPROACH

LBNL uses two independent numerical simulators (TOUGH-FLAC and ROCMAS) for modeling of coupled THM processes associated with nuclear waste disposal and for modeling of the aforementioned heater experiments. The TOUGH-FLAC simulator developed at LBNL is the primary analysis tool, because this simulator has the required capabilities to model a large variety of problems associated with

nuclear waste disposal for various engineering and natural systems. The ROCMAS code, also developed at LBNL, is used for confidence building through code-to-code verification. That is, models of a particular problem might be built in both TOUGH-FLAC and ROCMAS, and if the simulation results agree, they provide confidence in the models.

Both the TOUGH-FLAC and ROCMAS codes solve THM coupled problems, but are two different codes with different characteristics. TOUGH-FLAC can simulate coupled THM processes under multiphase flow conditions through a sequential coupling of the TOUGH2 multiphase flow simulator with the FLAC3D geomechanical code (Rutqvist et al. 2002; Rutqvist 2011). TOUGH-FLAC has recently been modified for applications related with to bentonite-backfilled repositories in clay host formations (Rutqvist et al., 2014b). ROCMAS simulates coupled THM processes in unsaturated media, including single-phase liquid flow and vapor diffusion in a static gas phase (Rutqvist et al. 2001a). The code has been extensively applied in earlier phases of the DECOVALEX project for THM analysis in bentonite-rock systems (Rutqvist et al., 2001b; 2005; 2009). Thus, ROCMAS is simplified compared to that of TOUGH-FLAC, foremost in the handing of multiphase fluid flow processes and in the geomechanical constitutive models, which are much more advanced in TOUGH-FLAC. Another difference is ROCMAS uses full implicit coupling between fluid flow and geomechanics, whereas sequential coupling technique is adopted in TOUGH-FLAC. In the following, the TOUGH-FLAC simulator (primary analysis tool) is described in more detail.

The TOUGH-FLAC simulator (Rutqvist 2011), is based on linking the TOUGH2 multiphase flow and heat transport simulator (Pruess et al., 2012) with the FLAC3D geomechanical simulator (Itasca 2011). In this approach, TOUGH2 (Pruess et al., 2012) is used for solving multiphase flow and heat transport equations, whereas FLAC3D (Itasca, 2011) is used for solving geomechanical stress-strain equations. The two codes are sequentially coupled so that a TOUGH-FLAC simulation runs seamlessly.

For analysis of coupled THM problems, TOUGH2 and FLAC3D are executed on compatible numerical grids and linked through a coupled THM model (Figure 2.1) with coupling functions to pass relevant information between the field equations that are solved in the respective codes. In the coupling scheme between TOUGH2 and FLAC3D, the TOUGH2 multiphase pressures, saturation, and temperature are provided to update temperature, and pore pressure to FLAC3D (Figure 2.1). After data transfer, FLAC3D internally calculates thermal expansion, swelling, and effective stress. Conversely, element stress or deformation from FLA3D is supplied to TOUGH2 to correct element porosity, permeability, and capillary pressure for the fluid-flow simulation in TOUGH2. The corrections of hydraulic properties are based on material-specific functions.

In a TOUGH-FLAC simulation, the calculation is stepped forward in time with the transient multiphase fluid flow analysis in TOUGH2, and at each time step or at the TOUGH2 Newton iteration level, a quasi-static mechanical analysis is conducted with FLAC3D to calculate stress-induced changes in porosity and intrinsic permeability (Figure 2.2). In this scheme, the fluid-flow sequence is solved first under fixed stress, and the resulting pressure and temperature are prescribed in the mechanical sequence. This corresponds to so-called stress-fixed iterations in the sequential scheme, in which the solution becomes unconditionally stable. The resulting THM analysis may be explicit sequential method, meaning that the porosity and permeability is evaluated only at the beginning of each time step, or the analysis may be implicit sequential method, with permeability and porosity updated on the Newton iteration level towards the end of the time step using an iterative process.

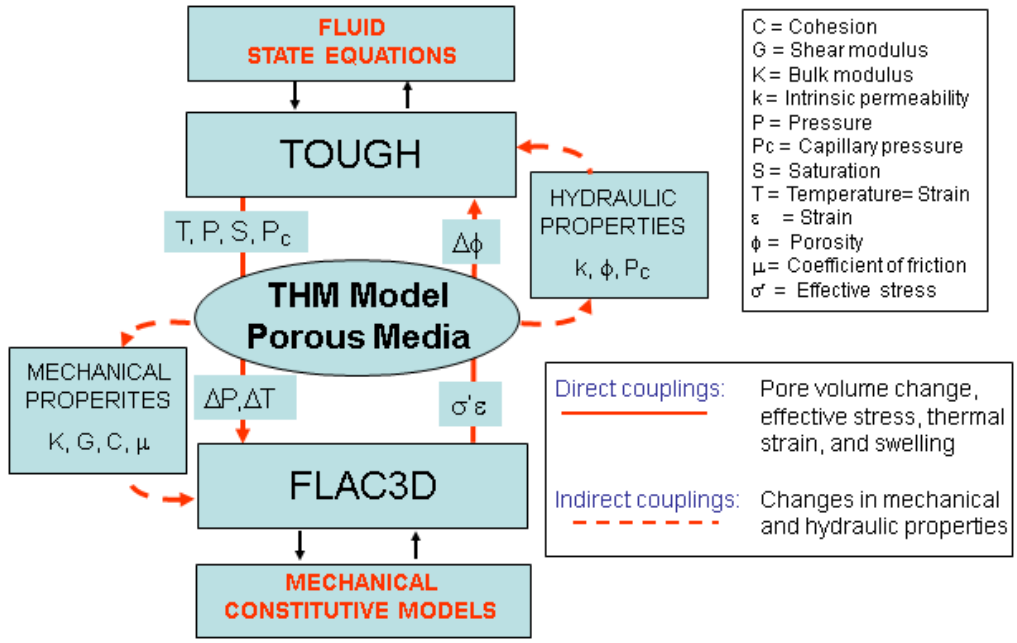

Figure 2.1. Schematic of linking of TOUGH2 and FLAC3D in a coupled TOUGH-FLAC simulation.

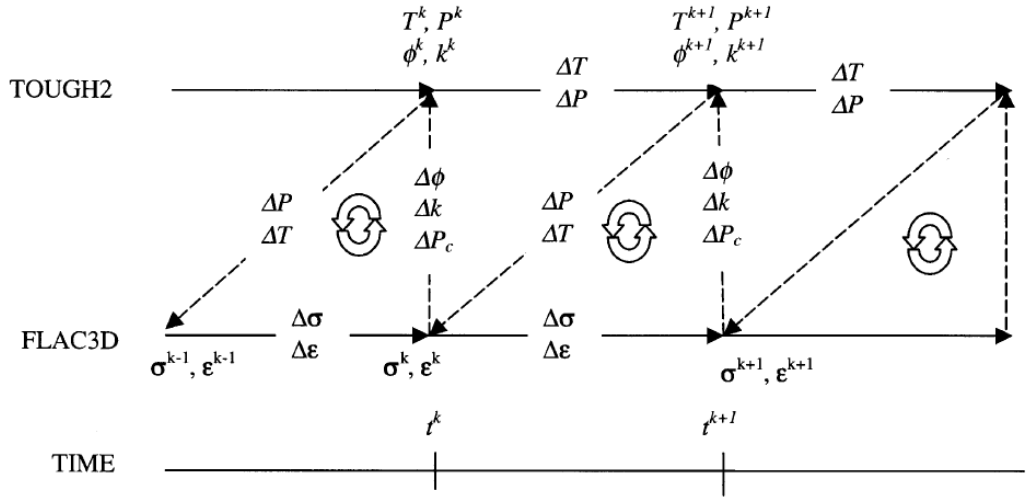

Figure 2.2. Numerical procedure of a linked TOUGH2 and FLAC3D simulation with subscript k signifying time step.

A great advantage with TOUGH-FLAC is that both TOUGH2 and FLAC3D are continuously developed and widely used in both academia and industry. In TOUGH2, a large number of fluid equation-of-state modules are available, while in FLAC3D, a large number of geomechanical constitutive models are available. This means that the simulator can be relatively easily extended to new application areas.

As part of the UFD effort, the TOUGH-FLAC simulator has been extended and applied to issues related to nuclear waste disposal with bentonite backfilled tunnels (Rutqvist et al., 2011; 2014b). This includes implementation of the Barcelona Basic Model (BBM) (Alonso et al., 1990), for the mechanical behavior

of unsaturated soils, which has been applied for modeling of bentonite backfill behavior (Rutqvist et al., 2011). The BBM was first developed and presented in the early 1990s as an extension of the Modified Cam Clay (MCC) model to unsaturated soil conditions (Alonso et al., 1990). The model can describe many typical features of unsaturated-soil mechanical behavior, including wetting-induced swelling or collapse strains, depending on the magnitude of applied stress, as well as the increase in shear strength and apparent preconsolidation stress with suction (Gens et al., 2006). More details about the BBM model are given in Section 2.2.1.

The BBM has been used for modeling bentonite-buffer behavior in various national nuclear waste programs in Europe and Japan. For example, the BBM was successfully applied to model the coupled THM behavior of unsaturated bentonite clay associated with the FEBEX *in situ* heater test at the Grimsel Test Site, Switzerland (Gens et al., 2009). The BBM has also been applied to other types of bentonite-sand mixtures based on MX-80, considered as an option for an isolating buffer in the Swedish KBS-3 repository concept (Kristensson and Åkesson 2008). As part of the UFD program, the BBM was also used by Rutqvist et al. (2014b), for modeling of coupled THM processes around a generic repository in a clay host formation.

In the last few years, as part of the UFD EBS program, the BBM has been extended to a dual structure model, corresponding to the Barcelona Expansive Model (BExM). In a dual-structure model, the material consists of two structural levels: a microstructure in which the interactions occur at the particle level, and a macrostructure that accounts for the overall fabric arrangement of the material comprising aggregates and macropores (Figure 2.3) (Gens et al., 2006; Sánchez et al., 2005; Gens and Alonso 1992). A dual-structure model has important features for modeling the mechanical behavior of a bentonite buffer, such as irreversible strain during suction cycles. However, most importantly, a dual-structure model provides the necessary link between chemistry and mechanics, enabling us to develop a coupled THMC model for the analysis of long-term EBS behavior. This approach enables mechanistic modeling of processes important for long-term buffer stability, including effects of pore-water salinity on swelling (loss of swelling), conversion of smectite to nonexpansive mineral forms (loss of swelling), and swelling pressure versus exchangeable cations. Details of the development, testing and applications of the dual structure model, were presented in the FY2014 milestone report titled “Investigation of Coupled THMC Processes and Reactive Transport: FY14 Progress” (Rutqvist et al. 2014a) and has also recently been published in a journal paper (Vilarrasa et al., 2015).

Based on model simulation in the DECOVALEX-2015 project with TOUGH-FLAC, considering full multiphase flow (gas and liquid) we found that a gas intrinsic permeability several orders of magnitude higher than the intrinsic permeability related to liquid flow would be required for accurate modeling of the evolution of the moisture content in the buffer. In the following simulations of the three heater experiments we simulated high intrinsic gas permeability in the bentonite through the Klinkenberg parameter according to:

$$K_g = K_l\left(1 + b/P\right) \qquad 2.1$$

where K_g is intrinsic permeability for gas flow, K_l is intrinsic permeability of water flow, b is the Klinkenberg parameter, and P is pressure. In this case, we assigned a high value of the Klinkenberg parameter of 2.5×10^{11} Pa^{-1}, which means that the intrinsic permeability for gas flow would be about 6 orders of magnitude higher than the intrinsic permeability for water flow. This was necessary as otherwise it is not possible to simulate the drying that usually occurs near the heaters.

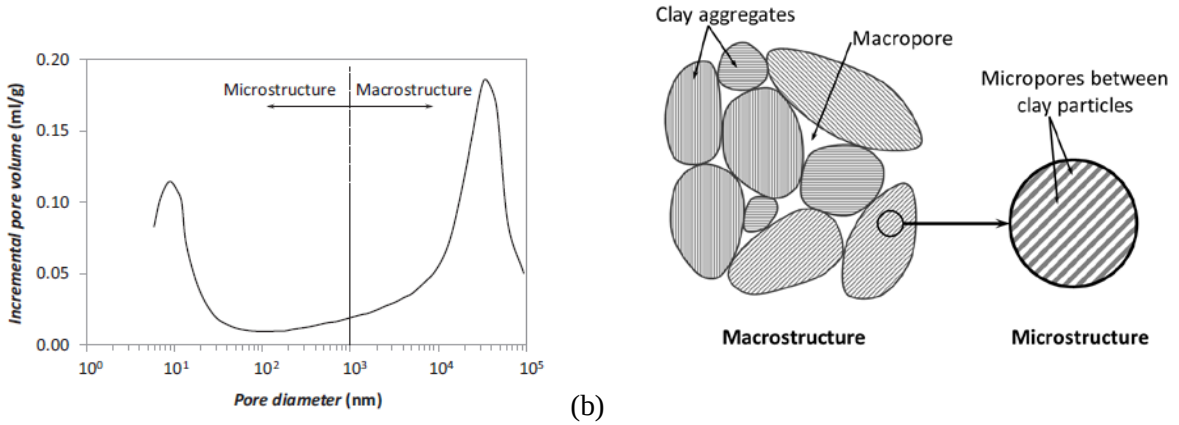

Figure 2.3. (a) Pore size distribution and (b) schematic representation of the two structural levels considered in the dual structure model. Clay particles are represented by the gray lines (Vilarrasa et al., 2015).

In FY2015, a substantial effort has been dedicated to improve the implementation of the BExM model into TOUGH-FLAC and to validate this implementation. The new implementation has resulted in increased efficiency.

2.2 IMPROVEMENT AND VALIDATION OF BExM IN TOUGH-FLAC

The dual structure model proposed by Alonso et al. (1999) and Sánchez et al. (2005) has been implemented into TOUGH-FLAC (Vilarrasa et al., 2015), by extending the previous implementation of the BBM (Rutqvist et al., 2011) to include the microstructural level and its interactions with the macrostructure. This year, the model has been implemented into the simulation tool, TOUGHREACT-FLAC3D, and has been improved to enhance the capability for modeling swelling behavior of bentonite:

1. The framework to compute dual-structural model has been revised to be compatible with FLAC3D, and a new solve command can be used for better efficiency and convergence.
2. The micro-structural strain evolution under anisotropic stress has been implemented in FLAC3D.
3. The interface for chemical-mechanical interaction has been integrated, so BExM can be linked with TOUGHREACT to account for chemical effects.
4. Some minor bugs have been fixed in the new version.

The implementation of the dual structure model in FLAC3D was done using the User Defined constitutive Model (UDM) option in FLAC3D, including C++ coding and dynamic link libraries. This also involves consideration of the sequential coupling of the TOUGH2/TOUGHREACT and FLAC3D simulators (Rutqvist, 2011), and constitutive stress-strain behavior in FLAC3D. With these improvements, the new simulator TOUGHREACT-FLAC3D can be used to study coupled THMC processes in bentonite-based backfill material. In this section, we present one swelling pressure test on Boom clay pellets, two cyclic wetting-drying tests, and two tests with combination of loading paths on compacted bentonite samples to validate the model implementation. The numerical analysis are launched with the set of material parameters calibrated by the model development team against laboratory experiments from published literature. The applications of BExM for THMC processes in expansive clays are presented in Sections 3 and 4.

2.2.1 The dual structure approach

Expansive clays present a bimodal or trimodal pore size distribution (Figure 2.3(a)). This pore size distribution leads to the differentiation of a microstructure, which is made of the active clay minerals, and a macrostructure, which is formed by the global distribution of clay aggregates and the macropores between them (Figure 2.3(b)). Thus, in the dual structure model, the total volume (V), the total void ratio (e), and porosity (ϕ), of the material are divided into micro-structural parts (V_{micro}, e_{micro}, ϕ_{micro}) and macro-structural parts (V_{macro}, e_{macro}, ϕ_{macro}). The microstructure can swell to invade the macroporosity, depending on the mechanical confinement and load level.

2.2.1.1 Macrostructural level

The macrostructural behavior is modeled based on the BBM, in which the yield surface is defined in the p-q-s space, where p is net mean stress (i.e., total stress minus gas-phase pressure), q is deviatoric stress (or shear stress), and s is suction (i.e., gas pressure minus liquid pressure) (Figure 2.4). The rate of the increase of the elastic domain, represented by the loading-collapse (LC) curve according to

$$f_{LC} = \frac{q^2}{g_y(\theta)^2} - \frac{M^2}{g_y(\theta=0)^2}(p + p_s)(p_0 - p) = 0 \qquad 2.2$$

where θ is the Lode angle, the function $g_y(\theta)$ describes the shape of the yield surface in the deviatoric plane, M is the constant slope of the critical state line, $p_s = k_s s$ represents the increase in cohesion with suction, k_s is an empirical material constant and function

$$p_0 = p_c\left(\frac{p_0^*}{p_c}\right)^{[\lambda(0)-\kappa]/[\lambda(s)-\kappa]} \qquad 2.3$$

is the net mean yield stress at current suction, where p_0^* is the net mean yield at full saturation, p_c is a reference stress, $\lambda(0)$ is a compressibility parameter in virgin soil states at zero suction, $\lambda(s) = \lambda(s)[(1-r)\exp(-\zeta s) + r]$ is a compressibility parameter in virgin soil states at suction s, r is a constant related to the maximum stiffness of the soil (for an infinite suction), ζ is a parameter that controls the rate of increase of soil stiffness with suction and κ is the elastic stiffness parameter for changes in net mean stress at current suction. The flow rule is given by

$$g_{LC} = \frac{\alpha_a q^2}{g_y(\theta)^2} - \frac{M^2}{g_y(\theta=0)^2}(p + p_s)(p_0 - p) \qquad 2.4$$

where α_a is a parameter that gives rise to a non-associative model, i.e., $g_{LC} \neq f_{LC}$.

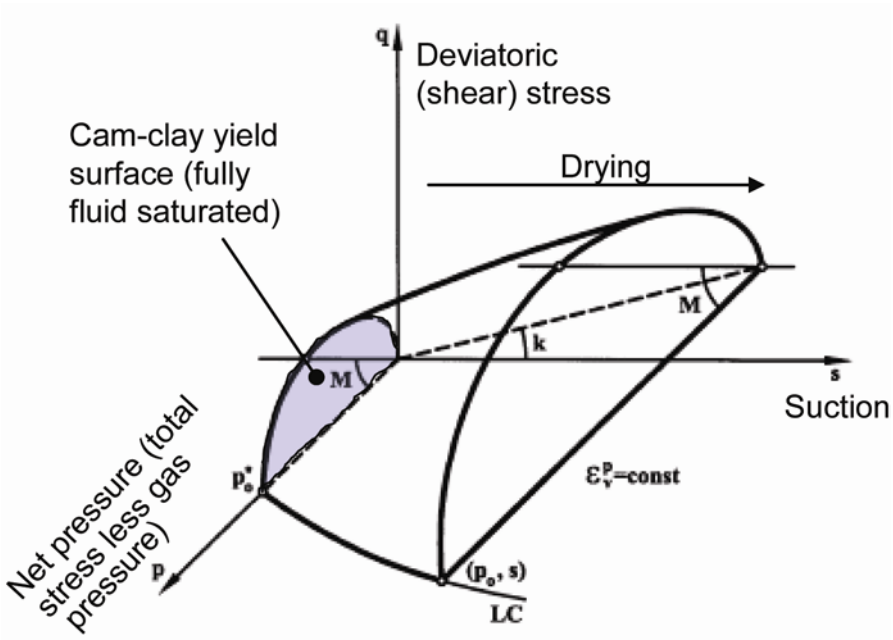

Figure 2.4. BBM constitutive model showing the yield surface in q-p-s space.

2.2.1.2 Microstructural level

The microstructure is controlled by the effective stress.

$$\hat{p} = p + \chi s \tag{2.5}$$

where $\hat{p}$ is mean effective stress, p is the mean net stress, and χ is a constant ($\chi > 0$) which is dependent on saturation. The microstructural strains $d\varepsilon_{vm}^{e}$ are elastic and volumetric, but will induce irreversible strains in the macroporosity. These irreversible macrostructural deformations induced by microstructural effects are considered proportional to the microstructural strain through interaction functions as

$$\mathrm{d}\varepsilon_{v\beta}^{p} = f\mathrm{d}\varepsilon_{vm}^{e} \tag{2.6}$$

where $\varepsilon_{v\beta}^{p}$ is the macrostructural plastic strain arising from the interaction between both structures. Two interaction functions are defined: $f = f_c$ for microstructural compression or shrinkage paths and $f = f_s$ for microstructural swelling paths. These functions can adopt several forms (Sánchez et al., 2005), but they always depend on the ratio p_r/p_0

$$f_c = f_{c0} + f_{c1}\left(p_r / p_0\right)^{n_c} \text{ and } \; f_s = f_{s0} + f_{s1}\left(1 - p_r / p_0\right)^{n_s}, \tag{2.7}$$

or

$$f_c = f_{c0} + f_{c1}\tanh\left[f_{c2}\left(p_r / p_0 - f_{c3}\right)\right] \text{ and } \; f_s = f_{s0} - f_{s1}\tanh\left[f_{s2}\left(p_r / p_0 - f_{s3}\right)\right], \tag{2.8}$$

where f_{ij} and n_i ($i = \{c, s\}$ and $j = \{0,1,2,3\}$) are constants. p_r is an isotropic stress status projected from the current stress status. The ratio p_r/p_0 is a measure of the distance from the current stress state to the yield locus for the macrostructure LC and has the same meaning as the over consolidation ratio for an isotropically consolidated soil. A low p_r/p_0 implies a dense packing of the material, while a high p_r/p_0 implies a looser macrostructure.

2.2.1.3 Elastic Strain

The macrostructural volumetric elastic strain increment for the dual structure model is associated with changes in net mean stress dp and suction ds (Alonso et al., 1999)

$$\mathrm{d}\varepsilon_{vM}^{e} = \frac{1}{K_M}\mathrm{d}p + \frac{1}{K_s}\mathrm{d}s, \tag{2.9}$$

where K_M is the macrostructural bulk modulus and K_s is the macrostructural modulus associated with suction strain. K_M and K_s are defined as

$$K_M = \frac{(1+e_M)p}{\kappa}, \tag{2.10}$$

$$K_s = \frac{(1+e_M)(s+p_{atm})}{\kappa_s}, \tag{2.11}$$

where e_M is macro-structural void ratio, $\kappa = \kappa_0(1 + s\alpha_{ps})$, $\kappa_s = \kappa_{s0}\left(1 + \alpha_{sp}\ln(p_r/p_0)\right)\exp(\alpha_{ss}s)$, κ_0, κ_{s0} are compressibility parameters for changes in net mean stress and suction, respectively, p_{ref} is a reference stress state for relating elastic compressibility to suction, and α_{ps}, α_{sp} and α_{ss} are empirical parameters. The microstructural volumetric strain depends on the change in the microstructural effective stress

$$\mathrm{d}\varepsilon_{vm}^{e} = \frac{1}{K_m}\mathrm{d}\hat{p}, \tag{2.12}$$

where K_m is the microstructural bulk modulus for changes in mean effective stress. Alonso et al. (1999) define two alternative expressions for the microstructural modulus

$$K_m = \frac{(1+e_m)\hat{p}}{\kappa_m} \text{ or } K_m = \frac{e^{\alpha_m \hat{p}}}{\beta_m} \tag{2.13}$$

where e_m is micro-structural void ratio, κ_m, α_m and β_m are compressibility parameters. Thermal strains are purely volumetric

$$\mathrm{d}\varepsilon_{v}^{T} = (\alpha_0 + 2\alpha_2\Delta T)\mathrm{d}T, \tag{2.14}$$

where α_0 and α_2 are material parameters corresponding to a temperature-dependent volumetric thermal expansion coefficient and T is temperature. The deviatoric elastic strain increment is defined as

$$\mathrm{d}\varepsilon_{q}^{e} = \frac{1}{3G}\mathrm{d}q, \tag{2.15}$$

where G is the shear modulus and may be obtained using a constant Poisson ratio ν in

$$G = \frac{3(1-2\nu)}{2(1+\nu)}K_M. \tag{2.16}$$

2.2.1.4 Plastic Strain

Macrostructural plastic strain occurs by two possible mechanisms: either when the stress lies on the LC yield surface, or as a result of microstructural shrinkage/swelling. While the plastic strain by

microstructural shrinkage/swelling is described by Equation 2.5, the LC plastic strains are obtained from the plastic flow rule

$$\mathrm{d}\varepsilon_{vLC}^{p} = \mathrm{d}\Lambda \frac{\partial g_{LC}}{\partial p}, \tag{2.17}$$

$$\mathrm{d}\varepsilon_{qLC}^{p} = \mathrm{d}\Lambda \frac{\partial g_{LC}}{\partial q}, \tag{2.18}$$

where $\mathrm{d}\Lambda$ is the plastic multiplier obtained from the consistency condition $\mathrm{d}f_{LC} = 0$ (recall Eq. 2.2). The calculation of the plastic multiplier $\mathrm{d}\Lambda$ is detailed in Rutqvist et al. (2011). The total plastic volumetric strain is the sum of both plastic mechanisms

$$\mathrm{d}\varepsilon_{v}^{p} = \mathrm{d}\varepsilon_{vLC}^{p} + \mathrm{d}\varepsilon_{v\beta}^{p} \tag{2.19}$$

The hardening variable of the macrostructure - the pre-consolidation pressure p_0^* - depends on the total plastic volumetric strain ε_v^p as

$$\frac{\mathrm{d}p_0^*}{p_0^*} = \frac{(1+e)\mathrm{d}\varepsilon_v^p}{\lambda(0)-\kappa}. \tag{2.20}$$

2.2.2 Swelling pressure test

The swelling pressure test is used to investigate the swelling capacity of expansive soils, which can be placed as a buffer in EBS to isolate the radioactive waste. In this section, we test the dual structure model by modeling a laboratory experiment carried out by Romero (1999) on a sample of Boom clay pellets. The microstructure in these materials is associated to the high density pellets (dry density 1.96 Mg/m^3), and the macrostructure corresponds to the granular-like arrangement of these pellets (dry density 1.37 Mg/m^3) with macro-pores between the pellets. Table 2.1 presents the values of soil parameters and initial values of state variables which are calibrated and suggested by Sánchez et al. (2005).

Table 2.1. Parameters used for swelling pressure test (Sánchez et al., 2005)

Parameters defining the Barcelona basic model for macrostructural behavior						
$\kappa = 0.02$	$\kappa_s = 0.01$	$\lambda(0) = 0.65$	$p_c = 0.01$ MPa	$r = 0.78$	$\zeta = 5$ MPa^{-1}	$p_0^* = 0.11$ MPa
Parameters defining the law for microstructural behavior						
$\kappa_m = 0.01$	$\chi = 1$					
Interaction functions						
$f_c = -0.10 + 1.10\left(\frac{p_r}{p_0}\right)^{0.5}$		$f_s = -0.10 + 1.1\left(1 - \frac{p_r}{p_0}\right)^2$				
$e_{macro} = 0.6$		$e_{micro} = 0.35$				

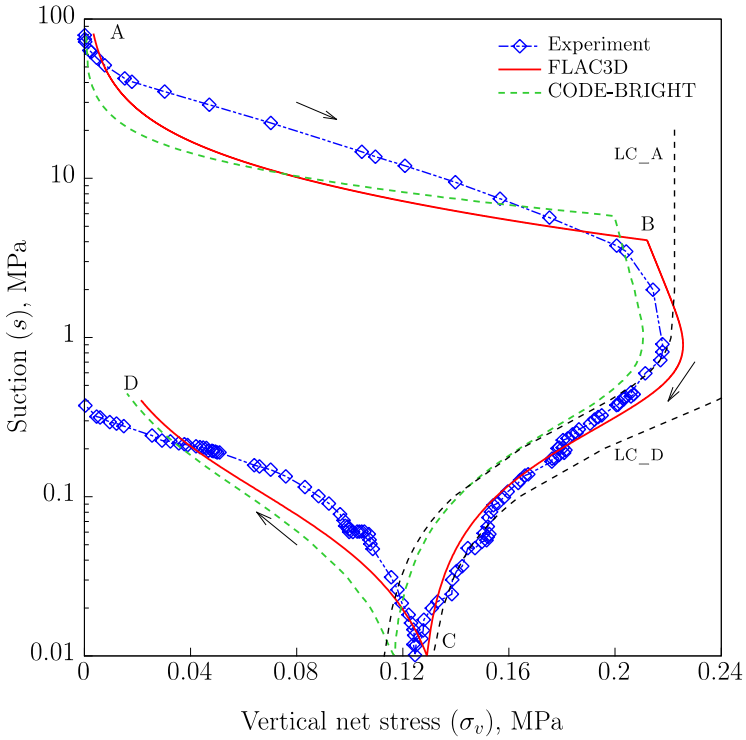

Figure 2.5. Observed (Romero, 1999) and computed stress path in the σ_v–s plane. LC_A (LC_D) represents the loading-collapse yield surface corresponding to the stress state at point A (point D) (calculated by FLAC3D). To the left of LC_A (LC_D) is elastic domain while to the right of LC_A (LC_D) corresponds to the plastic domain. The result noted as "CODE-BRIGHT" presents the work by Sánchez et al. (2005).

This swelling pressure test was operated under constant volume conditions, while the suction (s) was controlled as external loading changes. In Figure 2.5, the observed behavior during the test (noted as "Experiment") and the numerical simulation results (noted as "FLAC3D") are displayed with vertical net stress-suction (σ_v–s) path. The same simulation done by CODE-BRIGHT (Sánchez et al. 2005) is also presented in Figure 2.5 for comparison.

The experiment includes two loading steps. It started with an initial suction of 80 MPa and a low vertical stress (σ_v) (point A). First, a wetting path was followed up by decreasing the suction to 0.01 MPa (point C). In the second step (C-D), the sample was subjected to drying, up to a maximum suction of 0.4 MPa.

The numerical analysis has been carried out prescribing the same suction changes as in the test. Figure 2.6 shows the evolution of the hardening parameter, p_0^*, in the simulation, and Figure 2.7 displays the evolution of the interaction functions f_c and f_s. Three phases can be observed:

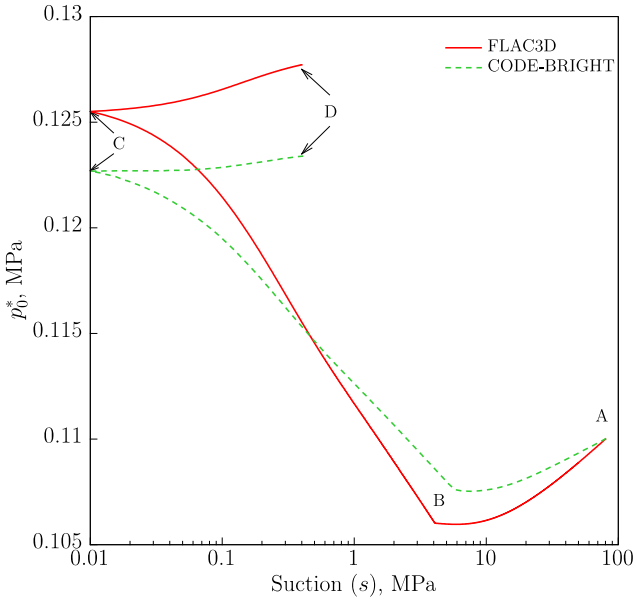

Figure 2.6. Evolution of the hardening parameter, p_0^*, in the simulation. The result noted as "CODE-BRIGHT" presents the work by Sánchez et al. (2005).

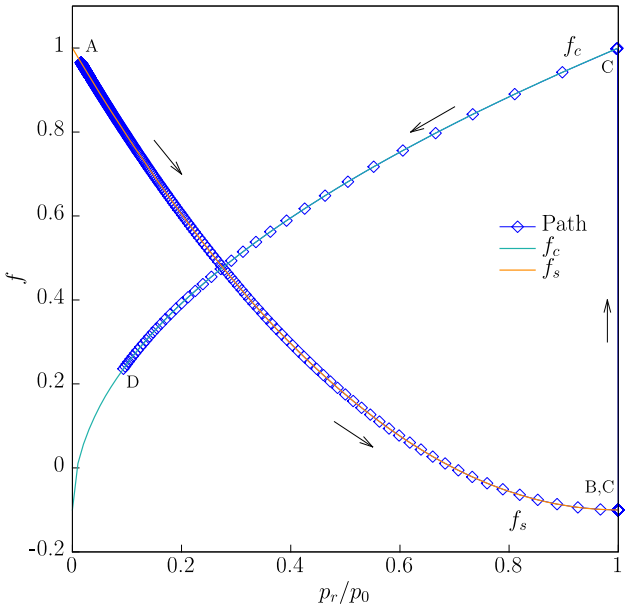

Figure 2.7. Evolution of the f_c and f_s interaction functions. (The function in A-B stage is plotted with every 2000th point, and the one in C-D stage is plotted with every 100th point.)

- From A to B: During this period, the suction decreases from 80 MPa to about 4MPa. When computation starts at point A, the initial collapse yield surface is at the position where LC_A locates (Figure 2.5). Thus, the initial state of material is inside the elastic domain of the macrostructure. In this stage, the material sample remains inside the LC yield surface but suction reduction induces that the microstructural-swelling (ms) mechanism is active. As a result, the

stress increases to compensate the swelling strains. The ms interaction function f_s is positive during most of this stage (Figure 2.7), which implies the induced macrostructural plastic strains due to ms mechanism are in expansion. The hardening parameter, p_0^*, decreases as well (Figure 2.6) and the material becomes a more open macrostructure (the structure is looser than before). The LC yield curve moves from the initial position LC_A to the left where point B locates. Negative values of f_s are obtained and result in the very slight change of tendency of p_0^* just before reaching point B (close to collapse). Point B corresponds to the contact point between the stress path and the LC curve.

- From B to C: During this period, the suction continues decreasing to 0.01 MPa. From point B, a collapse of the macrostructure occurs (plastic yield surface of macro-structures is reached) with a hardening of the material (an increase of p_0^* in Figure 2.6).
- Finally from C to D, the suction increases, inducing the microstructural-contraction (mc) mechanism is active. The LC yield curve moves right to the final position LC_D with a increase of hardening parameter, p_0^*. This corresponds to compressive plastic macrostructural strains associated with macrostructural hardening, and the final state of the sample is a denser macrostructure.

The model can reproduce satisfactorily the main trends observed during the swelling pressure test. The computation results obtained by our implementation (FLAC3D) is close to the result by CODE-BRIGHT which simulator used by the model developers (Sánchez et al. 2005). The fact that the results are slightly different might be a result of difference in numerical methods, including integration algorithms used in different simulators are distinct. The hardening of parameter p_0^* we obtained is higher than Sánchez et al. (2005) simulated. Moreover, it is observed that the stress path calculated with FLAC3D is dependent on the value of initial vertical stress, which may be due to the high non-linearity of BExM.

2.2.3 Cyclic wetting-drying test

In this section, we model cyclic wetting-drying laboratory experiments carried out by Pousada (1982). This kind of test provides valuable information on the behavior of expansive soil subjected to cyclic suction changes. The samples were prepared with a dry density of 1.34 Mg/m^3 and with an initial water content of 24%. Two tests have been operated under oedometric conditions at two different vertical stress levels. Then samples were subjected to six wetting-drying suction cycles (12 loading-unloading steps in total) with suction changing from 0.2 to 1.7 MPa and back, in which expansive clays show a non-reversible behavior. Table 2.2 summarizes the parameters of the dual structure model resulting from the calibration of the laboratory experiments.

Table 2.2. Parameters used for cyclic wetting-drying tests (Sánchez et al., 2005).

Parameters defining the Barcelona basic model for macrostructural behavior
$\kappa = 0.05$ $\kappa_s = 0.01$ $\lambda(0) = 0.065$ $p_c = 0.01$ MPa $r = 0.96$ $\zeta = 0.2$ MPa^{-1} $p_0^* = 0.11$MPa
Parameters defining the law for microstructural behavior
$\alpha_m = 0.8$ MPa^{-1} $\beta_m = 0.02$ MPa^{-1} $\chi = 1$
Interaction functions
$f_c = 1.6 + 0.6 \tanh\left[10\left(\frac{p_r}{p_0} - 0.54\right)\right]$ $f_s = 1.6 - 0.6 \tanh\left[10\left(\frac{p_r}{p_0} - 0.54\right)\right]$
$e_{macro} = 0.55$ $e_{micro} = 0.45$

The experimentally observed responses of the material at two different vertical stresses (0.01 and 0.1 MPa) are presented in terms of volumetric deformations (Figures 2.8(a) and 2.9(a)) and compared with the numerical results with FLAC3D. Estimations of the micro- and macro-void ratios calculated during the numerical simulations using the dual structure model are plotted as well in both figures. The simulation results obtained are good in qualitative terms with experiment data. The upper points in each figure represent the strains or deformation associated with the suction reduced to 0.2 MPa, while the lower points correspond to the state for suction up to 1.7 MPa. A are in agreement is obtained between simulated and observed volumetric deformations for the sample. The microstructural behavior is reversible and the changes in the microstructural void ratio are not greatly affected by the stress level (Figures 2.8(a) and 2.9(a)). On the other hand, the macrostructural void ratio is influenced by the values of applied stress. This can be attributed to the increased difficulty of modifying the macrostructural arrangement when the material confinement is higher. With cycles accumulate, the increments of the irreversible strains decrease as well in both tests. Figure 2.8(b) and 2.9(b) display the evolution of the micro-macro interaction function for first two cycles of suction changes. The tests started at the initial position A. Then suction decreases, so ms mechanism occurs (positive value of f_s function), inducing expansive macrostructural plastic strains (the path curves in Figures 2.8(b) and 2.9(b)). During the drying path, the sample shrinks with activate mc mechanism. Due to this effect (with positive interaction function f_c), the external suction change induces compressive macrostructural plastic strains.

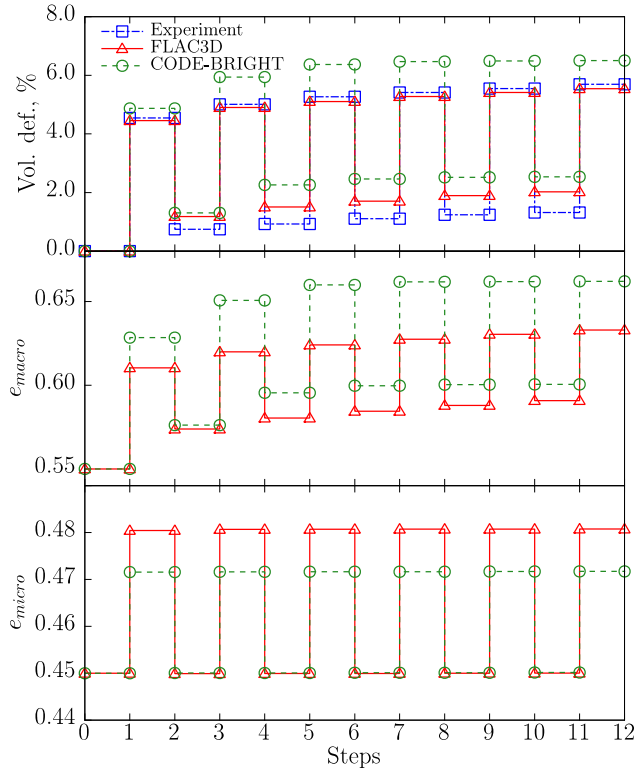

a)

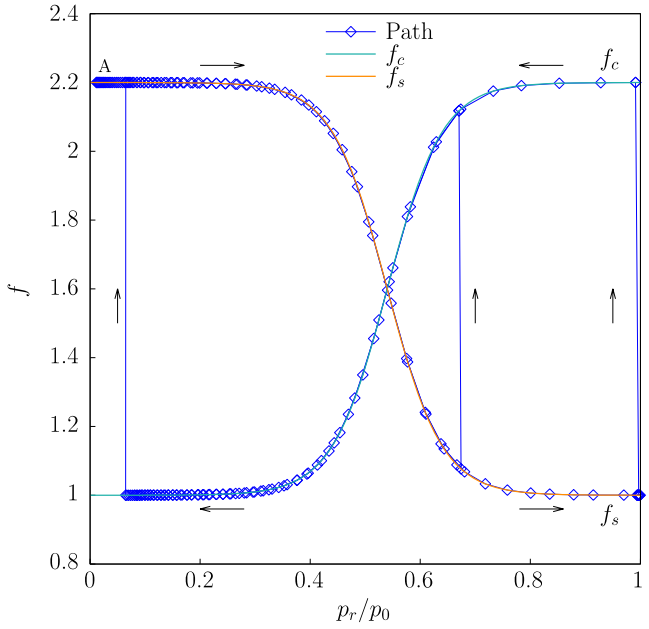

b)

Figure 2.8. Observed and computed results of cyclic suction loading test with $\sigma_v = 0.01$ MPa. (a) Values of volumetric deformations (observed and computed), micro- and macro-void ratios induced by loading-unloading steps. (b) Evolution of the interaction functions for first two cycles of suction changes (plotted with every 200th points during each loading cycle).

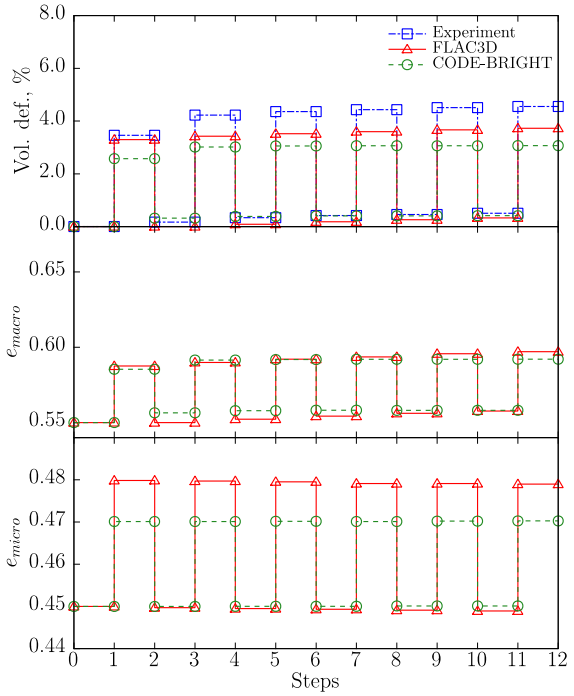

a)

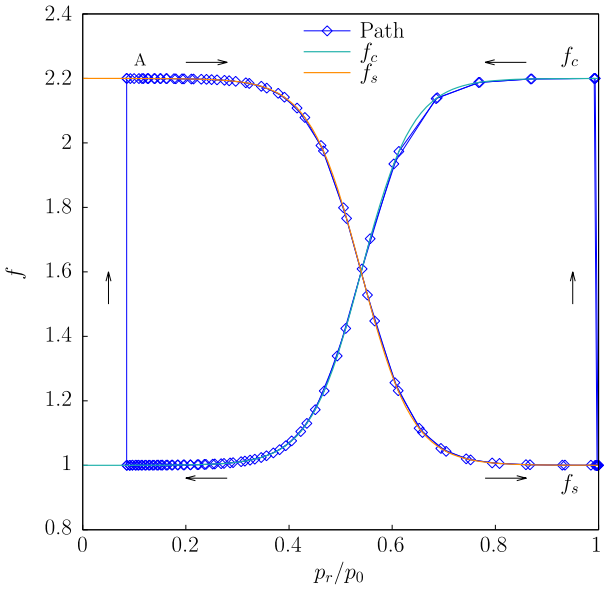

b)

Figure 2.9. Observed and computed results of cyclic suction loading test with $\sigma_v = 0.1$ MPa. (a) Values of volumetric deformations (observed and computed), micro- and macro-void ratios induced by loading-unloading steps. (b) Evolution of the interaction functions for first two cycles of suction changes (plotted with every 200th points during each loading cycle).

The model implemented on TOUGHREACT-FLAC3D can satisfactorily reproduce the main trends observed during the cyclic wetting-drying tests. The evolution of the micro-macro interaction function (Figures 2.8(b) and 2.9(b), we obtain from the simulation with FLAC3D is quite similar with the results by CODE-BRIGHT (Sánchez et al. 2005). To be clear, here we do not present their results of interaction functions. However, other mechanical deformation results by two simulators are slightly different (Figures 2.8(a) and 2.9(a)). The micro-void ratios we obtain at suction of 0.2 MPa in both experiments are higher than their results. The macro-void ratios we obtain in the test under low vertical stress ($\sigma_v = 0.01$ MPa) are lower than CODE-BRIGHT's results, while two simulators obtain close results of macro-void ratio results in the test under high vertical stress ($\sigma_v = 0.1$ MPa). The volumetric deformations we obtain match better with experiment data than theirs.

2.2.4 Tests with combination of loading paths

Two oedometer tests carried out at Centre for Energy, Environment and Technology (CIEMAT) with suction control are simulated with BExM in this section. Samples were compacted statically to a dry density of 1.70±0.02 Mg/m^3 with the material at hygroscopic water content. In the tests, a combination of loading paths at constant suction and wetting and drying paths at constant load were applied. A special technique (axistranslation technique) required by suction control procedure has been used in the oedometer cell. Suction values have been applied by prescribing a value of the relative humidity of the atmosphere in contact with the sample. The oedometer cell used in this case is depicted in Figure 2.10.

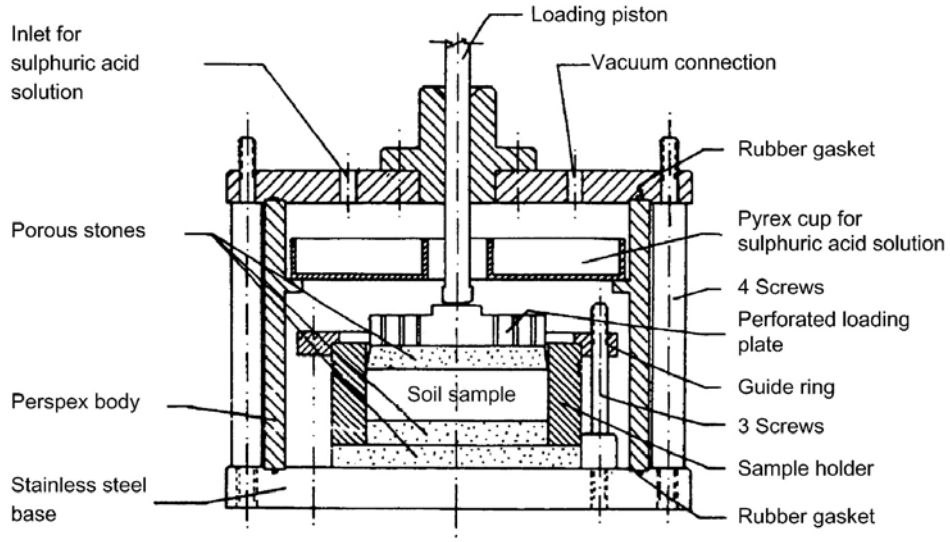

Figure 2.10. Schematic layout of the high-suction oedometer used in the CIEMAT laboratory (Esteban, 1990)

Table 2.3 presents the initial conditions, in terms of dry densities (ρ_d) and water contents (w), and the stress paths, in terms of applied suction and vertical loads, of two tests performed at CIEMAT laboratory. In order to use a logarithmic scale a constant value of 0.1 MPa has been added to all suction values plotted in Figure 2.11. The same convention has been used in other figures (Figures 2.12, 2.13, 2.15 and 2.16) plotted with suction.

Table 2.3. Stress paths of the tests, in which a combination of loading paths was applied. Tests performed at CIEMAT laboratory. (Lloret et al., 2003)

Test	Initial conditions		Path							
	ρ_d Mg/m^3	w %	A		B		C(S1) or D(S5)		E	
			σ_v Mpa	s Mpa	σ_v Mpa	s Mpa	σ_v Mpa	s Mpa	σ_v Mpa	s Mpa
S1	1.72	13.0	0.1	138	0.1	550	5.1	460	5.1	0
S5	1.72	13.2	0.1	138	0.1	520	0.1	0	5.0	0

The parameters of BExM used in the modelling are shown in Table 2.4. As Lloret et al. (2003) illustrated, the calibration of the material parameters for compacted bentonite was determined by the behavior of tests S1 and S5.

Table 2.4. Parameters used for combination of loading paths tests (Lloret et al., 2003).

Parameters defining the Barcelona basic model for macrostructural behavior $\kappa = 0.005$ $\kappa_s = 0.001$ $\lambda(0) = 0.08$ $p_c = 0.5$ Mpa $r = 0.90$ $\zeta = 1$ MPa^{-1} $p_0^* = 12$ MPa
Parameters defining the law for microstructural behavior $\alpha_m = 0.021$ MPa^{-1} $\beta_m = 2.3 \times 10^{-3}$ MPa^{-1} $\chi = 1$
Interaction functions $f_c = 1 + 0.9 \tanh\left[20\left(\frac{p_r}{p_0} - 0.25\right)\right]$ $f_s = 0.8 - 1.1 \tanh\left[20\left(\frac{p_r}{p_0} - 0.25\right)\right]$ $e_{macro} = 0.11$ $e_{micro} = 0.45$

Here we present the numerical analysis on tests S1 and S5, which can be compared with the corresponding experimental results. The two tests share the same initial and final generalized stress states but their trajectories are different (Figure 2.11). Test S1 was loaded up to a 5.1 MPa vertical load under a high suction of 550 MPa and was then wetted to full saturation. In contrast, test S5 was first wetted to saturation at a low vertical stress of 0.1 MPa and then was loaded to a vertical stress of 5.0 MPa. Figure 2.12 shows the computed variation of void ratio over the stress paths and over suction changes for the two tests, together with the experimental results.

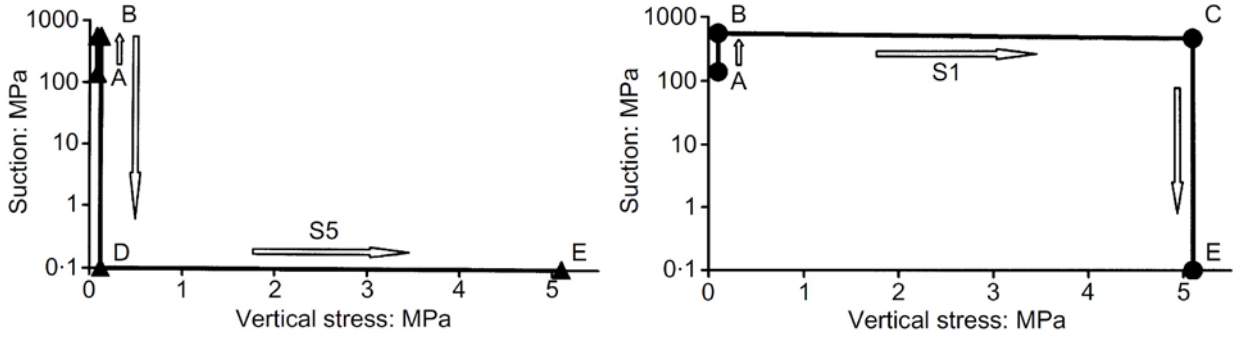

a) b)

Figure 2.11. Stress paths of tests (a) S5 and (b) S1 from Lloret et al.(2003)

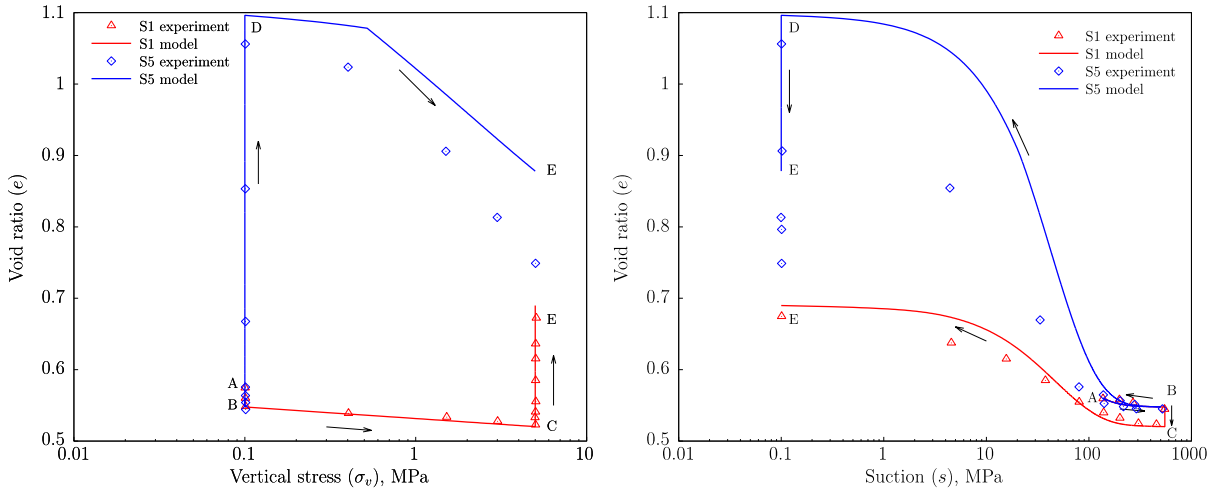

a) b)

Figure 2.12. Experimental results and computed variation of void ratio for tests S1 and S5: (a) variation over stress paths; (b) variation over suction changes.

Figure 2.12 presents the evolution of total void ratio for test S5 against vertical stress change (Figure 2.12 (a) and against suction changes (Figure 2.12 (b)). The evolution of the microstructural and macrostructural void ratio computed for test S5 is displayed in Figure 2.13. Figure 2.14 shows the evolution of the interaction functions during the test S5. The first drying process (from A to B) does not induce much changes of total void ratio (Figures 2.12 (a) and 2.12 (b)) as well as micro- and macro-void ratio changes (Figure 2.13). With the reduction of suction, both micro- and macro-structures contract during this period. Since the stiffness is high at this stage, due to high suction, the compressive strains of both structures are small. The interaction effect between two scales is low with a small value of f_c (Figure 2.14). During the following swelling stage (path B-D), the microstructure swells, inducing larger plastic strains in the macrostructure (Figure 2.13) because of the positive value of the interaction function f_s (Figure 2.14). As a result of that, the total void ratio during this stage changes from about 0.55 to 1.1 (Figure 2.12). During the final loading stage (path D-E), the specimen is already saturated, so the external loading induces small compressive strains. In contrast, the compression of the macrostructure is significant, which is dominant during this stage.

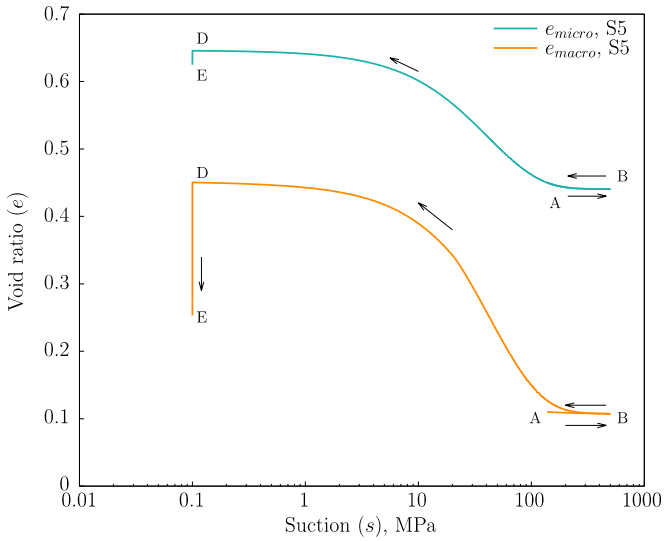

Figure 2.13. Evolution of computed microstructural and macrostructural void ratio for test S5.

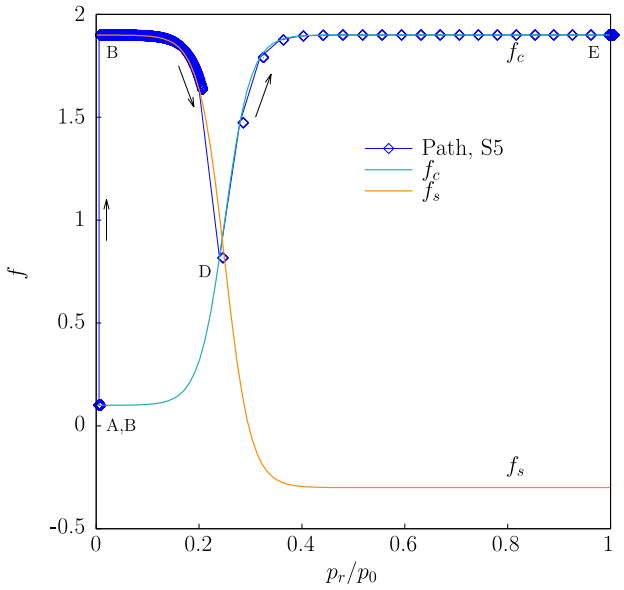

Figure 2.14. Interaction functions involved in the various stages of test S5.

The yield point observed and computed (between points D and E in Figure 2.12(a)) corresponds to the crossing of the LC yield curve during the final loading stage (from D to E). The evolution of the hardening parameter, p_0^* is plotted in Figure 2.15. This parameter is reduced during the swelling stage (path B-D) and then increases in the subsequent loading stage (path D-E).

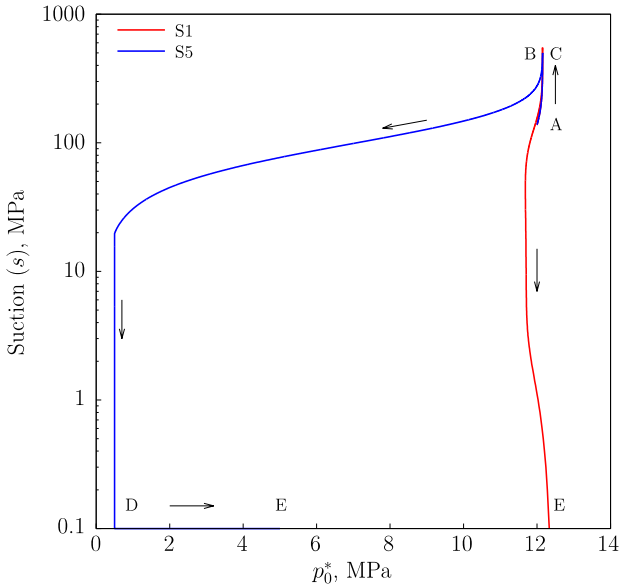

Figure 2.15. Evolution of hardening parameter p_0^* for tests S1 and S5.

The behavior of sample S1 is quite different from the sample S5. The evolution of microstructural strains and macrostructural strains is presented in Figure 2.16, and the evolution of total void ratio against vertical stress change and against suction changes for test S1 is presented in Figure 2.12. During the first drying stage (path A to B) and subsequent loading stage (path B to C), the deformations of microstructure and macrostructure are both very small, inducing the change of total void ratio is also small (Figure 2.12). During the swelling stage (path C to E), the microstructural strains are significant. However, the macrostructural strains are small. The plot of interaction function (Figure 2.17) shows the macro-strains induced by micro-swelling strains are small contraction because of the negative values obtained before reaching point E. As a result, the total void ratio changes from about 0.52 to 0.7 during this stage (Figure 2.12). The evolution of the hardening parameter for test S1 has also been plotted in Figure 2.15 and the changes are very slight.

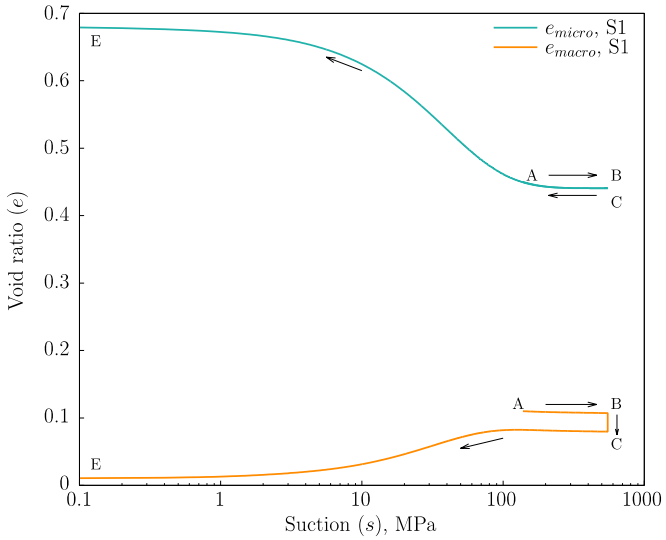

Figure 2.16. Evolution of computed microstructural and microstructural void ratio for test S1.

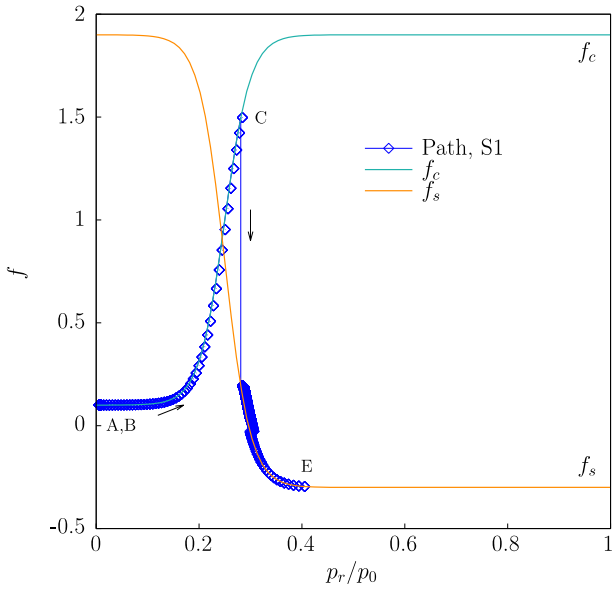

Figure 2.17. Interaction involved in the various stages of test S1.

Good reproduction of behavior between model computation and experimental results was achieved for test S1. However, some deviations are observed at intermediate and final stages of the swelling of test S5, especially the final contraction of S5 is less than the experiment observed (Figure 2.12). The model is capable of simulating observed results with the set of parameters adopted. It takes into account the two levels of structure in the material. Most of the main features of behavior are correctly reproduced and the two levels of structure in the material are taken into account by the model. The limitation of this case is that the model is used one-dimensionally, so the simulations provided by Lloret et al. (2003) and here are under isotropic conditions, which actually cannot represent the stress states in oedometer testing with constrained lateral displacements. The oedometer testing does not provide full information on the stress state of the material, as the horizontal confining stress is not usually measured. In addition, in the case of unsaturated soils, there is also uncertainty regarding the degree of saturation of the soil, which is always unknown, although the retention curves obtained at constant volume may provide an approximate water content for every suction value. These limitations may affect the model calibration on parameters.

2.2.5 Summary and status of BExM in FLAC3D

The dual structure model is implemented into FLAC^{3D} using the UDM option. The model implementation has been validated by modeling one swelling pressure test on Boom clay pellets, two cyclic wetting-drying tests on one type of expansive clay and two tests with combination of loading paths on compacted bentonite samples. Based on the simulation results, the model is capable repoducing the observed behavior of expansive clays during experiments associated with suction changes. The computation results we obtained with BExM agree well with the experiment data, and also follow the same tendency of results presented by BExM developers. In conclusion that the implementation of dual- structure model, BExM, on FLAC^{3D} is validated and can be used for more complicated cases including THM or THMC processes for clays in a repository environment.

2.3 MODELING OF MONT TERRI HE-E EXPERIMENT (DECOVALEX-2015)

The Mont Terri HE-E Experiment focuses on the THM behavior of bentonite barriers in the early nonisothermal resaturation stage and their THM interaction with Opalinus Clay (Figure 2.18). The

objective is to better understand the evolution of a disposal system for high level waste in the early post-closure period, with emphasis on the thermal evolution, buffer resaturation (*in situ* determination of the thermal conductivity of bentonite and its dependency on saturation), pore-water pressure in the near field, and the evolution of swelling pressures in the buffer (Gaus et al., 2014). Because the test is conducted in a micro-tunnel, it is considered a validation, not a demonstration experiment. The heating test involves two types of bentonite buffer materials: (i) a bentonite pellets and (ii) a sand bentonite mixture emplaced in two sections isolated from the rest of the micro-tunnel (Figure 2.18 (b)) by three plugs. The heater-buffer interface is heated to a maximum temperature of 135°C and a temperature of 60–70°C is expected at the buffer-rock interface. A dense instrumentation network was in place in the host rock surrounding the micro-tunnel from a previous experiment testing the impact of ventilation on the clay host rock, and has been improved for the purpose of the HE-E Heater Test (up to 40 piezometers in total); various sensors have also been placed in the buffer material. The heating phase started in the late summer of 2011 and is still ongoing.

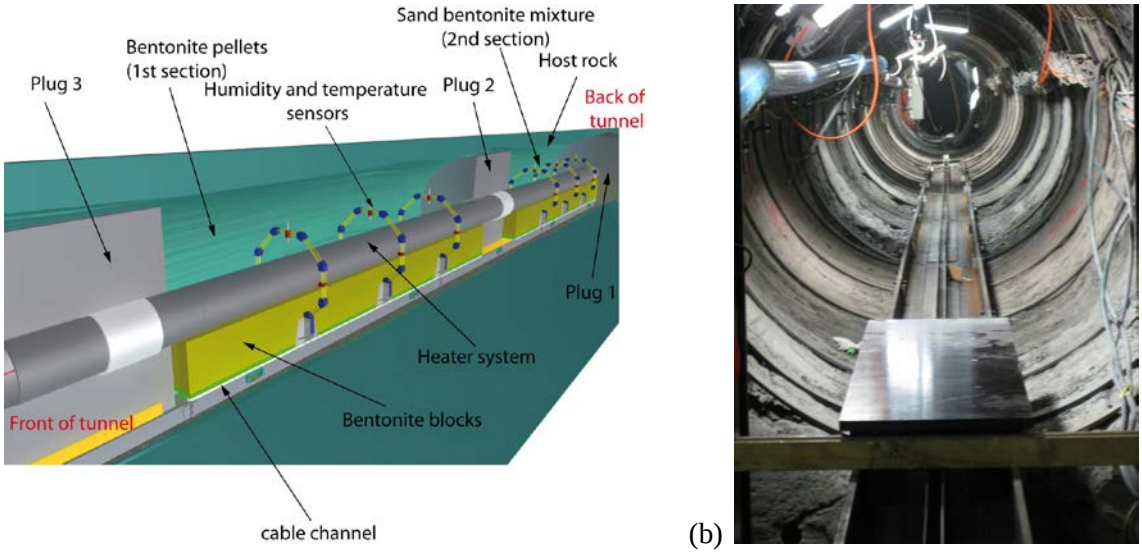

Figure 2.18. (a) Schematic setup of HE-E experiment at Mont Terri and (b) photo of micro-tunnel (Garitte, 2012).

2.3.1 DECOVALEX-2015 Task B1 and international modeling teams

In DECOVALEX-2015 (Task B1), eight international research teams were participating in the modeling of the HE-E experiment. Task B1, which was running over three years (2012 to 2015), was divided into the following steps:

- Step 1a: Opalinus Clay study including HE-D experiment, literature study, processes understanding and parameter determination.
- Step 1b: Buffer material study including CIEMAT column cells, literature study, processes understanding and parameter determination.
- Step 2: HE-E predictive modeling using as-built characteristics and true power load.
- Step 3: HE-E interpretative modeling and forward analysis

Step 1a started in 2012 with the modeling of the previous HE-D experiment for *in situ* characterization of THM material parameters for the Opalinus Clay and was completed in November 2013. The HE-D experiment involved one year of heating of the Opalinus Clay without any bentonite buffer. The modeling of the HE-D experiment and comparison of the TOUGH-FLAC modeling results to the results of other

modeling teams were reported in the FY2013 milestone report titled "Report on THMC modeling of the near field evolution of a generic clay repository: Model validation and demonstration" (Liu et al., 2013). Step 1b, which is a study of buffer material properties through modeling of laboratory experiments on buffer material samples, has been completed by all the modeling teams in DECOVALEX-2015. LBNL's final analysis of the CIEMAT column experiments associated with Step 1b was presented in the FY2014 milestone report entitled "Investigation of Coupled Processes and Impact of High Temperature Limits in Argillite Rock" (Zheng et al., 2014). In FY2015 milestone report titled "Investigation of Coupled Processes and Impact of High Temperature Limits in Argillite Rock" we presented the TOUGH-FLAC model prediction of the Mont Terri HE-E experiment with some initial comparison to field data.

In this section we provide a summary of results related to DECOCALEX-2015 Task B1, Steps 1 to 3, including comparison with other research teams in the DECOVALEX-2015 project. Table 2.5 shows an overview of the eight modeling teams, including their codes and models for Step 1 to 3 in DECOVALEX 2015 Task B1. The predictive analysis involved a blind prediction of the responses during the three years of heating using material properties determined from modeling of the HE-D and column experiments. Then a refined or interpretative analysis was done once the field data had been distributed to the research teams. Finally, the forward analysis involved a prediction of the time to full saturation of the bentonite buffer, if the heating were to be turned off after eight years.

Table 2.5. Modeling teams, codes and models of DECOVALEX-2015 Task B1 related to the Mont Terri HE-E experiment.

Team	Code	HE-D	Column test	HE-E (all 3D THM, excepted CNWRA)		
				Predicted	Refined	Forward
BGR/UFZ	OpenGeoSys	3D THM	2D THM	√	√	√
CAS	EPCA3D	3D THM	3D THM	√	√	-
LBNL	TOUGH-FLAC	3D THM	2D THM	√	√	√
ENSI	OpenGeoSys	3D THM	2D TH	√	-	-
CNSC	COMSOL	3D THM	1D THM	√	-	-
JAEA	THAMES	3D THM	2D THM	√	-	-
KAERI	FLAC	3D THM	2D TH	√	√	-
CNWRA	xFlo-FLAC	2D THM	2D THM	√	√	√

2.3.2 Modeling of the HE-D Experiment for THM Characterization of Opalinus Clay

Step 1 of DECOVALEX-2015 involved modeling of the Mont Terri HE-D experiment with main purpose of determining and validating in situ THM properties of Opalinus Clay. The HE-D experiment was conducted between March 2004 and June 2005 by *in situ* heating of Opalinus Clay from two heaters placed in a horizontal borehole (Figure 2.19) (Wileveau, 2005; Gens et al., 2007). Around this heating borehole, about 30 temperature sensors, 10 water pressure sensors, and 3 extensometers were placed, which allowed for monitoring the evolution of the variables induced by the heating (Wileveau, 2005; Gens et al., 2007). Approximately one month after installation, the heaters were switched on with a total power of 650 W (325 W per heater). The heaters were then left under constant power for 90 days. Afterwards, the power was increased threefold, to 1950 W (975 W per heater), and maintained at that level for a further 248 days. At the end of this second heating stage, the heaters were switched off and the clay was allowed to cool down. Temperature, pore pressure, and deformation were measured throughout. In Figure 2.19, the positions of the main temperature and pore pressure sensors with respect to the heater axis are indicated.

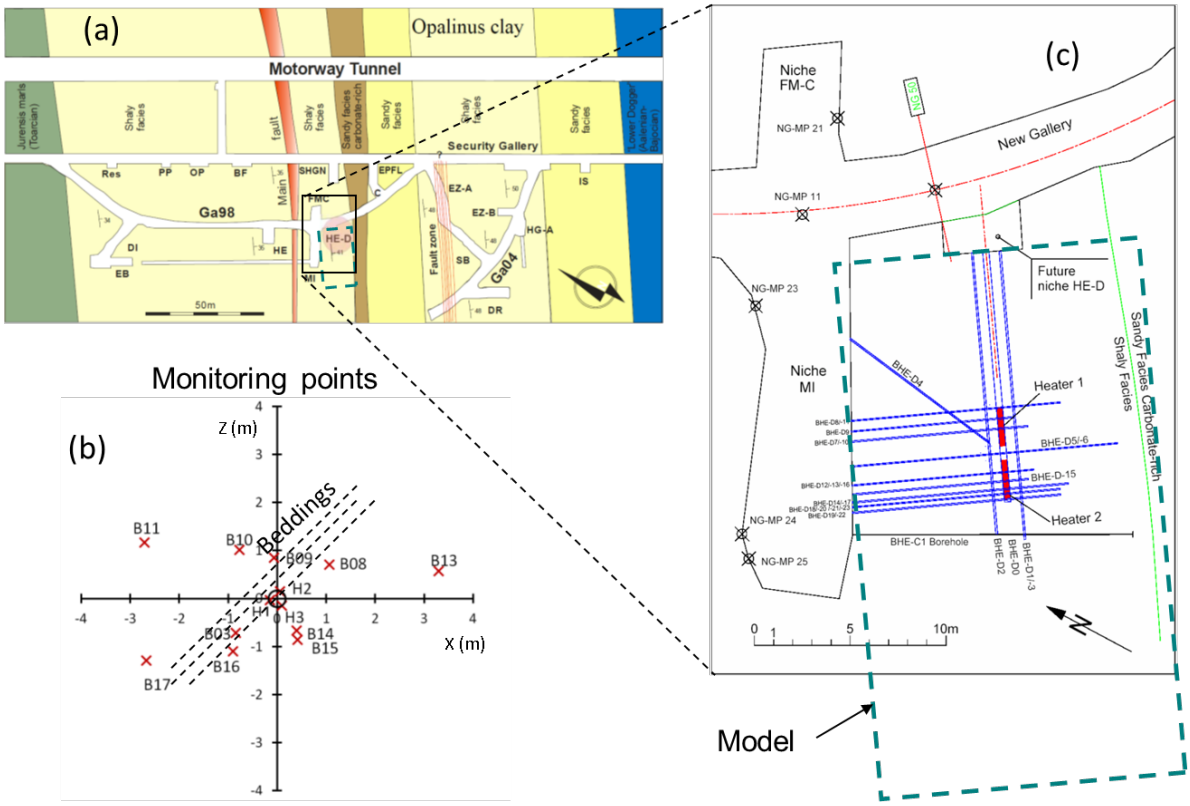

Figure 2.19. Layout of the HE-D experiment including. (a) Horizontal cross-section showing the location of the HE-D experiment in the Mont Terri URL. (b) Vertical cross-section showing monitoring points and directions of bedding planes, and (c) top view of experiment including monitoring borehole layout (Wileveau, 2005).

2.3.2.1 LBNL Model Setup of HE-D experiment

We modeled the HE-D experiment using the TOUGH-FLAC simulator employing an anisotropic material model considering the beddings of the Opalinus Clay. To accurately model anisotropic thermal behavior in TOUGH2, the mesh was inclined along with the beddings (Figure 2.20). Anisotropic mechanical material behavior is simulated using a so-called ubiquitous joint model, available in FLAC3D, with properties derived from published work (Corkum and Martin, 2007). These included parameters for the

FLAC3D ubiquitous joint model defining anisotropic strength properties, a bulk modulus of 4.17 GPa, and a shear modulus 1.92 GPa. The thermal expansion coefficient was set to 1.4×10^{-5} °C^{-1} which is a representative isotropic average value of the Opalinus Clay (Gens et al., 2007). Finally, we assigned an isotropic permeability of 5×10^{-20} m^2, and pore compressibility of 1×10^{-9} Pa^{-1}, based on Gens et al. (2007). In the simulation presented here the permeability was set to an isotropic value 5×10^{-20} m^2 according to previous simulations by Gens et al. (2007), although permeability at the Mont Terri is anisotropic by a factor of about 4.

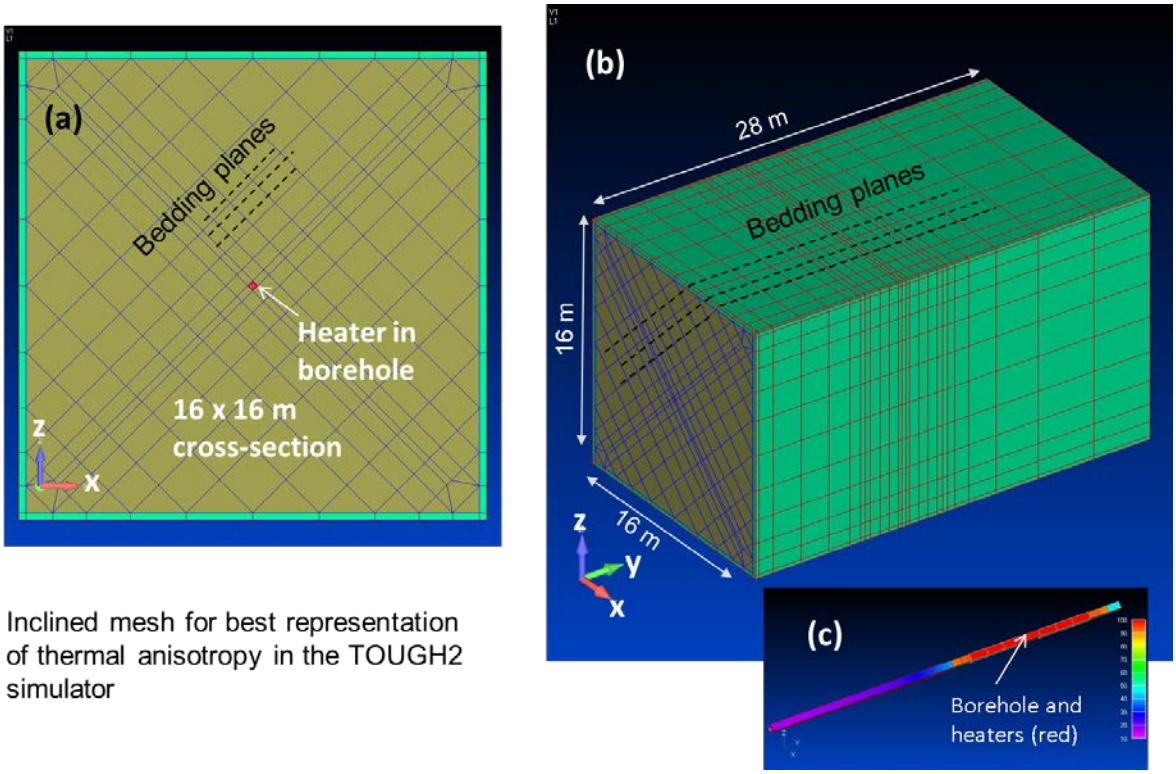

Figure 2.20. TOUGH-FLAC model for the analysis of coupled THM processes at the HE-D experiment.. (a) vertical cross-section showing the inclined mesh along bedding, (b) Entire 3D model, and (c) view of the micro-tunnel with heater shown in red.

The initial hydraulic and thermal conditions for the model simulation were 0.9 MPa in pore fluid pressure and 15°C in temperature within the host rock. The 0.9 MPa of pore pressure is not under hydrostatic conditions, and the process is affected by the existing tunnel system at the site. A stress field was applied based on the best estimated Mont Terri *in situ* stresses. The vertical stress was set to 7 MPa, whereas the maximum and minimum horizontal stresses were respectively set to 5 MPa (along x-axis) and 2 MPa (along y-axis, which correspond to the strike of bedding) (Figure 2.20 (b)).

2.3.2.2 LBNL Results with Comparison to HE-D Field Data

The modeling shows that the heating of the rock mass is the driving force for the THM responses in the HE-D experiment. Temperature changes strongly affect hydraulic and mechanical responses whereas

thermal processes are not significantly impacted by the hydraulic and mechanical processes. Heat transfer is dominated by thermal conduction and the temperature evolution can be calculated independently of the hydraulic and mechanical processes. In this case we input the measured heat load and then calibrated the transversely anisotropic thermal conductivity until a are in agreement was obtained between simulated and measured temperature evolution at 31 locations in the rock mass. A good overall temperature match was obtained for thermal conductivity parallel to the bedding planes, $K_{\parallel}$ = 2.15 W/m-K, and perpendicular to bedding planes, $K_{\perp}$ = 1.19 W/m-K; a thermal conductivity anisotropy factor, $K_{\parallel}/K_{\perp}$ = 1.8. Moreover, an additional heating-system power loss of 5% was assumed for achieving the best overall match between simulated and measured temperature evolution.

Figure 2.21 shows comparison of LBNL simulated and measured temperature (Figures 2.21 (a) and (b) and pressure (Figure 2.21 (c) and (d)) at two monitoring points (B16 and B15), and strain at another location close to B04. The simulation shows a correlation between temperature and fluid pressure as a result of thermal pressurization, which occurs as a result of the differences in the coefficient of thermal expansion between the fluid and the solid rock. As previously mentioned, a good temperature agreement is achieved using an anisotropic thermal conductivity. A reasonably are in agreement between simulated and measured pressure is achieved with the permeability set to 5×10^{-20} m^2 and a pore compressibility of 1×10^{-9} Pa^{-1}. This pore compressibility was estimated from the elastic properties of the rock assuming uniaxial strain conditions (Rutqvist et al., 2014a). The strain results shown in Figure 2.21(e) were measured from the relative displacement between two anchor points located about 1 m from each other and in the radial direction from the heater hole (represented in Figure 2.21(e) by endpoints of the green line. The fact that these anchor points are located in the radial direction means the radial strain can be back calculated from the relative displacements between these anchor points. The radial strain mainly shows a compression during heating as rock is expanded from the heated borehole.

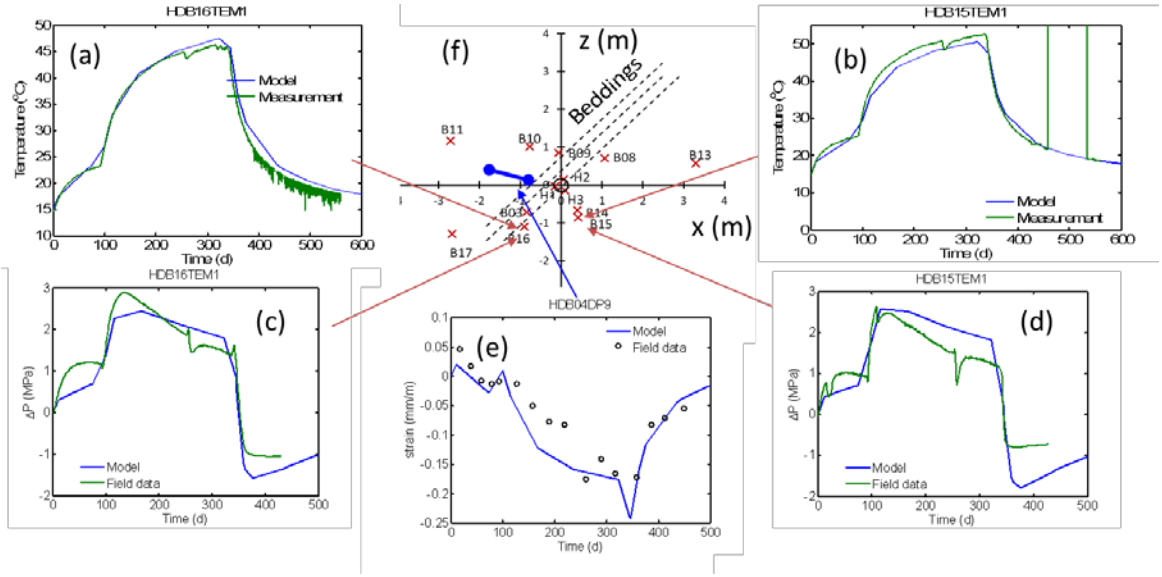

Figure 2.21. Comparison of simulated and measured (a and b) temperature and (c and d) pressure at two monitoring points (B15 and B16) and €strain at a location close to the heater. (f) location of the monitoring points relative to the heater and position of the two anchor points used to estimate the radial strain.

2.3.2.3 Comparison between 8 DECOVALEX-2015 modeling teams and HE-D data

As previously mentioned, a total of eight modeling teams were involved in comparative calculations of the THM processes with different codes (Table 2.5). The comparison of the results for the temperature field shows a are in agreement between the teams and the simulated temperatures are close to the measurements. One example is shown in Figure 2.22 for two temperature sensors. Sensor HEDB03 is located at a distance of 1.11 m away from the center of the heater parallel to bedding, whereas sensor HEDB14 is located 0.775m away perpendicular to bedding. Figure 2.22 shows a are in agreement between the results of the different groups as well as between simulations and observations. The comparison of these sensors also illustrates the effect of the anisotropic heat conductivity of Opalinus clay. Despite the different distance to the heater, both sensors show a similar course of temperature evolution over time. The largest disagreement shown is for one team at sensor HEDB14 in which the temperature was overestimated because the simulation was conducted with an axisymmetric model in which the thermal anisotropy could not be considered. Other comparisons of thermal pressurization and displacements were not as good for temperature, though the main THM responses were captured by all the modelling teams (Garitte, 2016).

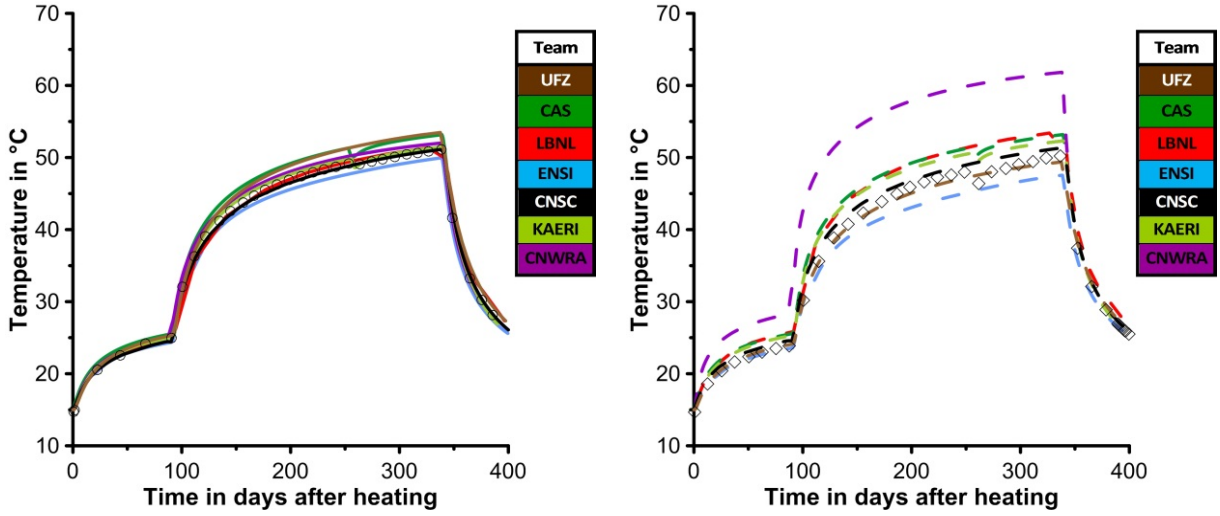

Figure 2.22.Comparison of measurements and model results of for the temperature evolution over time at sensors (a) HEDB03 and (b) HEDB14 (Graupner et al., 2013).

2.3.3 Buffer material characterization using CIEMAT column experiments

In this subsection we summarize the results of the modeling of CIEMAT column experiments (Villar 2012). The modeling of the CIEMAT column experiments are done for characterization of the buffer material. In CIEMAT column experiments, two buffer materials, granular bentonite (or bentonite pellets) and sand/bentonite mixture, were tested. However, in DECOVALEX-2015, only the granular bentonite experiment was required to be modeled by the research teams, whereas it was optional to model the sand/bentonite experiment.

The design of the column experiments mimicked the HE-E conditions, with the height of the column equal to the thickness of the buffer filled between the canister and host rock (Figure 2.23). A heater was placed at the bottom and a cooler was placed at the top of the column, so that the column was heated while the top remains at an ambient temperature of approximately 21.5 ˚C. During the experiments, temperature and relative humidity were measured at three points along the axis of the column (T1, T2, and T3, and Fig. 2.23). The wall of the column is made up of Teflon. The column was wrapped with a layer of foam, which was later replaced with rock wool and BT-LV insulation materials (Villar, 2012).

The power input was monitored as well. In this study, the objectives were to model the fluid flow and heat transfer processes that occur in the experiment, and to calibrate the flow and thermal properties of the two buffer materials against the experimental measurements. The initial modeling of the experiment revealed substantial heat loss through the equipment and it was necessary to consider this heat loss in the numerical modeling. Actually, the model simulation indicated that only about 20% of the power input entered the bentonite sample.

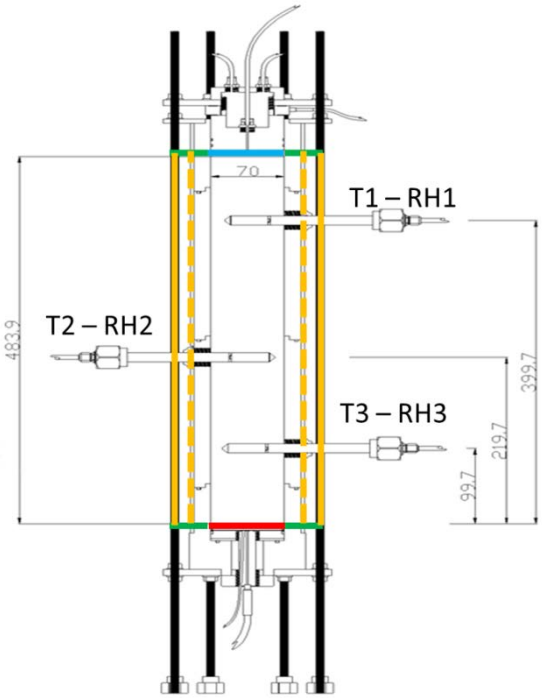

Figure 2.23. Experiment layout of the CIEMAT column test, dimensions given in mm (Garitte, 2016). Heater is in red at the bottom and cooler in blue on top.

2.3.3.1 LBNL model setup of column experiment

A 2D radial symmetric mesh of 9×28 elements was created for the modeling of this column experiment (Figure 2.24). Bentonite is represented in a zone of 4×25 elements (grey zone in Figure 2.24). The multiple stages of the experiment were simulated sequentially and the boundary conditions of each step were adjusted according to the experiment. This also includes the aforementioned addition of more insulation materials after 1566 hours of heating. During the experiment, the hydration valve was closed and therefore no water flowed into the column before the start of heating. Fixed temperature conditions at the heater were simulated by assigning a large heat capacity to the heater elements. To simulate the temperature increase at the heater elements, e.g., from 21.5 to 100 ºC, and from 100 to 140 ºC, a heating rate was applied to the heater element, such that the heating rate equal to the experiment. Hydration was simulated by assigning a constant absolute pressure of 1.1×10^4 Pa at the top boundary.

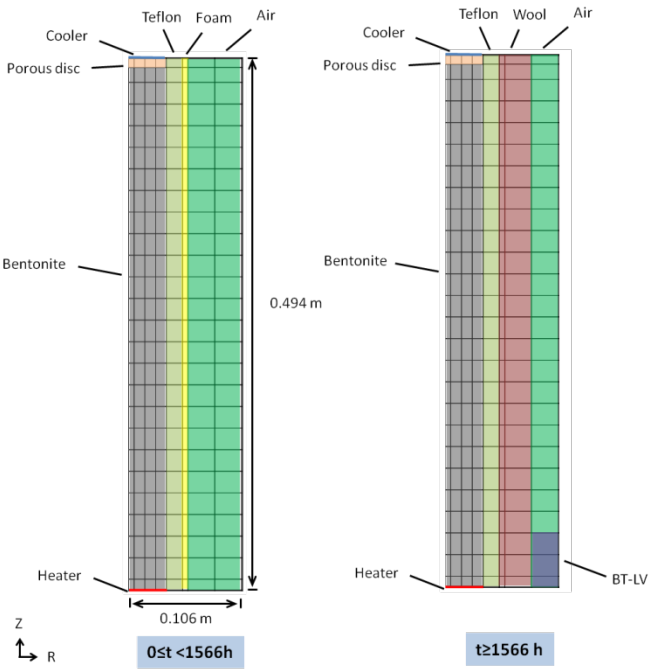

Figure 2.24. Model mesh and the materials represented in the model at different steps for column experiment on bentonite pellets. The reference time (t = 0) is the start of heating.

The granular bentonite has a solid grain density of 2700 kg/m^3 and a porosity of 0.46 (Villar, 2012). The specific heat of the bentonite is 950 J/kgºC. The pores were initially saturated with 22% of water and the measured relative humidity was 40% uniformly along the column. Olivella and Gens (2000) reported that the measured permeabilities of FEBEX and Boom clay samples to gas are about 6-7 orders of magnitude higher than those to liquid. To account for the increased gas permeability, we considered vapor and air diffusion and Klinkenberg effect in the model. A diffusion coefficient of 2.13×10^5 m^2/s was used for both vapor and air and a tortuosity factor of 0.67 was used in the model. An artificial Klinkenberg parameter of a very high value of 2.5×10^{11} Pa was used. This high value of the Klinkenberg parameter was applied to simulate the effect of a very high gas intrinsic permeability.

2.3.3.2 LBNL Back-analysis of THM properties

The model analysis of the column experiment was conducted to back-analyze a number of THM properties of the granular bentonite. The most important parameters back-analyzed were

1) Thermal conductivity of the granular bentonite and its dependency on water saturation was back-calculated by examining the transient and steady state behavior

2) A temperature dependent capillary pressure curve was determined using previous experimental results of water retention and by further model calibration against moisture movements in the column experiment.

3) Calibration of intrinsic permeability against and initial infiltration test on the column

Figure 2.25 shows the best match simulation results and measured data. After the heater was turned on (t=0h), the simulated relative humidity increased rapidly at 10 cm (orange curve on Fig. 2.25a). This is caused by the upward-flowing vapor from the heated zone beneath the sensor. Over time, the relative

humidity decreases at the 10-cm location, as a result of drying that occurred at the 10-cm location caused by continued heating. A discrepancy between the simulated and measured relative humidity appears after 3527 h, when insulation was improved (foam replace by wool, see Fig. 2.24). This might be caused by the fact that the van Genuchten function overestimates the increase of capillary pressure at low water saturations, causing the underestimation of relative humidity at the 10-cm location. The upflow of vapor is evidenced by the continuous increases in relative humidity at the 22- and 40-cm locations (blue and red curves, respectively). Overall, the simulated relative humidity and the temperature evolution (Fig.2.25b) at these three locations are in are in agreement with the measured ones.

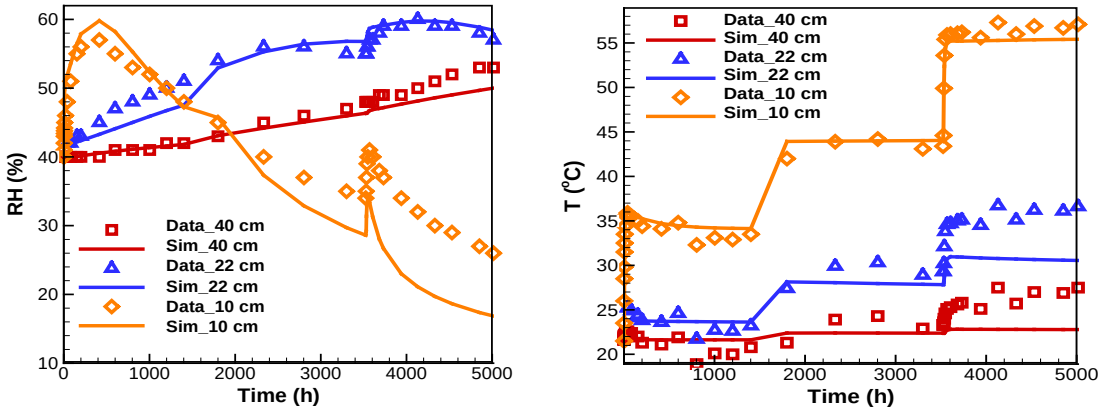

(a) (b)

Figure 2.25. Simulated and measured (a) relative humidity and (b) temperature at 10, 22, and 40 cm from the heater.

2.3.3.3 Comparison between 8 DECOVALEX-2015 modeling teams

Figure 2.26 shows the comparison of relative humidity evolution calculated by eight DECOVALEX-2015 research teams and measured data. Figure 2.26 shows two stages of data and modelling results

1) The initial 5000 hours (208 days) of data during heating that was used to calibrate the THM properties of the bentonite

2) The following 5000 to 20000 hours (208 to 833 days) of data that was given to teams after their modelling and thus represent a model prediction of the longer term resaturation.

The initial 5000 hour part in Figure 2.26 is the same as shown in Figure 2.25 (the yellow diamonds, triangle and circle in Figure 2.26 correspond to the orange, blue and red lines in Figure 2.26 (b). The modelling teams could model the general responses of drying near the heat source and wetting near the cold and end of the column and infiltration boundary. Note that there was no infiltration before 5000 days, meaning that increased relative humidity at the cold end as seen in Figure 2.25 (a) (blue triangle) is a result of vapor transport in the gas phase from the hot end towards the cold end where condensation takes place. The overall agreement between models and measurement is very good. This is also clear from Figure 2.27, which shows a are in agreement of the overall relative humidity distribution profile at 5000 and 10000 hours.

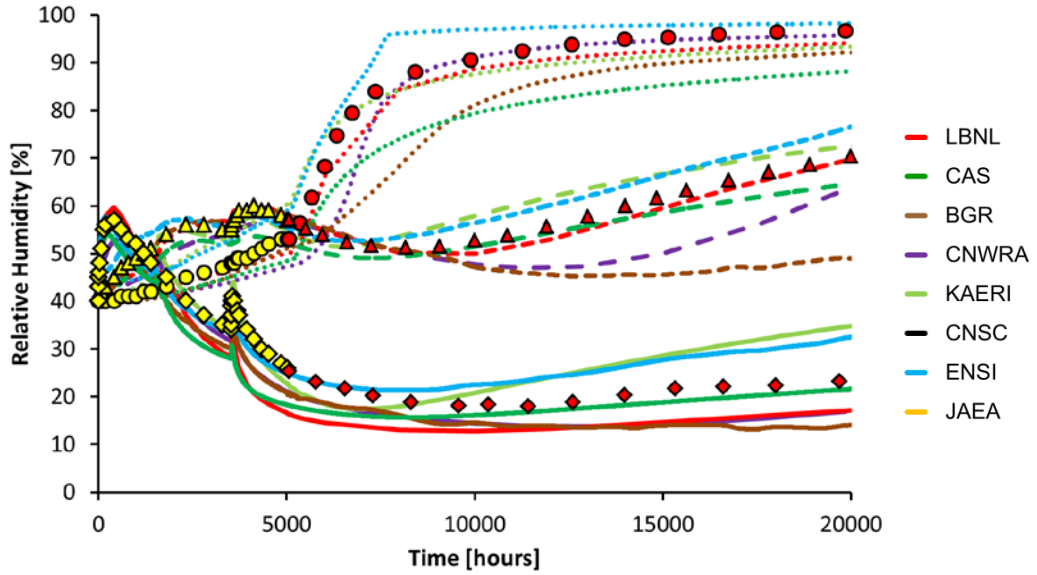

Figure 2.26. Measured and modelled relative humidity in the column at RH1 (circles and dotted lines), RH2 (triangles and dashed lines) and RH3 (diamonds and full lines) during the heating and hydration phase. (Yellow measurement dots, before hydration phase were used by the teams to calibrate the models; red measurement dots were acquired during the hydration phase and the corresponding modelling results are predicting results) (Garitte, 2016).

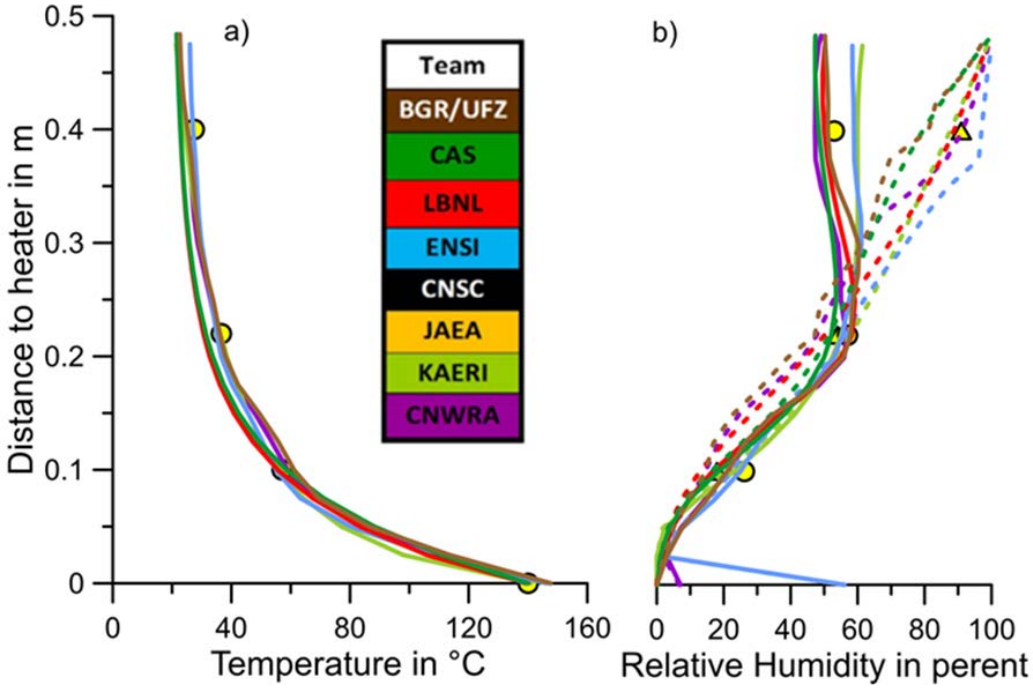

Figure 2.27. Vertical measured and modelled profiles for (a) temperature at 5000 hours and (b) relative humidity after 5000 and 10000 hours. The measurements at 5000 hours are shown as discrete points marked with circles whereas measured relative humidity at 10000 hours are marked with triangles. Solid lines are modeling results at 5000 hours and dashed lines are relative humidity modeling results at 10000 hours (Garitte, 2016).

2.3.4 Predictive Modeling of the Terri HE-E experiment

In the predictive modeling of the HE-E experiment, the models applied and input material parameters were based on those determined and validated using data from the HE-D experiment and the CIEMAT laboratory column experiment as described in the previous section.

2.3.4.1 LBNL Model setup of the Mont Terri HE-E experiment

Figure 2.28 shows a 3D model grid for the HE-E experiment and its location within the Mont Terri URL, whereas Figure 2.29 shows more details of the materials in a vertical cross-section that is also the geometry of a 2D plane strain model. It is a half symmetric model with a vertical symmetry plane along the tunnel axis. In the model, the relevant materials are represented, including the different types of bentonite materials. The most important thermal and hydraulic properties, listed in Table 2.6, were derived from modeling of the Mon Terri HE-D and CIEMAT column laboratory experiment as well as literature data.

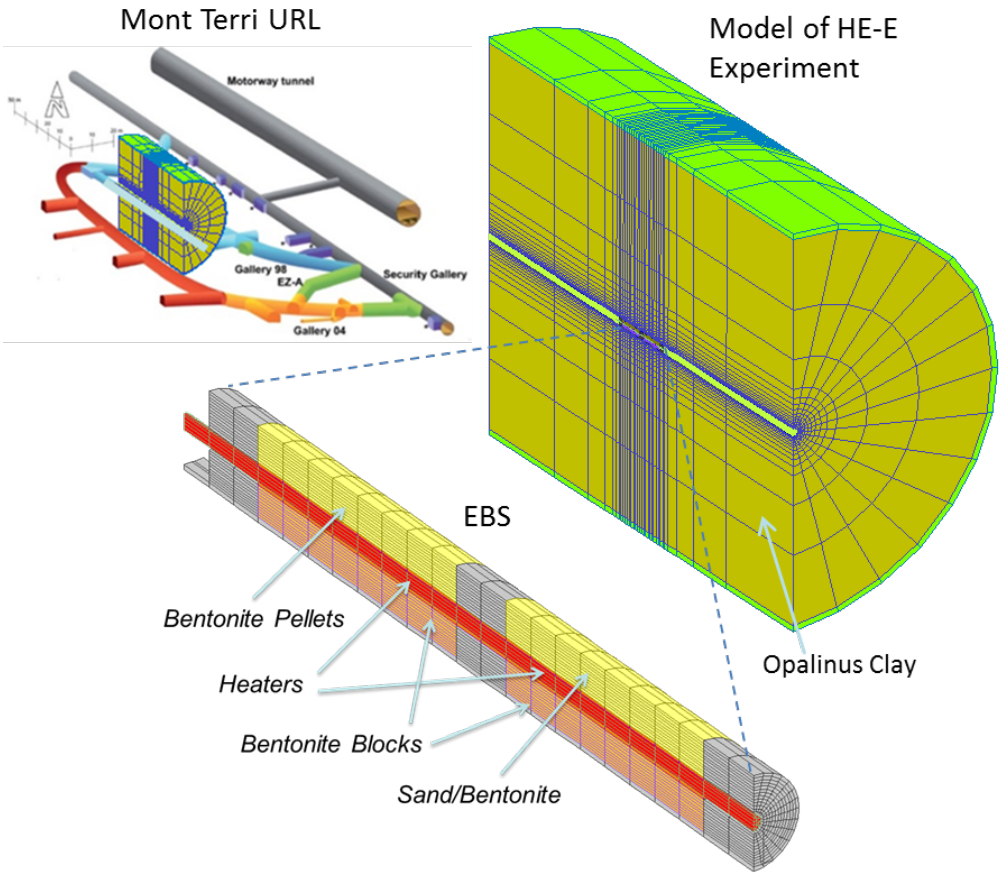

Figure 2.28. TOUGH-FLAC 3D model of the Mont Terri HE-E experiment.

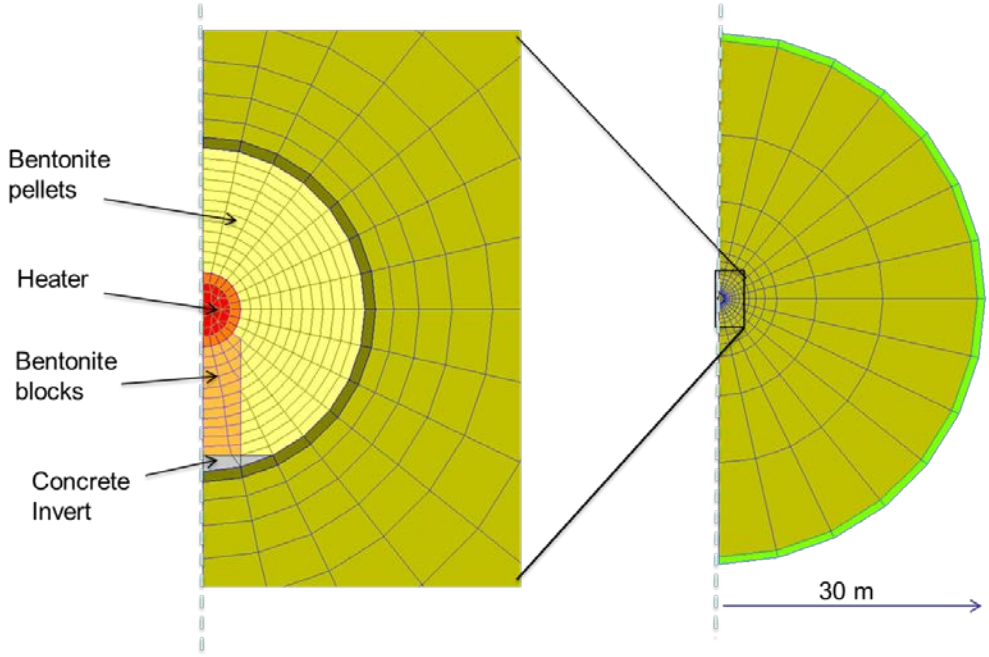

Figure 2.29. Vertical cross-section through the model grid.

Table 2.6. Parameters used in the predictive modeling of the Mont Terri HE-E experiment.

Parameters	Symbol	Opalinus Clay	Granular Bentonite	Bentonite blocks	Concrete (shotcrete and plugs)	Unit
Grain density	ρ_g	2.7×10^3	2.7×10^3	2.7×10^3	2.7×10^3	kg/m^3
Porosity	$Ø$	0.15	0.46	0.389	0.15	-
Intrinsic permeability	k	5.0×10^{-20}	5.0×10^{-21}	2.0×10^{-21}	3.5×10^{-21}	m^2
Liquid relative permeability (van Genuchten, 1980) $k_{lr}(S_l)=\left(\frac{S_l-S_{lr}}{S_{ls}-S_{lr}}\right)^A$	A	-	5	3	-	-
Liquid relative permeability (van Genuchten, 1980) $k_{lr}(S_l)=\left(\frac{S_l-S_{lr}}{S_{ls}-S_{lr}}\right)^{1/2}\left[1-\left\{1-\left(\frac{S_l-S_{lr}}{S_{sl}-S_{lr}}\right)^{1/m}\right\}^m\right]^2$	m	0.52	-	-	0.52	-
Capillary curve (van Genuchten, 1980) $\psi(S_l)=P0\left\{\left(\frac{S_l-S_{lr}}{S_{ls}-S_{lr}}\right)^{-1/m}-1\right\}^{1-m}$	P_0	1.09×10^7	1.0×10^7	3.0×10^7	1.09×10^7	Pa
	M	0.29	0.4	0.32	0.29	-
	S_{ls}	1.0	1.0	1.0	1.0	-
	S_{lr}	0.01	0.0	0.0	0.01	-
Thermal conductivity (wet)	λ_{sat}	1.7	1.3	1.0	1.7	W/m°K
Thermal conductivity (dry)	λ_{dry}	1.06	0.3	0.5	1.06	W/m°K
Grain specific heat	C	800	950	950	800	J/kg°K

The modeling of the HE-E experiment was conducted in several steps (Figure 2.30), including

1) The tunnel being open for thirteen years at a constant relative humidity of 98%
2) Bentonite buffer and heaters emplaced for 75 days before start of heating
3) Heating for 1000 days

The simulation of the tunnel open for thirteen years at a constant relative humidity of 98% is simulated applying a constant suction value of 2.6 MPa at the tunnel wall. In reality, the tunnel was exposed to a complex history including ventilation experiments, and the average 98% relative humidity was inferred from information in Gaus et al. (2014). This created a pressure sink around the tunnel with a slight desaturation of the near field rock. The bentonite buffer and heaters where then simulated into the model by changing material properties for elements within the tunnel. Also the initial saturation of about 20% in the granular bentonite buffer was assumed based on in-situ observations Gaus et al. (2014). Finally, after another 75 days, the heaters were turned on following the heater power used in the actual experiment. In the simplified 2D model simulations used for the initial model predictions, the actual heat power was scaled down to represent the heat input per meter tunnel.

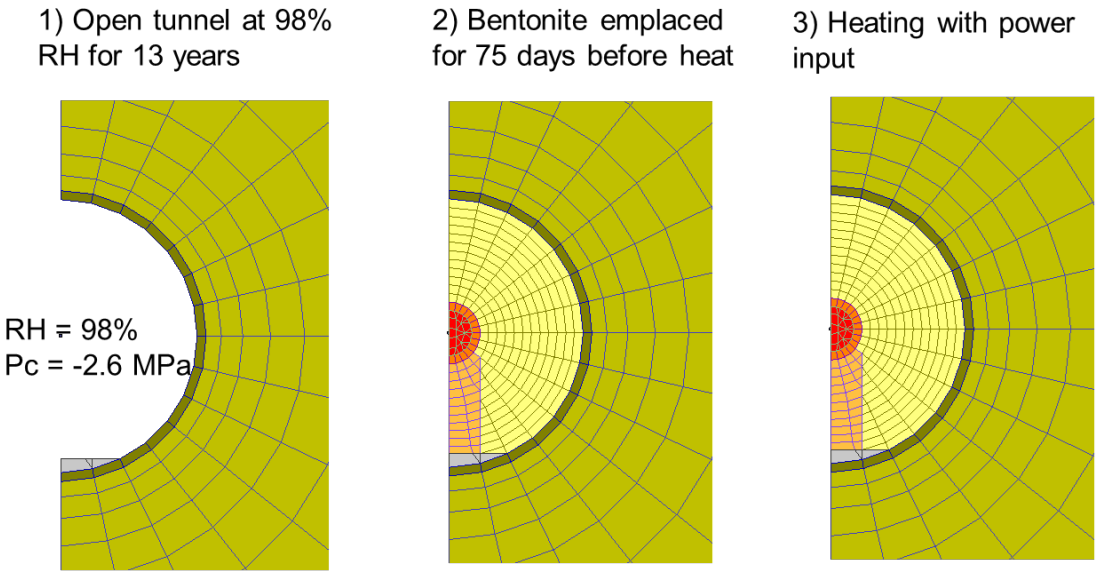

Figure 2.30. Steps for modeling the Mont Terri HE-E experiment. (RH= relative humidity, Pc = capillarity pressure)

2.3.4.2 LBNL model prediction results with comparison to measurements

Figure 2.31 shows the simulation results related to the evolution of liquid saturation and temperature from -100 to 1000 days, i.e. from 100 days before the start of the heating. Figure 2.31a shows that as soon as the bentonite buffer is installed (at -75 day), water is sucked into the bentonite from the adjacent rock. This is seen as a drop in liquid saturation in the rock (orange curve), while the saturation in the bentonite adjacent to the rock wall increases (blue curve). When the heating is turned on, a typical drying occurs at the inner part of the buffer (e.g. red line). Using the given heat power input, the maximum temperature of about 140°C is reached in less than 400 days, while the temperature at the rock wall gradually increases to about 60°C.

Figure 2.32 compares the simulated responses at two points located in the granular bentonite section with two points located within bentonite blocks, but located at about same distance from the heater. In this case the results are presented in terms of relative humidity and temperature. At the initial saturation of 20% in the granular bentonite, the relative humidity is about 40%, whereas in the bentonite block initial saturation was about 65% with a relative humidity of about 60%. The relative humidity for a given degree of saturation depends on the capillary pressure and hence the water retention curve. A higher saturation in the bentonite blocks, results in a higher thermal conductivity which explains the difference in the temperature between the monitoring points in the granular bentonite and the bentonite blocks.

A comparison of the predicted and observed evolutions of relative humidity and temperature is shown in Figure 2.33. The figure shows that the general humidity behavior of the bentonite at the rock wall and drying of the inner parts of the bentonite buffer are captured in the modeling. Modeling results for relative humidity, which is related to saturation, show very are in agreement with measurements for the blue and red curves (i.e., close to the rock wall and close to the heater). However, the model overestimates relative humidity in the mid part of the bentonite buffer (green curve). Nevertheless, the overall evolution of relative humidity was reasonably predicted by the modeling.

Figure 2.34a shows the evolution of fluid pressure within Opalinus Clay at a monitoring point located 3.54 m from the tunnel wall. This increase in fluid pressure is a result of so-called thermal pressurization, caused by thermal expansion of the pore fluid that cannot escape in the relatively low-permeability host rock. The magnitude and duration of this excess pressure pulse depends on parameters such as rock permeability and compressibility of water and rock (Rutqvist et al., 2014b). Using the Opalinus Clay properties determined from the modeling of the HE-D experiments, it appears that the model could predict this pressure increase fairly well. However, when considering the initial pressure we can observe some more deviation between modeling and measurements.

Figure 2.34 (b) shows the pressure evolution in two other points that where selected as part of the model comparison for the DECOVALEX-2015, Task B1. Although these points are located in a borehole adjacent to the pressure changes are much smaller and the initial fluid pressure is much smaller. A better agreement might be obtained by reducing the initial fluid pressure in the model.

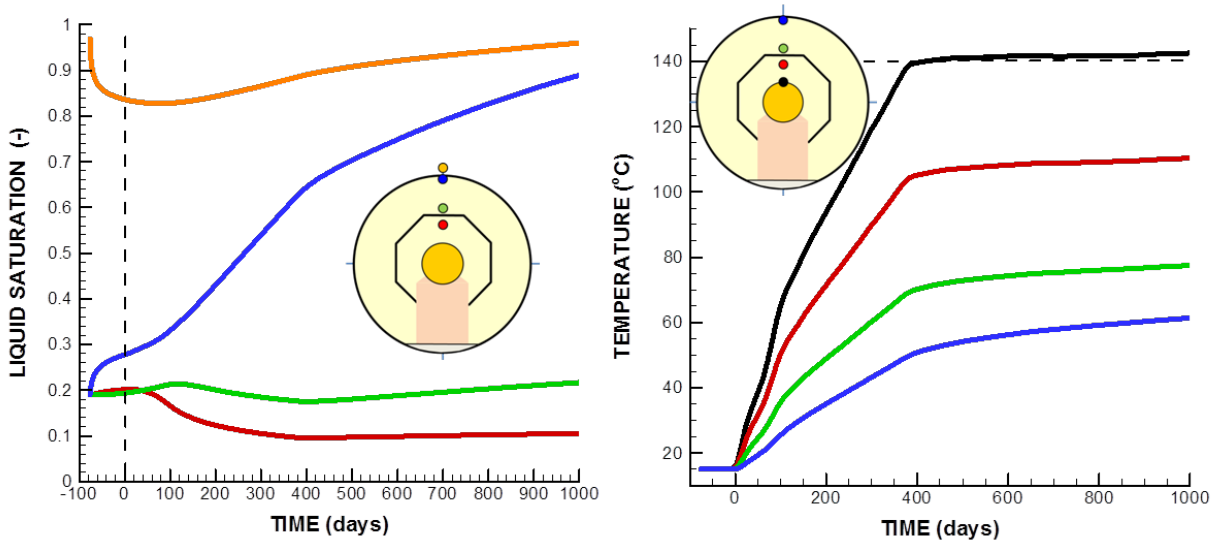

(a) (b)

Figure 2.31. Calculated evolution of (a) liquid saturation and (b) temperature.

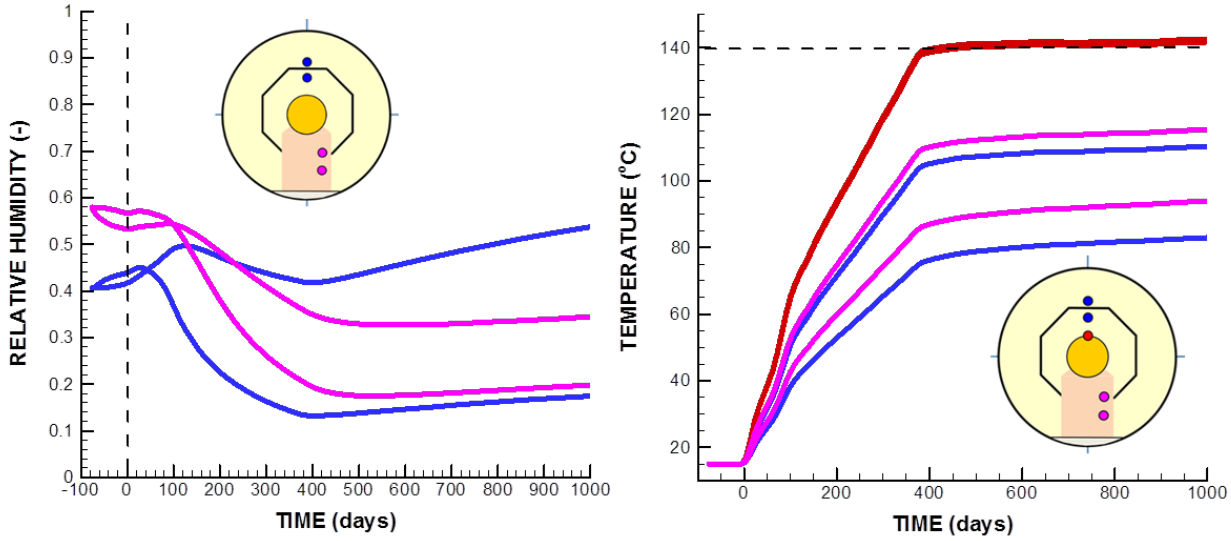

Figure 2.32. Calculated evolution of (a) liquid saturation relative humidity and (b) temperature at monitoring points in the granular bentonite (above heater) and bentonite blocks (below heater).

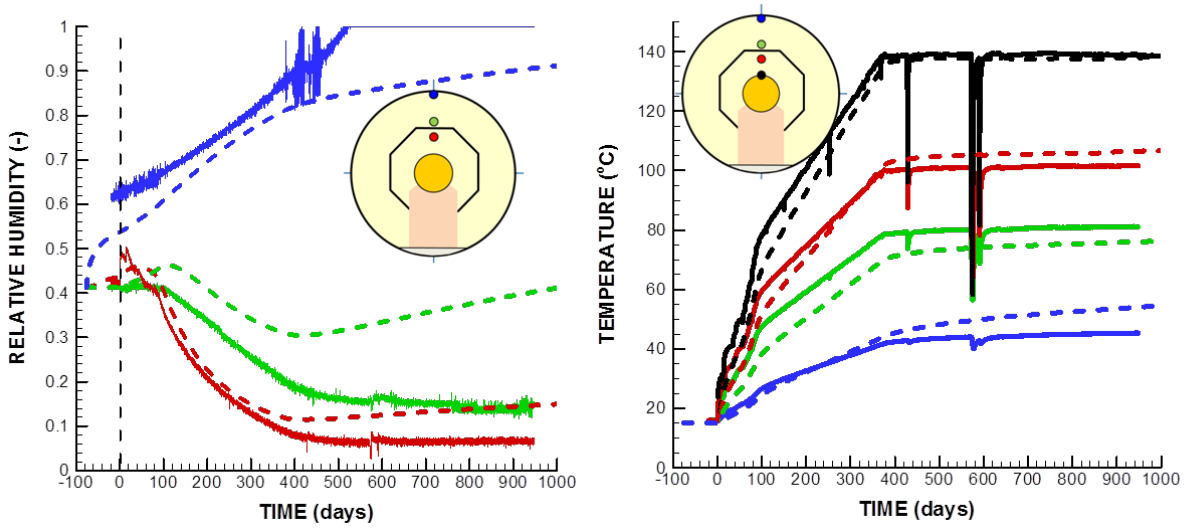

Figure 2.33. Comparison of predicted (dashed lines) and measured (solid lines) evolutions of (a) liquid saturation relative humidity and (b) temperature.

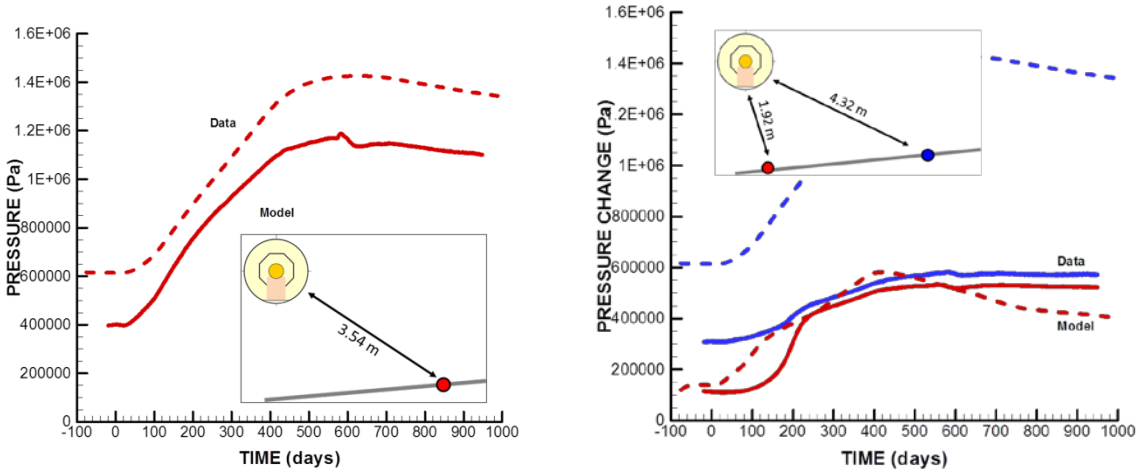

(a) (b)

Figure 2.34. Comparison of predicted (dashed lines) and measured (solid lines) evolutions of pore pressure in Opalinus Clay at a various distances from the tunnel.

2.3.4.3 Comparison between 8 DECOVALEX-2015 modeling teams

Figures 2.35 and 2.36 show the comparison of the modeling predictions by eight DECOVALEX-2015 modeling teams and measured data at different locations within granular bentonite and bentonite blocks. The results in Figure 2.35 for locations closest to the heater show are in agreement between models and measurements. Some larger deviations between models and measurements can be observed in Figure 2.36 for locations at the mid-distance between heater and rock wall. Such disagreement is consistent with what can be observed in Figure 2.33 (a). Thus, it appears that the transient moisture movement in the buffer at the mid-distance between the heater and the rock wall is not captured very well in the model. There are a number of potential reasons for this which will be the subject of future studies.

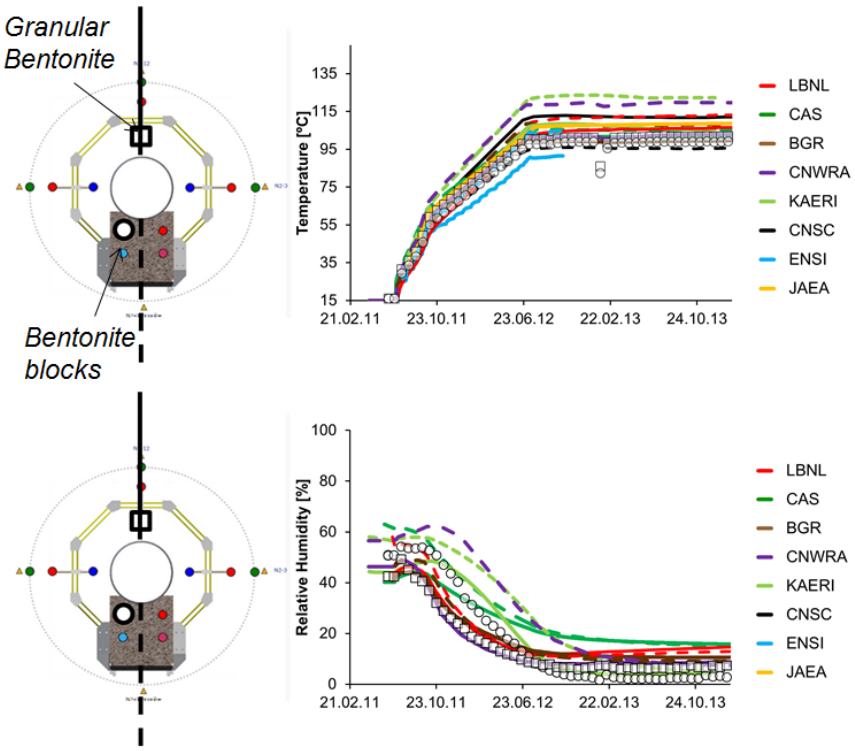

Figure 2.35. Comparison of predicted (lines) and measured (symbols) evolutions of temperature and relative humidity at points located 10 cm (in granular bentonite, white square in left figures) and 7 cm (in bentonite blocks, bigger white circle in left figures)) for eight modeling teams within the DECOVALEX-2015 project. Solid lines for modeling results in granular bentonite and dashed lines for modeling results in bentonite blocks (Garitte, 2016)

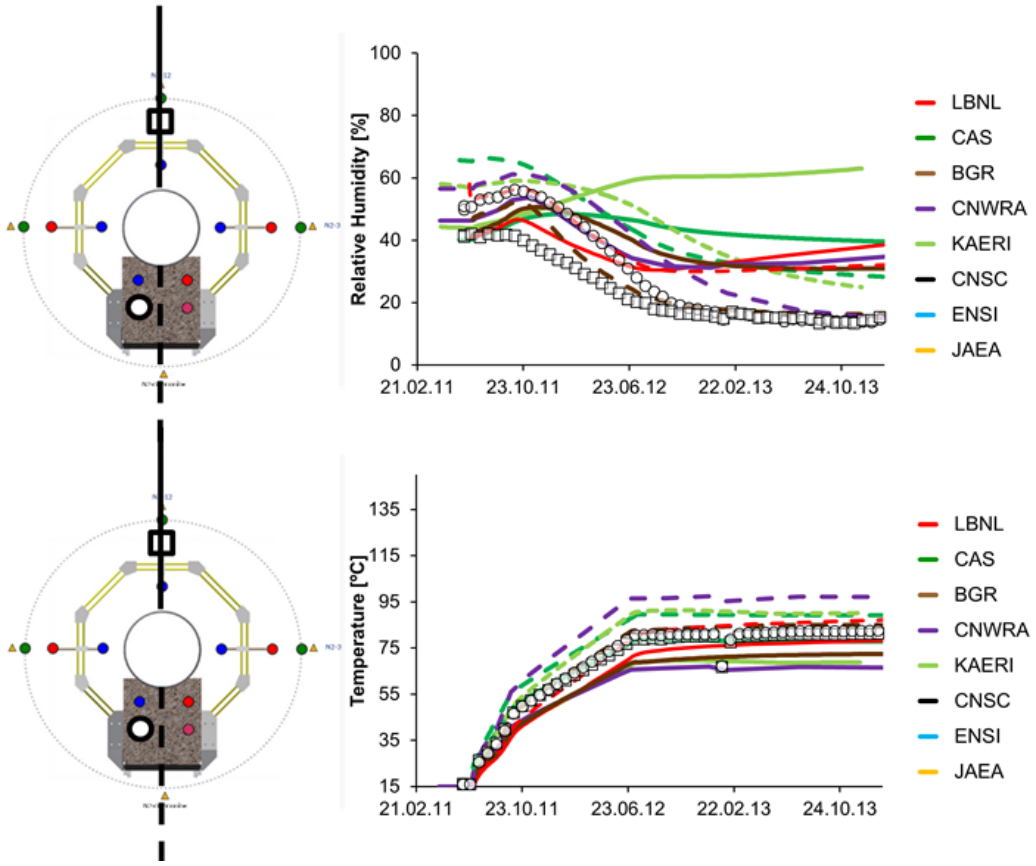

Figure 2.36. Comparison of predicted (lines) and measured (symbols) evolutions of temperature and relative humidity at points located 25 cm (in granular bentonite, white square in left figures) and 17 cm (in bentonite blocks, bigger white circle in left figures) for 8 modeling teams within the DECOVALEX-2015 project. Solid lines for modeling results in granular bentonite and dashed lines for modeling results in bentonite blocks (Garitte, 2016)

2.3.5 Interpretative Modeling of the Terri HE-E experiment

This section presents some of the interpretative modeling conducted in order to try to improve the modeling and material properties by calibration. This was defined as Step 3 in the DECOALEX-2015, Task B1 as described above. One obvious deviation between the initital predictive modeling (blind prediction in DECOVALEX-2015 Step 2) and measurements is the evolution of relative humidity in the mid-section of the buffer (green lines in Figure 2.33 (a). A parameter study was performed in order to try to find a way to improve the match of the relative humidity in the buffer mid-section, but it turned out that it was not possible to achieve a better match with the current model. The parameter study can be summarized as follows:

1) Buffer absolute permeability (no significant effect)
2) Diffusion coefficient (did not help)
3) Buffer relative permeability (lowered but did not help)
4) Water retention curve (varied but did not help)

The modeling showed that the moisture content in the inner and mid parts of the buffer achieves a pseudo steady state dictated by two-way diffusion, i.e. thermally driven vapor diffusion and a counter flow by capillary driven diffusion as been observed and modeled previously (e.g. Rutqvist et al., 2001b).

Another item that was studied in the interpretative modeling of the field data was an observed slight unsymmetrical temperature in the buffer. In the measurements, the temperature is somewhat lower in the lower part of the buffer, where buffer consists of pre-compacted blocks. A lower temperature was also observed at the heater surface on the lower part of the heater. This lowering of the temperature at the lower part of the heater could be modeled by reducing the thermal conductivity of the heater in the model from 12 W/ms to 6 W/ms. These appear to be artificially low values for steel, but it was sufficient to create spatially different temperatures around the heater surface in the model. On the other hand, using this approach it was not possible to model the observed lower temperature within the bentonite blocks compared to that of the granular bentonite buffer section.

The results of temperature and relative humidity with the updated parameters as a result of the interpretative modeling are presented in Figure 2.37 for the upper parts of the buffer. Compared to the model prediction shown in Figure 2.33, there are some improvements related to the relative humidity near the rock interface (blue curves), whereas there are only minor changes otherwise. The improvement near the rock interface was a result of a slight change in the water retention curve for the bentonite pellets.

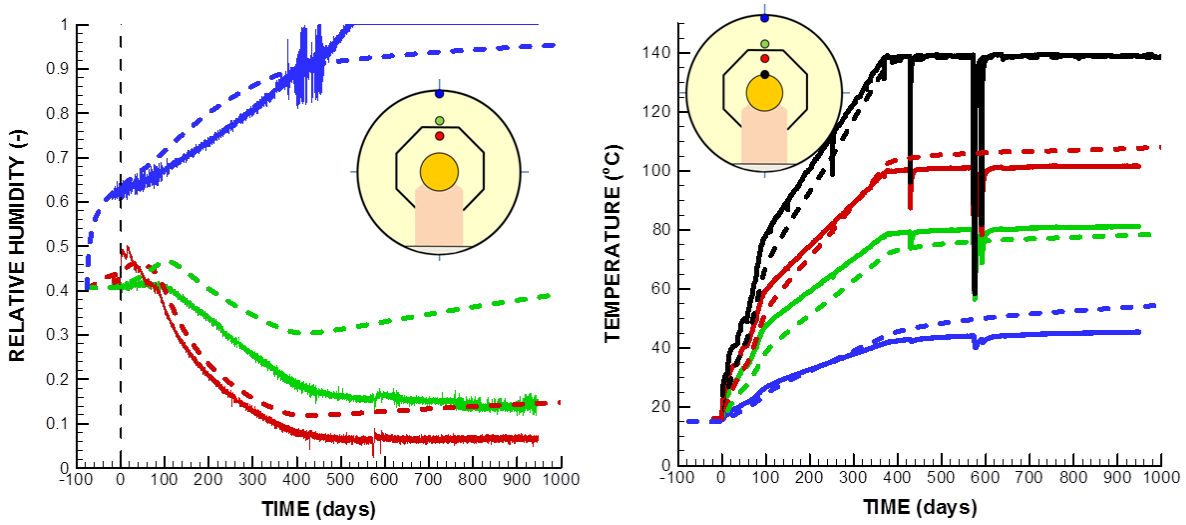

Figure 2.37. Comparison of calculated (dashed lines) and measured (solid lines) evolutions of (a) liquid saturation relative humidity and (b) temperature after interpretative modeling.

Figure 2.37 shows the data comparison, including both upper and lower parts of the buffer for the improved model parameters set obtained by the interpretative analysis. There is an excellent agreement for the heater temperature both on top and bottom of the heater. The temperature evolution in the upper part of the buffer, i.e., within the granular bentonite is also in are in agreement with measured data. The temperature evolution in the lower part of the buffer, i.e., in bentonite block section is not as satisfactory as the temperature is somewhat overestimated in the model simulations. The evolution of relative humidity are in general agreement with the data in trends, showing drying at the heater and wetting from the rock surface, but the measurement indicates more drying in the mid part of the buffer.

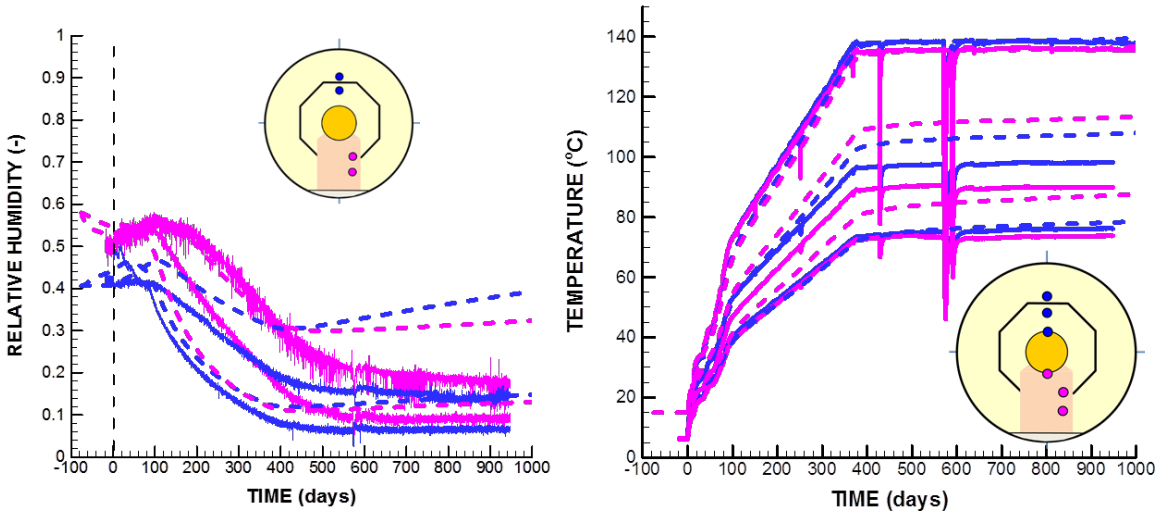

Figure 2.38. Comparison of calculated (dashed lines) and measured (solid lines) evolutions of (a) liquid saturation relative humidity and (b) temperature after interpretative modeling at top and bottom of buffer.

Finally, in order to establish an initial fluid pressure in the rock at some of the measurement point for the thermal pressurization, the pressure at the outer boundary of the model was reduced from 1.7 MPa to 1.2 MPa. Using such a low boundary pressure a low pressure similar to that observed was established in the model. The simulation results in Figure 2.39 show excellent agreement for one point (Figure 2.39 (a)), and mixed results for two other locations shown in Figure 2.39 (b). Thus the pressure increase may depend on local heterogeneities in the rock.

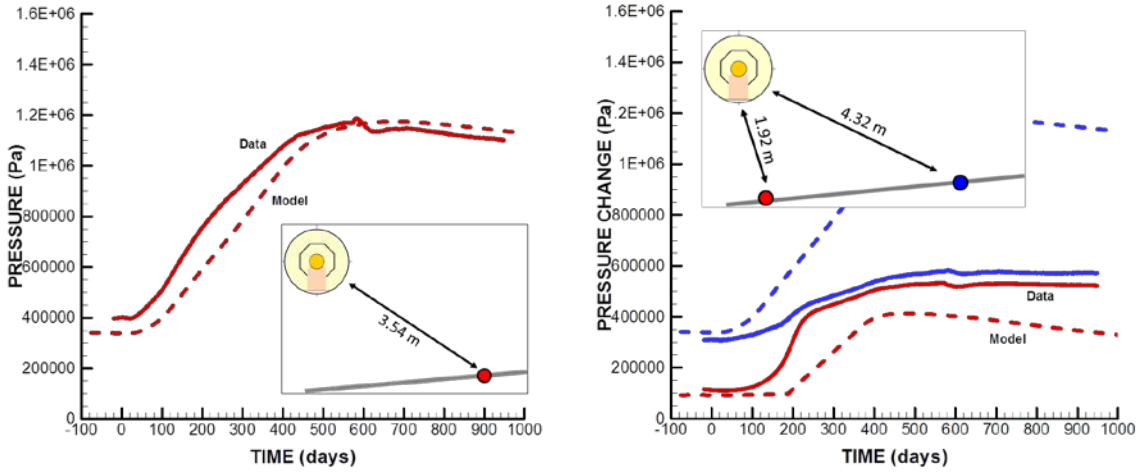

Figure 2.39. Comparison of modeled (dashed lines) and measured (solid lines) evolutions of pore pressure in Opalinus Clay at a various distances from the tunnel after interpretative modeling.

2.3.6 Longer-Term Modeling of the HE-E experiment

The modeling teams in DECOVALEX-2015 Task B1 were asked to perform a long-term simulation to estimate when the buffer will be completely resaturated if the heaters are turned off after eight years. The time to full resaturation is relevant as full resaturation will ensure complete and uniform swelling and tightness of the buffer. This was conducted by extending the simulation with the model from the interpretive modeling. Figure 2.40 shows a distinct saturation response when the heaters are turned off and the time to full resaturation is eighty two years. Figure 2.41 shows that after eighty two years the pressure is still low but would eventually increase to 1.2 MPa which is the pressure at the outer boundary of the model.

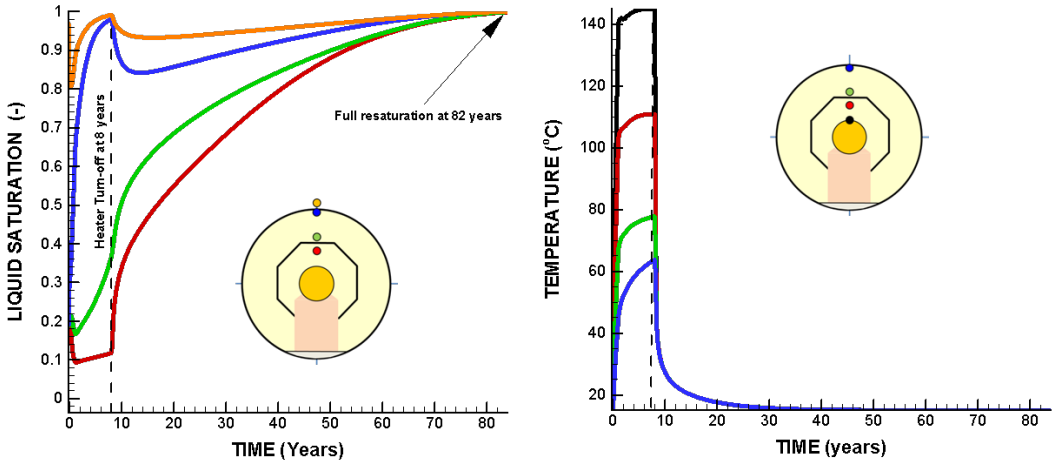

Figure 2.40. Calculated long-term evolution of (a) liquid saturation and (b) temperature.

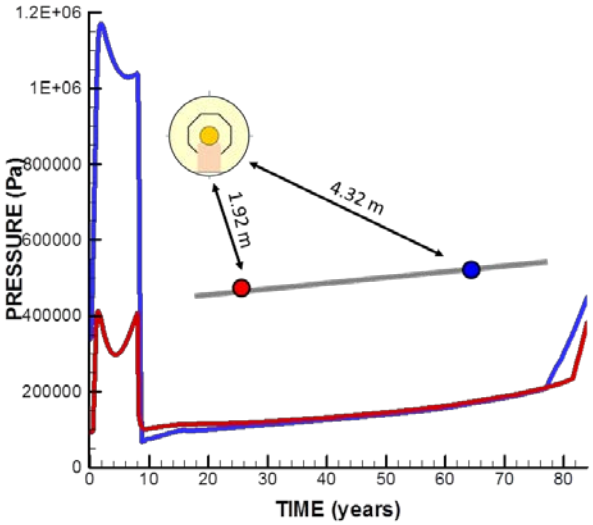

Figure 2.41. Calculated long-term evolution of pore pressure in the Opalinus Clay host rock.

2.3.7 Concluding remarks on Mont Terri HE-E modeling

Over the past three years, as part of the DECOVALEX-2015 project we have conducted modeling of coupled THM processes in bentonite backfill and Opalinus host rock associated with the Mont Terri HE-E experiment. Listed below are a few important findings and lessons learned from LBNL's participation in this modeling task:

- As one of 2 teams out of eight, we applied full two-phase (gas and liquid) flow modeling, whereas other teams used single (liquid) phase flow modeling with an additional flow term for vapor flow in a static gas phase. Our modeling using fully two-phase flow modeling revealed that very high intrinsic gas permeability of the bentonite is required to match observations of drying near the heat source. Such high gas intrinsic permeability has also been observed in laboratory experiments and reported in the literature and it is one of the assumptions for simplifying to single phase flow models. The fact that gas permeability is high in bentonite means that both full two-phase flow models and single phase flow models are adequate for modeling TH responses in the buffer.
- The HE-D Experiment was modeled with a 3D TOUGH-FLAC model with good match to experimental data. This was important for determining *in situ* TMH properties of Opalinus Clay, including anisotropic thermal conductivity and permeability. Based on the are in agreement between models and data for HE-D, we are confident about the THM parameters characterized for the Opalinus Clay.
- The modeling of the CIEMAT column experiment using a detailed transient analysis provided a unique back-analysis of bentonite thermal conductivity and a very good match with experimental data was obtained, including long term hydration. The are in agreement between model and CIEMAT experimental data shows adequate modeling of thermal-hydrological processes in bentonite.
- With the THM parameters determined from HE-D and CIEMAT experiments, the modeling of the HE-E experiment resulted in good prediction, though some disagreement occurred in the evolution of moisture content at the mid distance between heater and rock. The reason for these local disagreements in moisture evolution is still an open question.
- The modeling of these experiments has provided important model validation and THM properties of granular bentonite and Opalinus Clay that are currently being applied in the modeling of the larger scale Mont Terri FE experiment.

2.4 HORONOBE EBS EXPERIMENT (DECOVALEX-2015)

This task focuses on coupled THM modeling of a full-scale EBS experiment conducted by the Japan Atomic Energy Agency (JAEA) at the Horonobe URL, Hokkaido, Japan (Figure 2.42). The EBS experiment is carried out at a depth of 350 m in a very porous and soft, siliceous mudstone with the following basic properties:

- Porosity 35-60%
- Permeability 10^{-20} – 10^{-18} m^2
- UCS (Strength) 5-25 MPa
- Young's Modulus 1-4 GPa
- Thermal Conductivity 1.34-1.53 W/mK

Figure 2.43 shows the experimental layout with a vertical heater emplacement installed in a test pit at the bottom of an experimental drift. The detailed sequence of the experiment is given in Table 2.7. The experimental drift was backfilled after the installation of the heater and bentonite buffer into the test pit.

Bentonite buffer and backfill materials are based on the Japanese Kunigel V1 bentonite. For the buffer, Kunigel V1 bentonite is mixed with sand and emplaced at a dry density of 1600 kg/m^3, whereas for the backfill rock debris is mixed in for an emplacement dry density of 1400 kg/m^3. The experimental area was then isolated by a concrete plug and the heater was finally turned on January 15, 2015. Sensors have been installed in buffer, backfill and rock to monitor temperature, stress, strain, pore pressure, humidity, displacement, pH, resistivity, electric potential, and seismic velocity.

Figure 2.44 shows some early-time measurements of pressure at the bottom of the test pit (within the sand layer) and temperature at the three points on the heater. The locations of these monitoring points for both pressure and temperature are shown in Figure 2.44 (a) insert. During the construction and installation of the buffer, backfill and plug, water was pumped out of the test pit. The pump was turned off on December 22, 2014, i.e., 24 days before the heater was turned on. Figure 2.44 (a) shows that the water pressure increases due to inflow from the rock and reaches a steady value about 60 kPa after 15 to 20 days. Figure 2.44 (b) shows the temperature at the side and top of the heater stabilizes at a temperature slightly less the 100°C, whereas the temperature at the bottom of the heater stabilizes at about 80°C.

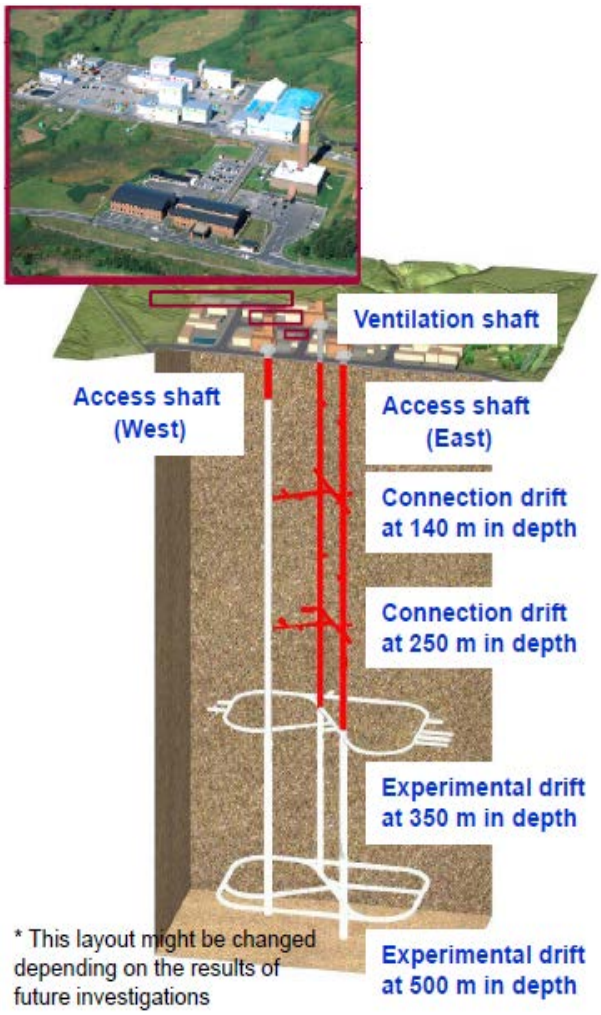

Figure 2.42. Layout of the Horonobe URL in Hokkaido, Japan (Sugita et al., 2016).

(a)

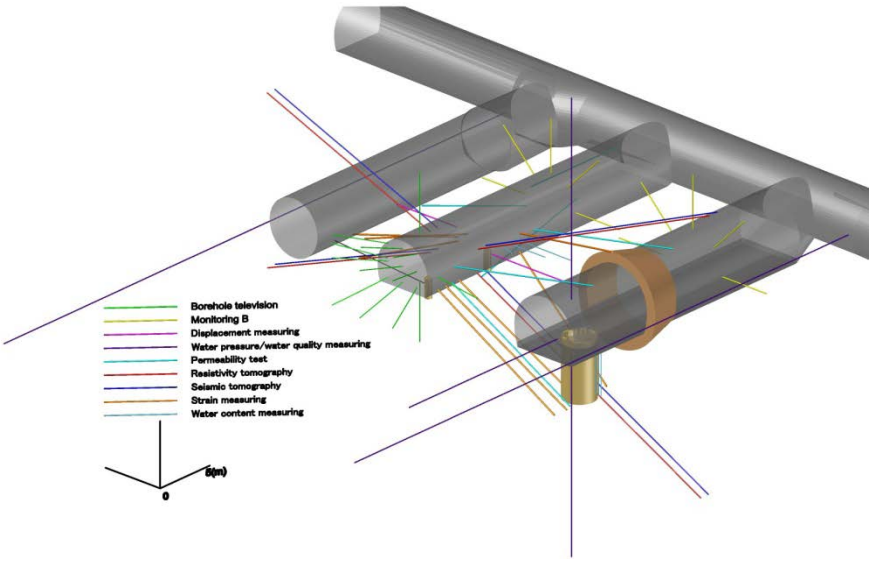

(b)

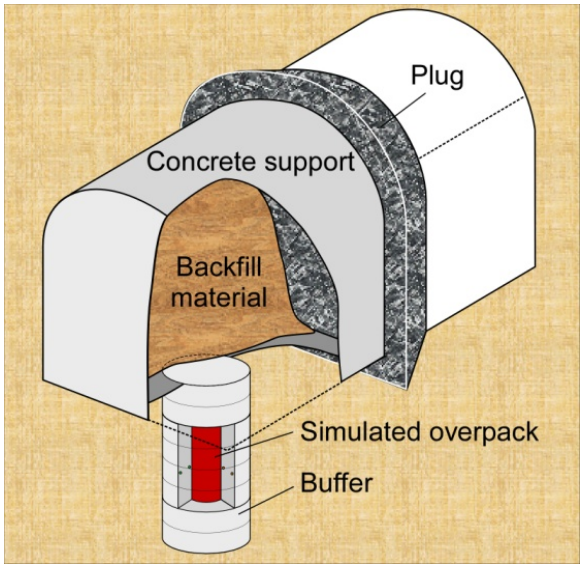

Figure 2.43. General description of the EBS experiment at the Horonobe URL Project in Japan (Sugita et al., 2016).

Table 2.7. Details on the sequence of construction and installation of the Horonobe EBS experiment

Sequence of the Horonobe EBS Experiment	
Excavation of the experimental gallery	**Oct 29 – Dec 6, 2013**
Opening of the test pit	**Feb 3 – 8, 2014**
Emplacement of the buffer	**Aug 18 – Sept 6, 2014**
Emplacement of the backfill	**Sep 8 – Oct 3, 2014**
Plugging	**Oct 9 – 27, 2014**
Stop pumping up water from pit	**Dec 22, 2014 at 14:00**
Start of heating	**Jan 15, 2015 at 14:20**

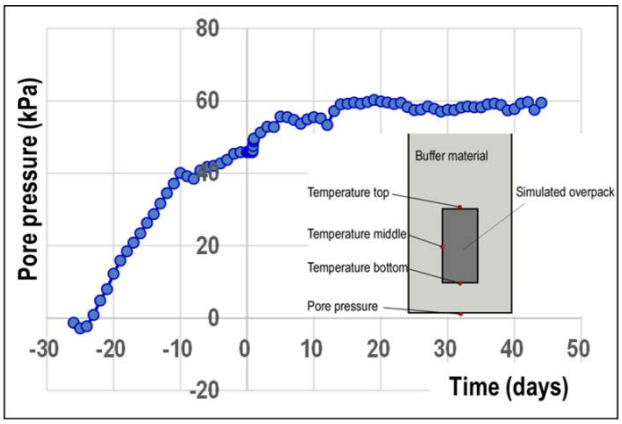

(a)

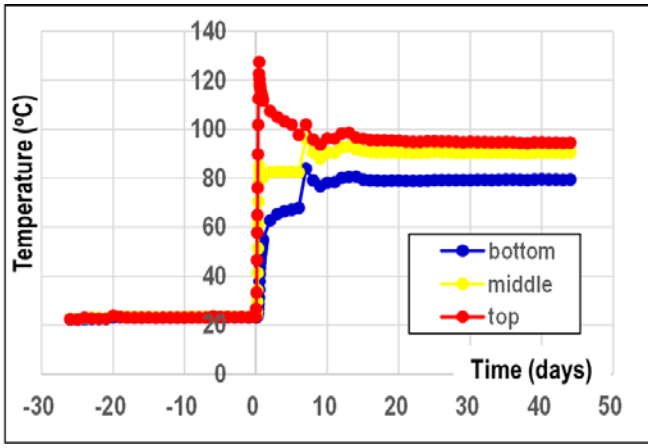

(b)

Figure 2.44. Early time monitored (a) fluid pressure in the test pit and (b) temperature evolution at three points located on the heater surface. The location of monitoring points for both pressure and temperature are shown in figure (a) insert.

2.4.1 DECOVALEX-2015 modeling tasks related to Horonobe EBS experiment

The DECOVALEX Task B2 related to the Horonobe EBS experiment was divided into the following steps;

- Step 1 (1D benchmark test with comparison of numerical models)
- Step 2 (Prediction analysis)
- Step 3 (Calibration analysis)

The 1D benchmark test (Step 1) was defined with exact properties and boundary conditions given by the JAEA. The benchmark test was conducted for the teams to familiarize themselves with the problem and for precise comparison of computer codes before going into the more complex full-scale case. Thereafter, in Step 2, a model of the real experimental design should be constructed and a first predictive analysis will to be performed for several years from the start of the heating. The heating started on January 15, 2015, and the plan was that JAEA would eventually provide the monitored data for the first six months of heating to the research teams. The research teams should then calibrate their models against this first sixmonths of field data and then carry out coupled numerical analysis for long-term predictions (100 – 1,000 years) using the test conditions of the EBS experiment.

JAEA provided reports from the investigations at the Horonobe URL for input parameters related to the mudstone host rock and buffer material properties for the Kunigel V1 bentonite from the previous H12 project, whereas properties for the backfill were investigated along with the project.

In the FY14 milestone report titled “Investigation of Coupled Processes and Impact of High Temperature Limits in Argillite Rock” (Zheng et al., 2014), we presented the final results of the Step 1 benchmarking with comparison to the results of other DECOVALEX-2015 teams. In the FY15 milestone titled “Investigation of Coupled Processes and Impact of High Temperature Limits in Argillite Rock” (Zheng et al., 2015) we presented Step 2 model predictions of the full-scale EBS experiment with comparison of the results to other DECOVALEX-2015 modeling teams. In this report we present comparison of model prediction with actual measured data during the first 75 day of heating. The data used and provided to the research teams included temperature, suction, stress and displacement in the buffer. However, the suction and displacement data were very limited so we focused our comparison to temperature and stress. We also present comparison of modeling results from other DEOCOVALEX-2015 research teams participating in this task. In total five DECOVALEX-2015 research teams have participated in the modeling of the Horonobe EBS experiment with the models listed in Table 2.8. Some of the models listed in Table 2.8 have been extensively applied in previous DEOCOVALEX project phases, whereas some are new and being developed.

Table 2.8. DECOVALEX research teams and numerical simulators in modeling Horonobe EBS experiment

Research Team	Numerical Simulator	Brief Description of Numerical Simulator
DOE U.S. Department of Energy's Research Team: Lawrence Berkeley National Laboratory (LBNL)	TOUGH-FLAC	TOUGH-FLAC is a simulator for analysis of coupled THM processes under multiphase fluid flow conditions being developed at the LBNL (Rutqvist et al., 2002). The simulator is based on linking of the existing computer codes TOUGH2 and FLAC3D, and has been extended for modeling of coupled THM and THMC processes associated with nuclear waste disposal with backfilled emplacement tunnels in clay formations (Rutqvist et al., 2014b).
	ROCMAS	ROCMAS is a finite element program for analysis of coupled THM processes in porous and fractured rock developed at LBNL (Rutqvist et al., 2001a). It can model unsaturated media with single-phase liquid flow and vapor diffusion in a static gas phase. The code has been extensively applied in earlier phases of the DECOVALEX project for THM analysis in bentonite-rock systems (Rutqvist et al., 2001 (b); 2005).
BGR Bundesanstalt für Geowissenschaften und Rohstoffe's Research Team: University of Tübingen	GeoSys/ Rockflow	GeoSys/Rockflow is based on object-oriented programming (Kolditz et al., 2003). It was first applied in previous DECOVALEX phases for analysis of thermal-hydrological and thermal-mechanical processes and has been extended to THM (Wang et al., 2006). For the present study, an unsaturated single-phase liquid flow and vapor diffusion is considered.
CAS Chinese Academy of Sciences' Research Team	EPCA3D	The EPCA code (Elasto-Plastic Cellular Automata) uses the concept of cellular automata inspired by the self-organizing theory in biology. This code has been successfully used to simulate the failure process of heterogeneous rocks with and without consideration of hydro-mechanical coupling (Feng et al., 2006; Pan et al., 2008).
JAEA Japan Atomic Energy Agency's Research Team, including Hazama Cooperation	THAMES	THAMES is a finite element program for analyzing coupled THM processes in porous and fractured rock developed at the Kyoto University. The code has been extended to unsaturated media with single-phase liquid flow and vapor diffusion in a static gas phase (Chijimatsu et al., 2005).
KAERI Korean Atomic Energy Research Institute	FLAC/ FLAC3D/ Tough2	Simulation tools being developed along with the DECOVALEX-2015 project based on FLAC and FLAC3D linked with TOUGH2.

2.4.2 Model predictions of the full scale Horonobe EBS experiment

A 3D model was developed for prediction of the THM responses at the Horonobe EBS experiment. The model is half symmetric, including half of the tunnel, and half of the deposition hole (Figure 2.45). It contains all relevant materials, including mudstone rock, buffer, backfill, a sand layer at the rock/buffer interface, concrete lining and plug. In this model prediction, we use the properties of the buffer and rock developed associated with the 1D benchmark calculation (Table 2.9). Additional properties for the backfill, sand layers, concrete lining and plug were provided by the JAEA to DECOVALEX-2015 modeling teams. The intrinsic permeability of gas flow in the bentonite is about six orders of magnitude higher than the intrinsic permeability for liquid flow and this is simulated in TOUGH2 using a high value of the Klinkenberg parameter.

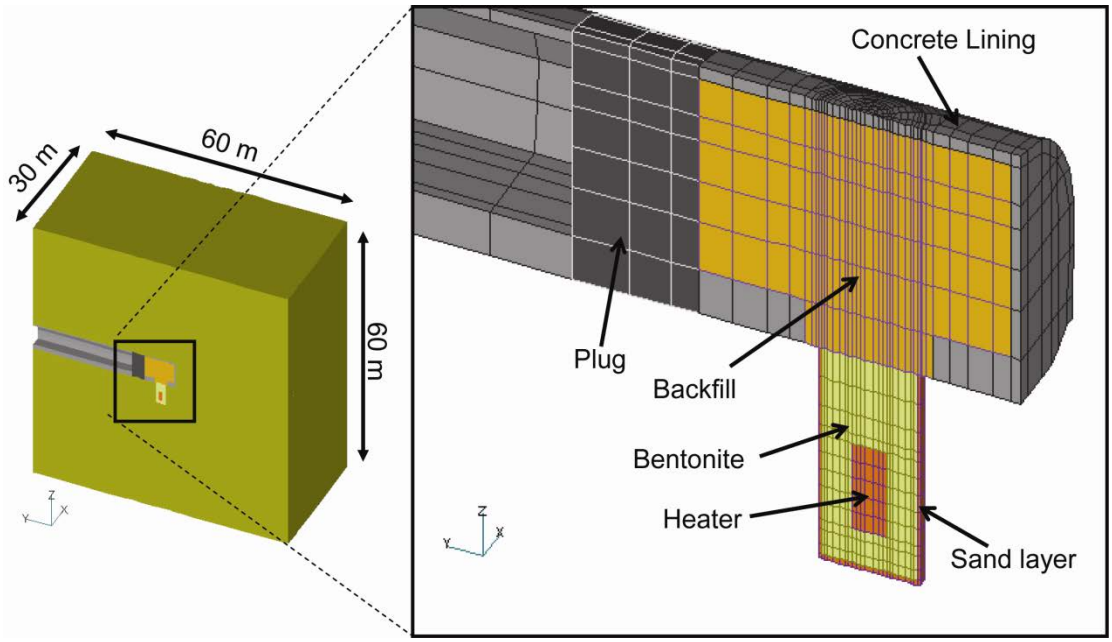

Figure 2.45. TOUGH-FLAC 3D numerical grid of the Horonobe EBS experiment.

Table 2.9. Material parameters for modeling Horonobe EBS experiment.

Parameter	Symbol	Overpack	Buffer	Backfill	Rock
Grain density (kg/m^3)	ρ_g	10,000.	2680.	2680.	2454.
Porosity	ϕ	0.403	0.403	0.460	0.4482
Permeability (m^2)	K	5 x 10^{-51}	4 x 10^{-20}	1.5 x 10^{-19}	1.33 x 10^{-15}
Thermal conductivity (saturated) (W/m^{o}C)	λ_{wet}	20	1.986	1.250	1.231
Specific heat (solids) (J/kg°C)	C	10,000	341	341	626
Thermal conductivity (desaturated) (W/m^{o}C)	λ_{dry}	20	0.444	0.444	0.579
Liquid relative permeability (van Genuchten, 1980) $k_{rl}(S_l) = \left(\frac{S_l - S_{;r}}{S_{ls} - S_{;r}}\right)^A$	A	1.3	1.3	1.3	NA
	S_{lr}	0	0	0	NA
	S_{ls}	1	1	1	NA
Water relative permeability parameters (van Genuchten, 1980) $k_{rl}(S_l) = \left(\frac{S_l - S_{lr}}{S_{ls} - S_{lr}}\right)^{1/2}\left[1 - \left\{1 - \left(\frac{S_l - S_{lr}}{S_{ls} - S_{lr}}\right)^{1/m}\right\}^m\right]^2$	m	NA	NA	NA	0.503
	S_{lr}	NA	NA	NA	0
	S_{ls}	NA	NA	NA	1
Capillary pressure parameters using van-Genuchten equation $\psi(S_l) = 1/\alpha\left\{\left(\frac{S_l - S_{lr}}{S_{ls} - S_{lr}}\right)^{-1/m} - 1\right\}^{1-m}$	$\alpha\,(m^{-1})$	8 x 10^{-3}	8 x 10^{-3}	8 x 10^{-3}	9.928 x 10^{-3}
	M	0.375	0.375	0.375	0.503
	S_{lr}	0	0	0	0
	S_{ls}	1	1	1	1
Vapor diffusion coefficients (m^2/s)	D_v	3.5 x 10^{-6}	3.5 x 10^{-6}	3.5 x 10^{-6}	3.5 x 10^{-6}
Young's modulus E, (GPa)	E	200.000	37	3	1820.0
Poisson's ratio (-)	ν	0.3	0.3	0.4	0.21
Linear thermal expansion coefficient (C^{-1})	C^{-1}	1 x 10^{-6}	1 x 10^{-6}	1 x 10^{-6}	1.33 x 10^{-5}
Moisture swelling coefficient, β_{sw}	β_{sw}	0	0.0108	0.0108	0

We simulated the experiment in 3 steps:

1) Excavations are open for three months.
2) Excavations are filled with backfill and the heater, buffer and plug are all installed for 6 months.
3) Heating with heater temperature of 100°C.

Figures 2.46 and 2.47 show comparisons of LBNL predicted and measured evolution of temperature and radial stress during the first 75 days of heating at six different points. The temperature predictions are excellent, whereas stress predictions are not as perfect. However, we can state that both the modeling predictions and measurements show stress changes in the buffer are small during this initial phase. On the other hand the trends of the stress evolutions are quite different between the model predictions and measurements. This might be, because in this case a simple linear swelling model was applied in which the swelling strain is a linear function of changes in liquid saturation. Such a model maybe used to predicte the final swelling stress, but may not be accurate in prediction the path of the swelling strain and stress along with changes in saturation.

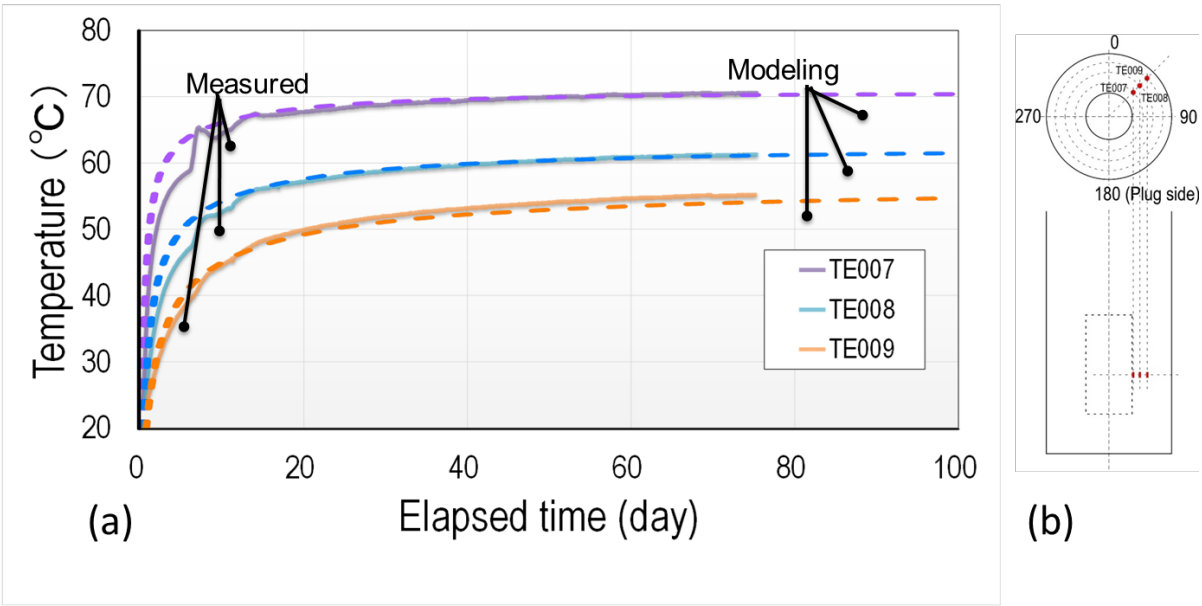

Figure 2.46. (a) Predicted and measured temperature evolution at three monitoring points in the buffer and (b) map view and vertical cross-section of the test pit with the locations of the monitoring points.

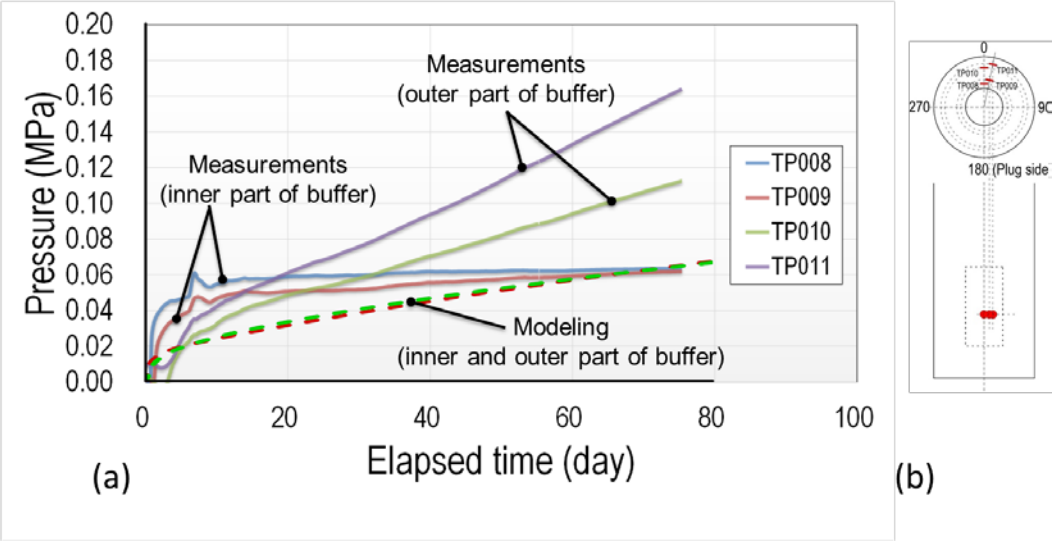

Figure 2.47. (a) Predicted and measured stress evolution at four monitoring points in the buffer and (b) map view and vertical cross-section of the test pit with the locations of the monitoring points

Figure 2.48 shows the comparison of the model prediction by five DECOVALEX-2015 modeling teams and measurements of temperature and radial stress in the buffer. The results again show the temperature evolution could be predicted in close agreement with the measurements, whereas the calculated stress results are not as consistent. Again, we emphasize these are very early time data and swelling stress have not developed very substantially at such an early time, because the buffer is far from being fully saturated.

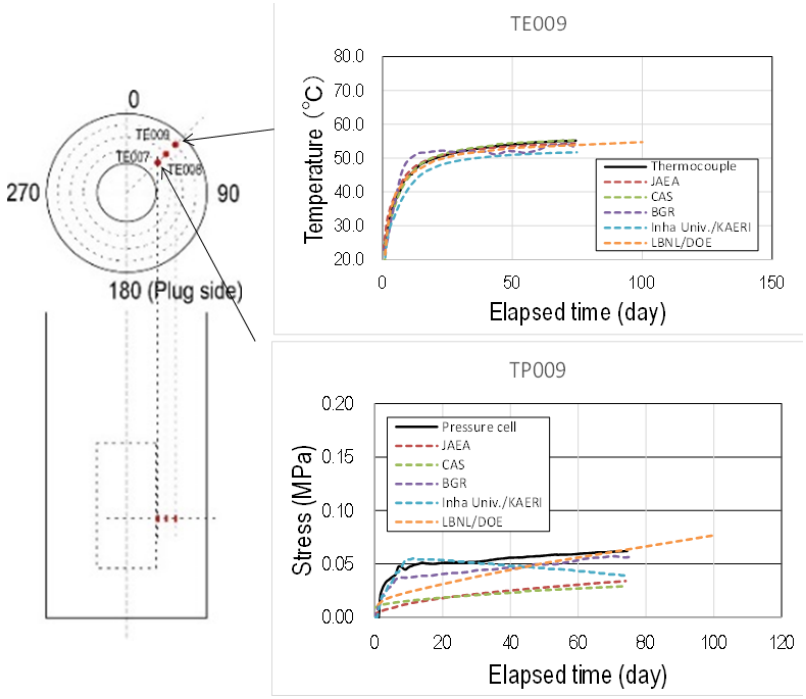

Figure 2.48. Simulated evolution of temperature and stress evolution in the buffer for five DECOVALEX-2015 modeling teams with comparison to measured data during the first 75 days of heating (modified from Sugita et al., 2016).

2.4.3 Interpretative modeling of early time buffer stress evolution

The TOUGH-FLAC model prediction showed a very are in agreement related to temperature evolution, whereas the calculated early time evolution of stress in the buffer could be improved. We therefore decided to conduct some interpretative modeling of the buffer stress evolution. We observe early on, during the first ten days, the buffer stress increase seems to be correlated with temperature increase in the buffer. For example, a temporal stress peak at about seven days is very well correlated with temporal temperature peak (Figure 2.49). On the other hand, at the outer boundary there is a gradual increase in stress that seems to be correlated with increasing saturation near the outer boundary. Thus, initial stress increase during the first 10 days seems to be due to thermal expansion while the following slow increase in compressive stress occurring at the outer boundary maybe a result of moisture swelling.

Figure 2.50 shows modeling results for two different model simulations. In one case the moisture swelling coefficient was set to zero (no moisture swelling) and thermal expansion coefficient was increased as to provide a stress response of pure thermal expansion (red dashed line), which matches measured data at the inner parts of the buffer. In the second simulation the moisture swelling coefficient was increased to give higher moisture swelling stress and this matched the measurements in the outer part of the buffer. However, the modeling using this simple linear swelling approach always produced a uniform swelling stress resulting in equivalent swelling stress evolution at the inner and outer parts of the buffer. Thus, a model should be applied that can result in different stress evolution in the inner and outer parts of the buffer. This will be further investigated in future studies.

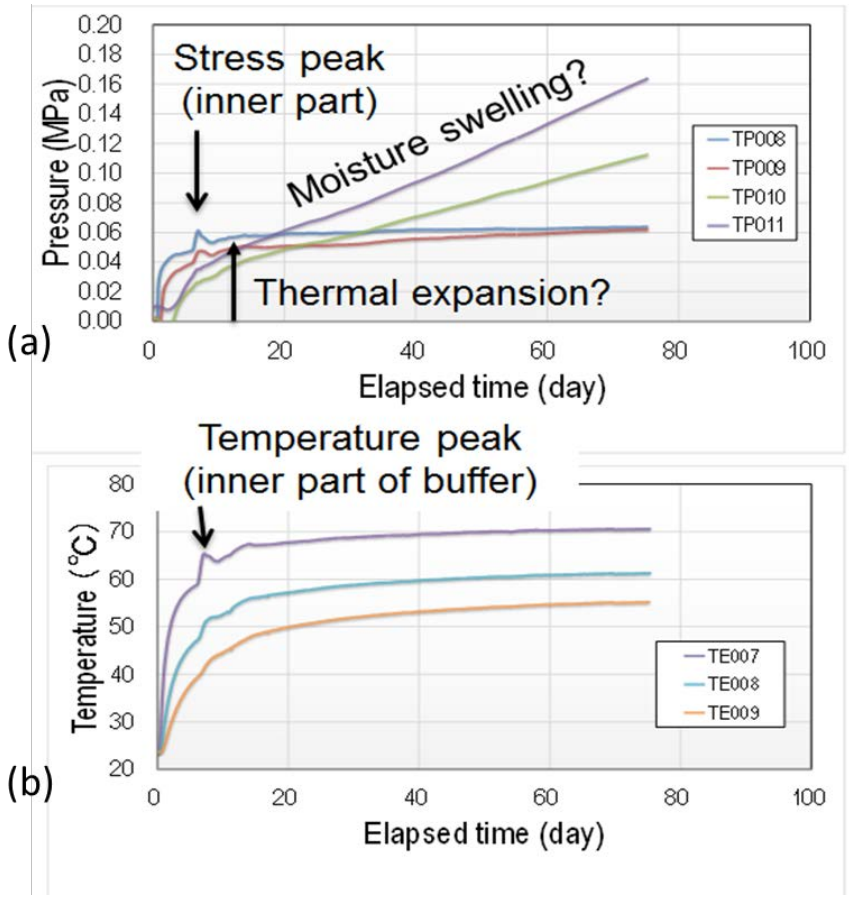

Figure 2.49. Measured (a) buffer stress and (b) temperature evolution indicating thermal and moisture swelling effects on the stress evolution (modified from Sugita et al., 2016).

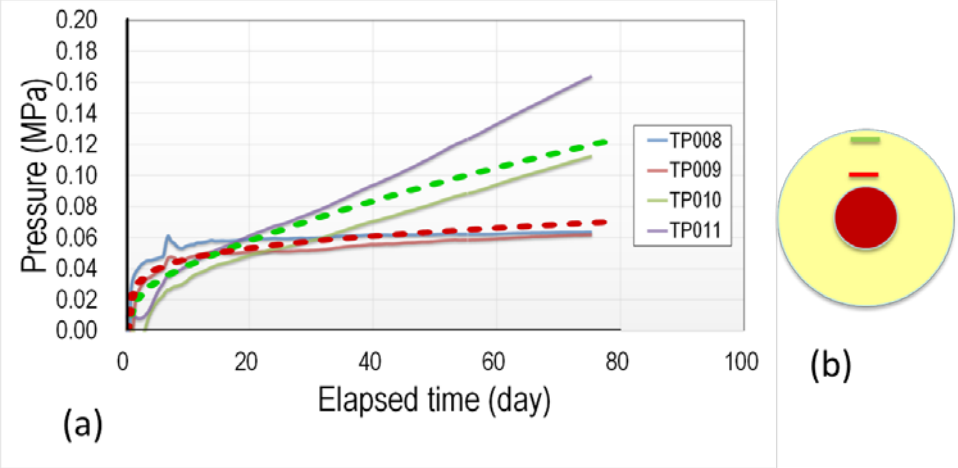

Figure 2.50. Interpretative model simulation of radial buffer stress (pressure) showing in (a) the results of two different simulations (red and green dashed lines) with different parameters for thermal expansion and moisture swelling that can each provide a good match to measured data with the approximate locations shown in (b) on a plane view of the buffer (field data from Sugita et al., 2016).

2.4.4 Summary and lessons learned from modeling the Horonobe EBS experiment

Over the past three years, as part of the DECOVALEX-2015 project, we conducted modeling of coupled THM processes in bentonite backfill and mud stone at the Horonobe site. Here we list a few important findings and lessons learned from LBNL participation in this modeling task:

- We applied full two-phase (gas and liquid) flow modeling which again revealed a very high intrinsic gas permeability is required to match observations of drying near the heat source. As mentioned, such high gas intrinsic permeability has been observed in laboratory and reported in the literature and is one of the assumptions when simplifying to single phase flow models.
- The Horonobe EBS experiment was modeled with a 3D TOUGH-FLAC model, in this case applied to system of vertical emplacement, a backfilled tunnel, a different type of bentonite, and relatively high permeability and high porosity host rock.
- With the THM parameters determined from laboratory scale experiments on bentonite and backfill, and based on site investigations on mudstone properties, the modeling of the Horonobe EBS experiment resulted in good prediction in temperature, whereas some disagreement occurred in the stress evolution. The reason for these local disagreements in stress evolution is still an open question.
- The Horonobe EBS experiment provides good mechanical measurement data in the buffer, including stresses and displacements at various parts of the buffer that with longer time data can be used to evaluate different constitutive models for bentonite mechanical behavior.
- The 75 days of measured data is too short and it will be important to continue to follow the evolution and compare with modeling much beyond 75 days.

2.5 FE EXPERIMENT AT THE MONT TERRI SITE (MONT TERRI PROJECT)

Presented in this section is the current status of the FE Experiment and modeling. For the Mont Terri FE experiment is that all the heaters, bentonite buffer and instrumentation have been installed, the tunnel has been plugged, and the final heater was turned on February 15, 2015 (Figure 2.51). Field data from the first year of heating was distributed to the international modeling teams participating in the modeling of the FE experiment were distributed in February 2016. LBNL as a modeling team is currently in the midst of interpretative modeling of the first year of data in preparation for the next modeling meeting expected to be held in November 2016.

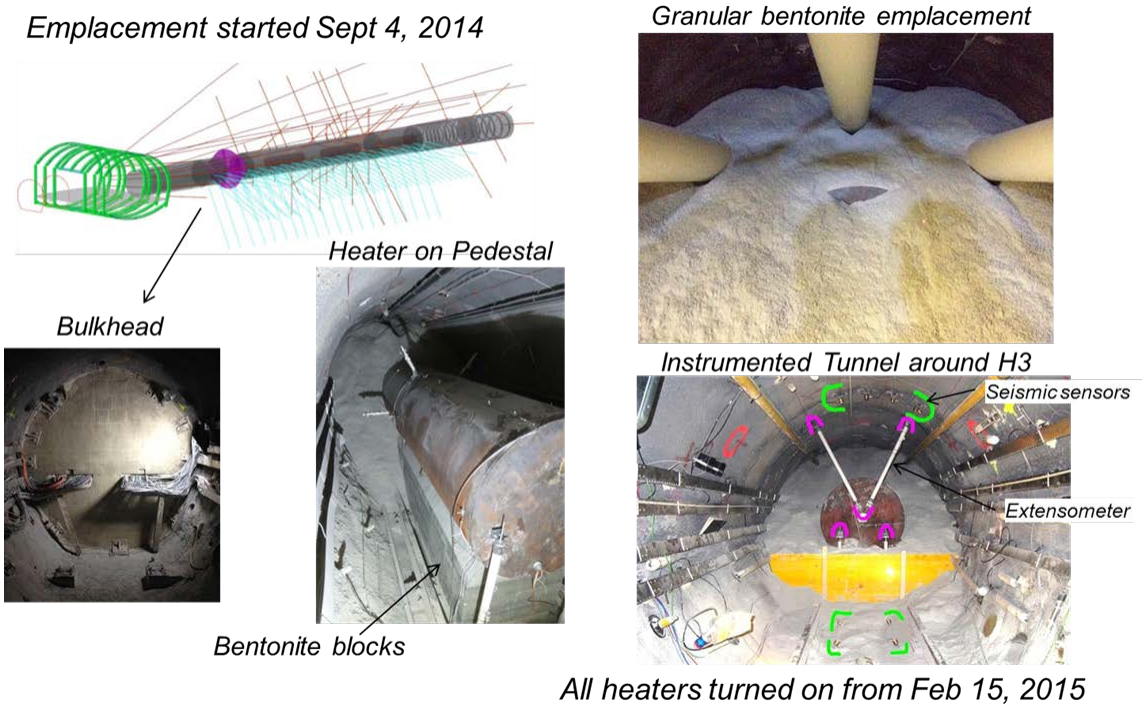

Figure 2.51. Images from the construction and installation of heaters, bentonite buffer and plugs from NAGRA daily reports by Herwig Müller, NAGRA on FE experiment progress during its construction.

As mentioned, the Mont Terri FE Experiment will be one of the largest and longest-duration heater tests worldwide, with focus on both the EBS components and the host-rock behavior. The FE experiment is conducted in a side tunnel at Mont Terri, excavated along the claystone bedding planes for this purpose, extending 50 m in length and about 2.8 m in diameter (Figure 2.52). Heating from emplaced waste will be simulated by three heat-producing canisters of 1500 W maximum power. The temperature is expected to exceed 100°C, with a target temperature 125 to 135°C at the inner parts of the buffer. A sophisticated monitoring program is planned, including dense pre-instrumentation of the site for *in situ* characterization, dense instrumentation of the bentonite buffer and host rock, and extensive geophysical monitoring (seismic and electric tomography).

The experiment will provide data useful for the validation of THM coupling effects regarding the processes in the host rock, while correctly accounting for (and examining) the conditions in the emplacement tunnel (temperature, saturation, and swelling pressure). Due to the 1:1 scale of the experiment, it will be possible to achieve realistic temperature, saturation, and stress gradients. It will also

be possible to test backfilling technology with granular bentonite, as well as lining technology with shotcrete, anchors, and steel ribs. Processes examined in the test cover many aspects of repository evolution, such as creation and desaturation of the EDZ during tunnel excavation and operation (including ventilation for about one year), as well as reconsolidation of the EDZ, resaturation, thermal stresses, and thermal pore-pressure increase after backfilling and heating (heating and monitoring period > ten years).

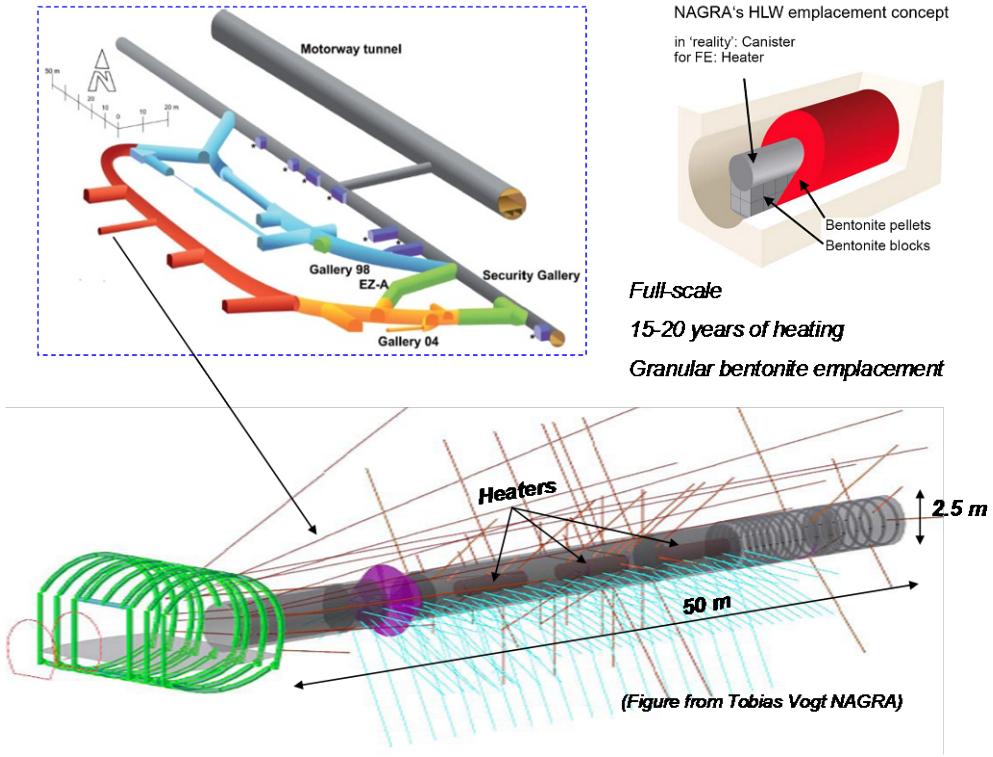

Figure 2.52. Plan view of FE experiment setup and borehole layout.

In 2011, a niche in front of the FE tunnel was constructed, followed by a first phase of instrumentation of the rock mass surrounding the tunnel, using boreholes from the niche. The FE tunnel was then excavated by road-header in 2012; this was followed by another phase of instrumentation. The tunnel was open for a one year ventilation period. This was followed by the emplacement of the heaters, bentonite buffer, and a concrete plug, after which the heating was gradually turned on during the fall of 2014. The heating is then expected to go on for at least fifteen years, with continuous monitoring of THM processes in both the bentonite buffer and surrounding rock.

2.5.1 FE-E experiment modeling tasks

DOE is one of the experimental partners for the FE heater experiment, and LBNL is one of the modeling teams. In addition to LBNL, six other modeling teams are currently involved in the Mont Terri FE experiment from Germany (2 teams), United Kingdom, Spain, Switzerland, and Canada.

The THM modeling program includes three types of computations:

1) Scoping calculations
2) Bench Marking
3) Predictive computations

The scoping calculations include brainstorming on potential ongoing processes, evaluating their significance and parameter range, comparing simulation results and input parameters derived by each team, and lessons learned (parameter range, importance, expected response). The benchmarking uses well-defined geometry problems with exact parameter values given to the teams, focusing on process modeling with precise comparison of codes. In the predictive calculations, likely parameters values and the as-built information of the experiment will be frozen.

Each modeling team developed conceptual models and material properties using available literature (papers and reports) on lab experiments and previous Mont Terri *in situ* tests, etc. Moreover, this is complemented with a restricted benchmark test for code comparison, in which properties and model geometry are set by NAGRA. The FY13 UFD milestone report titled "Report on International Collaboration Involving the FE Heater and HG-A Tests at Mont Terri (Houseworth et al., 2013), presented results on the scoping calculations and the benchmarking which was completed in April 2014. We also made a first full THM 3D simulation of the FE heater test, was created including the BBM model for calculating the mechanical responses. These were scoping and preliminary predictions with the material properties available at the time, though in some cases including a different kind of bentonite.

The FY2015 UFD milestone report title "Investigation of Coupled Processes and Impact of High Temperature Limits in Argillite Rock" (Zheng et al., 2015), presented simulation results related to the thermal evolution for different heat power schemes. This included a staged heating during the first few months of the experiment. A staged heating schedule was also adopted in the real experiment to be able to use early data for determining the maximum heat load so that temperatures would not exceed certain limits. For example, the maximum temperature should not exceed 150°C as such high temperature could potentially damage the monitoring system. The modeling presented in the FY15 UFD milestone report indeed showed that temperature could increase about 150°C in the maximum heat power of 1500 W would be applied on each of the heaters. It was decided by NAGRA, to limit the maximum heat power to 1380 W to be well below 150°C in maximum temperature.

This report presents initial interpretative modeling of the FE experiment with comparison to field data for the first year of heating. The approach was to use the previously developed 3D model of the FE experiment but with THM properties updated and determined from the modeling of the smaller scale HE-E experiment.

2.5.2 TOUGH-FLAC model of the Mont Terri FE Experiment

For the modeling of the FE experiment, conceptual model and modeling approach that was presented and used for model predictions in previous milestone reports (Houseworth et al., 2013; Zheng et al., 2014; Zheng et al., 2015). The host rock is modeled using TOUGH-FLAC with anisotropic properties considering bedding planes of the Opalinus Clay. To accurately model anisotropic thermal and hydrological behavior, we created an inclined TOUGH2 mesh. Anisotropic mechanical material behavior is simulated using the FLAC3D ubiquitous joint model, with initial properties of those derived from the excavation design analysis of the experimental tunnels. In the ubiquitous joint model weak planes are assumed along the bedding planes of the Opalinus Clay in which the shear strength properties are different along bedding versus across bedding (Housworth et al. 2013). For the bentonite, we started with the BBM model as applied by the CINEMAT and UPC (Garitte and Gens, 2012), and derived specific input material parameters for the MX-80 bentonite pellets that is used as the emplaced bentonite buffer around the heaters. With this modeling approach, we are able to simulate THM processes in both the bentonite and host rock, as well as their interactions.

Figure 2.53 presents the 3D TOUGH-FLAC numerical grid of the FE experiment. This model grid includes all vital material components for the modeling of the FE experiment, including layered Opalinus Clay host rock, excavation disturbed zone, tunnel, three heaters, bentonite buffer, concrete liner, and concrete plug. The initial conditions for the model simulation are 2 MPa pore-fluid pressure and 15°C

temperature for the host rock. The 2 MPa pore pressure is not under hydrostatic conditions, and the process is affected by the existing tunnel system at the site. In our simulations, we first run a simulation with an open tunnel at atmospheric pressure for one year, creating a pressure drop and hydraulic gradient around the tunnel. Thereafter, we assume instantaneous emplacement of the heater and buffer, and start our heating simulation.

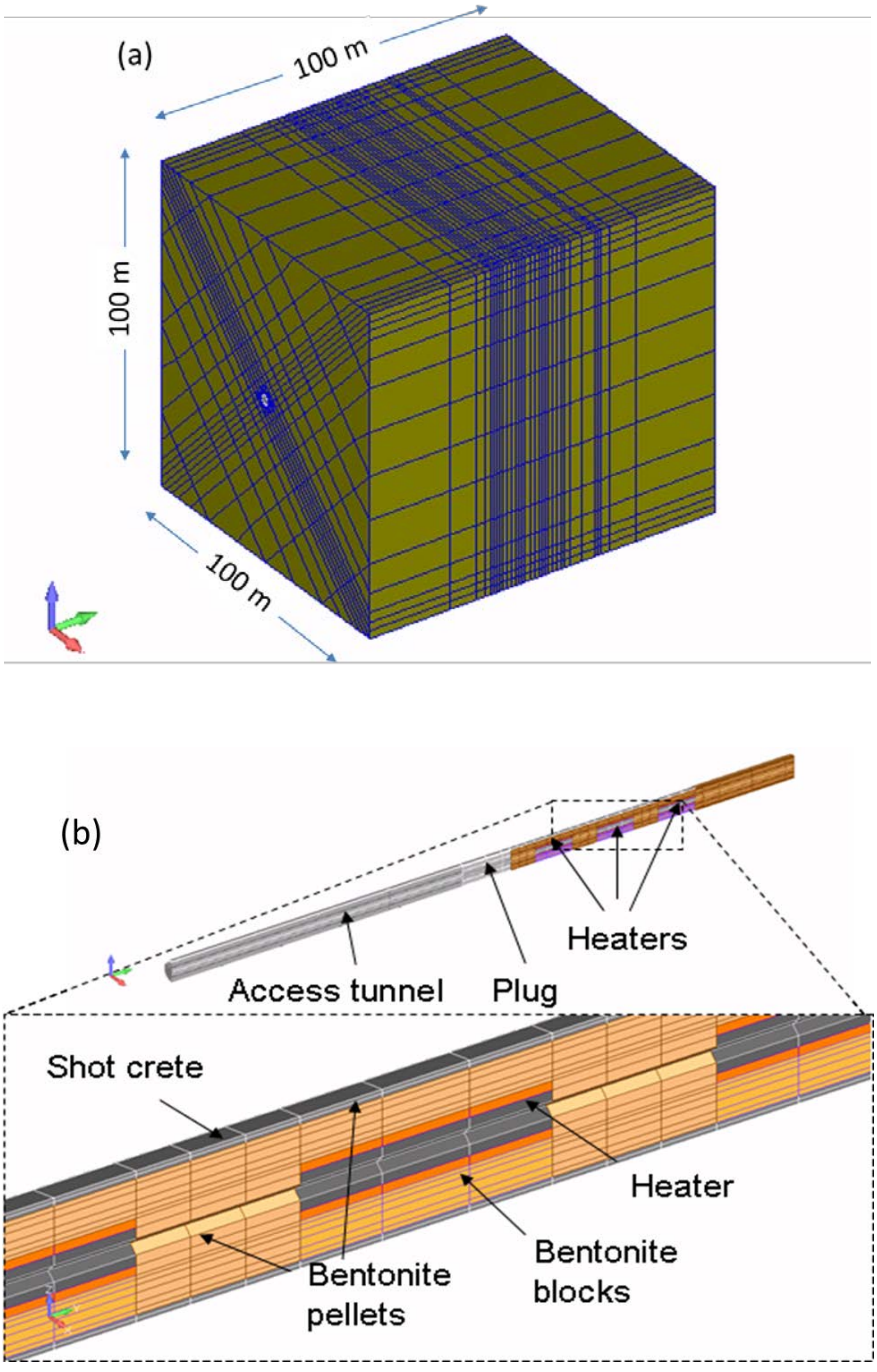

Figure 2.53. TOUGH-FLAC 3D numerical grid of the FE experiment. (a) entire model and (b) details of the materials and gridding of the EBS.

The thermal and hydraulic material properties for modeling the FE experiment are identical to those given in Table 2.6 for the HE-E experiment. These properties are based on the modeling studies of several other smaller scale heater experiments, including the HE-D and HE-E experiments and are therefore expected to be the best estimate of properties at the FE experiment. The intrinsic permeability of gas flow in the bentonite is about six orders of magnitude higher than the intrinsic permeability for liquid flow and this is simulated in TOUGH2 using a high value of the Klinkenberg parameter.

Our initial approach was to use the initial saturation in the buffer corresponding to the one observed in HE-E experiment, which based on an initial measured relative humidity and the adopted retention curve would be about 20% in the granular bentonite and 65% in the bentonite blocks. However, as it turned out from the relatively humidity measurement, the initial buffer saturation was slight different in the FE experiment compared to that of the HE-E experiment. To match the initial relative humidity in the FE experiment, the initial saturation was set to 16.5% for granular bentonite and to 75% for bentonite blocks.

Figures 2.54 and 2.55 shows the comparison of modeling and measured data for the evolution of temperature and relative humidity within the buffer at the middle heater. Figure 2.54 shows that the modeled evolution of temperature is in excellent agreement with measurements, while Figure 2.55 shows a reasonable are in agreement between modeled and measured relative humidity. These results show that the modeling in general very well captures the TH responses in the buffer during the first year of heating.

The modeling results in Figures 2.54 and 2.55 are not strictly blind predictions as a few model parameters were adjusted in an interpretative analysis to achieve the best possible agreement between model and measurements. As mentioned, the starting point was to use the material properties determined from the previous modeling of the HE-E experiment. Using these properties, an excellent agreement was indeed achieved for the temperature evolution. However, the thermal properties of the heater assembly were adjusted to achieve the observed difference in temperature between the granular bentonite and bentonite bocks and to achieve a rapid increase in temperature during the initial phase of the heating. This was achieved by reducing both the thermal conductivity and heat capacity of the heater assembly compared to that of solid steel. As shown in Figure 2.54, the temperature at the heater surface is substantially lower below the heater (adjacent to bentonite blocks, around 118°C after 400 days) compared to the temperature at the side of the heater (adjacent to granular bentonite, around 125°C after 400 days). From the modeling we can explain this difference by the fact that the thermal conductivity of the compacted bentonite blocks are much higher than that of the granular bentonite at the initial saturation. To achieve a are in agreement between modeled and measured evolution of relative humidity, a porous medium tortuosity factor of 0.14 was multiplied to the diffusion coefficient. No other material parameter for bentonite or Opalinus Clay was modified compared to that of the HE-E experiment. As a sensitivity case we may try to use a medium tortuosity factor of 1.0 that results in a higher effective diffusion coefficient. The result in Figure 2.56 shows that the modeled and measured relative humidity evolution strongly deviated for such a case indicating too high effective diffusion coefficient.

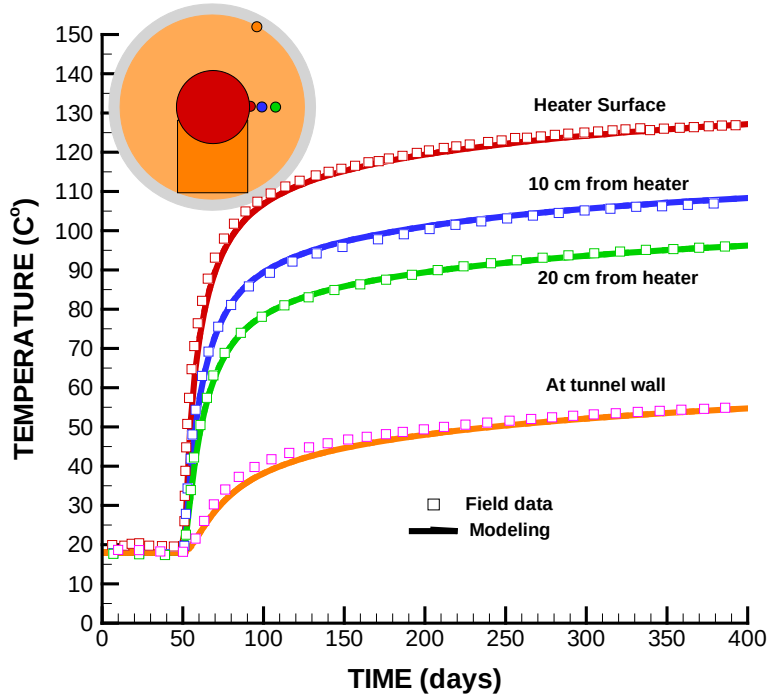

(a)

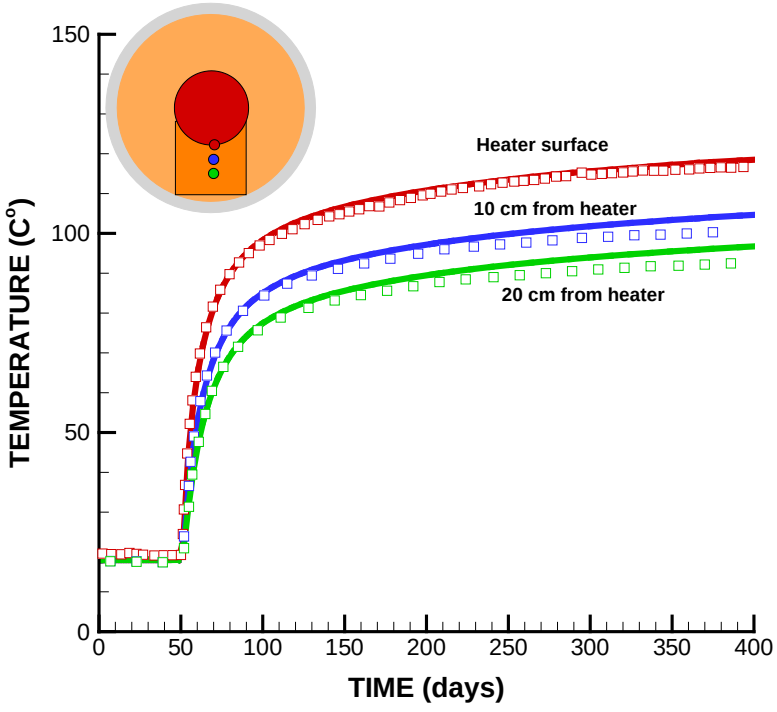

(b)

Figure 2.54. Comparison of modeled (lines) and measured (symbols) evolutions of temperature at monitoring point located in (a) granular bentonite and (b) bentonite blocks.

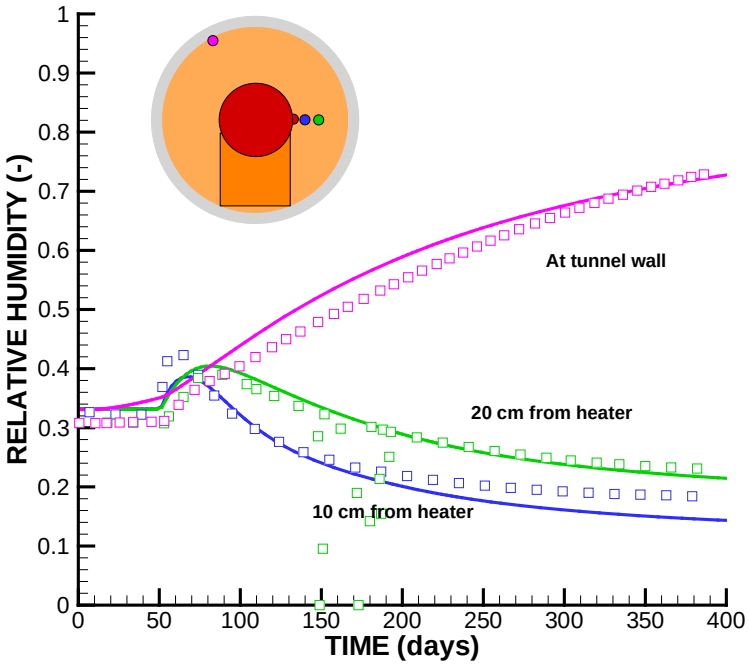

(a)

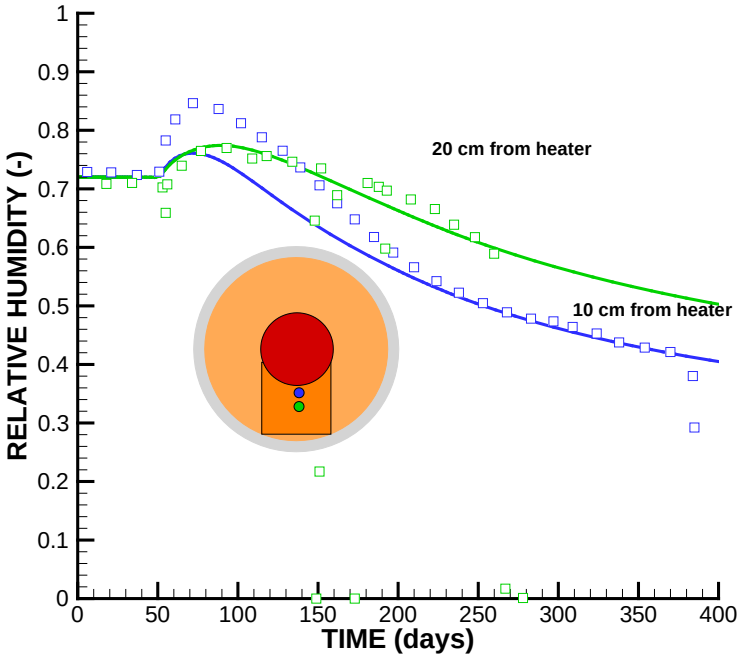

(b)

Figure 2.55. Comparison of modeled (lines) and measured (symbols) evolutions of relative humidity at monitoring point located in (a) granular bentonite and (b) bentonite blocks for a diffusion tortuosity factor of 0.14.

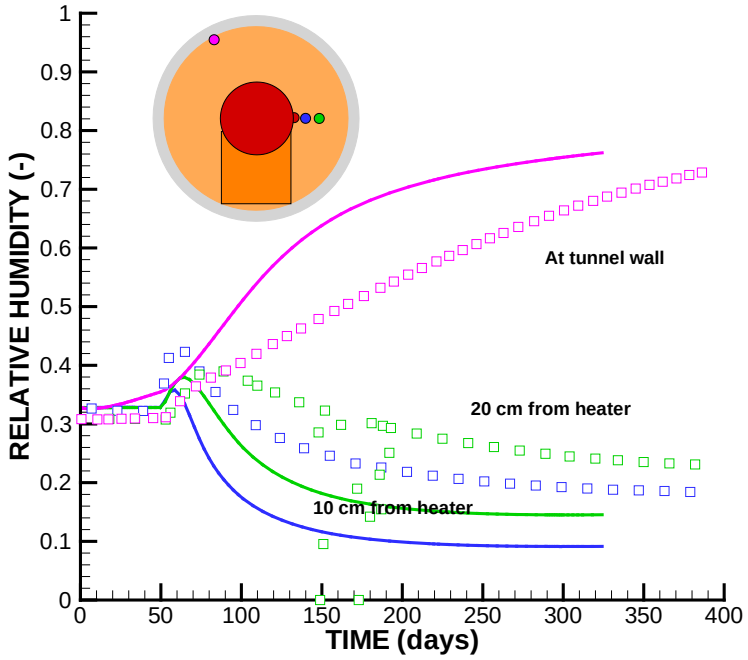

(a)

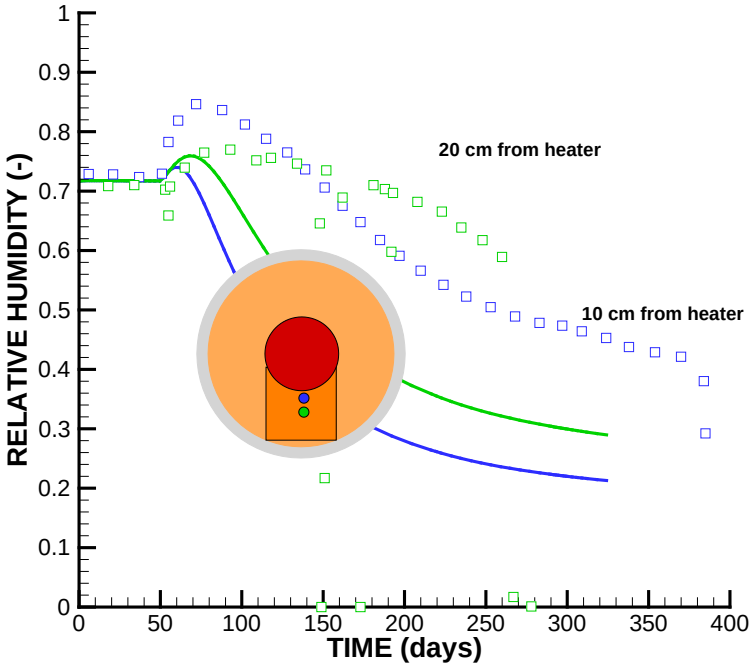

(b)

Figure 2.56. Comparison of modeled (lines) and measured (symbols) evolutions of relative humidity at monitoring point located in (a) granular bentonite and (b) bentonite blocks for a diffusion tortuosity factor of 1.0 showing the sensitivity to this parameter.

2.5.4 Summary and status the FE experiment modeling

As a modeling team in the Mont Terri FE experiment, we have conducted various types of modeling over the past few years, including benchmarking, heating design modeling, and model predictions and interpretations of the first year of heating data. We have done some initial comparison of the basic temperature and relative humidity evolution in both granular bentonite and bentonite blocks. Some finding and lessons learned from this:

The initial relative humidity in the FE experiment was slightly different from that of the HE-E experiment, although the buffer materials were the same. The reason for this difference is an open question. Maybe related to the initial relative humidity in the Mont Terri URL depending on season.
A are in agreement between modeled and measured evolutions in buffer temperature and relative humidity was achieved at the FE experiment based on a model prediction using properties of bentonite and Opalinus Clay determined associated with the previous HE-E experiment.

A value of the effective vapor diffusion coefficient (and medium tortuosity factor) could be precisely calibrated against measured relative humidity evolution, but their values were much lower than those used for modeling of the HE-E experiment. This difference and the potential role of enhanced thermal diffusion of the early time TH response in the buffer are open questions.

By studying field data going beyond one year, we will be able to model stress evolution in the buffer and validate mechanical models as well as study the questions related to diffusion mentioned in the previous bullet.

2.6 SUMMARY AND STATUS OF THM AND HEATER TEST MODELING

UFD and LBNL greatly benefit from participating in these international activities for developing expertise and testing advanced models for coupled THM processes to be used for predicting long-term THM evolution of a multibarrier nuclear waste repository system, involving backfilled emplacement tunnels in argillite host formations. FY16 work has been focused on modeling of large scale in situ heater experiments involving both bentonite and rock, including the Mont Terri HE-E, Horonobe EBS, and Mont Terri FE experiments. Modeling these experiments require large 3D models, involving all relevant components, such as simulated waste package, bentonite buffer, and host rock, as well as their interactions. Modeling a real system at full scale is the ultimate test of the numerical models and provides valuable experience in preparation for the performance assessment of future high-level nuclear waste disposals sites in the U.S.

In FY16 we have been able to successfully complete the DECOVALEX-2015 modeling associated with the Mont Terri HE-E experiment and Horonobe EBS experiment, and for the first time able to analyze field data from the largest ongoing underground heater test in the worlds; the Mont Terri FE experiment. The main accomplishments in FY16 include the improvement of the implementation and efficiency of the Barcelona Expansive Model (BExM) in TOUGH-FLAC as well as the interpretative modeling of field data from all the three underground heater experiments included in LBNL's international commitments on heater experiments.

The interpretative analyses of heater experiments as well as the evaluation of the outcome of predictive modeling have confirmed that the temperature and moisture evolution can be predicted with confidence. Related to the evolution of moisture content and buffer resaturation some questions remain related to the thermally driven diffusion, how strong this process is and why we observe some apparent inconsistencies

between the modeling of different experiments; we observed some difference in moisture evolution between the Mont Terri HE-E and FE experiments that should be studied further.

Related to the mechanical evolution of the buffer, it is well known this is more complex as it depends on a number of processes such as moisture swelling, pore pressure and thermal expansion in turn depends on the evolution of saturation, temperature, pressure and 3D geometrical mechanical confinement effects. No mechanical measurements were conducted in the buffer for the HE-E experiment, whereas the stress in the buffer has not yet been developed very much in the case of the Horonobe EBS experiment and Mont Terri FE experiment. The stress in the buffer will take years to develop and this should be modeled in the future, especially related to the Mont Terri FE experiment which is comprehensively monitored regarding mechanical changes in both buffer and host rock.

2.7 FUTURE WORK

In FY17 we plan to continue our work on participating in major international underground heating experiments, by continuing modeling of the Mont Terri FE experiment as one of the international modeling teams and starting on a new modeling tasks in the new DECOVALE-2019 project. These commitments in the new DECOVALEX-2019 project will replace our previous commitments related to the Mont Terri HE-E and Horonobe EBS experiments in the DECOVALEX-2015, which has been completed.

The DECOVALEX-2019 tasks to be started in FY17 are denoted Task A and Task E in the new DECOVALEX-2019 project. Task A is related to gas migration in bentonite, and TOUGH-FLAC with dual-structure model is one of the approach that will be tested. Task E is related to upscaling of modeling results from small scale to one-to-one scale based in heater test data in Callovo-Oxfordian claystone (COx) at MHM underground research laboratory in France. This will be a perfect task for our development and application of the model capabilities we have developed and tested over the last few years within the UFD Campaign. Upscaling is an important issue for the repository design and safety calculation. The question is how to go from sample to a repository scale? This task will include modeling at difference scales, from laboratory scale to field scale heater experiments and all the way to repository scale.

The FY17 work on the Mont Terri FE experiment will be focused on modeling of the mechanical evolution of the buffer and host rock, including the application of the BExM model at a large scale. It will be a great opportunity to apply and test the BExM at the larger scale on the FE experiment, in particular because one the other international modeling teams is the University of Catalonia group in Barcelona, Spain that is the origin of the BExM model and they will apply BExM for the modeling of the Mont Terri FE experiment, but using a different numerical simulator. At the same time we will continue to validate and gain experiences in the use of the BExM.

In addition to these tasks related to underground heater experiments, in FY17 we intend to study a few important technical issues that arose from the DECOVALEX-2015 work on HE-E and Horonobe experiments. The first is related to the strength of thermally driven diffusion which did not seem consistent between different experiments, such as the HE-E and FE experiments. We will investigate different options of enhanced thermal diffusion which may resolve the small deviation between modeling and measurements of the evolution of relative humidity the buffer as observed for the HE-E experiment. The second is related to the small inconsistencies we observed in the early time stress evolution at the Horonobe EBS experiment. We now have longer term measurement data from the experiment and using this we plan to try different constitutive mechanical models, such as BBM instead of simple swelling, to investigate whether a more consistent mechanical behavior can be modeled.

Finally, the implementation and application of a continuum damage model for the evolution of the excavation disturbed zone is another needed addition to the current model for the calculating the evolution of permeability along with damage as well as sealing and healing. Different approaches can be tested, including continuum damage models considering fracture evolution implicitly. Such a model can be benchmarked against discrete fracture modeling of damage zone fractures using TOUGH-RBSN. The goal is to build a pragmatic continuum model that can be validated against field experiments such as sealing experiments conducted in underground research laboratories.

2.8 REFERENCES

Alonso EE, Gens A, Josa A (1990) A constitutive model for partially saturated soils. Geotechnique. 40: 405-430.

Alonso, E. E., Vaunat, J., Gens, A. (1999). Modelling the mechanical behaviour of expansive clays. Engng Geol. 54, 173–183.

Chijimatsu M, Nguyen TS, Jing L, de Jonge J, Kohlmeier M, Millard A, Rejeb A, Rutqvist J, Souley M, Sugita Y (2005) Numerical study of the THM effects on the near-field safety of a hypothetical nuclear waste repository – BMT1 of the DECOVALEX III project. Part 1: Conceptualization and characterization of the problems and summary of results. Int. J Rock Mech & Min Sci 42:720–730.

Corkum A.G., Martin C.D. (2007) The Mechanical Behaviour of Weak Mudstone (Opalinus Clay) at Low Stresses, International Journal of Rock Mechanics and Mining Sciences, 44, 196-209.

Esteban, F. (1990). Caracterización experimental de la expansividad de una roca evaporítica. PhD thesis, Universidad de Canabria, Santander (in Spanish).

Feng Xia-Ting, Pan Peng-zhi, Zhou Hui (2006) Simulation of rock microfracturing process under uniaxial compression using elasto-plastic cellular automata. Int J Rock Mech & Min Sci 43: 1091–1108.Garitte B. and Gens A. (2012). TH and THM Scoping computations for the definition of an optimal instrumentation layout in the Full-scale Emplacement (FE) experiment NAGRA NIB 10-34, March 2012.

Garitte B. DECOVALEX-2015 Task B1 Final Report. May (2016). Garitte, B. (2012) HE-E experiment - In situ Heater Test, Presentation given at 1th DECOVALEX 2015 workshop, April 2012, Berkeley.

Garitte B. and Gens A. (2012) TH and THM Scoping computations for the definition of an optimal instrumentation layout in the Full-scale Emplacement (FE) experiment NAGRA NIB 10-34, March 2012.

Gaus I, Wieczorek K, Schuster K, Garitte B, Senger R, Vasconcelos R and Mayor JC (2014) EBS behaviour immediately after repository closure in a clay host rock: HE-E experiment (Mont Terri URL). Geological Society, London, Special Publications, first published March 7, 2014; doi 10.1144/SP400.11

Gens A, Sánchez, M Sheng, D (2006) On constitutive modelling of unsaturated soils. Acta Geotechnica. 1, 137-147.

Gens, A, Alonso, E. A framework for the behaviour of unsaturated expansive clays. Can. Geotech. J. 29, 1013–1032 (1992).

Gens, A., Garitte, B., Wileveau, Y. (2007) In situ Behaviour of a Stiff Layered Clay Subject to Thermal Loading: Observations and Interpretation, Geotechnique, 57, 207-228.

Gens, A., Sánchez, M., Guimaraes, L.D.N., Alonso, E.E., Lloret, A., Olivella, S., Villar, M.V., Huertas, F. (2009) A full-scale in situ heating test for high-level nuclear waste disposal: observations, analysis and interpretation. Geotechnique 59, 377–399

Graupner, B.J., Lee, C., Manepally, C., Pan, P., Rutqvist, J., Wang, W., Garitte, B. (2013) The Mont Terr HE-D Experiment as a Benchmark for the Simulation of Coupled THM Processes. Extended abstract for the European Association of Geoscientists & Engineers (EAGE) International Workshop Geomechanics & Energy, Lausanne, Switzerland, 26-28 November, 2013.

Houseworth J., Rutqvist J., Asahina D., Chen F., Vilarrasa V., Liu H.H., Birkholzer J. Report on International Collaboration Involving the FE Heater and HG-A Tests at Mont Terri. Prepared for U.S. Department of Energy, Used Fuel Disposition Campaign, FCRD-UFD-2014-000002, Lawrence Berkeley National Laboratory (2013).

Itasca, FLAC3D V5.0, Fast Lagrangian Analysis of Continua in 3 Dimensions, User's Guide. Itasca Consulting Group, Minneapolis, Minnesota (2011).

Kolditz O, Bauer S, Beinhorn M, de Jonge J, Kalbacher T, McDermott C, Wang W, Xie M, Kaiser R, Kohlmeier M (2003) ROCKFLOW - Theory and Users Manual, Release 3.9, Groundwater Group, Center for Applied Geosciences, University of Tübingen, and Institute of Fluid Mechanics, University of Hannover.

Kristensson, O., Åkesson, M., (2008) Mechanical modeling of MX-80 – Quick tools for BBM parameter analysis. Phys Chem Earth, Parts A/B/C. 33, Supplement 1: S508-S515.

Liu H.H., Houseworth J., Rutqvist J., Zheng L., Asahina D., Li L., Vilarrasa V., Chen F., Nakagawa S., Finsterle S., Doughty C., Kneafsey T., Birkholzer J. Report on THMC Modeling of the Near Field Evolution of a Generic Clay Repository: Model Validation and Demonstration. Prepared for U.S. Department of Energy, Used Fuel Disposition Campaign, FCRD-UFD-2013-000244, Lawrence Berkeley National Laboratory (2013).

Lloret A, Villar MV, Sánchez M, Gens A, Pintado X, Alonso EE. Mechanical behaviour of heavily compacted bentonite under high suction changes. Géotechnique 2003; 53(1):27–40.

Olivella, S., Gens, A., 2000. Vapour transport in low permeability unsaturated soils with capillary effects. Transp. Porous Media 40, 219e241.

Pan Peng-zhi, Feng Xia-Ting, Huang Xiao-Hua, Cui Qiang, Zhou Hui (2008) Study of coupled THMC processes in crystalline rock in the EDZ using an ECPA code. Environmental Geology.

Pousada P.E. Deformabilidad de arcillas expansivas bajo succión controlada. Ph.D. Thesis, Technical University of Madrid, Spain, 1982.

Pruess, K., Oldenburg, C.M., Moridis, G. (2012) TOUGH2 User's Guide, Version 2.1, LBNL-43134(revised), Lawrence Berkeley National Laboratory, Berkeley, California.

Romero E. Characterisation and thermal-hydro-mechanical behaviour of unsaturated Boom clay: an experimental study. Ph.D. Thesis, Technical University of Catalonia, Spain, 1999.

Rutqvist J. Status of the TOUGH-FLAC simulator and recent applications related to coupled fluid flow and crustal deformations. Computers & Geosciences, 37, 739–750 (2011).

Rutqvist J., Barr D., Birkholzer J.T., Fujisaki K., Kolditz O., Liu Q.-S., Fujita T., Wang W. and Zhang C.-Y. A comparative simulation study of coupled THM processes and their effect on fractured rock permeability around nuclear waste repositories. Environ Geol, 57, 1347–1360 (2009)

Rutqvist J., Börgesson L., Chijimatsu M., Nguyen T. S., Jing L., Noorishad J., Tsang C.-F. (2001b) Coupled Thermo-hydro-mechanical Analysis of a Heater Test in Fractured Rock and Bentonite at Kamaishi Mine – Comparison of Field Results to Predictions of Four Finite Element Codes. Int. J. Rock Mech. & Min. Sci. 38, 129-142.

Rutqvist J., Chijimatsu M., Jing L., De Jonge J., Kohlmeier M., Millard A., Nguyen T.S., Rejeb A., Souley M., Sugita Y. and Tsang C.F. Numerical study of the THM effects on the near-field safety of a

hypothetical nuclear waste repository – BMT1 of the DECOVALEX III project. Part 3: Effects of THM coupling in fractured rock Int. J. Rock Mech. & Min. Sci, 42, 745-755 (2005).

Rutqvist J., Davis J., Zheng L., Vilarrasa V., Houseworth J.,Birkholzer J. Investigation of Coupled THMC Processes and Reactive Transport: FY14 Progress. Prepared for U.S. Department of Energy, Used Fuel Disposition, FCRD-UFD-2014-000497, Lawrence Berkeley National Laboratory, LBNL-6720E (2014a).

Rutqvist J., Zheng L., Chen F, Liu H.-H, and Birkholzer J. Modeling of Coupled Thermo-Hydro-Mechanical Processes with Links to Geochemistry Associated with Bentonite-Backfilled Repository Tunnels in Clay Formations. Rock Mechanics and Rock Engineering, 47, 167–186 (2014b).

Rutqvist, J., Börgesson, L., Chijimatsu, M., Kobayashi, A., Nguyen, T.S., Jing, L., Noorishad, J., Tsang, C.-F. (2001a) Thermohydromechanics of partially saturated geological media – Governing equations and formulation of four finite element models. Int. J. Rock Mech. & Min. Sci. 38, 105-127.

Rutqvist, J., Ijiri, Y. and Yamamoto, H. Implementation of the Barcelona Basic Model into TOUGH-FLAC for simulations of the geomechanical behavior of unsaturated soils. Computers &Geosciences, 37, 751-762 (2011).

Rutqvist, J., Wu, Y.-S., Tsang, C.-F. and Bodvarsson, G. (2002). A modeling approach for analysis of coupled multiphase fluid flow, heat transfer and deformation in fractured porous rock. International Journal of Rock Mechanics & Mining Sciences, 39, 429-442.

Sánchez, M., Gens, A., Guimarães, L. do N., Olivella, S. A double structure generalized plasticity model for expansive materials. Int. J. Numer. Anal. Meth. Geomech., 29, 751–787 (2005).

Sugita Y., Kwon, S., Lee C., Maßmann J., Pan P., and Rutqvist J. DECOVALEX-2015 Task B2 Final Report. May (2016).

van Genuchten, M.T. (1980) A closed-form equation for predicting the hydraulic conductivity of unsaturated soils. Soil Sci Soc Am J 1980, 44, 892-898.

Vilarrasa V., Rutqvist J., Blanco-Martin L., and Birkholzer J. (2015). Use of a dual structure constitutive model for predicting the long-term behavior of an expansive clay buffer in a nuclear waste repository. Int. J. Geomech., D4015005.

Villar, M.V. (2012) THM Cells for the HE-E Test: Setup and First Results; PEBS Report D2.2.7a. CIEMAT Technical Report CIEMAT/DMA/2G210/03/2012; Euratom 7th Framework Programme Project: PEBS: Madrid, Spain.

Wang W, Xie M, Nowak T, Kunz H, Shao H, Kolditz O (2006) Modeling THM coupled problem of Task D of the DECOVALEX project. Proc. GEOPROC2006 International symposium: 2nd International Conference on Coupled Thermo-hydro-mechanical-chemical processes in Geosystems and Engineering, HoHai University, Nanjing, China, May 22-25, 2006, 226–232, HoHai Univers

Wileveau, Y. THM behaviour of host rock: (HE-D experiment): Progress Report September 2003–October 2004. Mont Terri Project, TR 2005-03 (2005).

Zheng L., Rutqvist J., Kim K., Houseworth J. Investigation of Coupled Processes and Impact of High Temperature Limits in Argillite Rock. Prepared for U.S. Department of Energy, Used Fuel Disposition, FCRD-UFD-2015-000362, Lawrence Berkeley National Laboratory, LBNL-187644 (2015).

Zheng L., Rutqvist J., Steefel C., Kim K., Chen F., Vilarrasa V., Nakagawa S., Houseworth J., and Birkholzer J. Investigation of Coupled Processes and Impact of High Temperature Limits in Argillite Rock. Prepared for U.S. Department of Energy, Used Fuel Disposition, FCRD-UFD-2014-000493, Lawrence Berkeley National Laboratory, LBNL-6719E (2014).

This page is intentionally left blank

3. INVESTIGATION OF THE IMPACTS OF HIGH TEMPERATURE LIMITS WITH THMC MODELING

3.1 INTRODUCTION

Radioactive waste from spent fuel emanates a significant amount of thermal energy due to decay processes, which causes temperature increases in the surrounding environment particularly in the early stages of waste emplacement. The temperature to which the EBS (engineered barrier system) and natural rock can be exposed is one of the most important design variables for a geological repository, because it determines waste package spacing, distance between disposal galleries, and therefore the overall size (and cost) of repository for a given amount of heat-emanating waste (Horseman and McEwen, 1996). This is especially important for a clay repository, because argillaceous rocks have relatively small heat conductivity. Temperature governs chemical alteration and the subsequent changes in mechanical properties of the EBS. A high temperature could result in chemical alteration of buffer and backfill materials (bentonite) within the EBS through illitization and cementation, which compromise the function of these EBS components by reducing their plasticity and capability to swell when wetting (Pusch and Karnland, 1996; Pusch et al., 2010; Wersin et al., 2007). The swelling capability of clay minerals within the bentonite is important for sealing gaps between bentonite blocks, between bentonite and other EBS components, and between the EBS and the surrounding host rock. Chemical alteration may also occur in the near-field host rock, which could reduce the clay capability for self-sealing within the excavation damaged zone (EDZ). Because the permeability of clay rock is low, a high temperature may induce significant pore pressure build-up (through pore water expansion and vaporization) in the near field, which could generate adverse mechanical deformation (such as fracturing), damaging the integrity of the host rock (Horseman and McEwen, 1996).

All disposal concepts throughout the world, despite their differences in design, unanimously impose a temperature limit of about 100^{o}C (Hicks et al., 2009). However, Wersin et al. (2007), after reviewing a number of data sets, concluded that the criterion of 100^{o}C for the maximum temperature within the bentonite buffer is overly conservative. Their conclusion was based on their findings that no significant changes in bentonite hydraulic properties occur at temperatures of up to 120^{o}C under wet conditions and that bentonite is chemically stable to much higher temperature under dry conditions. The impact of high temperature on bentonite and clay host rock behavior, and consequences on repository performance, remain largely an open question for a clay repository system. While various studies have shed light on certain aspects of this question, there is no study that integrates the relevant THMC processes and considers the interaction between EBS and host rock.

In UFDC, LBNL has used coupled THMC modeling to evaluate the chemical alteration and mechanical changes in EBS bentonite and the NS (natural system) clay formation under various scenarios, attempting to provide necessary information for decisions on temperature limits. After an extensive review of the THMC alteration of EBS and argillite under various temperature conditions, fully coupled THMC simulations were developed for a nuclear waste repository in a clay formation with a bentonite-backfilled EBS (Liu et al., 2013). Two scenarios were simulated for comparison: (1) a case in which the peak temperature in the bentonite near the waste canister is about 200^{o}C and, (2) a case in which the temperature in the bentonite near the waste canister peaks at about 100^{o}C. In these simulations, it was assumed that the host rock properties were representative of Opalinus Clay (Bossart 2011; Lauber et al., 2000) and the EBS bentonite was Kunigel-VI bentonite (Ochs et al., 2004) or FEBEX bentonite (ENRESA, 2000). Simulations were first conducted for one thousand years (Liu et al., 2013; Zheng et al., 2014) and then were extended to one hundred thousand years thanks to improvement of efficiency of TOUGHREACT-FLAC3D simulator (Zheng et al., 2015). Model results (Liu et al., 2013; Zheng et al., 2014; Zheng et al., 2015) found out the illitization is enhanced at high temperature. However, the

magnitude of illitization varies a great deal and has to be evaluated case by case. In general illitization leads to reduction in swelling stress but the degree of reduction varies with the type of bentonite.

The coupling between chemical and mechanical processes is the key part of THMC model that allow us to evaluate the direct impact of chemical changes on mechanical behavior. In previous THMC model (e.g. Zheng et al., 2015), the coupling between chemical and mechanical processes was carried out via an extended linear swelling model which is simple and key parameters are relatively easy to be calibrated. However, such model does not accurately describe the transient state of swelling, neglect the history of mechanical change and is unable to account for the impact of cations exchange on the swelling. In FY16, THMC models uses double structure Barcelona Expansive Clay Model (BExM) (Sánchez et al., 2005) to link mechanical process with chemistry. As a result, the model can simultaneously incorporate the effects of exchangeable cations, ionic strength of pore water and abundance of swelling clay on the swelling stress of bentonite. In addition, the corrosion of steel canister was considered in the chemical model to evaluate whether the iron-bentonite interaction would aggravate the negative impact on swelling stress by forming some Fe bearing clay minerals. In this report, we first summarize the key findings from previous modeling work (Liu et al., 2013; Zheng et al., 2014; Zheng et al., 2015) which set the stage for the simulations conducted in FY16; second, we present the THMC model that takes into account of the interaction between corroded steel canister and bentonite, and third we discuss the coupled THMC model using BExM and the chemical effect on stress.

3.2 MODEL DEVELOPMENT

Because the model used in this report is similar to that in previous years (Liu et al., 2013; Zheng et al., 2014; Zheng et al., 2015), we briefly describe each element of the THMC model here, focusing on the updates in FY16. Additional details on the THMC model are presented in Liu et al. (2013).

3.2.1 Simulator

Although codes that can simulate THMC processes are fairly sparse, numerous codes that are capable of simulating either THC or THM process have been developed in the last two decades. Examples of THC codes include: TOUGHREACT (Xu et al., 2006; 2011), RETRASO (Saaltink et al., 2004), CRUNCH (Steefel, 2001), NUFT (Nitao, 1996), GEOCHEMIST'S WORKBENCH (Bethke, 2002), and examples of THM codes are ROCMAS (Noorishad and Tsang, 1996; Rutqvist et al., 2001), CODE_Bright (Olivella et al., 1994), and Open-Geosys (Wang et al. 2011). In recent years, some codes have also been expanded to have THMC capability such as versions of CODE_BRIGHT (Guimaraes et al., 2007; 2013); FADES-CORE (Zheng and Samper, 2008) and TOUGH2-CSM (Zhang et al., 2012), TR-FLAC (Taron et al., 2009), TOUGHREACT-FLAC (Zheng et al., 2014), and TOUGHREACT-ROCMECH (Kim et al., 2015). The OPEN-GEOSYS (Wang et al., 2011) and MOOSE (Gaston et al., 2009) model frameworks are open and flexible software environments that allow coupling of THMC processes.

Consideration of the coupling between chemistry and mechanics differs depending on the application, e.g. geothermal versus nuclear waste disposal, and various simplifications have been employed in order to focus on relevant couplings and processes for the specific problem to be solved. The numerical simulations in this study are conducted with TOUGHREACT-FLAC3D, which sequentially couples the multiphase fluid flow and reactive transport simulator, TOUGHREACT (Xu et al., 2011), with the finite-difference geomechanical code FLAC3D (Itasca, 2009). The coupling of TOUGHREACT and FLAC3D was initially developed in Zheng et al. (2012) to provide the necessary numerical framework for modeling fully coupled THMC processes. It included a linear elastic swelling model (Zheng et al., 2012; Rutqvist et al., 2014) to account for swelling as a result of changes in saturation and pore-water composition and the abundance of swelling clay (Liu et al., 2013; Zheng et al., 2014). The major improvement in

TOUGHREACT-FLAC3D is the implementation of a time-step management scheme to reduce the simulation time. Figure 2.1 shows the coupling scheme of TOUGHREACT-FLAC3D. In each time step, TOUGHREACT calculates the primary variables for THC processes including temperature (T), liquid pressure (P_l) or gas pressure (P_g), water saturation (S_l), ion concentrations of pore water (C_i) and concentration of exchangeable cations and/or abundance of swelling clay minerals (X_i). These primary variables are then passed to FLAC3D via a coupling module to conduct stress and strain analysis (see Figure 3.1). The coupling between THC processes (provided by TOUGHREACT) and the mechanical part (FLAC3D) is carried out at every time step. The FLAC3D stress and strain analysis constitutes a large portion of the total computation time. For example, in the base case for FEBEX bentonite described below, a THC run took about 4.5 hours but the THMC run (which calls FLAC3D at every time step) took about 4 days. The length of time step is constrained by the chemical calculation to accommodate small changes in the concentrations. However, such small changes in chemical conditions lead to very minimal changes in stress and it is unnecessary to update the stress every time step. Therefore, a time step management scheme was implemented in TOUGHREACT-FLAC3D. A subroutine was inserted in TOUGHREACT to check the change of primary variables from the previous time step and decide if the change is large enough to warrant an update in stress/strain based on the predetermined criteria. An optimal criteria that reduces computational time but also minimizes error was determined. A criteria of 2% reduces computation time significantly and the calculated stress is very close (within 0.1% difference) to that obtained by updating stress/strain every time step.

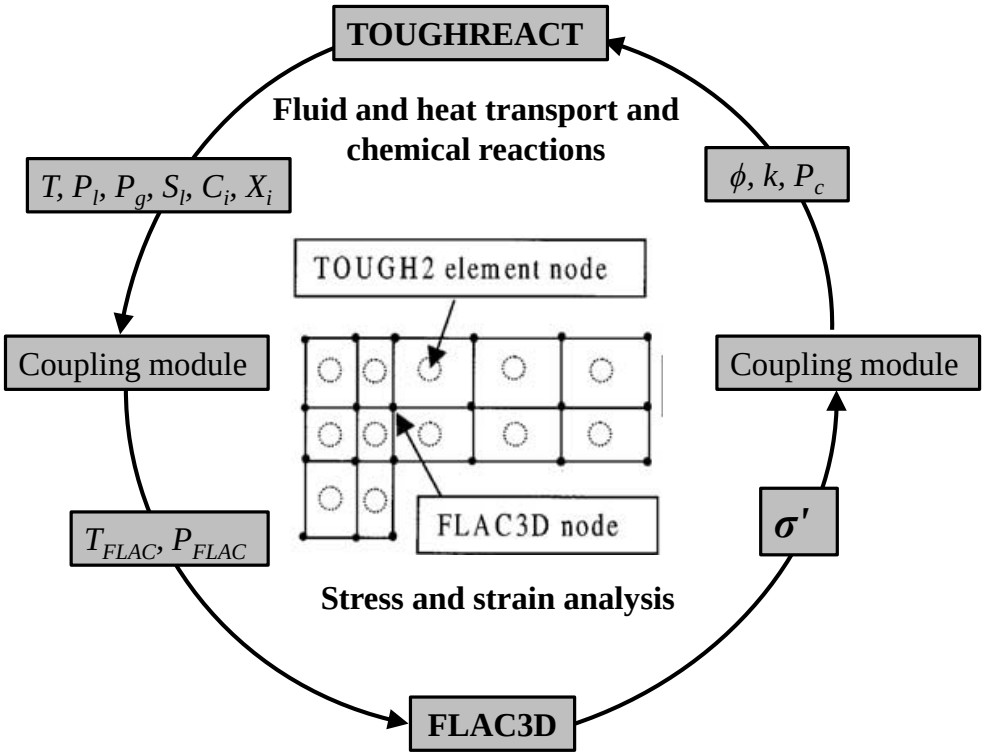

Figure 3.1.The coupling scheme for TOUGHREACT-FLAC3D.

Modeling scenario

The model scenario is still the same as in Liu et al. (2013) and Zheng et al., (2014). The model is applied to a hypothetical bentonite-backfilled nuclear waste repository in clay rock, a repository example that involves a horizontal nuclear waste emplacement tunnel at 500 m depth (Figure 3.2) (Rutqvist et al., 2013). The Z-axis is set as vertical, while the horizontal Y- and X-axes are aligned parallel and perpendicular to the emplacement tunnel, respectively (Figure 3.2) in this 2-D model. Note that while the canister is modeled as a heat source with mechanical properties of steel, the THC changes in the canister and their interactions with EBS bentonite are not considered here for the sake of simplicity.

An initial stress field is imposed by the self-weight of the rock mass. Zero normal displacements are prescribed on the lateral boundaries of the model. Zero stress is applied to the top and vertical displacements are prevented at the bottom. An open boundary is applied to the liquid pressure at top and bottom and initially the model domain is in a hydrostatic state. The initial temperature at the top is about 11 ^{o}C, with a thermal gradient of 27 ^{o}C/km, the initial temperature at the bottom is 38 ^{o}C. The model simulation was conducted in a nonisothermal mode with a time-dependent heat power input (Rutqvist et al., 2014). The power curve in Figure 3.2 was adopted from representative heating data from the U.S. DOE's Used Fuel Disposition campaign for pressurized water reactor (PWR) used fuel. This heat load is then scaled in the 2D model to represent an equivalent line load, which depends on the assumed spacing between individual waste packages along an emplacement tunnel. The heat load for the "low-T" case corresponds to an initial thermal power of 3144 W for a 4-PWR-element waste package after aging for sixty years, a 50-m spacing between emplacement tunnels, and 3-m spacing between the 5-m long packages. The heat load for the "high T" case represents similar waste package and spacing, except with only twenty years of aging. Initially the EBS bentonite has a water saturation of 65% and the clay formation is fully saturated. From time zero, the EBS bentonite undergoes simultaneously re-saturation, heating, chemical alteration, and stress changes.

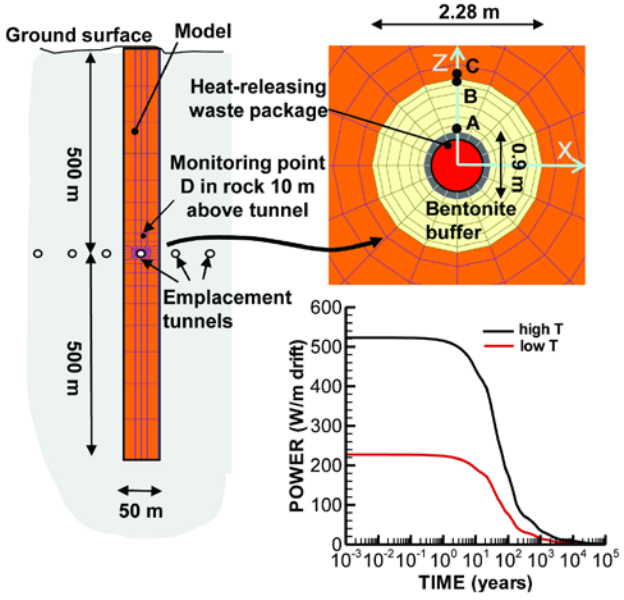

Figure 3.2. Domain for the test example of a bentonite back-filled horizontal emplacement drift at 500 m (Rutqvist et al 2013). Modeling monitoring points: A: inside the bentonite near the canister, B: inside the bentonite and near the EBS-NS interface, C: inside the clay rock formation and near the EBS-NS interface, D: inside the clay rock formation at a distance of 10 m from the canister. "High T": 200 ºC; "Low T": 100ºC.

3.2.2 Mechanical Model

3.2.2.1 Linear elastic model

Details of mechanical model implemented in the TOUGHREACT-FLAC3D are given in Rutqvist et al., (2014). Here we briefly describe the mechanical models for the EBS bentonite and clay formation. For nonisothermal behavior of unsaturated soils, we may partition the total incremental strain into elastic (ε^e), plastic (ε^p), suction (ε^s), thermal strains (ε^T) and chemical strains (ε^c):

$$d\varepsilon = d\varepsilon^e + d\varepsilon^p + d\varepsilon^s + d\varepsilon^T + d\varepsilon^c \quad 3.1$$

where the suction strain represents the strain associated with changes in suction and chemical strain represents the strains associated with change in chemical conditions, including changes in ion concentration and abundance of swelling clays. Each of these types of strain, except chemical strain, is described in Rutqvist et al., (2014).

Similar to thermally induced strains, chemical strains are purely volumetric:

$$d\varepsilon^c = -A_n^* \, dC + A_{sc}^* dMs \quad 3.2$$

where A_n^* is a constant that linearly relates ion concentration (C) variation and the corresponding strain change. A_{sc}^* is a constant that relates the change in mass fraction of swelling clay, m_s, to change in strain.

A linear elastic swelling model essentially defines the suction stress as a function of water saturation:

$$d\varepsilon^s = \beta_{sw} dSl \quad 3.3$$

where Sl is the water saturation and β_{sw} is a moisture swelling coefficient.

Under mechanically constrained conditions and considering the linear relationship between swelling stress and suction strain, $d\sigma_s = 3Kd\varepsilon^s$, we have a swelling stress that is linearly proportional to the saturation:

$$d\sigma_s = 3K\beta_{sw} dSl \quad 3.4$$

where K is the bulk modulus. Equation (4) is what was used for EBS bentonite in Rutqvist et al. (2011). In this report, β_{sw} is 0.048, calibrated based using the swelling pressure of 1 MPa for Kunigel-VI bentonite (Börgesson et al. 2001) under the condition that bentonite is saturated with dilute solution (e.g. deionized water), and K is 20 MPa (Rutqvist et al., 2011).

To consider the swelling due to both moisture and chemical changes, we include the stress due to a change of ion concentration in the pore water and abundance of swelling clay:

$$d\sigma_s = 3K(d\varepsilon^s + d\varepsilon^c) = 3K(\beta_{sw}dSl + A_n^* dC + A_{sc}^* dMs) = 3K\beta_{sw}dSl + A_n dC + A_{sc} dMs \quad 3.5$$

where $A_n = 3KA_n^*$ is a constant that linearly relates ion concentration (C) variation and the corresponding swelling stress change. $A_{sc} = 3KA_{sc}^*$ is a constant that relates the change in mass fraction of swelling clay, *Ms*, to change in swelling stress.

A_n is typically calculated from swelling pressures measured using a different solution (e.g. deionized water versus 1 M NaCl solution) to saturate the bentonite. Laredj et al. (2010) proposed the following expression for A_n:

$$A_n = \frac{(5.312\ln C - 23.596)}{\sqrt{C}} - \frac{7.252\times10^{-4}}{C^2} \quad 3.6$$

An empirical value for A_{sc} is derived through a linear regression of swelling pressure versus smectite mass fractions as shown in Figure 3.3, and A_{sc} is the slope of the linear correlation. However, probably because these bentonite materials differ not only in the mass fraction of smectite but also in other properties, these data points are fairly scattered. This makes it impossible to establish a unique linear regression between swelling pressure change and mass fraction change of smectite. Therefore, we chose a linear correlation line that crosses the measured swelling pressure for Kunigel VI bentonite and used the slope of this line as the value of A_{sc} which is 2.5×10^6 Pa. For FEBEX bentonite, we used the slope of line that crosses the measured swelling pressure of FEBEX bentonite as the value of A_{sc} which is 6.5×10^6 Pa.

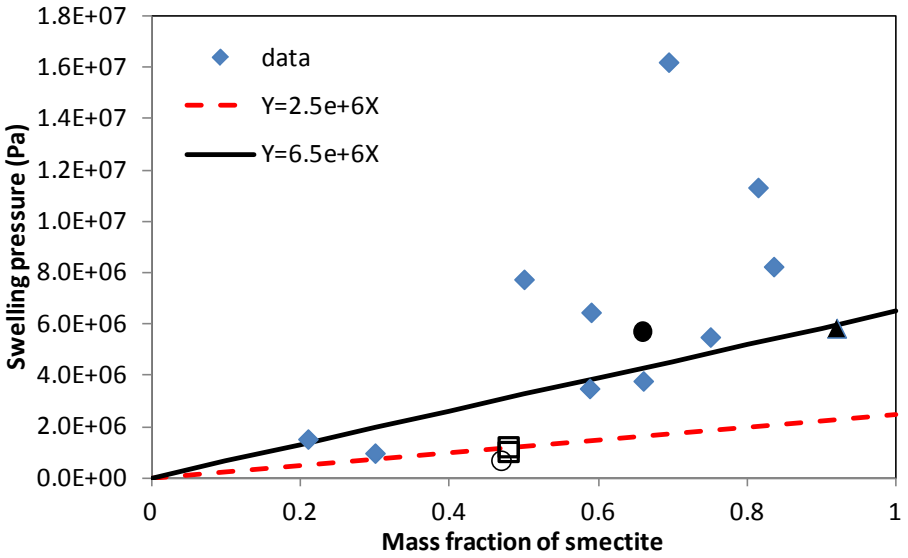

Figure 3.3. Swelling pressure versus mass fraction of smectite for various bentonites. ▲, FEBEX bentonite (ENRESA, 2000); ●, Montigel bentonite (Bucher and Muller-Vonmoos, 1989); □, Kunigel VI bentonite (JNC, 1999); ○, Kunigel bentonite (Komine and Ogata, 1996), ♦ are data for reference material from Czech, Danish, Friedland, Milos Deponit CA-N, Kutch (Indian) and Wyoming MX-80 (Karnland et al., 2006).

For clay formations, we extend the elastic model used in Rutqvist et al., (2014) to consider the chemical strain as in Equation (2). The parameters, A_n and A_{sc}, are same as those used for bentonite, with an assumption that compact bentonite and clay rock behave similarly in terms of the effect of chemical change on strain. However, the validity of this assumption needs to be confirmed with more data.

3.2.2.2 Double structure BExM

In the dual structure model, the macrostructure is modeled with a constitutive model for unsaturated soils, such as the Barcelona Basic Model (BBM). The microstructure is incorporated to extend BBM to a dual structure model, which enables simulating the behavior of expansive soils, such as the dependency of swelling strains and swelling pressures on the initial stress state and on the stress path, strain accumulation upon suction cycles and secondary swelling. Thus, in the dual structure model, the total volume (V), the total void ratio (e), and porosity (ϕ), of the material are divided into a micro-structural part and a macro-structural part. The micro-structure can swell to invade the macro-porosity, depending on the mechanical confinement and load level. This is relevant when considering permeability changes during the soil swelling, because fluid flow takes place mostly through the macro-porosity, which is not proportional to the total strain and deformation of the expansive soil. Equations to describe the mechanical behavior of micro-structural and macro-structural levels and the interaction between structural levels are given in Section 2.

Chemical-mechanical coupling via BExM

We develop a one-way coupling approach, in which chemical changes affect mechanical behaviors of bentonite through the evolution of volume fraction of smectite, exchangeable cation concentration, and ionic strength (via osmotic suction). In this report, these effects are taken into account using a dual-structure model (BExM). The mathematical formulations for CM coupling are summarized below.

The original BExM predicts the micro-strains induced by the effective stress for the whole micro-structure, ignoring the effects of smectite. When the material is hydrated, instead of the whole micro-structure, only the parts of the smectite within the micro-structures that interact with the water invasion swell. Here, we introduce the volume fraction of smectite, f_s, into the micro-structure in BExM for C-M coupling. The swelling capacity of the material should decreases with the reduction of the volume fraction of smectite. Thus, the micro-structural volumetric strains are assumed to depend on the change in the microstructural effective stress as follows:

$$\mathrm{d}\varepsilon_{vm}^{e} = \frac{f_s}{K_m}\mathrm{d}\hat{p} \tag{3.7}$$

where $\hat{p} = p + s_m$, p is the effective mean stress, and s_m is the microstructural suction. K_m is using Equations (3.8):

$$K_m = \frac{e^{\alpha_m \hat{p}}}{\beta_m} \tag{3.8}$$

The total suction, s_m, contains two components, matric suction, s, and osmotic suction, s_o, i.e. $s_m = s + s_o$. The effect of ionic strength of the pore water on microstructural strain is carried out via the osmotic suction. It is computed as:

$$s_o = -10^{-6}\frac{RT}{V_w}\ln a_w \qquad 3.9$$

where V_w is the molar volume of water (in m^3/mol), and a_w is the activity of water. a_w is calculated in TOUGHREACT (Xu et al. 2011) as follows:

$$\ln a_w = -\Phi m^* \frac{1}{55.51} \qquad 3.10$$

where Φ is osmotic coefficient of the solution and m^* is the sum of the molalities of all species in solution. The effect of exchangeable cations is linked to mechanics through the dependence of β_m (Equation 3.11) on exchangeable cation concentration as shown in the following equation (Gens, 2010):

$$\beta_m = \sum_i \beta_m^i x_i \qquad 3.11$$

As shown in Equation 3-110-1, the larger the β_m, the more soil swells. Gens (2010) and Guimaraes et al. (2013) proposed that β_m^i is proportional to the ionic hydrated radius and inversely, proportional to its valence, and typically $\beta_m^{Li} > \beta_m^{Na} > \beta_m^K$. Thus, Na-smectite which contains exclusively Na in the interlayer space should swell more than Ca-smectite, provided that other conditions are the same.

Parameters of BExM used for the FEBEX bentonite

The parameters of BExM utilized for these studies are summarized in Table 3.1 The set of parameters are calibrated based on compacted bentonite by Lloret et al. (2003), and are used in the numerical analysis for Mock-up test by Sanchez et al. (2012). In Lloret et al.'s work, the simulation is one-dimensional, which can be treated as an isotropic case in 3D. However, the lateral displacements are constrained in oedometer test but the vertical loading is controlled by stresses. Thus, the stress status in oedometer test is anisotropic and the assumption of isotropy is not appropriate for this test. In Sanchez et al.'s work, although a are in agreement between numerical results and observed behavior during experiments is obtained, the macro-structural bulk modulus of bentonite can reach as high as 2 GPa. Based on the report by Rutqvist and Tsang (2002), the bulk modulus of FEBEX bentonite should be in the order of 10 MPa~100 MPa. Therefore, the bulk modulus evolved too high during the simulation. Here we determine the parameters related to macro-structural bulk modulus, κ, which gives reasonable bulk modulus (in the order of 10 MPa~1000 MPa), from the observed results during experiment. In order not to affect the hydraulic effects on macro-structures, we increase the parameters κ_s to keep the same ratio of $\frac{\kappa}{\kappa_s}$ as Lloret et al. (2003) and Sanchez et al. (2012) used in their simulations. The void ratios e_{micro} and e_{macro} are recalculated based on the experiment data. To match the order of magnitude of β_m which is related to exchangeable cation concentration, a smaller α_m suggested by Sanchez et al. (2012) is used here.

Table 3.1. Parameters used for combination of loading paths tests (Lloret et al., 2003; Sánchez et al., 2012a).

Parameters defining the Barcelona basic model for macrostructural behavior						
$\kappa = 0.018$	$\kappa_s = 0.0036$	$\lambda(0) = 0.08$	$p_c = 0.5$ MPa	$r = 0.90$	$\zeta = 1$ MPa^{-1}	$p_0^* = 6.5$ MPa
$\alpha_a = 0.5$	$\alpha_0 = 1 \times 10^{-5}$°C					
Parameters defining the law for microstructural behavior						
$\alpha_m = -2.1 \times 10^{-6}$ MPa^{-1}	$\chi = 1$					
Interaction functions						
$f_c = 1 + 0.9 \tanh\left[20\left(\frac{p_r}{p_0} - 0.25\right)\right]$		$f_s = 0.8 - 1.1 \tanh\left[20\left(\frac{p_r}{p_0} - 0.25\right)\right]$				
Initial conditions						
$e_{macro} = 0.21$	$e_{micro} = 0.48$	$f_s = 0.6164$	$s_o = 0.777$ MPa	$\beta_m = 2.74 \times 10^{-6}$ MPa^{-1}		

Note that the parameters (κ and κ_s) related to macro-structural bulk modulus is higher than original ones used in (Lloret et al., 2003; Sánchez et al., 2012a)

3.2.3 Chemical Model

In these generic cases, it is assumed that that the host rock properties are representative of Opalinus Clay (Bossart 2011; Lauber et al., 2000). Two cases are used for the EBS backfill: one is Kunigel-VI bentonite (Ochs et al., 2004) and the other is FEBEX bentonite (ENRESA, 2000). The mineral compositions of the bentonite and clay formation are listed in Table 3.2. The pore-water compositions of the Kunigel-VI bentonite (Sonnenthal et al., 2008), FEBEX bentonite (Fernández et al., 2001) and the clay formation (Fernández et al., 2007) are listed in Table 3.3. The initial redox potential, expressed as the concentration of dissolved O_2 (O_2(aq)) in the model.

Table 3.3 lists the thermal and hydrodynamic parameters used in the model. The majority of these parameters are taken from Sonnenthal et al. (2008) for Kunigel-VI bentonite and from Thury (2002) for the EBS bentonite and the NS clay formation. Permeability for the clay formation is from Soler (2001) and bentonite permeability is from JNC (1999).

In this report, we used the same thermal conductivity and permeability for both FEBEX and Kunigel-VI bentonites. These parameters are actually fairly similar for the two types of bentonite — thermal conductivity for saturated Kunigel-VI bentonite is 1.5W/m-°C (see Table 3.2) and that for FEBEX bentonite is 1.3 W/m °C (ENRESA, 2000); permeability for Kunigel-VI bentonite is 2E-21 m^2 and that for FEBEX ranges from 1E-21 to 3.75E-21 m^2 (ENRESA, 2000; Zheng et al., 2011; Chen et al. 2009). Moreover, by using the same values of thermal conductivity and permeability for both bentonites, we can isolate the effect of variations in chemical and CM coupling parameters on the stress changes.

Table 3.2. Mineral volume fraction (dimensionless, ratio of the volume for a mineral to the total volume of medium) of the Kunigel-VIbentonite (Ochs et al., 2004), FEBEX bentonite (ENRESA, 2000; Fernández et al., 2004; Ramírez et al., 2002) and Opalinus Clay (Bossart 2011; Lauber et al., 2000).

Mineral	EBS Bentonite: Kunigel-VI	EBS Bentonite: FEBEX	Clay formation: Opalinus Clay
Calcite	0.016	0.0065	0.093
Dolomite	0.018	0.0	0.050
Illite	0.000	0.0	0.273
Kaolinite	0.000	0.0	0.186
Smectite	0.314	0.6	0.035
Chlorite	0.000	0.0	0.076
Quartz	0.228	0.026	0.111
K-Feldspar	0.029	0.0065	0.015
Siderite	0.000	0.0	0.020
Ankerite	0.000	0.0	0.045
Pyrite	0.000	0.01	0.000
Greenrust	0.000	0.000	0.000
Magnetite	0.000	0.000	0.000
Hematite	0.000	0.000	0.000
Goethite	0.000	0.000	0.000
Fe(oh)3(s)	0.000	0.000	0.000
Fe(oh)2	0.000	0.000	0.000
Vermiculites	0.000	0.000	0.000
Berthierine(Fe^{+2})	0.000	0.000	0.000
Berthierine(Fe^{+3})	0.000	0.000	0.000
Saponite(Fe, Ca)	0.000	0.000	0.000
Saponite(Fe,K)	0.000	0.000	0.000
Saponite(Fe, Na)	0.000	0.000	0.000
Saponite(Fe, Mg)	0.000	0.000	0.000

Table 3.3. Pore-water composition (mol/kg water, except pH) of Kunigel-VIbentonite(Sonnenthal et al., 2008), FEBEX bentonite (Fernández et al., 2001) and Opalinus Clay (Fernández et al., 2007).

	EBS Bentonite: Kunigel-VI	EBS Bentonite: FEBEX	Clay formation : Opalinus Clay
pH	8.40	7.72	7.40
Cl	1.50E-05	1.60E-01	3.32E-01
SO_4^{-2}	1.10E-04	3.20E-02	1.86E-02
HCO_3^-	3.49E-03	4.1E-04	5.18E-03
Ca^{+2}	1.37E-04	2.2E-02	2.26E-02
Mg^{+2}	1.77E-05	2.3E-02	2.09E-02
Na^+	3.60E-03	1.3E-01	2.76E-01
K^+	6.14E-05	1.7E-03	2.16E-03
Fe^{+2}	2.06E-08	2.06E-08	3.46E-06
$SiO_2(aq)$	3.38E-04	1.1E-04	1.10E-04
AlO_2^-	1.91E-09	1.91E-09	3.89E-08
$O_2(aq)$	2.57e-4	2.57e-4	1.2E-51

Table 3.4. Thermal and hydrodynamic parameters.

Parameter	Clay formation : Opalinus Clay	EBS Bentonite
Grain density [kg/m^3]	2700	2700
Porosity ϕ	0.162	0.33
Saturated permeability [m^2]	2.0×10^{-20}	2.0×10^{-21}
Relative permeability, k_{rl}	$m = 0.6$, $S_{rl} = 0.01$	$K_{rl} = S^3$
Van Genuchten α [1/Pa]	6.8×10^{-7}	3.3×10^{-8}
Van Genuchten m	0.6	0.3
Compressibility, β [1/Pa]	3.2×10^{-9}	5.0×10^{-8}
Thermal expansion coeff., [1/^{o}C]	1.0×10^{-5}	1.5×10^{-4}
Dry specific heat, [J/kg-^{o}C]	860	800
Thermal conductivity [W/m-^{o}C] dry/wet	1.48/1.7$^{\$}$	1.1/1.5
Tortuosity for vapor phase	$\phi^{1/3}S_g^{10/3}$	$\phi^{1/3}S_g^{10/3}$
Bulk modulus, (GPa)	4.17	0.02
Shear modulus, (GPa)	1.92	0.0067

From http://www.mont-terri.ch/internet/mont-terri/en/home/geology/key_characteristics.html

In previous simulations (Liu et al., 2013; Zheng et al., 2014; 2015), the corrosion of canister was neglected because chemical model focused on the illitization in bentonite and it is assumed that corrosion of canister won't interfere the illitization processes. In this report, in order to test this assumption, corrosion of a steel canister is included in the chemical model using the following reaction:

$$\text{Iron} + 2H^+ + 0.5O2(aq) \leftrightarrow Fe^{+2} + H_2O \qquad 3.12$$

The corrosion of steel canister might lead to formation of Fe-oxides and Fe-hydroxides. In current model, we added greenrust (fougerite), magnetite, hematite, goethite, $Fe(OH)_3(s)$ and $Fe(OH)_2$. If the Fe ion released by corrosion is not been consumed by the precipitation of Fe-oxides and Fe-hydroxides, there is a chance that some Fe bearing clay minerals could be formed, such as vermiculite, berthierine, saponite with different type of cations. These minerals are also listed in Table 3.2 as secondary minerals such that they could be formed.

Mineral dissolution/precipitation is kinetically controlled. The kinetic law for mineral dissolution/precipitation is given in Xu et al. (2011):

$$r = kA\left|\left(1-(\frac{\mathrm{K}}{\mathrm{Q}})^{\theta}\right)\right|^{\eta} \qquad 3.13$$

where r is the kinetic rate, k is the temperature-dependent rate constant (mol/m^2-s), A is the reactive surface area per kg water, K is the equilibrium constant for the mineral–water reaction (written for the destruction of one mole of mineral), and Q is the reaction quotient. Here, for simplicity, the exponents θ and η are assumed equal to 1.

The kinetic rate constants can usually be summed for three mechanisms (Lasaga et al., 1994):

$$k = k_{25}^{nu} \exp\left[\frac{-E_a^{nu}}{R}\left(\frac{1}{T}-\frac{1}{298.15}\right)\right] + k_{25}^{H} \exp\left[\frac{-E_a^{H}}{R}\left(\frac{1}{T}-\frac{1}{298.15}\right)\right] a_H^{n_H} + k_{25}^{OH} \exp\left[\frac{-E_a^{OH}}{R}\left(\frac{1}{T}-\frac{1}{298.15}\right)\right] a_{OH}^{n_{OH}} \quad 3.14$$

where superscripts *nu*, *H* and *OH* indicate neutral, acid, and alkaline mechanisms, respectively, *E* is the activation energy, k_{25} is the rate constant at 25 °C, *R* is the gas constant, *T* is the absolute temperature, α is the activity of the species, and *n* is a power term (constant). It should be noted that reaction rates depend on the reactive surface area *A* in Equation (3-13), which is a function of the product of the specific surface area and the volume fraction of each mineral. Therefore, the calibrated values of specific surface area and volume fraction should be viewed as arbitrary and non-unique (co-linearly varying) values, the product of which is relevant but not each value separately.

The kinetic rates and surface areas for the minerals considered in the model were taken mostly from Xu et al. (2006) (Table 3.5). However, the illitization rate (the rate of illite precipitation and smectite dissolution) was calibrated (Liu et al., 2013) based on the measured illite percentage in an illite/smectite (I/S) mixed layer from Kinnekulle bentonite, Sweden (Pusch and Madsen, 1995). The kinetics data for iron is taken from Birgersson and Wersin (2013). Surface areas and reaction rates for greenrust (fougerite), magnetite, hematite, goethite, $Fe(OH)_3(s)$ and $Fe(OH)_2$ are taken the same as ankerite. The kinetic data for vermiculite, berthierine, saponite are the same as smectite. The thermodynamic data were taken from the Data0.dat.YMPv4.0, an EQ3/6 (Wolery 1993) database qualified by the U.S. Department of Energy for the Yucca Mountain Project.

Table 3.5. Kinetic properties for minerals considered in the model (Xu et al., 2006).

Mineral	A (cm^2/g)	Parameters for Kinetic Rate Law							
		Neutral Mechanism		Acid Mechanism			Base Mechanism		
		k_{25} ($mol/m^2/s$)	E_a (kJ/mol)	k_{25} ($mol/m^2/s$)	E_a (kJ/mol)	$n(H^+)$	k_{25} ($mol/m^2/s$)	E_a (kJ/mol)	$n(H^+)$
Quartz	9.8	1.023×10^{-14}	87.7						
K-feldspar	9.8	3.89×10^{-13}	38	8.71×10^{-11}	51.7	0.5	6.31×10^{-12}	94.1	-0.823
Kaolinite	151.6	6.91×10^{-14}	22.2	4.89×10^{-12}	65.9	0.777	8.91×10^{-18}	17.9	-0.472
Illite	1.5×10^{2} (1)	1.3×10^{-11}	105 (2)						
Chlorite	9.8	3.02×10^{-11}	88	7.76×10^{-12}	88	0.5			
Calcite	3.5	1.63×10^{-7}	23.5						
Dolomite	12.9	2.52×10^{-08}	62.76	2.34×10^{-7}	43.54	1			
Ankerite	0.3	1.26×10^{-9}	62.76	6.46×10^{-4}	36.1	0.5			
Smectite	1.5×10^{2}(1)	1.3×10^{-11}	105 (2)						
Pyrite	0.3	$2.5X10^{-12}$	62.76						
Iron	1.68	4.47×10^{-9}	0.0						
Greenrust	0.3	1.26×10^{-9}	62.76						
Magnetite	0.3	1.26×10^{-9}	62.76						
Hematite	0.3	1.26×10^{-9}	62.76						
Goethite	0.3	1.26×10^{-9}	62.76						
Fe(oh)3(s)	0.3	1.26×10^{-9}	62.76						
Fe(oh)2	0.3	1.26×10^{-9}							
Vermiculites	1.5×10^{2}	1.3×10^{-11}	105						
Berthierine(Fe^{+2})	1.5×10^{2}	1.3×10^{-11}	105						
Berthierine(Fe^{+2})	1.5×10^{2}	1.3×10^{-11}	105						
Saponite(Fe, Ca)	1.5×10^{2}	1.3×10^{-11}	105						
Saponite(Fe,K)	1.5×10^{2}	1.3×10^{-11}	105						
Saponite(Fe, Na)	1.5×10^{2}	1.3×10^{-11}	105						
Saponite(Fe, Mg)	1.5×10^{2}	1.3×10^{-11}	105						

(1) calibrated based on the field illitization data (Liu et al., 2013)
(2) from Pusch and Madsen (1995)

3.3 MODEL RESULTS

In Liu et al. (2013) and Zheng et al. (2014) the model results for first one thousand years, expressed as the evolution of temperature, pore pressure, water saturation, concentration and stress, were discussed in detail and a sensitivity analyses to key chemical and mechanical parameters were conducted to understand the coupling processes. In Zheng et al. (2015), the simulations were conducted for one hundred thousand years thanks to the improvement in the efficiency of TOUGHRACT-FLAC3D, which helped to answer questions like when illitization stabilizes in the long run. In the following sections, we first briefly summarize these results in Sections 3.3.1 and 3.3.2, and then present new model results from FY16 effort in Section 3.3.3.

3.3.1 Key Findings from Previous Models Using Extended Linear Elastic Model

In the generic cases we used to study the effect of high temperature on the THMC evolution in bentonite and clay formation, two bentonites have been simulated: Kunigel-VI and FEBEX bentonite, and two scenarios were simulated for comparison: a case in which the temperature in the bentonite near the waste canister can reach about 200^{o}C and a case in which the temperature in the bentonite near the waste canister peaks at about 100^{o}C. All these simulations used extended linear elastic model to link chemistry with mechanics. In this section, we summarize the key findings from Liu et al. (2013), Zheng et al. (2014), and Zheng et al. (2015).

3.3.1.1 Enhancement of Illitization under Higher Temperature

The very first question we were attempting to answer by this series of simulations was whether illitization would occur in the EBS bentonite and host clay formation. Illitization, the transformation of smectite to illite, has caught great attention of researchers because it results in a loss of smectite which in turn causes a loss in the swelling capacity. Illitization is evident in geological systems (Wersin et al., 2007), as exemplified by several natural analogue studies (Pusch and Madsen, 1995; Kamei et al., 2005; Cuadros 2006; Casciello et al., 2011). Illite/smectite mixed-layer clay is commonly observed in clayey sediments, and deep formations typically contain more illite than shallow formations (Cuadros 2006), which leads to a conclusion that smectite is gradually transformed to illite during diagenesis and become of the basis for assuming the illitization would occur in EBS bentonite. Liu et al. (2013) did an extensive review of laboratory experiments (e.g. Mosser-Ruck and Cathelineau 2004; Pacovsky et al. 2005) and field tests (Pusch et al., 2010) and modeling studies (e.g. Montes-H et al., 2005), and found out there was no conclusive evidence that illitization will occur and swelling capacity will be lower in bentonite. While various studies shed light on certain aspects of this question, there is no study that integrates the relevant THMC processes and considers the interaction between EBS and host rock. One of the key findings from our simulations is that illitization does occur in the two bentonites we tested: Kunigel-VI (Ochs et al., 2004) and FEBEX (ENRESA 2000) bentonite and it is enhanced at higher temperature, as shown in Figure 3.4. In addition, we also have the following observations:

- The quantity of illitization, expressed as the smectite volume fraction change, is affected by many chemical factors and as a result varies over a wide range. The most important chemical factors for illitization are the concentration of K and dissolution rate of K-feldspar, as revealed by the sensitivity analyses conducted in Liu et al. (2013) and Zheng et al., (2014).
- The geochemical interaction between EBS bentonite and the clay formation has a strong effect on long term illitization in bentonite. Figure 3.4 shows that bentonite near the EBS-

NS interface undergo more illitization than that near the waste package by the end of one hundred thousand years for the "high T' scenarios (Figure 3.4). The reason is that after two thousand –three thousand years, the illitization process ceases in the clay formation and the K ion is not consumed by the local illitization and is, therefore, transported into the EBS bentonite to facilitate further illitization.

- Illitization is more pronounced for Kunigel-VI bentonite than FEBEX bentonite (Figure 3.5) due to their difference in chemical properties, indicating illitization in EBS bentonite has to be evaluated case by case. The key chemical properties that lead to different degree of illitization is the supply of K and Al, for example by the dissolution of K-feldspar (Figure 3.6).
- In additions to illitization, other chemical alterations include the dissolution of K-feldspar and calcite, and the precipitation of quartz, chlorite, and kaolinite. And, precipitation of quartz could affect the mechanical property of bentonite.
- The type of smectite contained in the bentonite, i.e., whether it is Na-smectite or Ca-smectite does not have a strong effect on illitization.
- Illitization also occurs in clay formation and is significantly enhanced under higher temperature (see Figure 3.4).

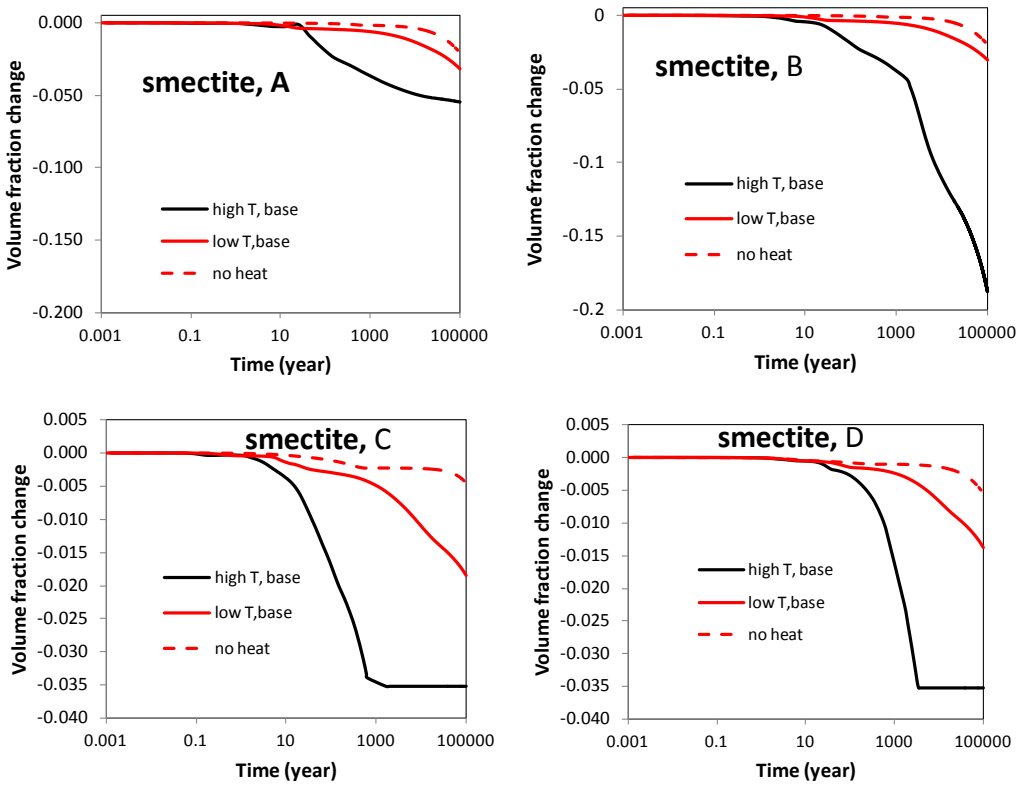

Figure 3.4. The temporal evolution of smectite volume fraction at points A, B, C, and D for the "high T" and "low T" cases, and a simulation that assumes no heat release from the waster package (A: inside the bentonite near the canister, B: inside the bentonite and near the EBS-NS interface, C: inside the clay rock formation and near the EBS-NS interface, D: inside the clay rock formation at a distance of 10 m from the canister).

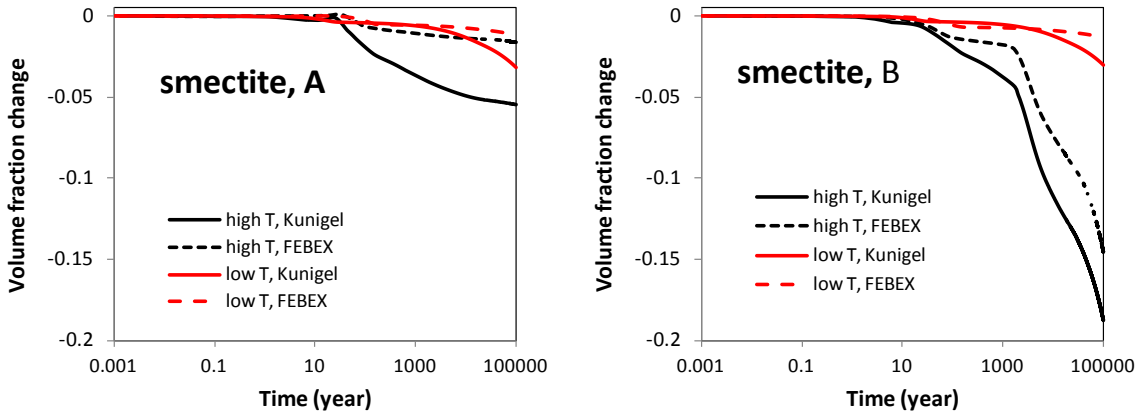

Figure 3.5. The temporal evolution of smectite volume fraction at points A and B for Kunigel and FEBEX bentonite.

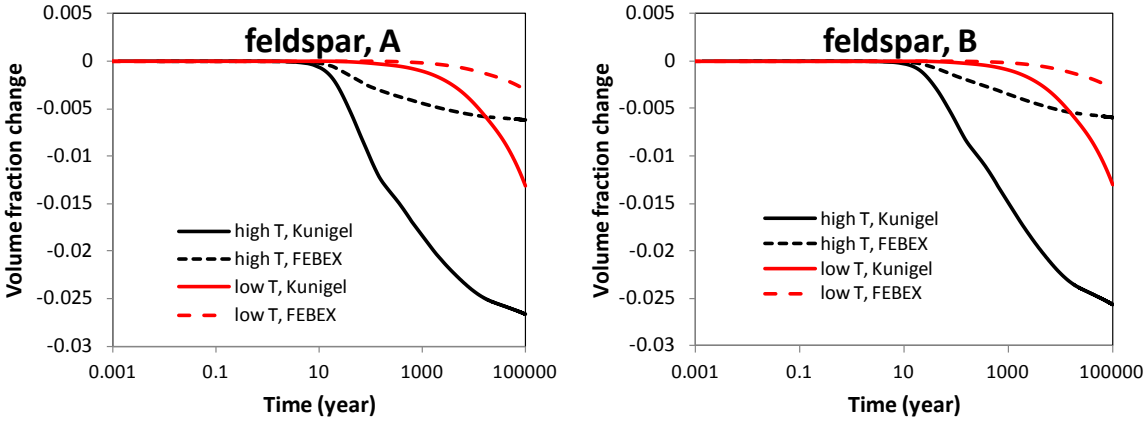

Figure 3.6. The temporal evolution of K-feldspar volume fraction at points A, B, C, and D in the base case with Kunigel bentonite and a sensitivity case with FEBEX bentonite.

3.3.1.2 Impact of Illitization on Swelling Stress

The mechanical-chemical coupling implemented in the model allows us to evaluate how the chemical changes may affect the mechanical behavior of the EBS bentonite in terms of swelling and total stress. Because of the extended linear swelling model used, we limit our analysis to the effects of ion concentration and illitization on swelling and do not include other potential effects of chemical changes on mechanics, such as changes in mechanical properties due to cementation.

Several processes combine to drive stress up in bentonite and peak at around one hundred years, and then decrease and stabilized after twenty to thirty thousand years. Reasons for the stress increase include the increase in pore pressure due to hydration and thermal pressurization (a processes caused by the difference in thermal expansion of the fluid and solid host rock), bentonite swelling, and thermal expansion. The stronger thermal pressurization in the “high T” case leads to much higher stress in the bentonite than the “low T” case. For both the “high T” and “low T” cases, the major contribution to total stress within the buffer is pore pressure, with smaller contributions from swelling and thermal stresses.

The constitutive relationship described by Equation (3.5) provides an opportunity to evaluate the effect of chemical changes on swelling stress. In order to isolate the contributions of ion concentration changes versus smectite changes on swelling stress changes, we present three sets of calculated swelling stress. In the first set, denoted in Figure 3.7 as "σ=f(Sl,C,Ms)", the swelling stress is calculated according to Equation (3.5) as a function of liquid saturation changes (Sl), ion concentration (C) changes, and smectite (Ms) changes. In the second set, denoted as "σ=f(Sl,C)", the contribution from smectite changes in Equation (3.5) is disregarded, and the swelling stress is only a function of liquid saturation and ion concentration. In the third set, denoted as "σ=f(Sl)", all chemical effects are neglected, and the swelling stress is only a function of liquid saturation changes. By the comparing the simulated swelling stresses in these three sets of simulations, we can calculate the swelling stress reduced by ion concentration and smectite dissolution, which are listed in Table 3.7 for both Kunigel-Vi and FEBEX bentonite.

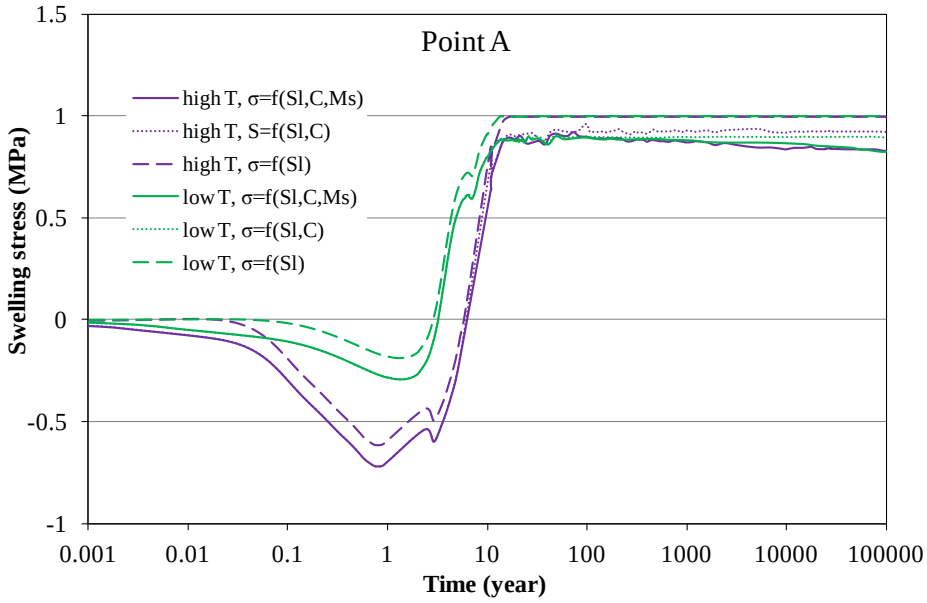

Figure 3.7. Simulation results of swelling stress at point A for the "low T" and "high T" scenarios for Kunigel-VI bentonite (Zheng et al., 2015), respectively.

Table 3.6.The geochemically induced swelling stress for Kunigel-VI and FEBEX bentonite at points A and B for "high T" scenario. Stress reduction by ion concentration is the difference between the swelling stress obtained with "σ=f(Sl)" and "σ=f(Sl,C)", and the stress reduction by smectite dissolution is the difference between the swelling stress obtained with "σ=f(Sl,C)" and "σ=f(Sl,C,Ms)" (see Figure 3.7), where the relative amount (%) use the results from "σ=f(Sl)" as the basis.

	Kunigel-VI bentonite				FEBEX bentonite			
	Stress reduction by ion concentration		Stress reduction by smectite dissolution		Stress reduction by ion concentration,		Stress reduction by smectite dissolution	
	MPa	%	MPa	%	MPa	%	MPa	%
Point A	0.07	7%	0.09	9%	0.006	0.1%	0.17	3.4%
Point B	0.08	8%	0.45	45%	0.06	1.1%	0.6	12%

In terms of the effect of chemical changes on swelling stress for bentonite, the modeling results (Zheng et al., 2015) leads to the following observations:

- More swelling stress reduction take place near the near the EBS-NS interface as more illitization occurs in this area, expressed as the smectite volume fraction change, For the "high T" case, Kunigel-VI bentonite near the EBS-NS loses as much as 53% swelling capacity and FEBEX bentonite near the EBS-NS has about 13% reduction in swelling stress whereas bentonite near the waste package undergoes a small reduction in swelling stress — 16% reduction for Kunigel-VI and 3.4% for FEBEX bentonite, respectively.
- High temperature leads to higher reduction in swelling stress. For the "low T" case, the stress reduction by chemical change is relatively homogeneous, 16% reduction for Kunigel-VI bentonite and around 3% reduction for FEBEX bentonite after one hundred thousand years, as opposed to as high as 53% swelling stress reduction for Kunigel-VI bentonite and 13% reduction for FEBEX bentonite.
- Although Kunigel-VI and FEBEX bentonite undergo similar magnitude reduction in swelling stress in absolute values (as in MPa), relative to their corresponding swelling capacity, it is a much minor reduction for FEBEX bentonite because FEBEX bentonite has a swelling capacity about 5 folds of that of Kunigel-VI bentonite. Using EBS bentonite with higher swelling capacity could alleviate the negative consequence of illitization.
- Despite the swelling stress is noticeably affected by illitization, the total stress is much less affected by the chemical change because swelling stress only accounts for a relatively small proportion of total stress.
- Chemical change leads to about a 2.6% decrease in stress near the EBS-NS interface and about 0.7% in the far field. In general, chemical change does not have significant impact on the stress in the clay formation.

3.3.2 Impact of iron-bentonite interaction on swelling stress

While the type of material for waste canister is a still open question, steel canister has been selected as one of the potential canister. For example, based on a series of selection criteria including canister lifetime, avoidance of detrimental impacts on other barrier, retrievability during the operational phase, etc, NAGRA proposed to use steel canister (NAGRA, 2002). In order to ensure very limited impact of the other barriers, extensive research have been conducted on the interaction of corroding iron with bentonite (e.g. Wersin et al., 2015; Shibata et al., 2014; Martin et al., 2014). Corrosion of steel under the repository conditions is a very complex process and affected by the both the environment inside and outside the canister. In addition to deterioration of canister itself, corrosion of steel could lead the generation of H_2(gas) and alteration of bentonite. In this report, it is for the first time that Fe-corrosion was simulated in conjunction with coupled THMC model for bentonite barrier, therefore we start with several simplifications such that we can focus on the alteration of smectite in bentonite barrier caused by steel corrosion. First, a constant reaction rate is applied to iron dissolution reaction, using a surface area of 1.68 cm^2/g and a rate constant of $10^{-8.35}$ $mol/m^2/s$ which corresponds to an average corrosion rate of 1 μm/a (Birgersson and Wersin, 2014). It is known that corrosion rate is affected by the geochemical and bacterial conditions in vicinity of canister (Landolt et al., 2009) and such conditions should be built in the reaction rate. However, we neglect this effect and use a constant rate in this report. Second, focused corrosion is neglected. Focused or localized corrosion processes result from the establishment of electrochemical cells due to spatial differences in the local environment or in the material properties. To simplify our simulation, we assume the corrosion is homogeneous at the canister surface.

Previous THMC models (Liu et al., 2013; Zheng et al., 2014; 2015) were conducted using both Kunigel-VI and FEBEX bentonite as the EBS bentonite. In FY16, because corrosion of steel canister and interaction of bentonite and corroded steel is very complex and information about the iron-bentonite

interaction for Kunigel-VI bentonite is very sparse, coupled THMC model with iron-bentonite was only conducted for the case using FEBEX bentonite as EBS. As presented in Section 4, extensive geochemical characterization of FEBEX bentonite after the dismantling of FEBEX in situ test was conducted. Once the geochemical data is available, they will used to constrain our iron-bentonite interaction conceptually model such that model prediction would be more reliable. In the remaining part of this section, the THMC model that takes into account of iron-bentonite interaction (for example, named "hgh T, with Fe-ben") are comparing the THMC model (Zheng et al. 2015) that did not consider iron-bentonite interaction (for example, named "hgh T, no Fe-ben").

In the model, it is assumed that the steel canister is 1.5 cm. With an average corrosion rate of 1 μm/a, the canister is totally corroded in about fifteen thousand years, as shown in Figure 3.8. Corrosion of steel typically undergoes an initial aerobic corrosion and then become anaerobic once oxygen is consumed. Because of the longer aerobic corrosion (due to longer unsaturation time in bentonite) and higher temperature in the "high T" case, the corrosion is faster in the "high T" case (Figure 3.8) than that in "low T" case, but eventually both cases have similar corrosion rate as the canister cool down.

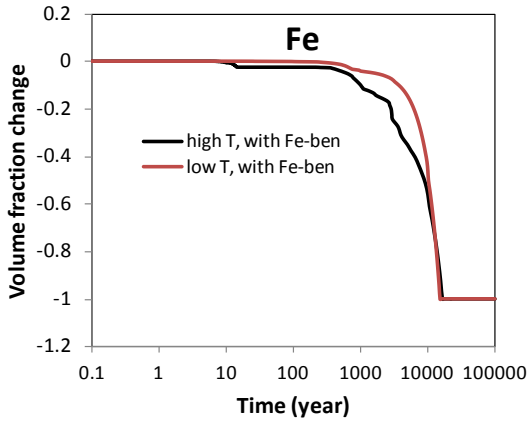

Figure 3.8. Simulation results of the corrosion of steel canister for the "low T" and "high T" scenarios for FEBEX bentonite.

Anaerobic corrosion of steel is an oxidation that involves direct formation of magnetite (Fe_3O_4) via a solid state reaction. $Fe(OH)_2$ can also be transformed to magnetite through Schikkor reaction:

$$3Fe(OH)_2 \rightarrow Fe3O4 + 2H_2O + 2H^+$$

Eventually the production of corrosion is dominated by the magnetite, with small amount of $Fe(OH)_3$(s) and $Fe(OH)_2$ remaining (Figure 3.9). Over the course of transferring steel to magnetite and iron-hydroxides, Fe^{+2} moves into bentonite via diffusion and current model shows the formation of goethite at the vicinity of canister (point A in Figure 3.10). At point B, the formation of goethite is firstly caused by the interaction between bentonite and host rock, but after about one thousand years, the formation of goethite is caused by arrival of Fe^{+2} front from the corrosion of steel canister.

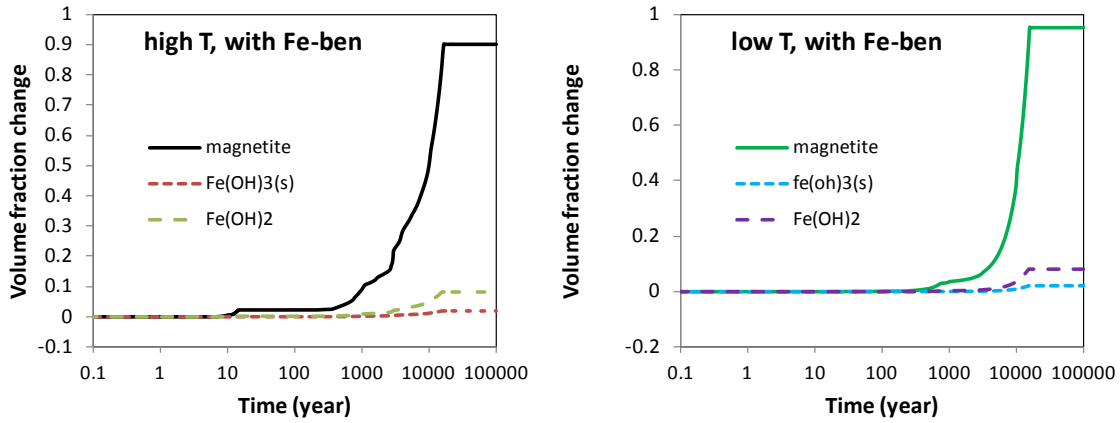

Figure 3.9. Simulated volume fraction change of magnetite, $Fe(OH)_3(s)$ and $Fe(OH)_2$ for ion for the "low T" (right) and "high T" scenarios (left) for FEBEX bentonite.

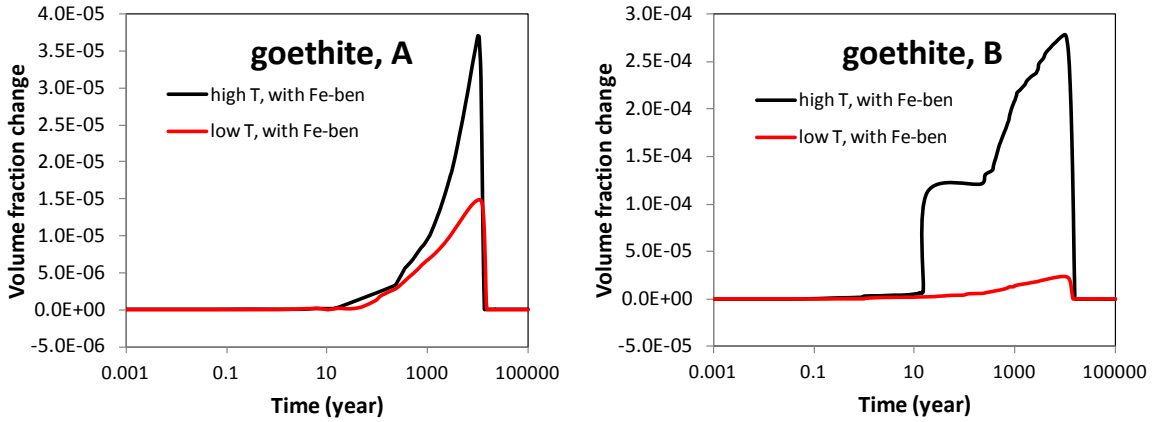

Figure 3.10. Simulated volume fraction change of goethite at point A and B for the "low T" (right) and "high T" scenarios (left) for FEBEX bentonite.

Although the formation of Fe-oxide and Fe-hydroxides as a result of corrosion of steel canister is relatively well understood, the Fe-bentonite interaction is far from conclusive. In the Alternative Buffer Materials (ABM) test conducted in the Aspo hard rock laboratory, Sweden, saturated MX-80 bentonite was in contact with steel canister and samples were collected after 881 days. Wersin et al. (2015) analyzed the samples and found no transformation of montmorillonite or newly formed clay phase. But Cheshire et al., (2014) showed that there were significant changes to the phyllosilicates at the metal-bentonite interface due to metal corrosion producing either Fe-phyllosilicates (i.e., Fe-saponite and chlorite) on steel surfaces. Based on Mosser-Ruck et al (2010), at 80 and 150 °C, montmorillonite underwent weak enrichment of Fe and depletion of Si. At 300 °C, vermiculite became dominant. Vermiculite is structurally similar to montmorillonite but has higher interlayer charge (0.5 to 0.7 per $O_{10}(OH)_2$ unit vs that of 0.2 to 0.5 in montmorillonite and therefore swells much less). Under neutral pH conditions, Mosser-Ruck et al (2010) concluded the possibility of forming Fe-rich dioctahedral smectite or berthierine or Fe-saponite depending on Fe/bentontie ratios and Liquid/bentonite ratios and temperature. In current model, we therefore added as vermiculite, berthierine, saponite with different type of cations as secondary minerals that they could be formed (Table 3.1). However, thermodynamically all these minerals are under-saturated, for example, as shown in Table 3.7 for their saturation indices at point

A at ten thousand years for the "high T" case. Therefore current model does not show the formation of these minerals.

Table 3.7. Saturation index (log(Q/K) of some Fe bearing clay minerals at point A at ten thousand years for "high T" case.

	Vermiculite	Berthierine (Fe^{+2})	Berthierine (Fe^{+3})	Saponite (Fe, Ca)	Saponite (Fe, K)	Saponite (Fe, Mg)	Saponite (Fe, Na)
Saturation index	-11.6	-7.2	-7.5	-6.9	-7.0	-7.3	-5.7

In previous THMC model (Zheng et al., 2015), although Fe-bentonite interaction was not considered, the excessive silicates and aluminum produced by the dissolution K-feldspar and smectite led to the precipitation of chlorite. In current model in which Fe-bentonite interaction is considered , as more Fe^{+2} is diffuse into bentonite, chlorite propitiation is enhanced slightly (see Figure 3.11), especially for the "high T" case. Consequently, more precipitation of chlorite seems to drive more dissolution of smectite (see Figure 3.12). However, the difference in smectite dissolution between models that consider Fe-bentonite interaction and that did not consider Fe-bentonite interaction is fairly moderate.

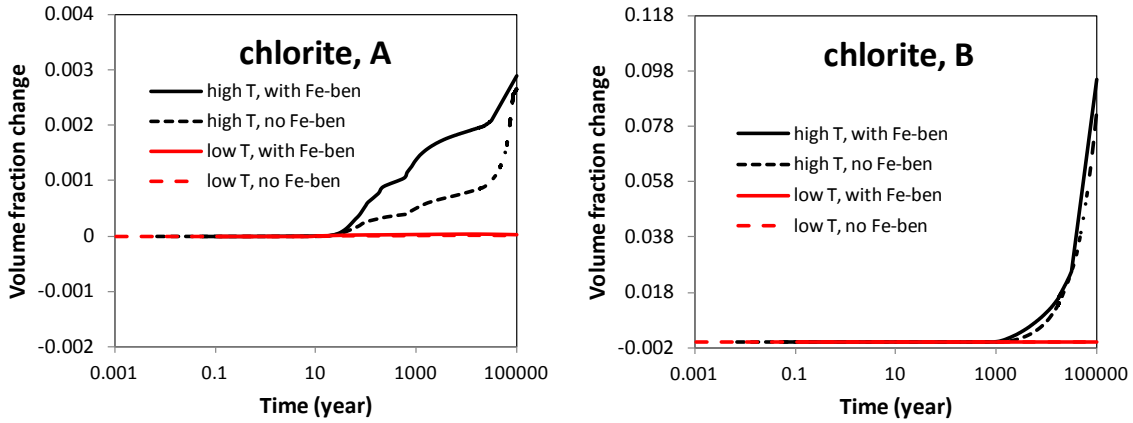

Figure 3.11. Simulated volume fraction change of chlorite at point A and B for the "low T" (right) and "high T" scenarios (left) for FEBEX bentonite, with Fe-bentonite interaction and without Fe-bentonite interaction (Zheng et al., 2015).

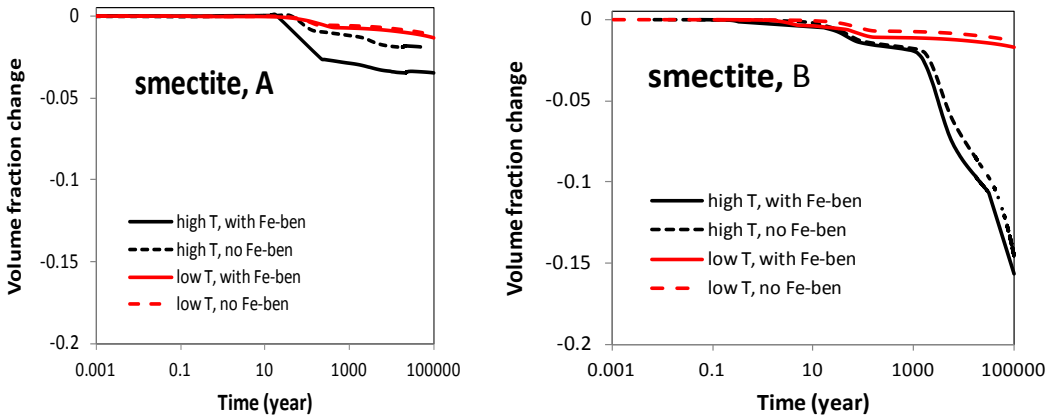

Figure 3.12. Simulated volume fraction change of smectite at point A and B for the "low T" (right) and "high T" scenarios (left) for FEBEX bentonite, with Fe-bentonite interaction and without Fe-bentonite interaction (Zheng et al., 2015).

As shown in Figure 3.12, model considering the Fe-bentonite interaction has slight more dissolution of smectite, which lead to slight more reduction in swelling stress. Table 3.8 lists the swelling stress reduction for the model with and without Fe-bentonite interaction. At point A, when Fe-bentonite interaction is considered in the model, the swell stress reduction by smectite dissolution is 7.2% in comparison with 3.4% for the model without considering Fe-bentonite interaction. At point B, the difference in stress reduction by smectite dissolution between the model with and without Fe-bentonite interaction is about 2%.

Table 3.8. The geochemically induced swelling stress for FEBEX bentonite with and without considering Fe-bentonite interaction at points A and B for "high T" scenario. Stress reduction by ion concentration is the difference between the swelling stress obtained with "σ=f(Sl)" and "σ=f(Sl,C)", and the stress reduction by smectite dissolution is the difference between the swelling stress obtained with "σ=f(Sl,C)" and "σ=f(Sl,C,Ms)", where the relative amount (%) use the results from "σ=f(Sl)" as the basis.

	with Fe-bentonite				Without Fe-bentonite			
	Stress reduction by ion concentration		Stress reduction by smectite dissolution		Stress reduction by ion concentration,		Stress reduction by smectite dissolution	
	MPa	%	MPa	%	MPa	%	MPa	%
Point A	0.0006	0.1%	0.36	7.2%	0.006	0.1%	0.17	3.4%
Point B	0.08	8%	0.68	13.7%	0.06	1.1%	0.6	12%

3.3.3 THMC results with the dual-structure model

BExM was implemented in TOUGHREACT-FLAC3D and a series of THMC simulations were conducted for both "high T" and "low T" using FEBEX bentonite as EBS. Coupled THMC model with BExM was not conducted for Kunigel-VI because the parameterization of BExM for Kunigel-VI bentonite requires addition modeling effort and reliable data to calibrate some of key parameters whereas parameters for BExM for FEBEX bentonite have been well calibrated (e.g. Sánchez et al., 2012). It is also noted that the chemical model in the THMC model using BExM for FEBEX bentonite presented in this sections is the same as in Zheng et al. (2015), which did not considered the iron related reactions as

articulated in Section 3.2.4. The reason is that Fe-bentonite interaction does not have significant effect on smectite alteration (as shown earlier in Section 3.3.2).

3.3.3.1 THMC simulation results

As section 3.2.3.2 illustrates, the chemical-mechanical coupling is implemented in the dual-structure model. It allows us to evaluate how the chemical changes may affect the mechanical behavior of the EBS bentonite in terms of effective/net and total stress. The effects considered in the model come from three components, volume fraction of smectite, exchangeable cation concentration, and osmotic suction.

We simulated a series of generic repository cases (described in Figure 3.2) with both high temperature ("high T") and low temperature ("low T") subjected to THMC processes (noted as "THMC"), in which C-M coupling is considered. The material for buffer is using FEBEX bentonite, whose mechanical behavior is computed with BExM. To account for the effects resulted by chemical reactions, we also simulated another scenario under the same loading conditions but without C-M coupling (noted as "THM"). Since the coupling is one-way, i.e. the mechanical behavior does not affect the fluid, thermal transports or chemical reactions. The evolution of temperature, liquid saturation and pore pressure is the same for result by "THMC" computation with high temperature and the one by "THM" with high temperature. The same situation is obtained with two "low T" cases. Figure 3.13 shows the temperature changes, and Figure 3.14 displays the evolution of liquid saturation and Figure 3.15 shows the evolution of pore pressure at point A and B for both "low T" and "high T" cases. At point A, the temperature can reach up to 200 °C in "high T" case and to 95 °C in "low T" case at around twenty years, and then it decreases again to the ambient temperature, 25 °C. Point B has lower temperature than point A since it is far from the heater. The temperature at point B goes up to 170 °C in "high T" case and to 80 °C in "low T" case at around twenty years, and then it decreases again to the ambient temperature, 25 °C. As Figure 3.14 shows, the liquid saturation at point A decreases firstly due to the drying process by the heater nearby. The material has been dried more during the high temperature case, inducing greater reduction in liquid saturation. Around one year, the bentonite at point A reaches the lowest saturation in both "high T" and "low T" cases. Then, the material is hydrated from the surrounding rocks to reach fully saturation status (about twenty years for "high T", fifteen years for "low T"). For point B, which is close to host rocks, the hydration starts at the beginning of the simulations. In "high T" case, the drying process near the heater helps the material at point B hydrate even faster. The bentonite reaches fully saturation at round five years in "high T" case, while it takes about eight years to saturate the material in "low T" case. There is no much difference of pore pressure between point A and point B. Since the point B is closer to host rocks than point A, the pore pressure at point B increases earlier than point A. In both "high T" and "low T" cases, pore pressures reach the peaks at around one hundred years (about 10.5 MPa in "high T", 3MPa in "low T"). After the peaks, pore pressures decreases to 2 MPa at around thirty thousand years, then they increase again.

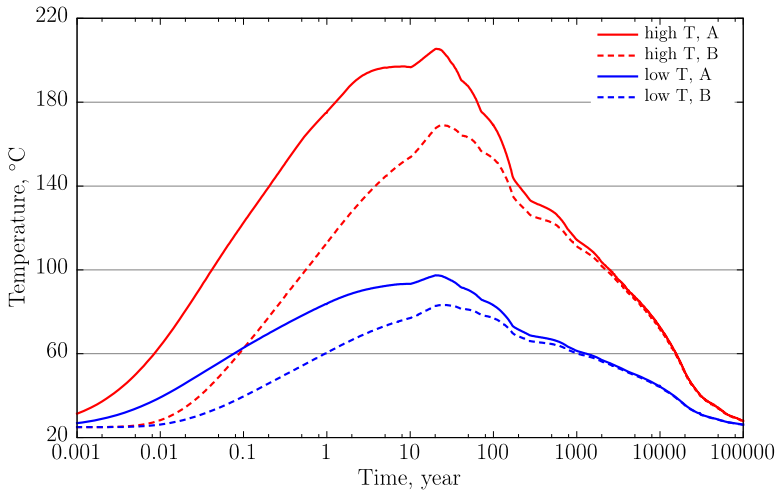

Figure 3.13. Simulation results of temperature evolution at point A and B with FEBEX bentonite for the "low T" and "high T" scenarios, respectively.

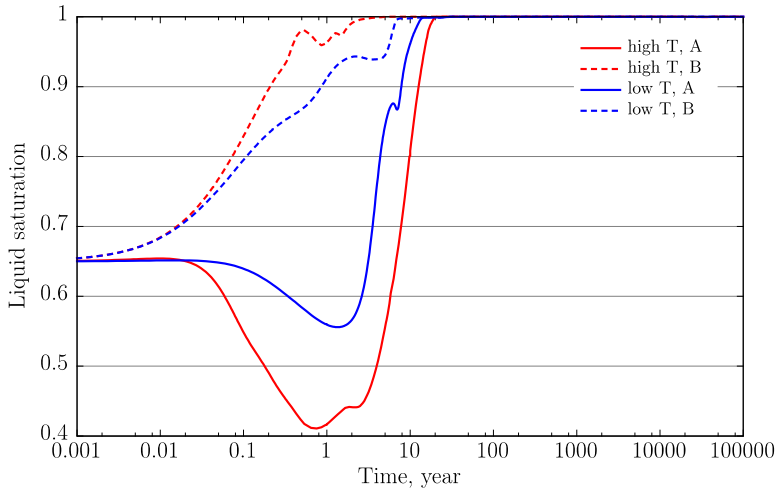

Figure 3.14. Simulation results of liquid saturation at point A and B with FEBEX bentonite for the "low T" and "high T" scenarios, respectively.

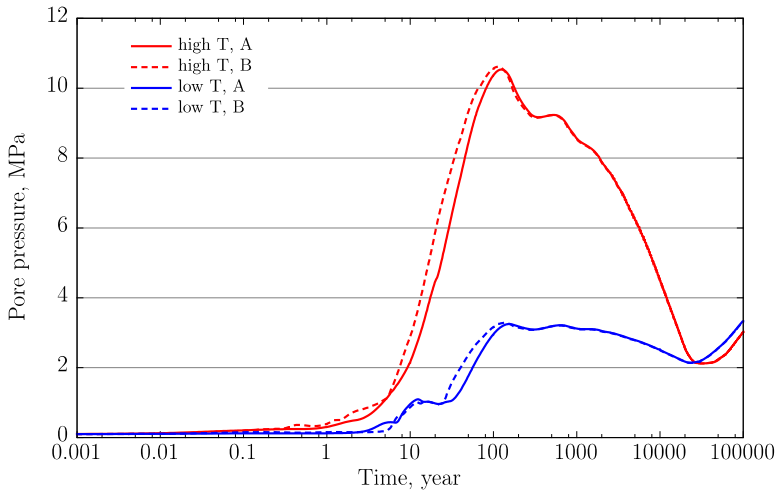

Figure 3.15. Simulation results of pore pressure at point A and B with FEBEX bentonite for the "low T" and "high T" scenarios, respectively. Note that before the material is fully saturated, the pore pressure is gas pressure, after fully saturation of the bentonite, the pore pressure refers to liquid pressure.

Figures 3.16 and 3.17 show the mean total stress changes at point A and B for both "low T" and "high T" cases. For both "THM" and "THMC" cases at point A, peak stresses in bentonite are about 4.5 MPa for the "low T" cases and 13 MPa for the "high T" cases, all at around one hundred years. Then the total stresses decrease until thirty thousand years, after when the stresses increase again to reach the hydrostatic status. The difference of stresses between "THM" and "THMC" cases are very small (less than 0.5 MPa), but it can be concluded that with the effects of chemical reaction, the total stresses decrease in both "high T" and "low T" cases at point A, inducing that the swelling capacity of the bentonite is reduced. For point B, the behavior is different. Peak stresses in bentonite at point B are about 6 MPa for the "low T" case and 14.5 MPa for the "high T" case, both at around one hundred years. The reason that stresses at point B are higher than stresses at point A is because point B is close to the surrounding Opalinus clay, which is subjected to high compression stress. In "low T" cases, the stress at point B by "THMC" computation is lower than the result by "THM" calculation, but the opposite result is obtained in "high T" cases. This phenomenon is caused from the combined results of three components of chemical reactions. The effects due to each component are investigated in the next section.

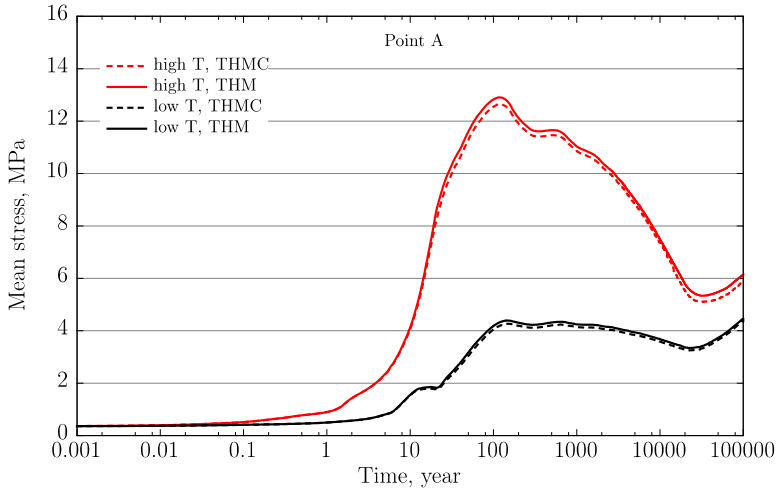

Figure 3.16. Simulation results of mean total stress at point A with FEBEX bentonite for the "low T" and "high T" scenarios, respectively.

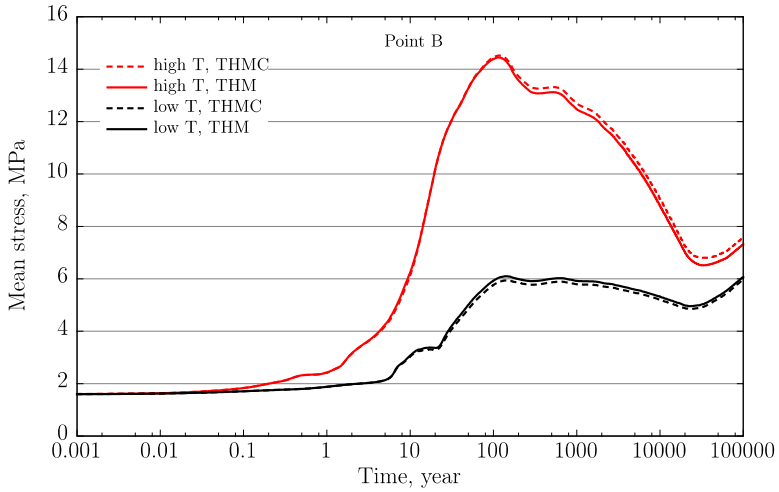

Figure 3.17. Simulation results of mean total stress at point B with FEBEX bentonite for the "low T" and "high T" scenarios, respectively.

Swelling stress is not clear in the simulation with the dual-structure model, because the micro-swelling strain is calculated directly in the framework of the model. Moreover, the non-linear plasticity induced from both micro- and macro-structures increases the difficulty to distinguish the swelling stress from the total stress. We present the mean effective/net stress (mean net stresses for unsaturated bentonite, and mean effective stress for fully saturated bentonite) during the simulation to illustrate the accumulation of stress in the solid skeleton of bentonite (Figures 3.18 and 3.19). At point A, mean effective/net stresses in "high T" cases (about 4 MPa at peak) are higher than the ones in "low T" (about 1.4 MPa at peak), and "THMC" cases have lower stresses than the corresponding "THM" cases as well. At the beginning of the simulation, bentonite is unsaturated. Thus, the net stress is plotted and it goes up to the peak stress at around twenty years when the material reaches fully saturation (Figure 3.18). Then effective stress is plotted instead. Since the pore pressures increase much from twenty years to one hundred years (about 6 MPa increase in "high T" and 2 MPa increase in "low T"), all effective stresses reduce until the turning point where pore pressures reach the peak and start to decrease at around one hundred years. Then the effective stresses in "low T" cases become stable only with small changes, while the effective stresses in

"high T" cases show the opposite changes against the evolution of pore pressures. Similar behaviors can be found with the point B, where the mean effective/net stresses reach the highest stress 4.5 MPa in "high T" cases and 2.7 MPa in "low T" cases. However, after the bentonite is fully saturated, the effective stresses at point B do not decrease as much as the ones at point A, and then the effective stresses increase to the highest stress which is more than the stresses at twenty years.

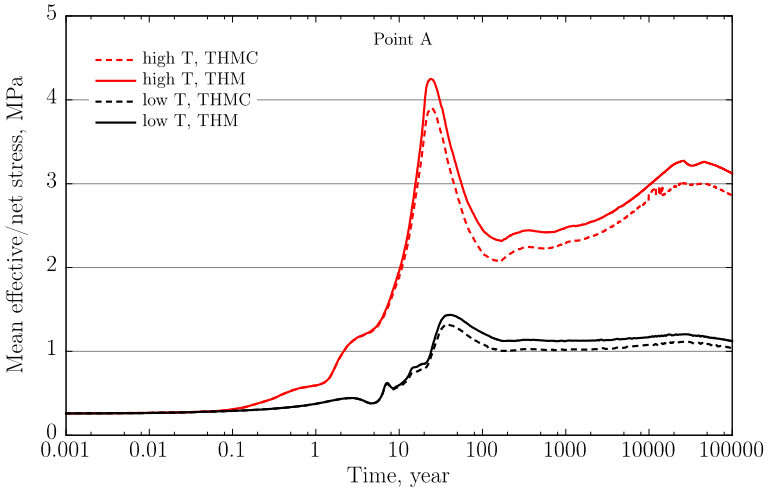

Figure 3.18. Simulation results of mean effective/net stress at point with FEBEX bentonite for the "low T" and "high T" scenarios, respectively.

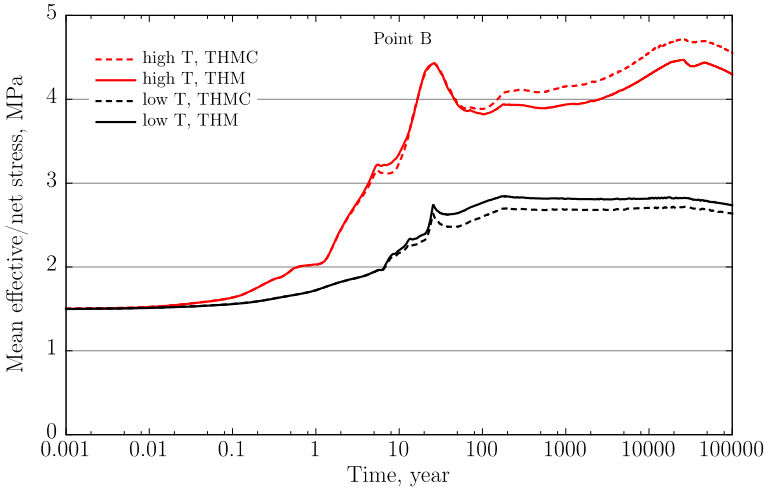

Figure 3.19. Simulation results of mean effective/net stress at point B with FEBEX bentonite for the "low T" and "high T" scenarios, respectively.

3.3.3.2 Effects of chemical changes on stress

The difference in calculated stresses between THMC and THM in Figures 3.18 and 3.19 clearly demonstrate the effect of chemical change on stress. Three chemical changes including the change in the volume fraction of smectite, change in exchanged cations and ionic strength contribute distinctively to the stress evolution in bentonite. In the current model, dissolution of smectite leads to decrease in the volume fraction of smectite (Figure 3.20), which tends to decrease the stress; β_m depends on the concentration of the exchanged Na, K, Ca and Mg, the enrichment of exchanged sodium in the interlayer leads to the increase of β_m (Figure 3.21), which tends to increase stress. The infiltration of more concentrated water

from clay formation to EBS bentonite leads to the increase in ionic strength of pore water in bentonite and subsequently osmotic suction, which tends to lower the stress. The relative importance of these three effects varies temporally and spatially and between cases ("high T" versus "low T"), and the combination of these three effects determines whether chemical change enhances or suppresses the stress. In order to delineate the contribution of each effect on stress, in addition to the THMC that considers all three effects, notated "THMC(f_s, β_m, s_o)" in the following figures, we also conducted simulations that take into account each individual effect independently of the others. These simulations are referred as "THMC(f_s)" that only the effect of volume fraction of smectite was considered, "THMC(β_m)" that only the effect of exchanged cations was considered and "THMC(s_o)" that only the effect of ionic strength via osmotic suction was considered.

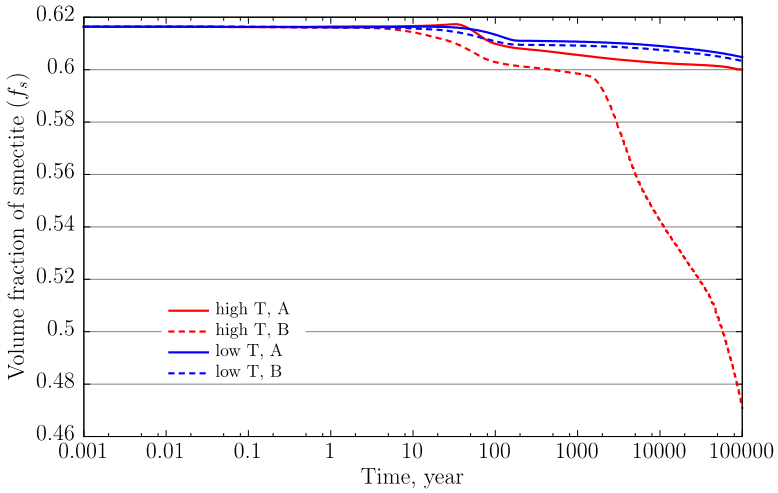

Figure 3.20. The evolution of the volume fraction of smectite at points A and B with FEBEX bentonite for the "low T" and "high T" scenarios, respectively.

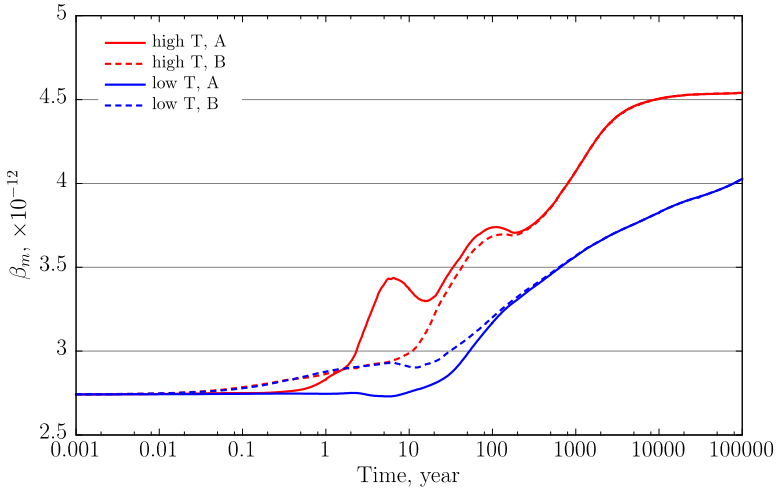

Figure 3.21. Simulation results of the evolution of β_m at points A and B with FEBEX bentonite for the "low T" and "high T" scenarios, respectively.

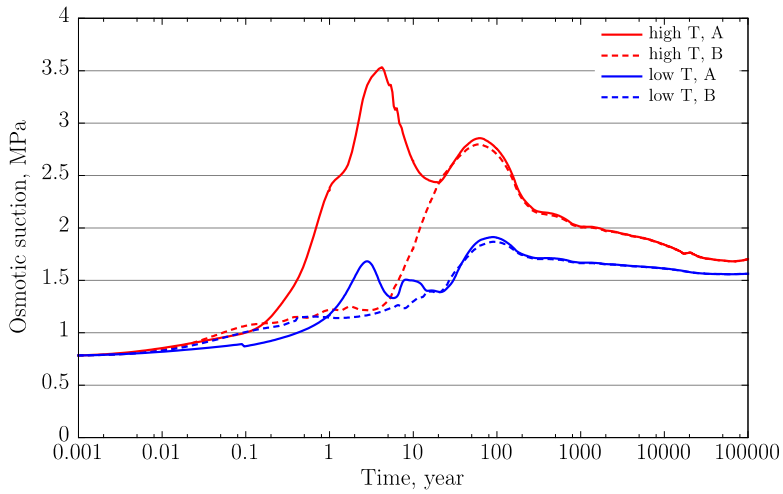

Figure 3.22. Simulation results of the osmotic suction at points A and B with FEBEX bentonite for the "low T" and "high T" scenarios, respectively.

Figure 3.22 shows the total stress evolution at point A for "high T" cases with C-M coupling schemes that includes different coupling schemes. "THM" means no C-M coupling, while "THMC(f_s, β_m, s_o)" indicates the C-M coupling with (f_s, β_m, s_o) effect is computed in the simulation. Overall, chemical effect leads to lower stress. By enlarging the curves between one hundred and ten years and one hundred and twenty years, it is found that the stress calculated without any C-M coupling ("THM") almost overlaps with the one with only the effect of volume fraction of smectite ("THMC(f_s)"), indicating that changes in volume fraction of smectite has only minimal effect on stress. The stress computed with only exchanged cation concentration ("THMC(β_m)") is higher than the "THM", which reveals that exchanged cations have positive effects on stress. The water infiltration from host rock leads to an increase of ionic strength of pore water in bentonite barrier which in turn cases the increase in osmotic suction (Figure 3.22). As a result, the swelling capacity of bentonite decreases, which is manifested by the reduction of the total stress for the case of "THMC(s_o)", i.e. a negative effect. Eventually, the negative effect of ionic strength via osmotic suction on stress outplays the positive effect of exchanged cations on stress, and consequently chemical changes result in lower stress overall (Figure 3.23).

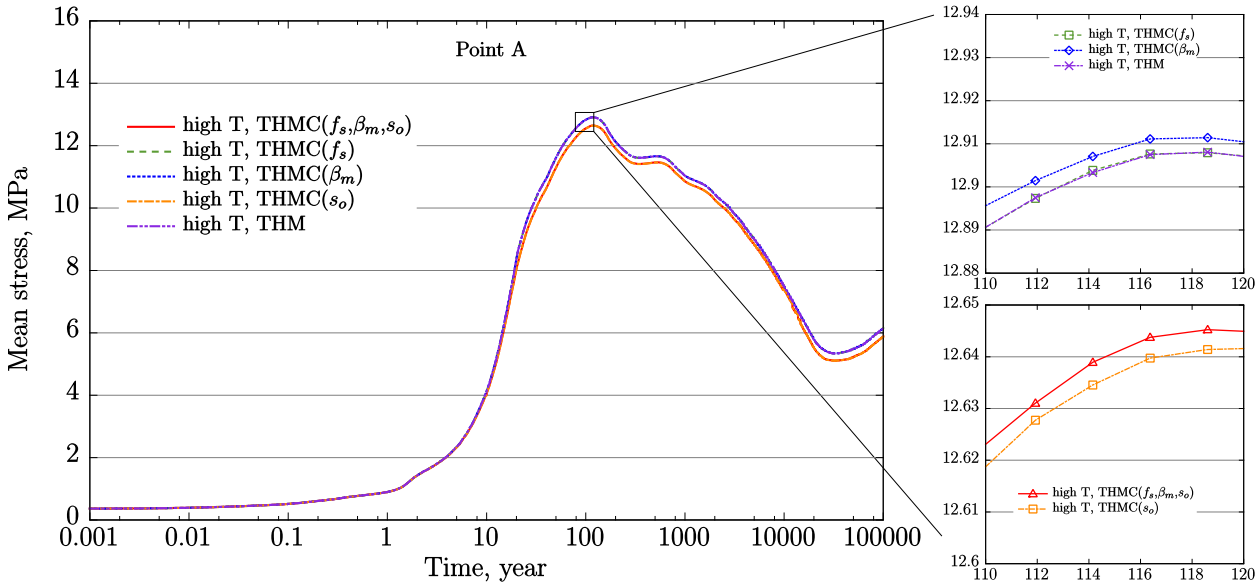

Figure 3.23. Simulation results of mean total stress at point A with FEBEX bentonite for the "high T" scenarios. Different C-M couplings are considered and computed.

The total stress evolutions at point A in "low T" cases are similar. The effect of osmotic suction is dominant and chemical changes overall lead to a decrease in stress. However, it is noteworthy that the difference between results by "THM", "THMC(f_s)" and "THMC(β_m)" are negligible (Figures 3.24).

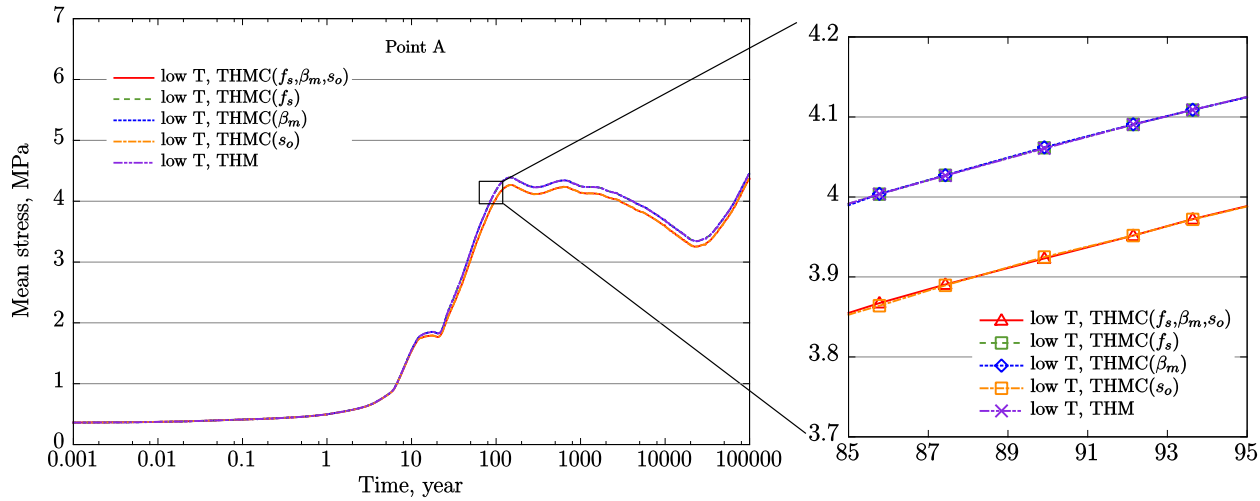

Figure 3.24. Simulation results of mean total stress at point A with FEBEX bentonite for the "low T" scenarios. Different C-M couplings are considered and computed.

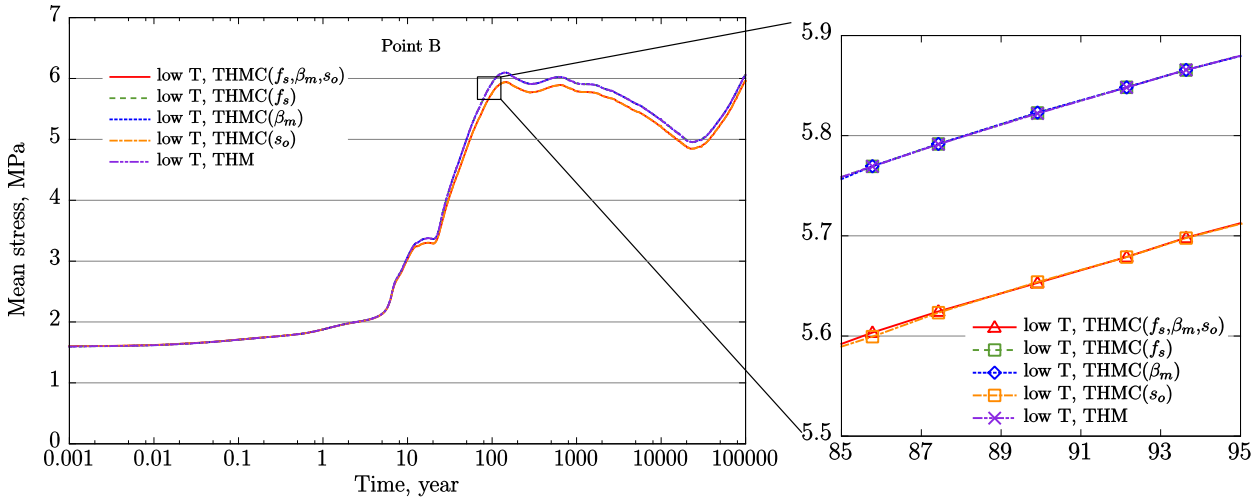

Figure 3.25. Simulation results of mean total stress at point B with FEBEX bentonite for the "low T" scenarios. Different C-M couplings are considered and computed.

Same observation can be obtained for the total stress at point B for "low T" cases (Figure 3.24). But the stress evolution at point B for "high T" is an outlier (Figure 3.25) — chemical effect as a whole lead to higher stress than the "THM" model, which is because that the effect of osmotic suction dominates whereas the effects induced by f_s and β_m are quite small. In comparison with the osmotic suction evolution at point A, the osmotic suction at point B went through different route (see Figure 3.22) — before the osmotic suction peaks at around one hundred years, point A went through up and down from 1 to ten years whereas point B underwent monotonic increase. The historical difference at point A and B was carried for longer simulation time due their effect on the bulk modulus. As a result, in terms of chemical effect on stress, point A and B exhibit different behavior: chemical effect as a whole lead to higher stress than the "THM" model at point B whereas the mean stress at point A computed with chemical effect is lower than the mean stress in "THM" model.

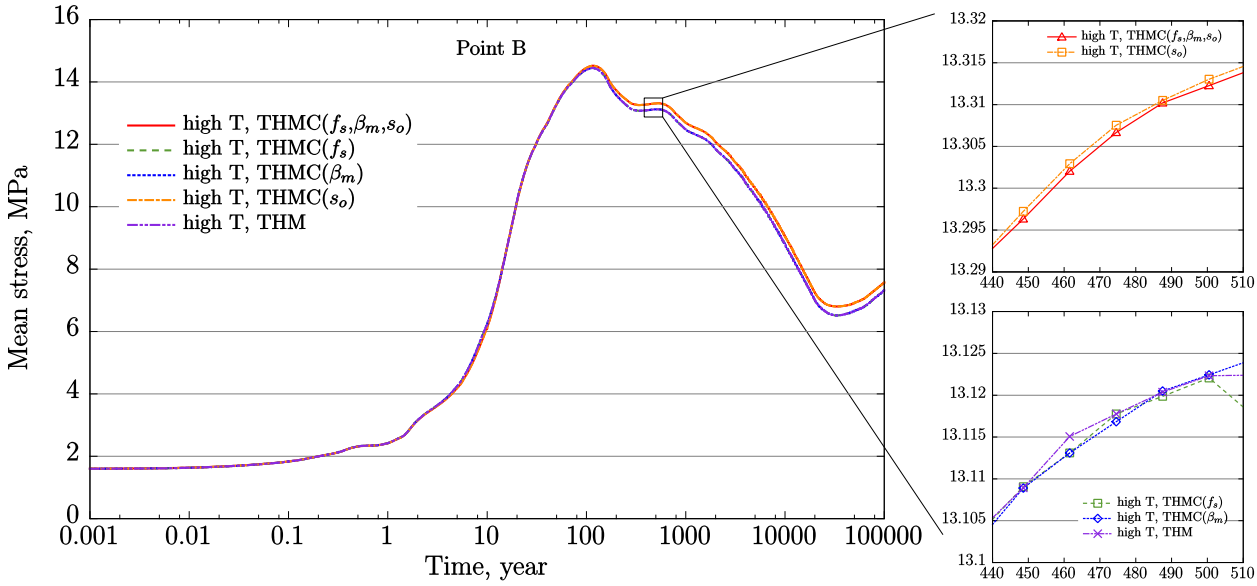

Figure 3.26. Simulation results of mean total stress at point B with FEBEX bentonite for the "high T" scenarios. Different C-M couplings are considered and computed.

3.3.3.3 Sensitivity to β_m

The current β_m calculated directly from the concentration of exchanged cations are three orders of magnitude smaller than that used by Sanchez et al. (2012). Thus, we introduce a factor α_β to correct β_m: $\beta_m' = \alpha_\beta \beta_m$. Here, 10^3 is used for α_β such that β_m will be in the same order of that in Sanchez et al. (2012). Note that in Sanchez et al. (2012) β_m is constant but in our model it is a function of exchange cations and therefore evolves spatially and temporally. In order to evaluate the effect of changing β_m, we conducted two sets of simulations, one is THMC model with C-M coupling that consider different effect as in section 3.3.3.2, the other is a THM simulation with $\beta_m = 0.021$ MPa^{-1} as in Sanchez et al. (2012. Another point, E, in the middle of the bentonite is picked for plotting stress evolutions (Figure 3.27). Larger β_m enlarges the effect of exchanged cations on stress. Therefore, "THMC(β_m)" that consider only the effect of exchanged cations has stress about 1 MPa higher than the "THM" case. Case "THMC(s_o)" has stress about 0.7 MPa lower than the "THM" case, indicating that osmotic suction suppress the stress. The results from case "THMC(f_s)" overlaps with the result by "THM", indicating that the dissolution of smectite has minimal effect on stress. The positive feedback of exchanged cations on stress outplay the osmotic suction and chemical change overall lead to an increase in stress.

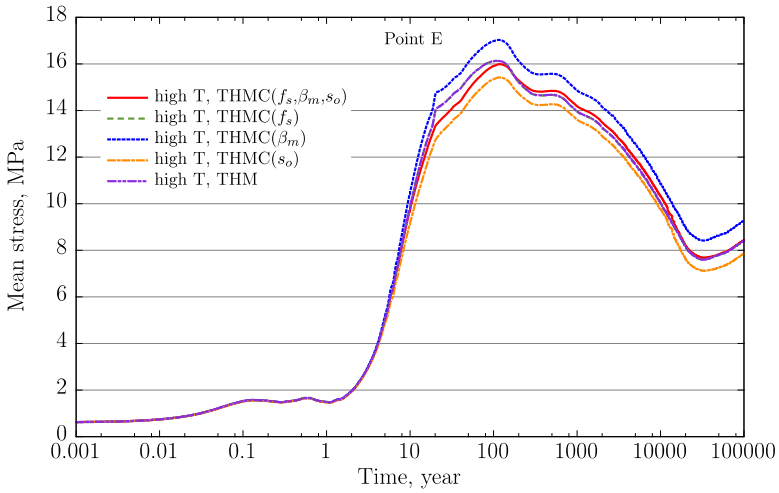

Figure 3.27. Simulation results of mean total stress at point E with FEBEX bentonite for the "high T" scenarios. Different C-M couplings are considered and computed.

3.4 CONCLUSIONS

3.4.1 Summary of current modeling work

Since FY13, we have been using coupled THMC modeling to evaluate the chemical alteration and associated mechanical changes in a generic repository to consider the interaction between EBS bentonite and the NS clay formation. Two main scenarios were developed for comparison: a "high T" case in which the temperature near the waste package can reach about 200 ^{o}C and a "low T" scenario in which the temperature peaks at about 100 ^{o}C. Conducting coupled THMC modeling proved challenging. The coupling between chemical and mechanical processes is the key part of THMC model that allow us to evaluate the impact of chemical changes on mechanical behavior. In FY16, THMC models utilize dual structure Barcelona Expansive Clay Model (BExM) (Sánchez et al., 2005) to link mechanical process with chemistry, allowing us to simultaneously incorporate the effects of exchangeable cations, ionic strength of pore water and abundance of swelling clay on the swelling stress of bentonite. In addition, the corrosion of steel canister was considered in the chemical model to evaluate whether the iron-bentonite interaction would aggravate the negative impact on swelling stress through the formation of Fe bearing clay minerals.

Coupled THMC models using BExM were developed for a generic case using FEBEX bentonite as EBS and Opalinus clay as NS. The following observations have been concluded from the model results: this newly developed model is used to predict the chemical-mechanical coupling in the geologic repositories for radioactive waste. The chemical effects on mechanics can be found as:

- The chemical changes as a whole reduce both total stress and effective/net stress in the bentonite buffer except the positions near the confinement rocks in the "high T" cases. However, the difference between the result computed with C-M coupling ("THMC") and the result without C-M coupling ("THM") is very small (less than 0.5 MPa).
- Three chemical changes, including the change in the volume fraction of smectite, change in exchanged cations and ionic strength contribute distinctively to the stress evolution in bentonite. In current model, dissolution of smectite leads to decrease in the volume fraction of smectite which decrease the stress; because the enrichment of exchanged sodium in the interlayer, the change in exchanged cations cause the increase in stress; the infiltration of more concentrated water from clay formation to EBS bentonite leads to the increase in osmotic suction and subsequently lowers the stress. The relative importance of these three effects varies temporally and spatially and between cases ("high T" versus "low T"), and the combination of these three effects determines whether chemical change enhances or suppresses the stress.
- The effect of chemical change on stress is very sensitive to the parameters that are related to the chemical-mechanical coupling.
- In comparison with the THMC that used extended linear swelling model (Zheng et al., 2015), THMC model using BExM showed much less chemical effect on stress. The first reason is that exchanged cations which was not able to be taken into account by extended linear swelling model, is now considered in BExM. For FEBEX bentonite, change in exchanged cations has positive effect on the stress, which cancel out the negative effect due to the change of ionic strength (via osmotic sunction) and consequently the chemical change overall has much less effect on stress in THMC model using BExM than that in the THMC that used extended linear swelling model. The second reason is that the chemical-mechanical coupling via BExM, the dissolution of smectite was factored in directly via the volume fraction of smectite by modifying the bulk modulus for micro-structure, but in BExM, bulk modulus is a function of stress and change significantly in the model, the bulk modulus changes by smectite dissolution was overshadowed by the stress change.

Interaction between corroded steel canister and bentonite was taken into account in a THMC model for FEBEX bentonite using extended linear swelling. The corrosion process was simplified and the model focused on the possibility of forming Fe bearing clay minerals. Based on literature survey, we included vermiculite, berthierine, saponite as the potential Fe-clay mineral forming in the model, but none of them is formed. However, including Fe-bentonite interaction leads to slightly more precipitation of chlorite and dissolution of smectite, which drives down the swelling stress reduction slightly. As far as the dissolution of smectite and swelling stress reduction is concerned, including Fe-bentonite interaction does not seem to be very important.

3.4.2 FUTURE WORK

The current coupled THMC model greatly improves our understanding of the coupled processes contributing to chemical and mechanical alteration in EBS bentonites and NS argillite formations and answers questions regarding the thermal limit of EBS bentonite in clay repository. However, more questions remain to be answered regarding the THMC alteration of bentonites and clay formations under high temperature. Further refinement of current models and improvements for the TOUREACT-FLAC3D simulator are needed in the future. In the remaining months of FY16 and FY17 the following activities are proposed:

- The current dual-structure model contains some limitations based on its physical assumptions. Moreover, the number of parameters for BExM is much more than other mechanical models, which increases the difficulty to calibrate the model for specific materials. The model needs to be simplified to improve its numerical robustness and to apply easily on different materials.
- The THMC model using BExM will be utilized in more numerical analysis with other buffer material such as Kunigel-VI bentonite. In current model, THMC model using BExM was only conducted for FEBEX bentonite because BExM had been calibrated for FEBEX bentonite and its concept fit better bentonite with high smectite content. However, the applicability of BExM for bentonite with low smectite such as Kunigel-VI bentonite need to be tested and how chemical-mechanical coupling via BExM work out for Kunigel-VI need to be evaluated.
- The geochemical model for the Fe-bentonite interaction will be refined and calibrated against data. In the current model, no significant iron-related bentonite alteration was found despite some laboratory and field studies have shown formation of iron-clay minerals. The geochemical conceptual model and thermodynamic data base are the key to raise our confidence on the model. In the FY17, the geochemical model for Fe-bentonite interaction will be tested from data obtained in an eighteen years' in situ test and then simulations with higher temperature and long time will be conducted.
- Current models show precipitation of silicate minerals during illitization, which could result in the cementation of bentonite and subsequently lead to change in the mechanical properties of bentonite. Although the formation of silicate minerals is only about 3-4%, the change of mechanical properties as result of cementation needs to be quantified before we can safely conclude that silicate cementation won't significantly affect the mechanical properties.

3.5 REFERENCES

Bethke C M (2002) The geochemists workbench release 4.0: A users guide to RXN, ACT2, TACT, REACT, and GTPLOT.

Birgersson M., Wersin p. (2004) Reactive Transport Modelling of Iron-Bentonite Interactions, an Update for the Olkiluoto Case, KBS-3H

Bossart P. (2011) Characteristics of the Opalinus Clay at Mont Terri, http://www.mont-terri.ch/internet/mont-terri/en/home/geology/key_characteristics.html

Bucher, F., and Müller-Vonmoos, M. (1989) Bentonite as a containment barrier for the disposal of highly radioactive waste. Applied Clay Science, 4(2): 157–177.

Casciello, E., J. W. Cosgrove, M. Cesarano, E. Romero, I. Queralt and J. Vergés 2011. Illite-smectite patterns in sheared Pleistocene mudstones of the Southern Apennines and their implications regarding the process of illitization: A multiscale analysis. Journal of Structural Geology 33(11): 1699-1711.

Chen, Y., C. Zhou and L. Jing 2009. Modeling coupled THM processes of geological porous media with multiphase flow: Theory and validation against laboratory and field scale experiments. Computers and Geotechnics 36(8): 1308-1329.

Cheshire, M. C., F. A. Caporuscio, M. S. Rearick, C. Jové-Colón and M. K. McCarney 2014. Bentonite evolution at elevated pressures and temperatures: An experimental study for generic nuclear repository designs. American Mineralogist 99(8-9): 1662-1675.

Cuadros, J. 2006. Modeling of smectite illitization in burial diagenesis environments. Geochimica et Cosmochimica Acta 70(16): 4181-4195.

ENRESA 2000. Full-scale engineered barriers experiment for a deep geological repository in crystalline host rock FEBEX Project, European Commission: 403.

Fernández, A. M., B. Baeyens, M. Bradbury and P. Rivas (2004). Analysis of the porewater chemical composition of a Spanish compacted bentonite used in an engineered barrier. Physics and Chemistry of the Earth, Parts A/B/C 29(1): 105-118.

Fernández, A. M., Turrero, M. J., Sánchez, D. M., Yllera, A., Melón, A. M., Sánchez, M., Peña, J., Garralón, A., Rivas, P., Bossart, P. and Hernán, P. (2007) On site measurements of the redox and carbonate system parameters in the low-permeability Opalinus Clay formation at the Mont Terri Rock Laboratory. Physics and Chemistry of the Earth, Parts A/B/C 32(1-7): 181-195 .

Fernández, A., Cuevas, J., Rivas, P., 2001. Pore water chemistry of the FEBEX bentonite. Mat. Res. Soc. Symp. Proc. 663, 573–588.

Gaston D, Newman C, Hansen G, Lebrun-Grandie D. MOOSE: A parallel computational framework for coupled systems of nonlinear equations. Nucl Eng Des 2009; 239(10): 1768–1778.

GENS, A. 2010 Soil environment interactions in geotechnical engineering. Géotechnique 60, 3-74

Guimarães LDN, Gens A, Olivella S (2007) Coupled Thermo-Hydro-Mechanical and Chemical Analysis of Expansive Clay Subjected to Heating and Hydration. Transport in Porous Media 66(3): 341-372.

Guimarães LDN, Gens A, Sánchez M, Olivella S (2013) A chemo-mechanical constitutive model accounting for cation exchange in expansive clays. Géotechnique 63, 221–234

Hicks, T.W., White, M.J. and Hooker, P.J. (2009) Role of Bentonite in Determination of Thermal Limits on Geological Disposal Facility Design, Report 0883-1, Version 2, Falson Sciences Ltd., Rutland, UK, Sept. 2009.

Horseman S.T. and McEwen, T. J. (1996) Thermal constrains on disposal of heat-emitting waste in argillaceous rocks, Engineering Geology 41, 5-16.

Itasca, 2009. FLAC3D, Fast Lagrangian Analysis of Continua in 3 Dimensions, Version 4.0, Minneapolis, Minnesota, Itasca Consulting Group.

JNC, Japan Nuclear Cycle Development Institute. (1999) H12: project to establish the scientific and technical basis for HLW disposal in Japan: supporting report 2 (respiratory design and engineering Technology). Japan Nuclear Cycle Development Institute, Tokyo.

Kamei, G., M. S. Mitsui, K. Futakuchi, S. Hashimoto and Y. Sakuramoto 2005. Kinetics of long-term illitization of montmorillonite—a natural analogue of thermal alteration of bentonite in the radioactive waste disposal system. Journal of Physics and Chemistry of Solids 66(2–4): 612-614.

Karnland, O., Olsson, S. and Nilsson, U. (2006) Mineralogy and sealing properties of various bentonites and smectite-rich clay materials, SKB Technical Report TR-06-30.

Kim J, Sonnenthal E, Rutqvist J (2015) A sequential implicit algorithm if chemo-thermo-poro-mechanics for fractured geothermal reservoir. Computers & Geosciences, 76; 59–71.

Komine, H., and Ogata, N. (1996) Prediction for swelling characteristics of compacted bentonite. Canadian Geotechnical Journal, 33: 11–22.

Landolt D., Davenport A., Payer J., Shoesmith D., (2009) A Review of Materials and Corrosion Issues Regarding Canisters for Disposal of Spent Fuel and High-level Waste in Opalinus Clay, Technical Report 09-02.

Laredj, N., Missoum, H. and Bendani, K. (2010) Modeling the effect of osmotic potential changes on deformation behavior of swelling clays. Journal of Porous Media 13(8): 743-748.

Lasaga, A. C., J. M. Soler, J. Ganor, T. E. Burch and K. L. Nagy 1994. Chemical weathering rate laws and global geochemical cycles. Geochimica et Cosmochimica Acta 58: 2361-2368.

Lauber, M., B. Baeyens and Bradbury, M. H. (2000) Physico-Chemical Characterisation and Sorption Measurements of Cs, Sr, Ni, Eu, Th, Sn and Se on Opalinus Clay from Mont Terri. PSI Bericht Nr. 00-10 December 2000 ISSN 1019-0643.

Liu, H.H., J. Houseworth, J. Rutqvist, L. Zheng, D. Asahina, L. Li, V. Vilarrasa, F. Chen, S. Nakagawa, S. Finsterle, C. Doughty, T. Kneafsey and J. Birkholzer. (2013) Report on THMC modeling of the near field evolution of a generic clay repository: Model validation and demonstration, Lawrence Berkeley National Laboratory, August, 2013, FCRD-UFD-2013-0000244.

Lloret A, Villar MV, Sánchez M, Gens A, Pintado X, Alonso EE. Mechanical behaviour of heavily compacted bentonite under high suction changes. Géotechnique 2003; 53(1):27–40.

Martin, F., S. Perrin, M. Fenart, M. Schlegel and C. Bataillon 2014. On corrosion of carbon steels in Callovo-Oxfordian clay: complementary EIS, gravimetric and structural study providing insights on long term behaviour in French geological disposal conditions. Corrosion Engineering, Science and Technology 49(6): 460-466.

Montes-H, G., B. Fritz, A. Clement and N. Michau 2005. Modelling of geochemical reactions and experimental cation exchange in MX80 bentonite. Journal of Environmental Management 77(1): 35-46.

Mosser-Ruck, R. and M. Cathelineau 2004. Experimental transformation of Na, Ca-smectite under basic conditions at 150 C. Applied Clay Science 26(1): 259-273.

Mosser-Ruck, R., M. Cathelineau, D. Guillaume, D. Charpentier, D. Rousset, O. Barres and N. Michau 2010. EFFECTS OF TEMPERATURE, pH, AND IRON/CLAY AND LIQUID/CLAY RATIOS ON EXPERIMENTAL CONVERSION OF DIOCTAHEDRAL SMECTITE TO BERTHIERINE, CHLORITE, VERMICULITE, OR SAPONITE. Clays and Clay Minerals 58(2): 280-291.

Nagra 2002: Project Opalinus Clay, Safety report, Nagra Technical Report 02-05, Nagra

Nitao J (1996) Reference Manual for the NUFT Flow and Transport Code, Version 1.0 Earth Sciences Department Lawrence Livermore National Laboratory.

Noorishad J, Tsang CF (1996) ROCMAS-simulator: a thermohydro-mechanical computer code. In: Stephansson O, Jing L, Tsang C-F, editors. Coupled Thermo-hydro-mechanical processes of fractured media, vol. 79. Elsevier: Developments in Geotechnical Engineering, 551–8.

Ochs, M., Lothenbach, B., Shibata, M. and Yui, M. (2004) Thermodynamic modeling and sensitivity analysis of porewater chemistry in compacted bentonite. Physics and Chemistry of the Earth, Parts A/B/C 29(1): 129-136.

Olivella S, Carrera J, Gens A, Alonso EE (1994) Nonisothermal multiphase flow of brine and gas through saline media. Transp Porous Media 15: 271–93.

Pacovsky, J., Svoboda, J., Zapletal, L., 2005. Saturation development in the bentonite barrier of the mock-up CZ geotechnical experiment. Clay in Natural and Engineered Barriers for Radioactive Waste Confinement—Part 2. Physics and Chemistry of the Earth 32(8–14), 767–779.

Pusch R. and Karnland, O. (1996) Physico/chemical stability of smectite clays, Engineering Geology 41: 73-85.

Pusch, R. and Madsen, F. T. (1995) Aspects on the illitization of the kinnekulle bentonites. Clays and Clay Minerals 43(3): 261-270.

Pusch, R., Kasbohm, J. and Thao, H. T. M. (2010) Chemical stability of montmorillonite buffer clay under repository-like conditions—A synthesis of relevant experimental data. Applied Clay Science 47(1–2): 113-119.

Ramírez, S., J. Cuevas, R. Vigil and S. Leguey 2002. Hydrothermal alteration of "La Serrata" bentonite (Almeria, Spain) by alkaline solutions. Applied Clay Science 21(5–6): 257-269.

Rutqvist J, Börgesson L, Chijimatsu M, Kobayashi A, Nguyen TS, Jing L, Noorishad J, Tsang CF (2001) Thermohydromechanics of partially saturated geological media – Governing equations and formulation of four finite element models. Int. J. Rock Mech. & Min. Sci. 38, 105–127.

Rutqvist, J. and Tsang, C.-F. (2002). Coupled Thermohydromechanical Analysis of FEBEX in Situ test with ROCMAS, Swedish Nuclear Power Inspectorate Research Team Report to DECOVALEX Task 1 Coordinator, Part B-THM modeling of the bentonite. Lawrence Berkeley National Laboratory, Berkeley, CA, USA.

Rutqvist, J., Y. Ijiri and H. Yamamoto 2011. Implementation of the Barcelona Basic Model into TOUGH–FLAC for simulations of the geomechanical behavior of unsaturated soils. Computers & Geosciences 37(6): 751-762.

Rutqvist, J., Zheng, L., Chen, F., Liu, H.-H. and Birkholzer, J. (2013). Modeling of Coupled Thermo-Hydro-Mechanical Processes with Links to Geochemistry Associated with Bentonite-Backfilled Repository Tunnels in Clay Formations. Rock Mechanics and Rock Engineering: 1-20.

Rutqvist, J., Zheng, L., Chen, F., Liu, H.-H. and Birkholzer, J. (2014) Modeling of Coupled Thermo-Hydro-Mechanical Processes with Links to Geochemistry Associated with Bentonite-Backfilled Repository Tunnels in Clay Formations. Rock Mechanics and Rock Engineering: 47(1): 167-186.

Saaltink MW, Batlle F, Ayora C, Carrera J, Olivella S (2004) RETRASO, a code for modeling reactive transport in saturated and unsaturated porous media. Geologica Acta 2(3): 235–251.

Sánchez, M., A. Gens and S. Olivella (2012). THM analysis of a large-scale heating test incorporating material fabric changes. International Journal for Numerical and Analytical Methods in Geomechanics 36(4): 391-421.

Sánchez, M., A. Gens, L. J. D. N. Guimarães and S. Olivella 2005. A double structure generalized plasticity model for expansive materials. International Journal for numerical and analytical methods in geomechanics 29: 751-787.

Shibata, T., M. Watanabe, N. Taniguchi and A. Shimizu 2014. Modelling of carbon steel corrosion under oxygen depleted environment. Corrosion Engineering, Science and Technology 49(6): 435-441.

Soler, J. M. 2001. The effect of coupled transport phenomena in the Opalinus Clay and implications for radionuclide transport. Journal of Contaminant Hydrology 53: 63-84.

Sonnenthal, E. Chapter 5 in: Birkholzer, J. Rutqvist, E. Sonnenthal, and D. Barr, Long-Term Permeability/Porosity Changes in the EDZ and Near Field due to THM and THC Processes in Volcanic and Crystalline-Bentonite Systems, DECOVALEX-THMC Project Task D Final Report, 2008.

Steefel CI (2001) GIMRT, Version 1.2: Software for Modeling Multicomponent, Multidimensional Reactive Transport. Users Guide. Livermore, California, Lawrence Livermore National Laboratory.

Taron J, Elsworth D, Min KB (2009) Numerical simulation of thermal–hydrologic–mechani-cal–chemical processes in deformable, fractured porous media, International Journal of Rock Mechanics Mining Sciences, 46: 842–854.

Thury, M., 2002. The characteristics of the Opalinus Clay investigated in the Mont Terri underground rock laboratory in Switzerland. Comptes Rendus Physique 3(7-8), 923-933.

Wang W, Rutqvist J, Görke UJ, Birkholzer JT Kolditz O (2011) Non isothermal flow in low permeable porous media: A comparison of Richards' and two-phase flow approaches. Environmental Earth Sciences, 62: 1197–1207.

Wersin P., Johnson, L.H. and McKinley, I.G. (2007) Performance of the bentonite barrier at temperature beyond 100oC: A critical review, Physics and Chemistry of the Earth 32: 780-788.

Wersin, P., A. Jenni and U. K. Mäder 2015. INTERACTION OF CORRODING IRON WITH BENTONITE IN THE ABM1 EXPERIMENT AT ÄSPÖ, SWEDEN: A MICROSCOPIC APPROACH. Clays and Clay Minerals 63(1): 51-68.

Wettingen, Switzerland

Wolery, T. J. 1993. EQ3/6, A software package for geochemical modelling of aqueous systems (Version 7.2). , Lawrence Livermore National Laboratory.

Xu, T., E. Sonnenthal, N. Spycher and K. Pruess 2006. TOUGHREACT: A Simulation Program for Non-isothermal Multiphase Reactive Geochemical Transport in Variably Saturated Geologic Media. Computers and Geosciences 32: 145-165.

Xu, T., Spycher, N., Sonnenthal, E., Zhang, G., Zheng, L. and Pruess, K. (2011) TOUGHREACT Version 2.0: A simulator for subsurface reactive transport under non-isothermal multiphase flow conditions. Computers & Geosciences 37(6): 763-774.

Zhang R, Yin X, Winterfeld PH, Wu YS (2012) A fully coupled model of nonisothermal multiphase flow, geomechanics, and chemistry during co2 sequestration in brine aquifers. Proceedings of the TOUGH Symposium, 838–848.

Zheng L, Samper J (2008) A coupled THMC model of FEBEX mock-up test. Physics and Chemistry of the Earth, Parts A/B/C 33, Supplement 1: S486-S498.

Zheng L., Rutqvist J. Kim, K. and Houseworth J. (2015), Investigation of Coupled Processes and Impact of High Temperature Limits in Argillite Rock. FCRD-UFD-2015-000362, LBNL-187644.

Zheng, L., J. Samper and L. Montenegro 2011. A coupled THC model of the FEBEX in situ test with bentonite swelling and chemical and thermal osmosis. Journal of Contaminant Hydrology 126(1–2): 45-60.

Zheng, L., Li, L., Rutqvist, J., Liu, H. and Birkholzer, J.T., (2012). Modeling Radionuclide Transport in Clays. Lawrence Berkeley National Laboratory. FCRD-URD-2012-000128

Zheng,L. Jonny Rutqvist, Carl Steefel, Kunhwi Kim, Fei Chen, Victor Vilarrasa, Seiji Nakagawa, Jiangtao Zheng, James Houseworth, Jens Birkholzer. (2014) Investigation of Coupled Processes and Impact of High Temperature Limits in Argillite Rock. FCRD-UFD-2014-000493, LBNL-6719E

4. UNDERSTANDING THE THMC EVOLUTION OF BENTONITE IN FEBEX-DP-COUPLED THMC MODELING AND EXAMINATION OF THE STRUCTURE OF BENTONITE

4.1 INTRODUCTION

The clay and crystalline radioactive water repository typically involves a multi-barrier system. In addition to the natural barrier system (NBS), i.e. the host rock and its surrounding subsurface environment, it also has an engineered barrier system (EBS). The EBS represents the man-made, engineered materials placed within a repository, including the waste form, waste canisters, buffer materials, backfill, and seals.

The most common buffer material for EBS is compacted bentonite, which features low permeability and high retardation of radionuclide transport. The safety functions of EBS bentonite include limiting transport in the near field; damping the shear movement of the host rock; preventing the sinking of canisters (if emplaced in the center of the tunnel), limiting pressure on the canister and rock, and reducing microbial activity. To assess whether EBS bentonite can maintain these favorable features when undergoing heating from the waste package and hydration from the host rock, we need a thorough understanding of the thermal, hydrological, mechanical, and chemical evolution of bentonite under disposal conditions. While numerous laboratory experiments, field tests, and numerical models have been conducted to improve the understanding of each individual process or coupled THC/THM processes, there is a lack of studies on coupled THMC processes due to the challenges of conducting experiments and developing models that can cover all the THMC processes. Recently in the UFD program, coupled THMC models have been developed for a generic disposal system in clayey host rock with EBS bentonite (Liu et al., 2013; Zheng et al., 2014; Zheng et al., 2015b). However, model validation was difficult for lack of THMC data from long-term, large-scale experiments. The FEBEX (Full-scale Engineered Barrier EXperiment) *in situ* test, which has been operated for eighteen years, provides a unique opportunity of validating coupled THMC models.

In the FEBEX *in situ* test, two heaters surrounded by bentonite blocks about 0.7 m thick were emplaced in a tunnel excavated in granite. The heaters were switched on in 1997. In 2002, heater 1 was dismantled; in 2015, the second heater was dismantled in the FEBEX-DP project, which is comprised of extensive THMC and biological characterization of bentonite, and development of numerical models. LBNL/DOE joined the FEBEX-DP project in FY15. The ultimate goal is to use THMC data from FEBEX-DP to validate THMC models and therefore enhance our understanding of coupled THMC process. In this section, we describe our progress in FY16, which includes the development of coupled THMC models that interpret the THM data and predict the chemical evolution in bentonite, and synchrotron X-ray microtomography measurements of the bentonite samples to examine the microstructure of bentonite that suffered eighteen years of *in situ* heating and hydration.

4.2 A BRIEF DESCRIPTION OF FEBEX EXPERIMENTS

FEBEX (**F**ull-scale **E**ngineered **B**arrier **Ex**periment in Crystalline Host Rock) is a research and demonstration project that was initiated by ENRESA (Spain). THE FEBEX objective was to study the behavior of components in the near-field for a high-level radioactive waste (HLW) repository in crystalline rock. Specifically, the project aimed to demonstrate the feasibility of fabricating and assembling the EBS and developing methodologies and models for evaluation of the thermo-hydro-mechanical (THM) and thermo-hydro-chemical (THC) behavior of the near-field (ENRESA, 2000). These objectives were to be attained through the combination of *in situ* and mock-up tests, and numerous small-scale laboratory tests, and THC/THM modeling. The project was initially scheduled for a period of seven years, from 1994 to 2001, but was extended several times as the experiments continued. Figure 4.1

shows the history of FEBEX projects, with different project names representing different operational stages.

Figure 4.1. The operational stages of FEBEX *in situ* test (Vomvoris, personal communication).

The centerpiece of FEBEX experiments is, of course, the *in situ* test conducted at the Grimsel underground laboratory, Switzerland. The test consists of five basic units: the drift, the heating system, the bentonite barrier, the instrumentation, and the monitoring and control system (Figure 4.2). The drift is 70.4 m long and 2.28 m in diameter. The test area, which was sealed with a concrete plug, is located at the last 17.4 m of the drift where heaters, bentonite and instrumentation were installed. The main elements of the heating system are two heaters (#1 and #2), 1 m apart, which simulate full-sized canisters. Heaters were placed inside a cylindrical steel liner. Each heater is made of carbon steel, measures 4.54 m in length and 0.9 m in diameter, and has a wall thickness of 0.1 m. Heaters were operated at a constant power output of 1200 W/heater during the first 20 days and 2000 W/heater for the following 33 days. Afterwards, the heaters were switched to a constant-temperature control mode to maintain a maximum temperature of 100 ºC at the steel liner/bentonite interface.

The bentonite barrier is made of blocks of highly compacted bentonite, situated in vertical sections normal to the axis of the tunnel. The cross section of bentonite barrier is shown in Figure 4.3. The dimension of fabricated bentonite blocks are shown in Figure 4.3 (right) and Table 4.1. There were gaps between blocks, but the volume of gaps has not been reliably estimated. Although the dismantling of bentonite barrier revealed that all gaps were sealed, these gaps might affect the initial hydration of bentonite, but such effect is difficult for model to take into account. The average values of the initial dry density and the water content of compacted bentonite blocks are 1.7 g/cm^3 and 14.4%, respectively.

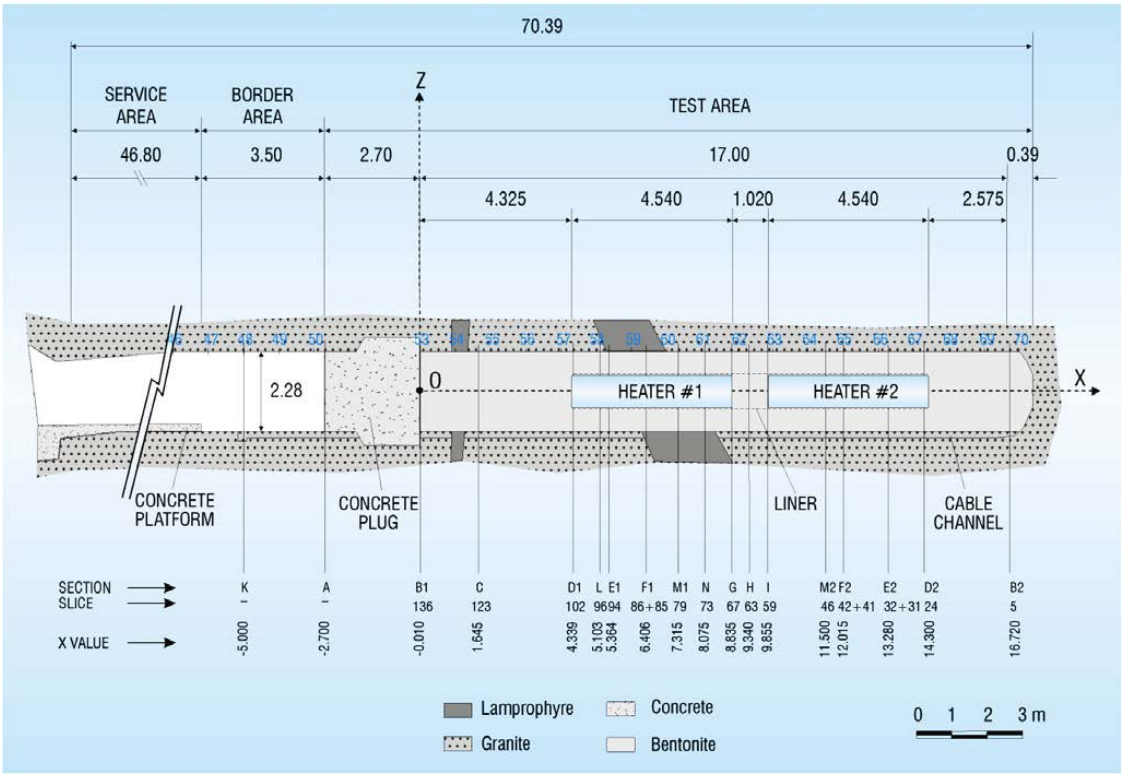

Figure 4.2. The initial configuration of the FEBEX *in situ* test at the Grimsel underground laboratory (Switzerland) (ENRESA, 2000).

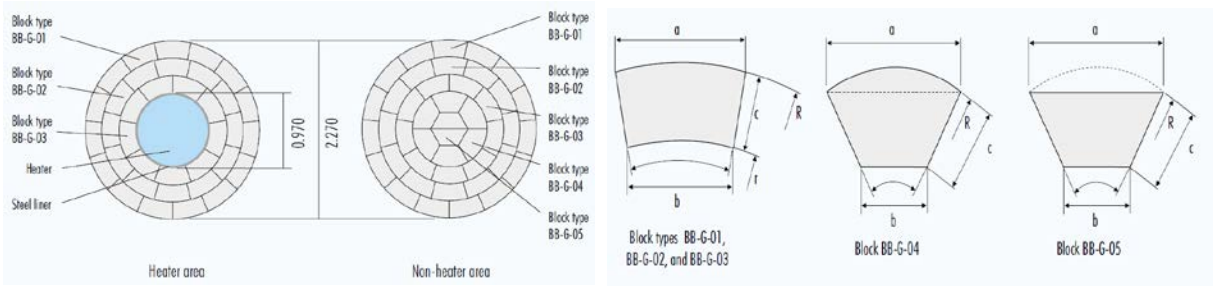

Figure 4.3. The geometry of clay barrier (left) and the type of bentonite blocks (right) with dimensions listed in Table 4.1 (ENRESA, 2000).

Table 4.1. Dimensions for bentonite blocks (ENRESA 2000)

Type	a mm	b mm	c mm	Thicknes mm	R mm	r mm	α
BB-G-01	470.0 $^{2.0}_{5.0}$	380.0 $^{2.0}_{4.0}$	214.0 $^{2.0}_{3.0}$	125.0 $^{2.0}_{2.0}$	1 133	919	24º
BB-G-02	473.0 $^{2.0}_{5.0}$	361.0 $^{2.0}_{4.0}$	214.0 $^{2.0}_{3.0}$	125.0 $^{2.0}_{2.0}$	917	703	30º
BB-G-03	478.0 $^{2.0}_{5.0}$	330.0 $^{2.0}_{3.0}$	214.0 $^{2.0}_{3.0}$	125.0 $^{2.0}_{2.0}$	701	487	40º
BB-G-04	483.0 $^{2.0}_{5.0}$	240.0 $^{2.0}_{3.0}$	240.0 $^{2.0}_{3.0}$	125.0 $^{2.0}_{2.0}$	485	—	60º
BB-G-05	483.0 $^{2.0}_{5.0}$	240.0 $^{2.0}_{3.0}$	240.0 $^{2.0}_{3.0}$	125.0 $^{2.0}_{2.0}$	—	—	60º

The *in situ* test began on February 27, 1997. Heater #1 was switched off in February 2002 and dismantled from May to September in 2002. The buffer and all components were removed up to a distance of 2 meters from heater #2 to minimize disturbance of the non-dismantled area. A dummy steel cylinder with a length of 1 m was inserted in the void left by heater #1 in the center of the buffer. The description of the partial dismantling operation is given in Bárcena et al. (2003). A comprehensive post-mortem bentonite sampling and analysis program was performed on the solid and liquid phases to check the physical and chemical changes induced by the combined effect of heating and hydration and to test THM and THC model predictions (ENRESA 2006a,b). The layout of the sampling sections for THC and THM measurements after the dismantling of heater #1 is given in Figure 4.4.

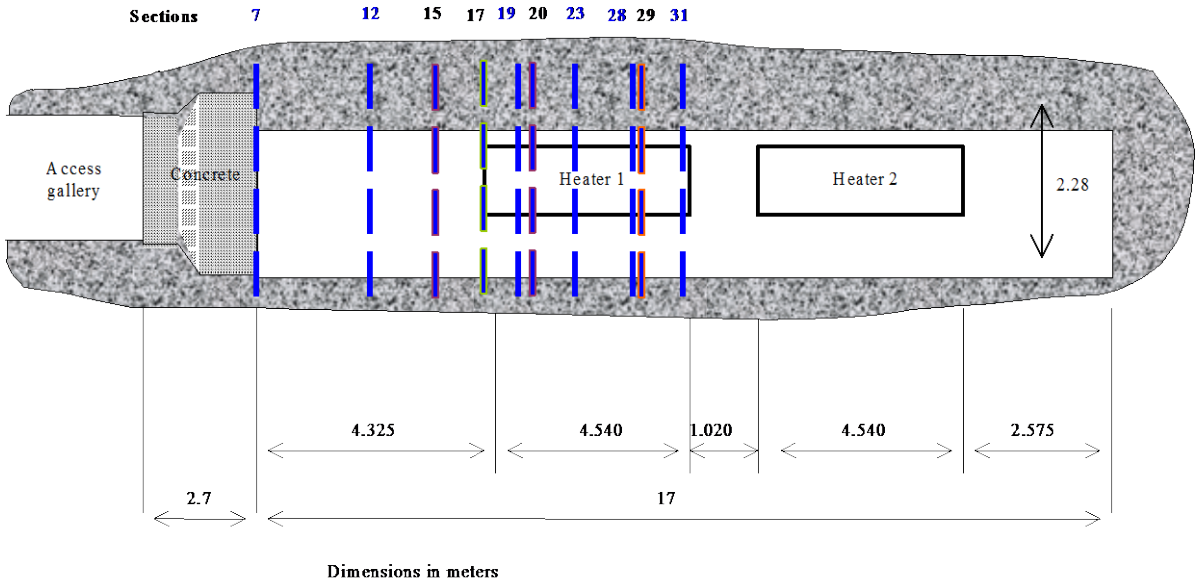

Figure 4.4. Layout of the sampling sections during the dismantling of heater 1 in 2002. In blue color are the common sections for THC and THM analyses (Fernandez and Rivas, 2003)

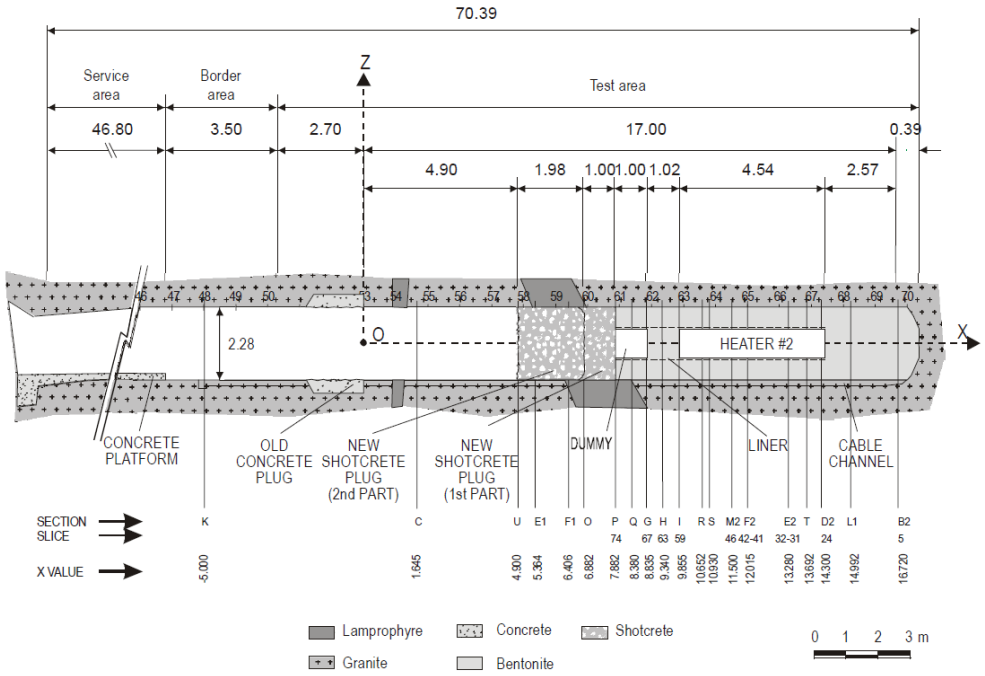

Figure 4.5. ***In situ*** **test configuration following dismantling of heater 1 (Huertas et al., 2005)**

After the dismantling of heater #1, the tunnel was plugged with shotcrete (Figure 4.5) and heater #2 was kept working under normal conditions to maintain a constant 100 ^{o}C at the steel liner/bentonite interface. In 2014, considering that changes in the state of bentonite buffer was very slow and it was unlikely for bentonite to reach fully saturation in the project lifetime, the decision was made to turn off and dismantle heater #2. The objective of the second dismantling operation, carried out throughout 2015, was to dismantle all the remaining parts of the *in situ* test, including heater #2. This operation included carrying out a complete sampling of the bentonite, rock, relevant interfaces, sensors, metallic components and tracers to allow the analysis of the barriers' condition after ~eighteen years of heating and natural hydration. On April 24, 2015, heater #2 was switched off. After a short cool off time period, dismantling was carried out from the shotcrete towards the bentonite section by sections (see Figure 4.6) and samples were taken for THMC and microbiological characterization. Details about the dismantling of heater #2 are given in Garcia-Sineriz et al. (2016). Preliminary THM characterization revealed that the bentonite away from the heater is fully saturated (see Figure 4.7), but the bentonite at the vicinity of heater #2 has not been fully saturated yet — gravimetric water content is around 17-19% (see Figure 4.7) and water saturation is about 80% near the heater (see Figure 4.8).

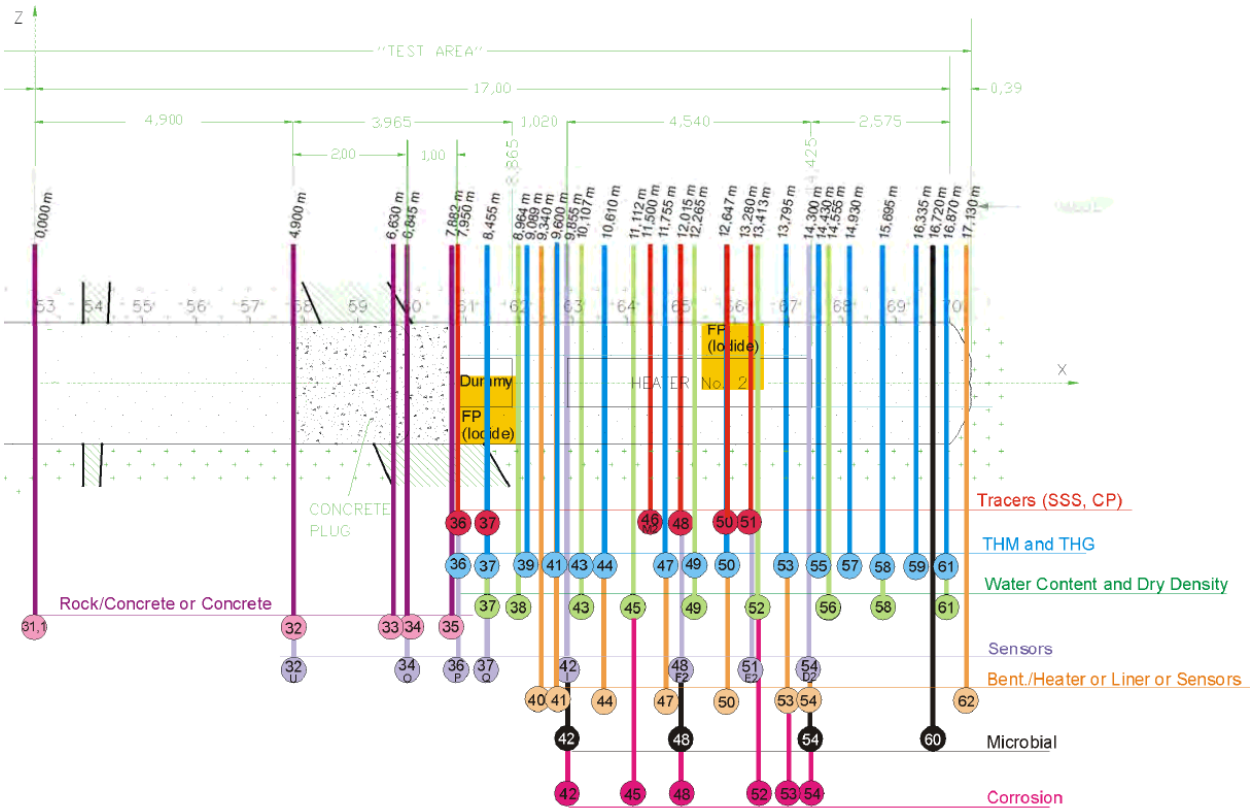

Figure 4.6. Section layout during the dismantling operation of heater #2 (Detzner and Kober, 2015)

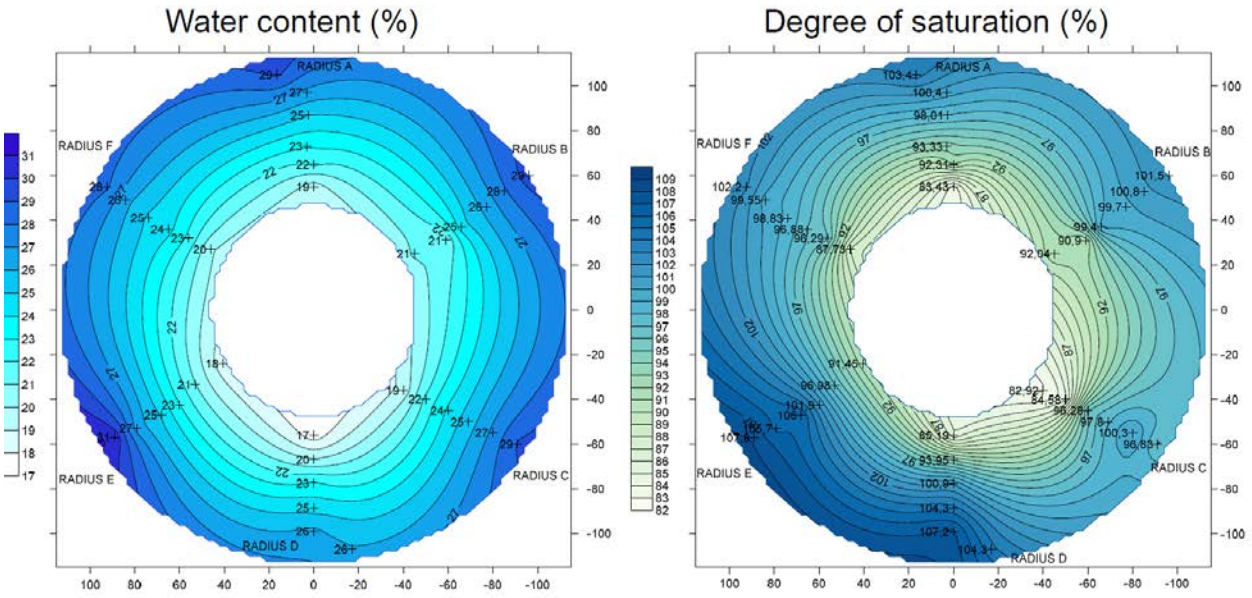

Figure 4.7. Spatial distribution of water content (left) and degree of saturation (right) at section 49 (see Figure 4.5 for the position of section 49) (Villar, weekly email communication).

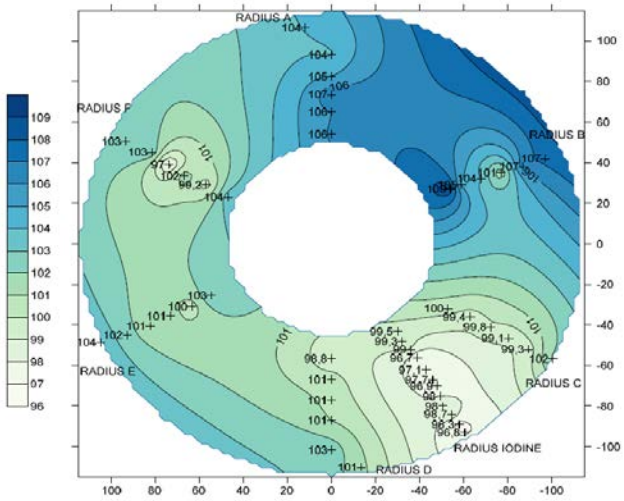

Figure 4.8. Spatial distribution of degree of saturation (right) at section 37 (see Figure 4.5 for the position of section 37) (Villar, weekly email communication).

The long-term FEBEX *in situ* test with comprehensive THMC data provides a unique opportunity to validate coupled THMC models and strengthen our understanding of coupled processes in bentonite. In addition, experiments at different scales with the same type of bentonite are also very useful to evaluate the key parameters obtained at different scales and study the scaling effect of modeling THMC processes. Up to now, several THM/THC models have been developed to interpret the FEBEX experiments, including the THM model for the mock-up test (Sánchez et al., 2005; 2012a) and *in situ* test (Sánchez et al., 2012b), and THC models for the small scale heating and hydration experiment (Zheng et al., 2010), mock-up test (Zheng and Samper, 2008), and *in situ* tests (Samper et al., 2008a; Zheng et al., 2011; Zheng et al., 2015b).

4.3 MODEL DEVELOPMENT

In FY15, the THC model was developed and tested against temperature, relative humidity and chemical data collected after the dismantling of heater #1. In FY16, the THMC model was developed based on the THC model by adding mechanical processes and compared with data collected during the dismantling of both heater #1 and heater #2.

4.3.1 Simulator

The numerical simulations are conducted with TOUGHREACT-FLAC3D, which sequentially couples the multiphase fluid flow and reactive transport simulator, TOUGHREACT (Xu et al., 2011), with the finite-difference geomechanical code FLAC3D (Itasca, 2009). The coupling of TOUGHREACT and FLAC was initially developed in Zheng et al. (2012) to provide the necessary numerical framework for modeling fully coupled THMC processes. It was equipped with a linear elastic swelling model (Zheng et al., 2012; Rutqvist et al., 2013) to account for swelling as a result of changes in saturation and pore-water composition and the abundance of swelling clay (Liu et al., 2013; Zheng et al., 2014). A recent addition to the code is the capability of simulating Non-Darcian flow (Zheng et al. 2015b) and thermal osmosis.

4.3.2 Modeling setup

As shown in Figure 4.7, the hydration of bentonite is fairly symmetrical, and radial symmetry has also been observed for heating (as shown later in Figures 4.11 to 4.15). We therefore use an axi-symmetrical mesh (Figure 4.9) to save computation time so that we can focus on the key coupling processes. However, such a model can only be used to interpret and predict the THMC behavior in the "hot sections", i.e. sections of bentonite block surrounding the heater including sections 41-54 (or more typically section 49) in Figure 4.6. 3-D models that have both "hot" and "cold" sections (such as sections 55-62 in Figure 4.6) could be developed in the future.

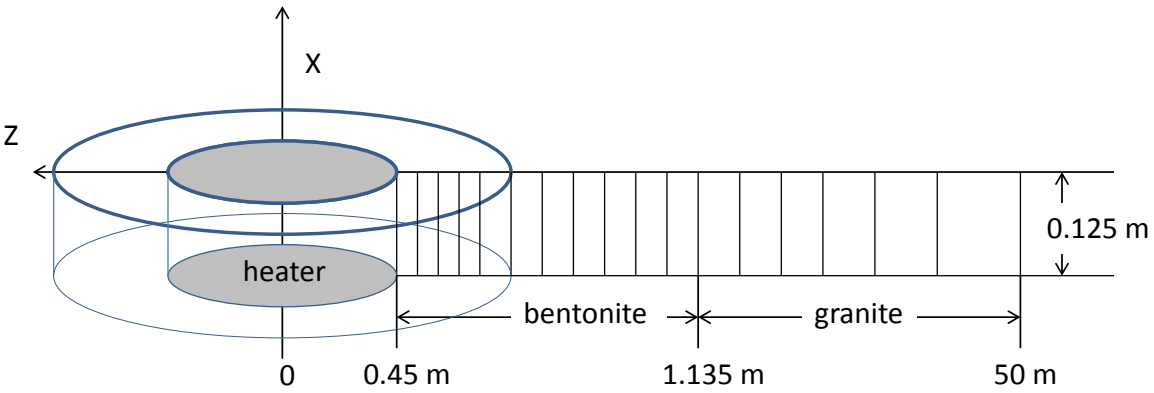

Figure 4.9. Mesh used for the model, not to the scale.

The model considers two material zones for the bentonite and granite. The first two nodes (1 and 2) are located on the external wall of the heater (r = 0.45-0.46 m). Bentonite is located within 0.45 m < r < 1.135 m. The remaining domain up to 50 m is used to simulate the granite. The simulation time starts on February 27, 1997 and ends on July 1, 2015, a total of 6,698 days (18.3 years).

The initial temperature is uniform and equal to 12 ºC. A constant temperature of 100 ºC is prescribed at the heater/bentonite interface (r = 0.45 m) while temperature is assumed to remain constant at its initial value of 12 ºC at the external boundary (r = 50 m) because the thermal perturbation induced by the heaters does not extend to this boundary.

The bentonite has initially a gravimetric water content of 14% which corresponds to a saturation degree of 55% and a suction of 1.11×10^5 kPa. The boundary conditions for flow include: 1) no flow at r = 0.45 m and 2) a prescribed liquid pressure of 7 bars at r = 50 m.

4.3.3 The TH model

The model considers non-isothermal two phase (air and water) flow, with each individual phase fluxes given by a multiphase version of Darcy's Law. For the vapor flow in the air phase, in addition to Darcy flow, mass transport can also occur by diffusion and dispersion according to Fick's law. Thermal behavior is relatively well understood because it is less affected by coupled processes in comparison with hydrological and chemical processes and the relevant parameters can be reliably measured. In current model, both conductive (Fourier's law) and convective heat flux are considered in the model and thermal conductivity is the key parameter. Figure 4.10 shows the measured thermal conductivity for FEBEX bentonite as a function of degree of water saturation.

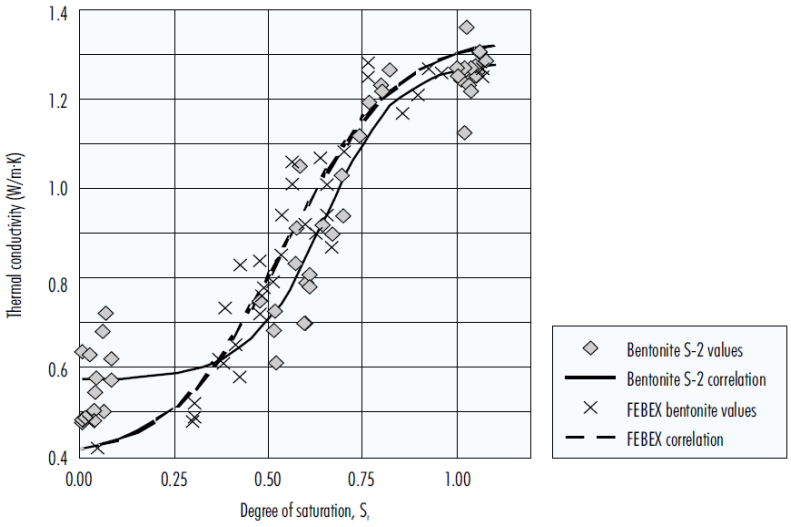

Figure 4.10. Thermal conductivity of FEBEX bentonite as a function of degree of saturation (ENRESA, 2000). Also shown is thermal conductivity for bentonite S-2 which has similar properties to FEBEX bentonite.

Because over the span of water saturation that FEBEX bentonite went through (from an initial degree of water saturation 55-59% to 100%), the thermal conductivity/water saturation relationship can sufficiently be represented by a linear relationship; we use a linear relationship implemented in TOUGH2 (Pruess et al., 1999):

$$K_{th} = K_{wet} + S_l(K_{wet} - K_{dry}) \qquad 4.1$$

where K_{wet} is the thermal conductivity under fully saturated conditions, K_{dry} is the thermal conductivity under dry conditions, and S_l is the liquid saturation degree. K_{wet} and K_{dry} are given in Table 4.1.

In previous modeling work (e.g. Sánchez et al., 2012b; Zheng and Samper, 2008), significant effort has been invested to find out why the hydration of FEBEX bentonite is slower than predicted by the typical Darcy flow model. Several processes have been proposed to explain the discrepancy between measured data and predictions by the Darcy flow model. These include the permeability decrease due to the dual-structural behavior of bentonite (Sánchez et al., 2005, 2012b), thermal osmosis, in which a moisture flux induced by the thermal gradient in the bentonite is in the opposite direction of water infiltration from the granite (Zheng et al., 2011), and permeability decrease due to swelling (Zheng and Samper, 2008), and Non-Darcian flow (Liu and Birkholzer, 2012).

In Zheng et al. (2015b), a TH model with Non-Darcian flow was developed and the threshold gradient, the key parameter for Non-Darcian flow, was calibrated based on a small scale column test for FEBEX bentonite. However, including Non-Darcian flow into the TH model led to a significant underestimation of the relative humidity data in the entire bentonite barrier (even in bentonite near the bentonite/granite interface). Although the relevance of Non-Darcian behaviour is clear for saturated flow in clay rock (Liu and Birkholzer, 2012 and references cited therein), Zheng et al. (2015b) showed two issues that prevented us from clearly delineating the contribution of Non-Darcian flow to water flow in unsaturated clay or bentonite. First and foremost, the calibration of the relative permeability and retention curves overshadows the effect of Non-Darcian flow. The non-linear relationship between water flux and hydraulic gradient, which motivates the relevance of Non-Darcian behavior to water flow, is already

accounted for, at least partially, by the relative permeability (which in turn is a function of the retention curve) in the flux-gradient relationship for unsaturated flow. However, in most modelling exercises, relative permeability is calibrated based on a Darcy-type flow. As a result, the calibration of the parameters associated with relative permeability overshadows the contribution of Non-Darcian flow— the parameters for relative permeability might be "over-calibrated" so that the effect of Non-Darcian flow looks irrelevant. For FEBEX bentonite, the relative permeability and retention curve were calibrated based on a Darcy type of flow model (ENRESA, 2000), which essentially obviates Non-Darcian flow for unsaturated bentonite. Thus, if Darcian flow is added on top of relative permeability that is calibrated based on Darcy flow, we double count the non-linearity between flux and gradient, and consequently the model significantly underestimates the water inflow from granite to bentonite. Second, Cui et al. (2008) reported that threshold gradients are different for different capillary pressure. Further research is needed to take into account the effect of capillary pressure when a threshold gradient is calculated. However, even though we can improve our threshold gradient calculation by taking into account capillary pressure, it is unlikely to eliminate the aforementioned issue of process uncertainties versus parameter uncertainties. Based on the findings from Zheng et al. (2015b) in the models presented in this report, Non-Darcian flow was not considered.

The key parameters affecting the hydration of bentonite are the permeability of granite, the relative permeability and retention curves of bentonite, the vapor diffusion coefficient and permeability of bentonite. In Zheng et al. (2015b), the most plausible values for these parameters were discussed and illustrated with sensitivity analyses and listed in Table 4.1.

Granite is a fractured medium and should ideally be represented by fractures and matrix. Just as previous models for *in situ* tests (Samper et al., 2008a; Sánchez et al., 2012b), current model also assumes granite is a homogeneous porous medium, which requires us to use an equivalent permeability. Based on the total water flow at the entire test zone (17.4 m, see Figure 4.3) (ENRESA, 2000), the permeability of granite is around 5×10^{-18} to 8×10^{-18} m^2. ENRESA (2000) also reports that the most frequent permeability is 1×10^{-18} but deems it is more representative of rock matrix. Zheng et al. (2011) used 8×10^{-18} m^2, Kuhlman and Gaus (2014) estimated a permeability of 6.8×10^{-19} m^2, and Sanchez et al. (2012b) used a surprisingly small value, 8.18×10^{-21} m^2. Based on the published values, it seems that permeability between 7×10^{-19} to 8×10^{-18} m^2 is plausible. Based on the evaluation in Zheng et al. (2015b), a permeability of 2×10^{-18} m^2 is used (Table 4.1).

The capillary pressure (retention curve) is calculated by van Genuchten function as:

$$P_{cap} = -\frac{1}{\alpha}\left(\left[S^*\right]^{-1/m} - 1\right)^{1-m} \qquad 4.2$$

where P_{cap} is the capillary pressure (Pa), $S^* = (S_l - S_{lr})/(1 - S_{lr})$ and S_l is the water saturation, S_{lr} is the residual water saturation. S_{lr} is 0.1 for bentonite and 0.01 for granite. The values of α and m are given in Table 4.1. The retention curve was fairly well studied for FEBEX bentonite. For example, ENRESA (2000) presented the retention curve for both drying and wetting path and van Genuchten function (van Genuchten, 1980) were derived with a m ranging from 0.3 to 0.6. Kuhlman and Gaus (2014) estimated an m of 0.3 and Zheng et al. (2011) and Sánchez et al. (2012b) use an m of 0.18, which is slightly lower.

The effective permeability of bentonite has been under scrutiny by modelers (e.g. Zheng et al., 2011) due to its critical role in determining the hydration of bentonite. It is the product of intrinsic permeability (k) (or saturated permeability, absolute permeability) and relative permeability (k_r). Relative permeability using $k_r=S_l^3$ (where S_l is water saturation degree) has been consistently used by different models (Zheng et

al., 2011; Sánchez et al., 2012b; Kuhlman and Gaus, 2014) and we use the same function here. The plausible saturated permeability for FEBEX bentonite in the initial state could be in a range from 1×10^{-21} to 9×10^{-21} m^2 based on various sources (Zheng et al., 2011; Sánchez et al., 2012b; Kuhlman and Gaus, 2014; Chen et al., (2009) and we use 2.15×10^{-21} m^2 in the model. However, as demonstrated by Zheng et al. (2015b), a constant intrinsic permeability for bentonite could not explain the relative humidity data in the entire thickness of the bentonite barrier. In the next section, we will discuss the change of permeability as a result of mechanical changes in bentonite.

Table 4.2. Thermal and hydrodynamic parameters.

Parameter	Granite	Bentonite
Grain density [kg/m^3]	2700	2780
Porosity ϕ	0.01	0.41
Saturated permeability [m^2]	2.0×10^{-18}	2.15×10^{-21}
Relative permeability, k_{rl}	$k_{rl} = S$	$k_{rl} = S^3$
Van Genuchten $1/\alpha$ [1/Pa]	4.76×10^{-4}	1.1×10^{-8}
Van Genuchten m	0.7	0.45
Compressibility, β [1/Pa]	3.2×10^{-9}	5.0×10^{-8}
Thermal expansion coeff. [1/^{o}C]	1.0×10^{-5}	1.5×10^{-4}
Dry specific heat [J/kg-^{o}C]	793	1091
Thermal conductivity [W/m-^{o}C] dry/wet	3.2/3.3	0.47/1.15
Effective vapor diffusion coefficient (m^2/s)	1.03×10^{-4}	1.03×10^{-4}

4.3.4 Mechanical Model

In current models, we tested two mechanical models for bentonite: a linear swelling model and dual structure Barcelona expansive clay model (BExM).

4.3.4.1 Linear swelling model

The linear swelling models have been used in the generic model evaluation of bentonite barrier in Zheng et al. (2015a; b). The advantage of this method is its simplicity and easy calibration of key parameters, but the disadvantage is that it does not describe correctly the transient of state of swelling. For nonisothermal behavior of unsaturated soils, we may partition the total incremental strain into elastic (ε^e), plastic (ε^p), suction (ε^s), thermal strains (ε^T) and chemical strains (ε^c) (Zheng et al., 2015b):

$$d\varepsilon = d\varepsilon^e + d\varepsilon^p + d\varepsilon^s + d\varepsilon^T + d\varepsilon^c \quad 4.3$$

where the suction strain represents the strain associated with changes in suction and chemical strain represents the strains associated with change in chemical conditions, including changes in ion concentration and abundance of swelling clays.

A linear elastic swelling model essentially defines the suction stress as a function of water saturation:

$$d\varepsilon^s = \beta_{sw} dS_l \tag{4.4}$$

where S_l is the water saturation and β_{sw} is a moisture swelling coefficient.

Under mechanically constrained conditions and considering the linear relationship between swelling stress and suction strain, $d\sigma_s = 3Kd\varepsilon^s$, we have a swelling stress that is linearly proportional to the saturation:

$$d\sigma_s = 3K\beta_{sw} dS_l \tag{4.5}$$

where K is the bulk modulus. Equation (4.5) is what was used for EBS bentonite in Rutqvist et al. (2011). In this report, β_{sw} is 0.238, calibrated based using the swelling pressure of 5 MPa for FEBEX bentonite under full saturation. The swelling pressure for FEBEX bentonite ranges from 4.5 MPa (Castellanos et al., 2008) to 7 MPa (ENRESA, 2000).

The porosity change in bentonite is given by the following state-surface expression (Lloret and Alonso, 1995):

$$e = A + B\ln\sigma' + C\ln(\psi + p^a) + D\ln\sigma'\ln(\psi + p^a) \tag{4.6}$$

where e is the void ratio, which is equal to the volume of voids divided by the volume of the solids; p^a is the atmospheric pressure (Pa), σ' is the mean effective stress (Pa); ψ is the suction (Pa), and A, B, C and D are empirical constants which for the FEBEX compacted bentonite are equal to A = 0.91, B = -0.0552, C = - 0.0606413 and D = 0.00479977.

The stress-dependence of permeability for low-permeability sedimentary rock is fairly well known and has been studied extensively (e.g. Ghabezloo et al., 2009; Kwon et al., 2001). Many empirical relationships have been put forward to describe the permeability changes with effective stress. One of them is the exponential law (David et al., 1994), which is used in the current model:

$$k = k_0 \exp[-\gamma(\sigma - \sigma_0)] \tag{4.7}$$

where k is the permeability at the effective stress σ, k_0 is the permeability at initial stress σ_0 and is equal to 2.15E-21 m^2; γ is the stress sensitivity coefficient and equal to 1E-7 Pa^{-1} in the current model based on the calibration against THM data.

4.3.4.2 Dual structure Barcelona expansive clay model (BExM)

The dual structure Barcelona Expansive Clay model (BExM) (Alonso et al., 1999; Sánchez et al., 2005) provide a more mechanistic way to describe the mechanical behavior of bentonite and have been used to

simulate the FEBEX mockup test (Sánchez et al., 2012a) and *in situ* test (Sánchez et al., 2012b). The dual structure BExM was also implemented in TOUGHREACT-FLAC3D and used in the report to simulate the mechanical behavior of the FEBEX *in situ* test.

In the dual structure model, the macrostructure is modeled with a constitutive model for unsaturated soils, such as the Barcelona Basic Model (BBM). The microstructure is incorporated to extend BBM to a dual structure model, which enables simulating the behavior of expansive soils, such as the dependency of swelling strains and swelling pressures on the initial stress state and on the stress path, strain accumulation upon suction cycles and secondary swelling. Thus, in the dual structure model, the total volume (V), the total void ratio (e), and porosity (ϕ) of the material are divided into a micro-structural part and a macro-structural part. The micro-structure can swell to invade the macro-porosity, depending on the mechanical confinement and load level. This is relevant when considering permeability changes during the soil swelling, because fluid flow takes place mostly through the macro-porosity, which is not proportional to the total strain and deformation of the expansive soil. Equations to describe the mechanical behavior of micro-structural and macro-structural levels and the interaction between structural levels are given in Section 2.

The parameters of BExM utilized for these studies are summarized in Table 4.2. The set of parameters are calibrated based on compacted bentonite by Lloret et al. (2003), and are used in the numerical analysis for the Mock-up test by Sanchez et al. (2012a). In Lloret et al. (2003), the simulation is one-dimensional, which can be treated as an isotropic case in 3D. However, the lateral displacements are constrained in oedometer test but the vertical loading is controlled by stresses. Thus, the stress status in oedometer test is anisotropic and the assumption of isotropy is not appropriate for this test. In Sanchez et al. (2012a), between numerical results and observed behavior during experiments are in agreement, the macro-structural bulk modulus of bentonite can reach as high as 2 GPa. Based on the report by Rutqvist and Tsang (2002), the bulk modulus of FEBEX bentonite should be in the order of 10 ─ 100 MPa. Therefore, the bulk modulus values evolve too high during the simulation of Sanchez et al. (2012a). Here we determine the parameters related to macro-structural bulk modulus, κ, which gives reasonable bulk modulus (in the order of 10 MPa~1000 MPa), from the observed results during experiment. In order not to affect the hydraulic effects on macro-structures, we increase the value of the parameter κ_s to keep the same ratio of $\frac{\kappa}{\kappa_s}$ as Lloret et al. (2003) and Sanchez et al. (2012) used in their simulations.

Table 4.3. Parameters used for combination of loading paths tests (Lloret et al., 2003; Sánchez et al., 2012).

Parameters defining the Barcelona basic model for macrostructural behavior						
$\kappa = 0.018$	$\kappa_s = 0.0036$	$\lambda(0) = 0.08$	$p_c = 0.5$ MPa	$r = 0.90$	$\zeta = 1$ MPa^{-1}	$p_0^* = 6.5$ MPa
$\alpha_a = 1$	$\alpha_0 = 1 \times 10^{-5}$°C^{-1}					
Parameters defining the law for microstructural behavior						
$\alpha_m = 0.021$ MPa^{-1}	$\beta_m = 2.3 \times 10^{-3}$ MPa^{-1}	$\chi = 1$				
Interaction functions						
$f_c = 1 + 0.9 \tanh\left[20\left(\frac{p_r}{p_0} - 0.25\right)\right]$		$f_s = 0.8 - 1.1 \tanh\left[20\left(\frac{p_r}{p_0} - 0.25\right)\right]$				
$e_{macro} = 0.21$		$e_{micro} = 0.48$				

Note that the parameters (κ and κ_s) related to macro-structural bulk modulus are higher than original ones used in (Lloret et al., 2003; Sánchez et al., 2012a). All other parameters are set to zero.

4.3.5 Chemical Model

The establishment of the chemical model requires first the knowledge of initial chemical conditions in bentonite and granite, i.e., the initial mineralogical and pore water compositions. Extensive mineralogical

characterization had been conducted by ENRESA (2000) and Fernández et al. (2004). Ramírez et al. (2002) also reported the mineralogical composition of FEBEX bentonite, which is slightly different from that reported by ENRESA (2000). In this report, we take the average of mass fraction reported in ENRESA (2000), Fernández et al. (2004) and Ramírez et al. (2002) and transformed the mass fraction to volume fraction (ratio of the volume for a mineral to the total volume of medium) using a porosity of 0.41 (see Table 4.3). Note the minerals that have zero volume fractions are the secondary minerals that could be formed. Detailed mineralogical composition of granite has not been found in current literature search, probably because the chemical conditions in granite are not supposed to be actively changed by repository conditions. Previous THC models for the *in situ* test (Samper et al., 2008a; Zheng et al., 2011) only include quartz in the minerals assemblage in granite. Siitari-Kauppi et al. (2007) reported that Grimsel granite is composed of quartz, K-feldspar, plagioclase and a small amount of "dark material". In the current model, we consider quartz, K-feldspar, plagioclase in granite with their volume fractions listed in Table 4.3.

Table 4.4. Mineral volume fraction (dimensionless, ratio of the volume for a mineral to the total volume of medium) FEBEX bentonite (ENRESA, 2000; Fernández et al., 2004; Ramírez et al., 2002) and granite (Zheng et al., 2011).

Mineral	**FEBEX Bentonite**	**Granite**
Calcite	0.00472	0
Smectite	0.546	0.
Chlorite	0.0024	0
Quartz	0.012	0.37
K-Feldspar	0.0059	0.35
Plagioclase	0	0.27
Dolomite	0.0	0
Illite	0.0	0
Kaolinite	0.0	0
Siderite	0.0	0
Ankerite	0.0	0

FEBEX bentonite blocks have an initial gravimetric water content of 13.5–14% (ENRESA 2000). As described in Bradbury and Baeyens (2003), obtaining the pore-water chemistry of compacted bentonite with such low water content is difficult. Because the concentration of ions for the initial state of compacted bentonite cannot be measured directly, indirect measurement methods must be used. Squeezing and aqueous extract are the most commonly used methods. Squeezing is a straightforward method — pore-water is squeezed out and concentrations are measured. However, pore water cannot be extracted by squeezing from clay samples with gravimetric water contents less than 20% (Fernández et al. 2001, 2004), which means that squeezing cannot be done for FEBEX bentonite blocks. In an aqueous extract test, a crushed sample is placed in contact with water at a low solid/liquid ratio (ranging from 1:16 to 1:1). After establishing equilibrium, the solid phase is separated and the liquid phase is analyzed (Fernández et al., 2001). Geochemical modeling was needed to retrieve the aqueous ion concentrations at low water content (Zheng et al., 2008). Therefore, any uncertainties associated with the geochemical models affect the evaluation of initial aqueous concentration levels at low water content (the water content at the initial state). The model presented in this report uses the pore water composition (see Table 4.4) inferred by Fernández et al. (2001) from aqueous extract data. The pore water composition for granite (Table 4.4) is taken from Zheng et al. (2011).

Table 4.5. Pore-water composition (mol/kg water except for pH) of FEBEX bentonite (Fernández et al., 2001) and granite (Zheng et al., 2011).

	EBS Bentonite: FEBEX	Granite
pH	7.72	8.35
Cl	1.60E-01	1.31E-05
SO_4^{-2}	3.20E-02	7.86E-05
HCO_3^-	4.1E-04	3.97E-04
Ca^{+2}	2.2E-02	1.81E-04
Mg^{+2}	2.3E-02	1.32E-06
Na^+	1.3E-01	3.76E-04
K^+	1.7E-03	7.80E-06
Fe^{+2}	2.06E-08	2.06E-08
SiO_2(aq)	1.1E-04	6.07E-04
AlO_2^-	1.91E-09	3.89E-08

In the chemical model, we consider aqueous complexation, cation exchange, surface complexation and mineral dissolution/precipitation. Aqueous complexes and their disassociation constants for reactions that are written in terms of the primary species in Table 4.4 are listed in Table 4.5. These thermodynamic data were taken from Data0.dat.YMPv4.0, an EQ3/6 (Wolery, 1993) database qualified by the U.S. Department of Energy for the Yucca Mountain project. Surface protonation reactions are given in Table 4.6 and cation exchange reactions are given in Table 4.7.

Table 4.6. Aqueous complexes and their dissociation constants

Species	Log K (25°C)	Species	Log K (25°C)
OH^-	13.99	$MgHCO_3^+$	-1.03
Al^{+3}	-22.88	CO_2(aq)	-6.34
$HAlO_2$(aq)	-6.45	CO_3^{-2}	10.33
$NaAlO_2$(aq)	0.75	$CaCO_3$(aq)	7.01
$AlOH^{+2}$	-17.87	KCl(aq)	1.50
$Al(OH)_2^+$	-12.78	$MgCl^+$	0.14
$Al(OH)_3$(aq)	-6.72	$MgSO_4$(aq)	-2.38
$CaCl^+$	0.70	$NaSO_4^-$	-0.81
$CaCl_2$(aq)	0.65	KSO_4^-	-0.88
$CaSO_4$(aq)	-2.10	$NaHSiO_3$(aq)	8.30
NaCl(aq)	0.78	$CaOH^+$	12.85
$FeCl^+$	0.17	NaOH(aq)	14.15
$FeHCO_3^+$	-2.04	$NaCO_3^-$	9.82
$FeCO_3$(aq)	4.88	$NaHCO_3$(aq)	-0.17
$FeCl_4^{-2}$	1.94	$CaHCO_3^+$	-1.04

Table 4.7. Surface protonation reactions on montmorillonite (Bradbury and Baeyens, 2005)

Surface complexation	Log K
mon_sOH_2^+ = mon _sOH + H^+	-4.5
mon_sO^- + H^+ = mon _sOH	7.9
mon_$w1OH_2^+$ = mon_w1OH + H^+	-4.5
mon_$w1O^-$ + H^+ = mon_w1OH	7.9
mon_$w2OH_2^+$ = mon_w2OH + H^+	-6
mon_$w2O^-$ + H^+ = mon_w2OH	10.5

Table 4.8. Cation exchange reactions on montmorillonite and illite (Bradbury and Baeyens, 2005)

Cation exchange reaction	$K_{Na/M}$
Na^+ + mon-H = mon -Na + H^+	1
Na^+ + mon -K = mon -Na + K^+	0.0775
Na^+ + 0.5 mon -Ca = mon -Na + 0.5Ca^{+2}	0.302
Na^+ + 0.5 mon -Mg = mon -Na + 0.5Mg^{+2}	0.302

Table 4.9.Equilibrium constants for mineral precipitation/dissolution

Primary Mineral	log(*K*)	Secondary Mineral	log(*K*)
Calcite	1.85	Siderite	1.543
Smectite-Na	-34.62	Dolomite	2.524
Quartz	-3.75	Ankerite	-1.035
K-feldspar	-22.91	Illite	-47.33
Albite	-20.133	Chlorite	4.298
Anorthite	-19.19	Kaolinite	-39.9

The equilibrium constants for precipitation/dissolution of primary minerals (minerals that are present initially) and secondary minerals are listed in Table 3.8. Note that plagioclase is a solid solution with albite and anorthite as its end members. In the current model, we assume plagioclase contains 10% anorthite and 90% albite so that there is quasi-equilibrium between pore water and plagioclase.

Mineral dissolution/precipitation is kinetically controlled. The kinetic law for mineral dissolution/precipitation is given in Xu et al. (2011). The kinetic rates and surface areas for the minerals considered in the model were taken mostly from Xu et al. (2006) (Table 4.9). However, the illitization rate (the rate of illite precipitation and smectite dissolution) was calibrated (Liu et al., 2013) based on the measured illite percentage in an illite/smectite (I/S) mixed layer from Kinnekulle bentonite, Sweden (Pusch and Madsen, 1995).

Table 4.10. Kinetic properties for minerals considered in the model (Xu et al., 2006).

Mineral	A (cm^2/g)	Parameters for Kinetic Rate Law							
		Neutral Mechanism		Acid Mechanism			Base Mechanism		
		k_{25} (mol/m^2-s)	E_a (kJ/mol)	k_{25} (mol/m^2-s)	E_a (kJ/mol)	$n(H^+)$	k_{25} (mol/m^2-s)	E_a (kJ/mol)	$n(H^+)$
Quartz	9.8	1.023×10^{-14}	87.7						
K-feldspar	9.8	3.89×10^{-13}	38	8.71×10^{-11}	51.7	0.5	6.31×10^{-12}	94.1	-0.823
Kaolinite	151.6	6.91×10^{-14}	22.2	4.89×10^{-12}	65.9	0.777	8.91×10^{-18}	17.9	-0.472
Illite	1.18×10^{4} (1)	1.66×10^{-13}	105 (2)						
Chlorite	9.8	3.02×10^{-13}	88	7.76×10^{-12}	88	0.5			
Calcite	3.5	1.63×10^{-7}	23.5						
Dolomite	12.9	2.52×10^{-12}	62.76	2.34×10^{-7}	43.54	1			
Ankerite	9.8	1.26×10^{-9}	62.76	6.46×10^{-4}	36.1	0.5			
Smectite - Na	1.18×10^{4} (1)	1.66×10^{-13}	105 (2)						

(1) Calibrated based on the field illitization data (Liu et al., 2013)
(2) From Pusch and Madsen (1995)

4.4 MODEL RESULTS

The ultimate goal of using coupled THMC model to interpret the data collected in the FEBEX *in situ* test is to understand the THMC evolution of bentonite under the repository condition so that we can use most plausible processes and parameters to describe the behavior of bentonite. Once the coupled THMC model that can simultaneously match the measured temperature, relative humidity, water content, stress, aqueous concentrations, and minerals phase change, we can further use it to predict the long term (e.g. one hundred thousand years as required by most performance assessment) under different conditions, such as under higher temperature as was done by Zheng et al. (2015a).

The THC model developed in FY15 (Zheng et al., 2015b) was expanded to include mechanical processes using both linear swelling model and dual structure BExM. In this section, we first present model results from THMC model using the linear swelling model (denoted in the following sections as THMC-LS) and then discuss the results from the model that uses the dual structure BExM (referred as THMC-BExM in the following sections).

4.4.1 THMC model using linear swelling model

4.4.1.1 THM data and model results

In the FEBEX *in situ* test, some data were collected real time by the sensors buried in the bentonite block such as temperature, relative humidity and stress; and some of them had to be measured in the laboratory using the bentonite sample that were taken after dismantling of test sections, including water content, dry density, concentration of ions in pore water and mineralogical composition. Table 4.10 list some key dates of the FEBEX *in situ* test to facilitate the discussion of the model results. The dismantling of heater

#1 in 2002 and heater #2 in 2015 provides two snapshots of measured water content, dry density, and concentrations of ions in pore water and mineralogical composition, which are very valuable for understanding the temporal evolution of these key data, as shown later in the report. Note that concentrations of ions in pore water and mineralogical composition have been analyzed by the other partner of FEBEX-DP project and are not available yet.

Table 4.11. Timeline of FEBEX in situ test.

Event	Date	Time (day)	Time (year)
Commencement of heating	2/27/1997	0	0.0
Shutdown of Heat #1	2/2/2002	1827	5.0
Sampling after heat #1 was dismantled	5/2/2002	1930	5.3
Shutdown of heat #2	4/24/2015	6630	18.2
Sampling after heat #2 was dismantled	7/3/2015	6700	18.3

Figures 4.11 through 4.14 compare the measured temperatures to two simulation results: a TH model and a THMC model with linear swelling (THMC-LS). Because the current model simulates only the "hot" sections that are normally located at the middle of the 4.5 m long heater, we used temperature measured at section F2 and E2 (see Figure 4.3) surrounding heater #2 to constrain the thermal calculation. Starting February 27, 1997, a constant power of 1200 W was applied to each heater for 20 days and then a constant power of 2000 W for another 33 days. After that, the system was switched to the constant temperature mode, allowing the power to fluctuate freely, but the maximum temperature at the surface of steel liner of the heater was maintained at 100 ^{o}C. After the shutdown of heater #1 on February 2, 2002 (1827 days), the temperature field changed, as manifested by the temperature evolution after 1827 days in Figures 4.11 to 4.14. Unfortunately the thermal sensors at radial distances of 0.48 m and 1.09 m failed shortly after 1827 days, but the temperature data from some sensors at a radial distance of 0.8 m (Figure 4.12) and 1.05 m (Figure 4.13) show the decrease in temperature after the shutdown of heater #1. The model results match well with the temperature data at all the radial distances. Near the steel liner, e.g., radial distance of 0.48 m in Figure 4.11, the temperature is almost the same as at the surface of the steel liner, but it decreases noticeably at a radial distance of 1.09 m (very close to the bentonite/granite interface) after the shutdown of heater #1 (Figure 4.14). The current model is a 1-D axi-symmetrical model that is designed to simulate the conditions of "hot" sections. In order to account for the heat dissipation from "hot" sections to "cold" sections (located outside of the heater in X direction, such as sections B1 and B2 in Figure 4.3) , we used a semi-analytical solution implemented in TOUGH2 (Pruess et al., 1999) with an adjusted heat exchange surface area to match the temperature data. After 1827 days, the heat exchange surface area was adjusted again to match the data to mimic further heat loss from heater #2 when heater #1 was removed. In general, a fairly good match between the models and data was achieved.

The temperature profiles calculated by TH and THMC model differ only slightly at locations away from the heater. The reason is that thermal conductivity is a function of degree of water saturation and the TH and THMC models give different degrees of water saturation.

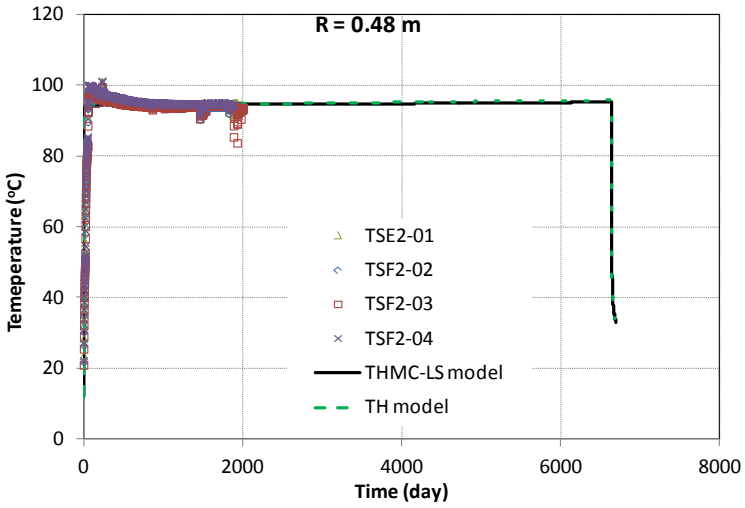

Figure 4.11. Measured temperature by sensors located at a radial distance of 0.48 m in sections E2 and F2 and model results from the TH model and THMC model with linear swelling (THMC-LS).

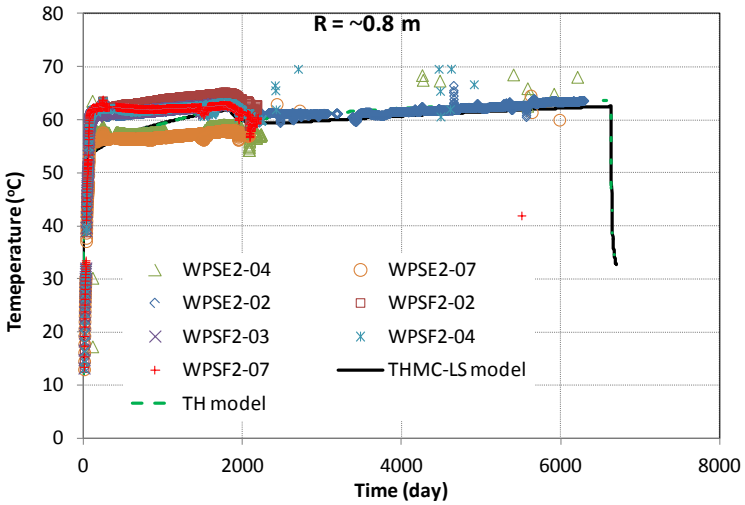

Figure 4.12. Measured temperature by sensors located at a radial distance of 0.8 m in sections E2 and F2 and model results from the TH model and THMC model with linear swelling (THMC-LS).

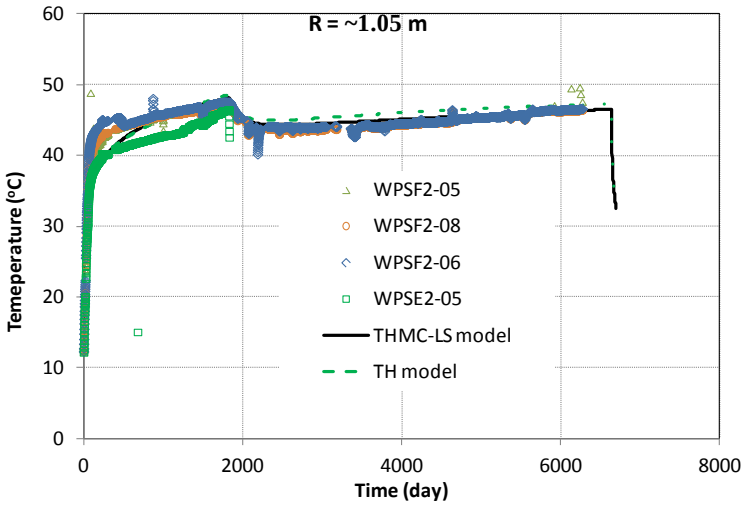

Figure 4.13. Measured temperature by sensors located at a radial distance of 1.05 m in sections E2 and F2 and model results from the TH model and THMC model with linear swelling (THMC-LS).

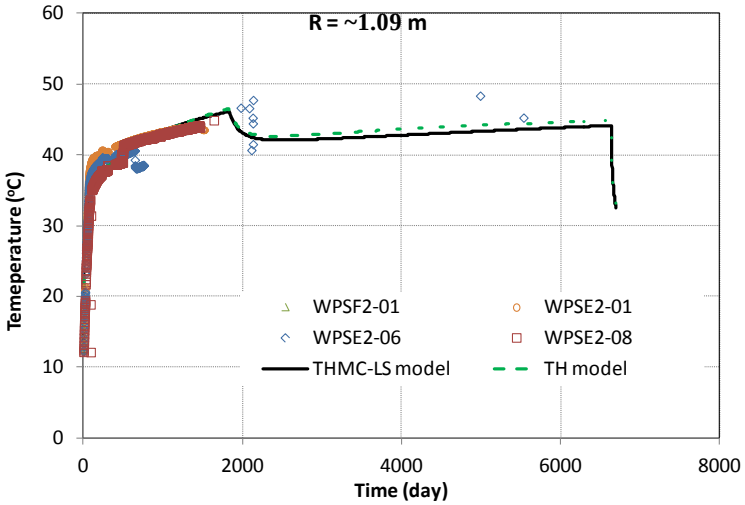

Figure 4.14. Measured temperature by sensors located at a radial distance of 1.09 m in sections E2 and F2 and model results from the base TH model.

Relative humidity, water content and dry density are three types of hydrological data that are available so far for comparing with model results. Water content and dry density were measured two times: one was after the dismantling of heater #1 (in 2002, 5.3 years after the start of heating) and the other was after the dismantling of heater #2 (in 2015, 18.3 years after the start of heating).

For the water content and dry density data, in this report we select data from sections 18, 28 and 29 (Zheng et al., 2011) (see Figure 4.4 for their locations) and sections 22 and 27 (Daucousse and Lloret, 2003) whose locations are given in Figure 4.15.

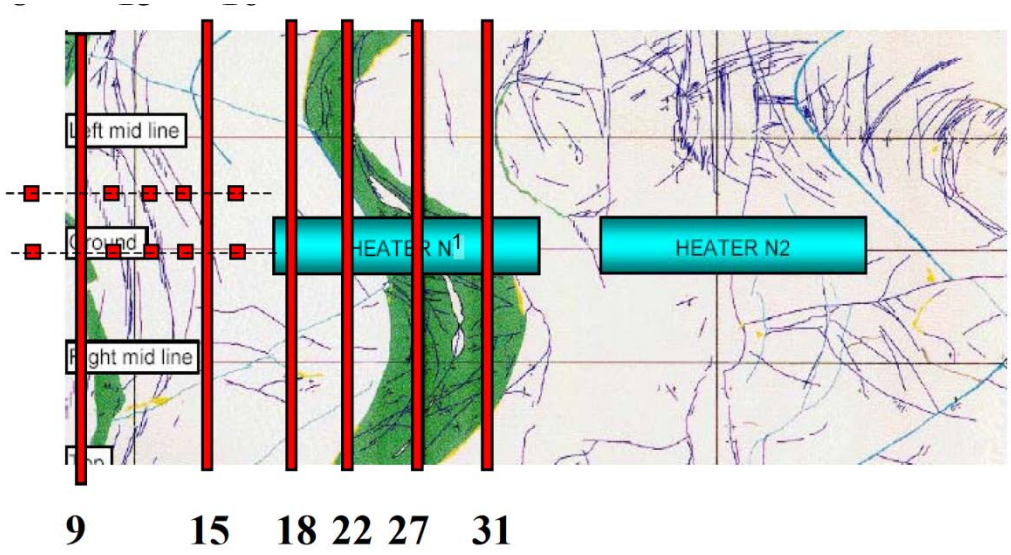

Figure 4.15. Layout of the sampling sections for water content and dry density measurement during the dismantling of heater #1 in 2002 (Daucousse and Lloret, 2003).

After about five years heating and hydration, bentonite near the heater remains fairly dry, with water contents close to the initial value, whereas bentonite near the granite become fully saturated and have water content ranging from 25% to 35% (Figure 4.16). The TH model with a constant porosity apparently fails to match the measured data at 5.3 years— model underestimates the water content data near the granite and overestimates the data in the middle of bentonite barrier. If the porosity is constant, the water content of fully saturated sample is 25%, higher measured water content near granite clearly indicates the swelling of bentonite upon hydration from the granite. The THMC model that accounts the swelling of bentonite and subsequent porosity and permeability clearly outperforms the TH model and matches reasonably well the data at 5.3 years. As the heating and hydration continues in the bentonite barrier surrounding heater #2, water contents near the heater kept increasing and reached about 18-19% at 18.3 years upon the dismantling of heater #2, but water contents near the granite (about 0.2 m from the bentonite/granite interface) at 18.3 years remained similar to that at 5.3 years because the bentonite had become fully saturated in early time and no more swelling is allowed in the confined gallery. Water content data at 18.3 years are nicely matched by the THMC model across the entire length of the bentonite barrier, but significantly overestimated by the TH model from a radial distance of 0.45 to 0.8 m and underestimated by the TH model from a radial distance of 0.8 m to the bentonite/granite interface.

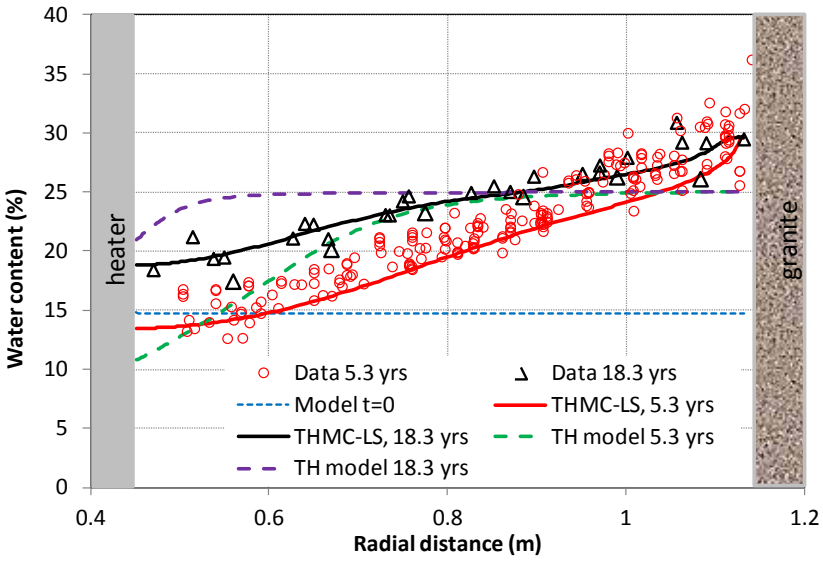

Figure 4.16. Measured water content data at sections 19, 28 and 29 (Zheng et al., 2011) and sections 22 and 27 (Daucousse and Lloret, 2003) after the dismantling of heater #1 ("data 5.3 yrs") and at section 49 after the dismantling of heater #2 ("data 18.3 yrs") and model results from the TH model (Zheng et al., 2015b), THMC model with linear swelling (THMC-LS).

The swelling of bentonite due to the hydration is clearly manifested by the measured dry density data. Initially the FEBEX bentonite blocks have a dry density of 1.7 g/cm^3. Considering the gaps between the bentonite blocks, the average dry density of the bentonite barrier shortly after the test started could be around 1.65 g/cm^3. After 5.3 and 18.3 years, the dry density ranges from 1.4-1.6 g/cm^3 near the granite, which indicate the swelling of bentonite. For bentonite near the heater, dry density is around 1.65-1.75 (Figure 4.17), indicating compression from the outer rings of the barrier. Model results show that the dry density at 5.3 years is higher than that at 18.3 years whereas measured data do not show any clear difference between 5.3 years and 18.3 years. As bentonite continues getting hydrated from granite and water content kept increasing from 5.3 years to 18.3 years, it is more conceivable that dry density decreases with time. One reason that measured dry densities at 5.3 and 18.3 years do not show clear difference might be measurement procedure. Dry density cannot be measured under *in situ* conditions in which the bentonite blocks were compressed by a confining stress of about 7-8 MPa. When samples were taken out of the gallery, they essentially underwent an unloading process which altered the volume of samples, i.e. the dry density measured in the laboratory does not necessary represent the *in situ* conditions anymore. The THMC model seems to match the dry density profile after 18.3 years pretty well (Figure 4.17).

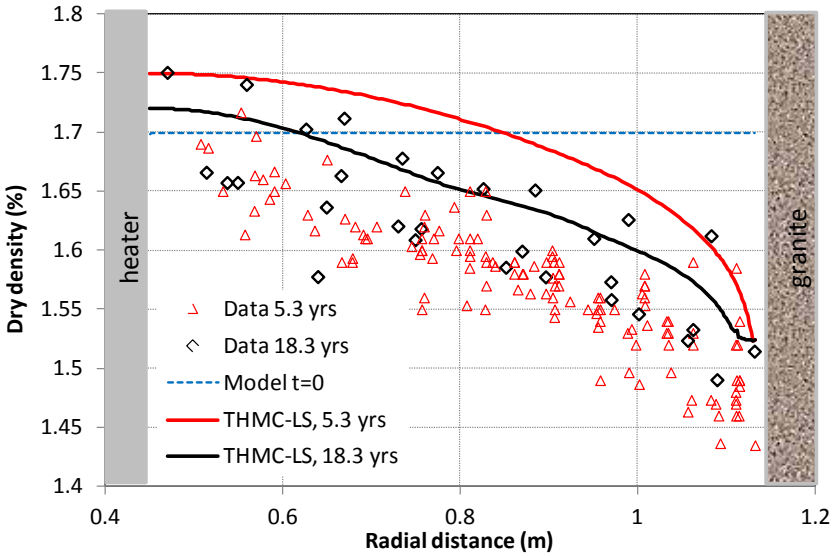

Figure 4.17. Measured dry density data at sections 22 and 27 (Daucousse and Lloret, 2003) after the dismantling of heater #1 ("data 5.3 yrs") and at section 49 after the dismantling of heater #2 ("data 18.3 yrs") and model results from THMC model with linear swelling (THMC-LS).

Assuming the solid phase in bentonite is not compressible, porosity can be calculated from dry density with a grain density of 2.78 g/cm^3, which are called 'inferred porosity data" in Figure 4.18. Model results show increase of porosity due to the swelling upon the continuous hydration of bentonite and match well the 'inferred porosity data" at 18.3 years (Figure 4.18). Similar to dry density data, porosity data do not show any difference between 5.3 years and 18.3 years. In Figures 4.17 and 4.18, the TH model with a constant porosity of 0.41 apparently cannot fit the measured dry density and porosity and is therefore not shown here.

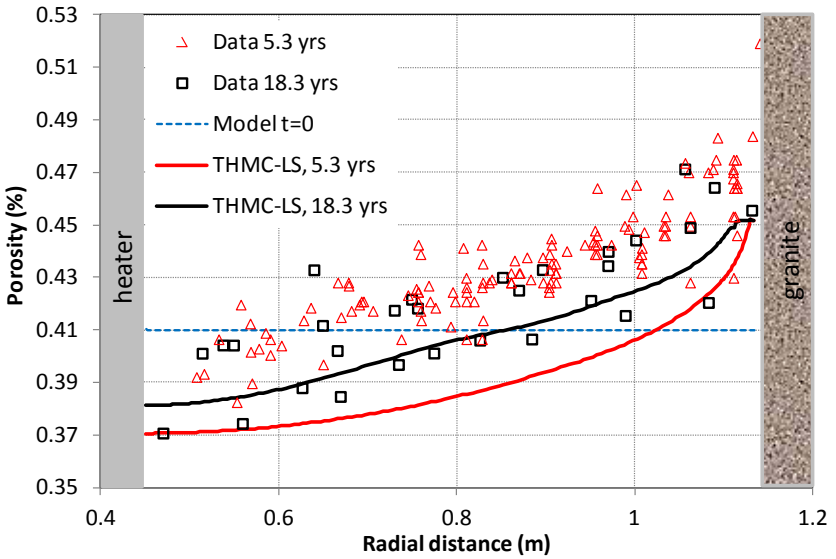

Figure 4.18. Inferred porosity data at sections 22 and 27 (Daucousse and Lloret, 2003) after the dismantling of heater #1 ("data 5.3 yrs") and at section 49 after the dismantling of heater #2 ("data 18.3 yrs") and model results from THMC model with linear swelling (THMC-LS).

Unlike water content and dry density, relative humidity data were measured real time by sensors at various positions in the bentonite. These data were grouped by the radial distance of the sensors. Previous modeling exercises (e.g. Zheng et al., 2011) showed that relative humidities near the heater have been overestimated and were the key data to test the models. Unfortunately, most sensors for relative humidities failed for the sections around heater #2, especially near the heater. For example, as shown in Figure 4.19, sensors at section E2 (WCSE2-03, WCSE2-04) at a radial distance of ~0.52 m only provide data until 147 days. We therefore have to rely on the relative humidity data measured at section E1 (located around heater #1) to constrain our model. A fairly good match between model results and relative humidity was achieved. The TH model overestimates the measured relative humidities after about 1000 days and seems not provide a correct trend of the evolution of relative humidity. A better fit between the model and data was obtained by the THMC model. In the THMC model, permeability decrease due to swelling is responsible for the lower calculated relative humidity near the heater. Another important parameter that controls the relative humidity is the vapor diffusion coefficient. In the base-case THMC model, the vapor diffusion coefficient is 1.03×10^{-4} m^2/s, which is about 5-10 fold larger than a typically measured value (e.g., LaManna and Kandlikar, 2011). In a sensitivity run based on the THMC-LS model, a vapor diffusion of 2×10^{-5} m^2/s is used and the model results significantly overestimate the data. It is not uncommon to use higher-than-normal vapor diffusion coefficient to interpret moisture movement in unsaturated medium under non-isothermal conditions, a phenomenon that was called enhanced vapor diffusion (Clifford and Webb, 1996).

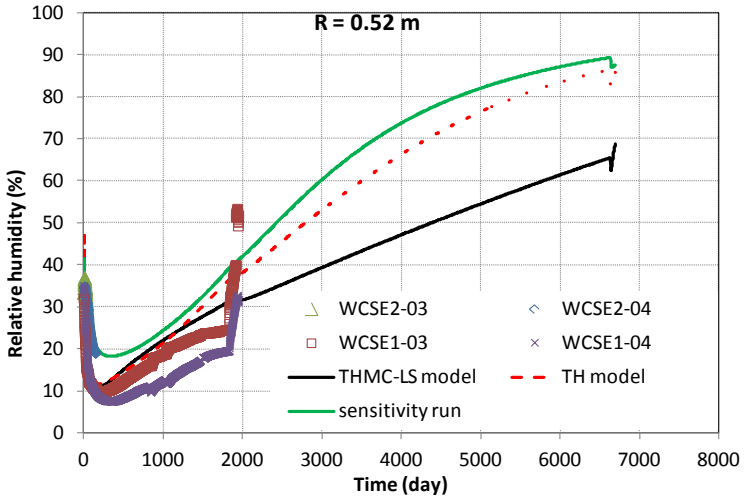

Figure 4.19. Measured relative humidity by sensors located at a radial distance of 0.52 m in sections E2 and E1 and model results from the TH model (Zheng et al., 2015b), THMC model with linear swelling (THMC-LS) and a sensitivity run that is based on THMC-LS but has a vapor diffusion coefficient that is 5 times lower.

Measured relative humidities in the middle of the bentonite barrier (radial distance of 0.8 m, Figure 4.20) and at the outer rings of the bentonite barrier (Figure 4.21 and 22) were adequately matched by both the TH and THMC-LS models. One interesting observation is that the THMC model, albeit having decreased permeability due to swelling at the outer ring area, shows rapid increase in relative humidity near the granite boundary, which actually matches the measured data better than the TH model.

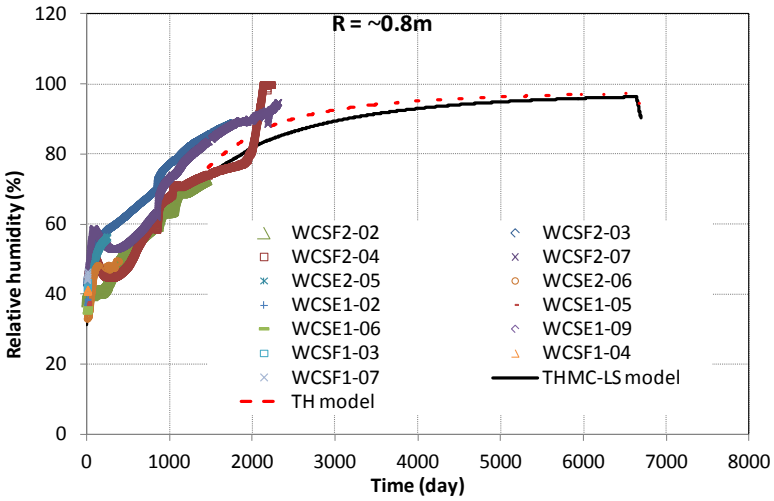

Figure 4.20. Measured relative humidity by sensors located at a radial distance of ~0.8 m in sections E1, E2, F1 and F2 and model results from the TH model (Zheng et al., 2015b) and THMC model with linear swelling (THMC-LS).

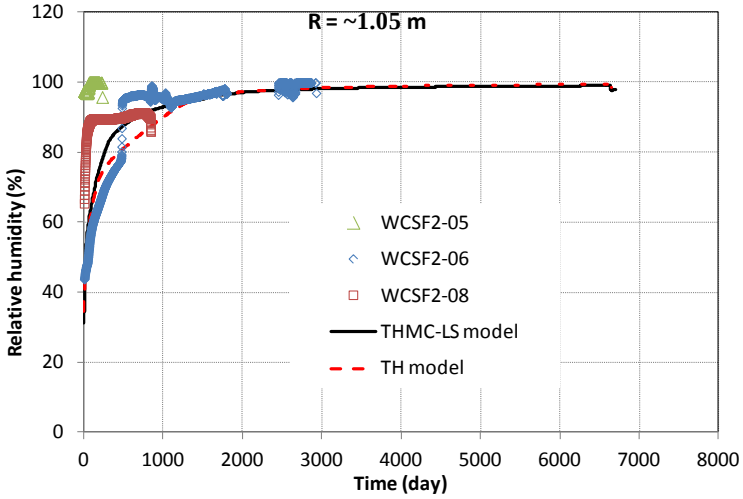

Figure 4.21. Measured relative humidity by sensors located at radial distance of ~1.05 m in section F2 and model results from the TH model (Zheng et al., 2015b) and THMC model with linear swelling (THMC-LS).

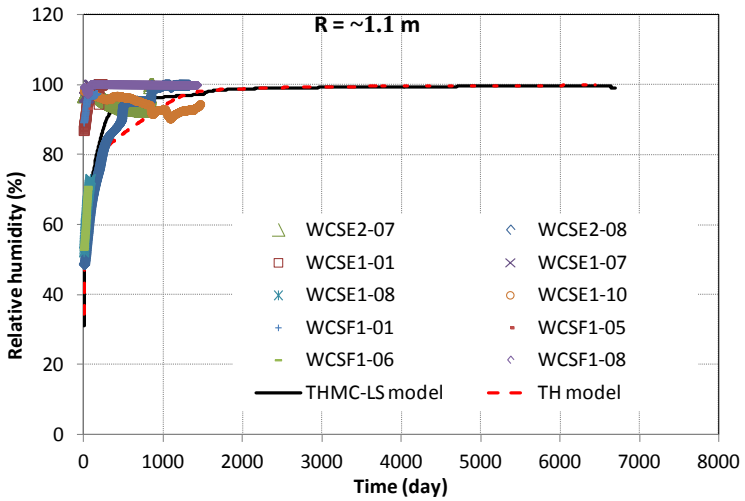

Figure 4.22. Measured relative humidity by sensors located at radial distance of ~1.1 m in sections E1, E2 and F1 and model results from the TH model (Zheng et al., 2015b) and THMC model with linear swelling (THMC-LS).

Sensors for measuring stress were also emplaced in the bentonite block. Although a majority of them stopped functioning, we still were able to extract data at two radial distances: one is 0.5 m, very near the heater and the other is 1.1 m, right at the bentonite/granite interface. No data were available for bentonite in the middle of the barrier. Figures 4.23 and 4.24 show the measured stress and model results. The total stresses in bentonite gradually increase as more water infiltrated into the bentonite. The swelling of bentonite creates a compressive force in the confined gallery, which eventually reaches a plateau as the bentonite barrier is close to being fully saturated, as shown clearly by the data and model result at radial distance of 1.1 m and to a lesser degree by the data at a radial distance of 0.5 m. It is expected that after the entire bentonite barrier becomes fully saturated, the stress field is fairly homogenous. The THMC model matches reasonably the data near the granite (Figure 4.24) but overestimates the data near the heater (Figure 4.23). However, it is noteworthy that the stress at a radial distance of 0.5 m might have similar uncertainties of measured stress at radial distance of 1.1 (see Figure 4.24).

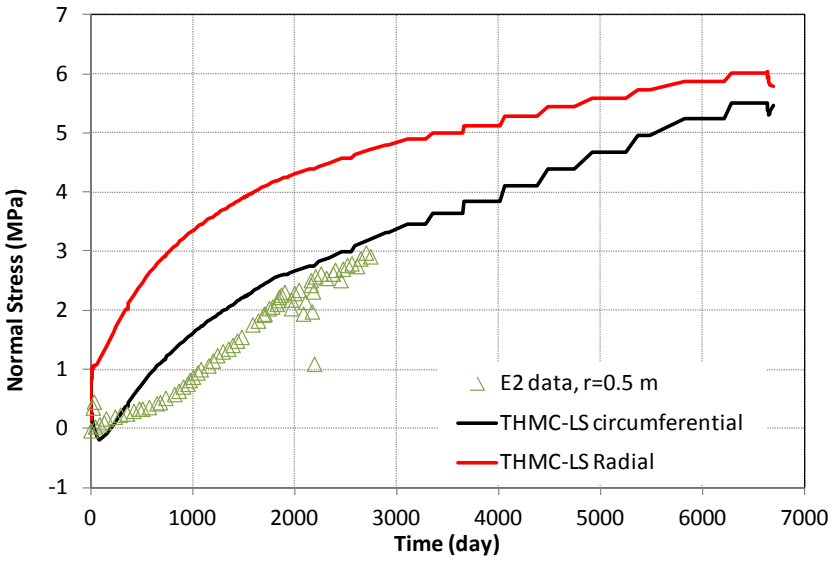

Figure 4.23. Measured stress by sensors located at a radial distance of ~0.5 m in section E2 and THMC model with linear swelling (THMC-LS).

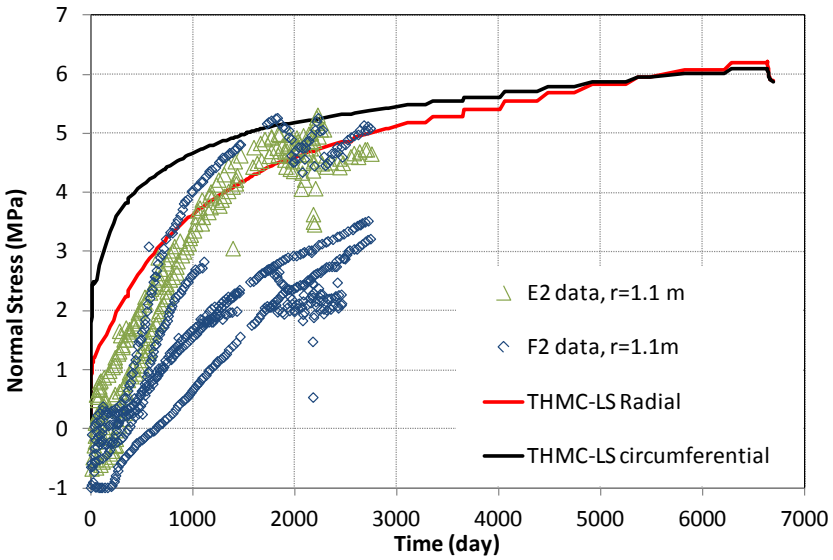

Figure 4.24. Measured stress by sensors located at radial distance of ~1.1 m in sections E2 and F2 and THMC model with linear swelling (THMC-LS).

4.4.1.2 Chemical data and model results

The two dismantling events in the FEBEX *in situ* test provide a unique opportunity to check the both the spatial and temporal evolution of the geochemistry in bentonite.

After the dismantling of heater #1 in 2002, samples were taken along several radii in each section (Zheng et al., 2011). Bentonite samples were taken for THC analyses from three sections surrounding the heater #1: 19, 28, and 29 (see Figure 4.4 for their locations). Each sampling section consists of an outer, central and inner layer of bentonite blocks. Bentonite blocks were preserved immediately after their extraction in plastic films, with two layers of aluminized PET sheets and vacuum-sealed plastic bags. Protection

against mechanical damage was used to ensure the integrity of the material (ENRESA, 2006a). Aqueous extract tests (AET) were used to obtain pore water chemistry for compacted FEBEX bentonite. AET is a method to quantify the total content of soluble salts of a clay sample. A *1:R* AET consists on adding to a mass M_s of powdered clay sample a mass of distilled water equal to R times M_s. The clay sample and water are stirred during a period of time, usually 2 days, during which water and clay are allowed to equilibrate. Chemical analyses are performed on the supernatant solution after phase separation by centrifugation (Sacchi et al., 2001). In addition to dilution, chemical reactions take place during pore water extraction, which changes the concentrations of dissolved species in a complex nonlinear manner. This makes it difficult to derive the chemical composition of the original pore water from the aqueous extract data (Bradbury and Baeyens, 1998; Sacchi et al., 2001). The inference of dissolved concentrations for reactive species requires geochemical modeling based on mineralogical data (Fernández and Rivas, 2005; Zheng et al., 2008). Aqueous extract tests and concentration of exchangeable cations are available for sections 19, 28 and 29 (Fernández and Rivas, 2003). Aqueous extract data from sections 29 and 19 were interpreted by inverse geochemical modeling (Zheng et al., 2008) and used to test the model predictions (Zheng et al., 2011).

After the dismantling of heater #2 in 2015, a similar procedure was taken to measure the pore water composition and mineralogical composition. Because these data won't be available until the end of 2016, in this report, we still use the chemical data obtained after the dismantling of heater #1 to evaluate our THMC models.

Chloride, as a conservative species, is only controlled by the transport processes, i.e. advection and dispersion, which is subsequently dictated by the THM model rather than chemical reactions. In Zheng et al. (2015b), when the THC model failed to match the profile of chloride concentration measured at 5.3 years, it was postulated that adding mechanical processes and the resulting porosity and permeability changes would diminish such a mismatch. Therefore, in FY16, great effort was therefore dedicated to develop coupled THMC and THM models; they seem to be sufficiently calibrated as shown in the previous sections. However, as shown in Figure 4.25, the THMC model is still unable to match chloride data—it overestimates the concentrations near the granite and underestimates concentrations near the heater. The decrease in permeability at the outer rings of the bentonite barrier in the THMC model leads to less water infiltration and thus less dilution, which is why the THMC model has higher chloride concentration near the granite than the THC model. Less water infiltration also means less evaporation near the heater, which explains why the THMC model has lower chloride concentration near the heater than the THC model. As shown later in the report, finding the right permeability-porosity relationship or considering thermal osmosis might allow the THMC model to match both the THM and chemical data.

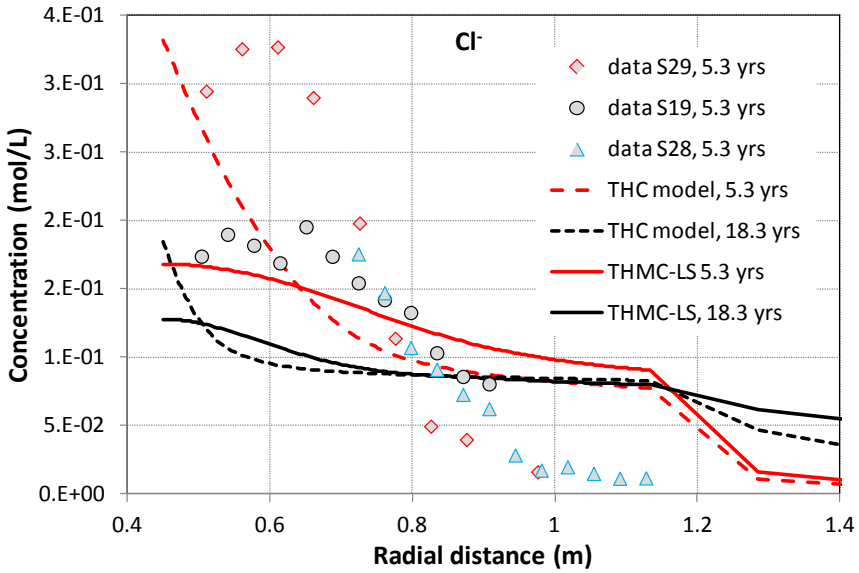

Figure 4.25. The concentration profile of chloride at 5.3 years (Zheng et al., 2011) and model results from the THC model (Zheng at al., 2015b) and THMC model with linear swelling (THMC-LS).

The concentration profiles of major cations are shown in Figures 4.26 to 4.28. As revealed in Zheng et al. (2015b), the spatial concentration profile of major cations, albeit subject to chemical reactions including cation exchange and minerals dissolution/precipitation, is largely controlled by transport processes and follow the trend of chloride. Chemical reactions alter concentration levels but not the overall trend of the concentration profiles. Similarly, just as the THMC model overestimates the concentration of chloride near the bentonite/granite interface, it also overestimates the concentrations of sodium, calcium, magnesium, and potassium as well. In addition to the transport processes, sodium concentration could also be affected by cation exchange and dissolution of smectite. However, because the sodium concentration is much higher than other cations and the concentration perturbation of other cations is fairly small, the sodium concentration is not impacted noticeably by cation exchange, and the amount of smectite dissolved (Zheng et al., 2015) is also too small to meaningfully alter the sodium concentration. The THMC model predicts that the concentration of sodium keeps going down until 18.3 years.

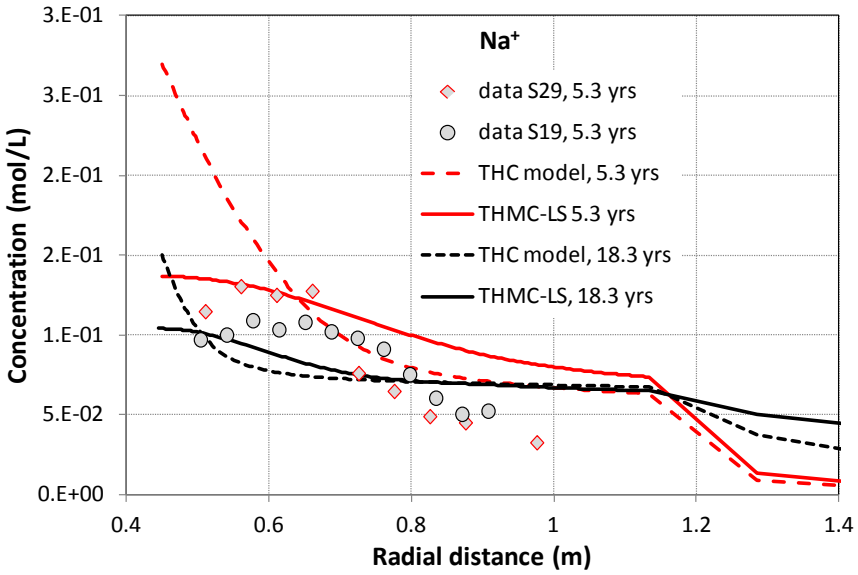

Figure 4.26. The concentration profile of sodium at 5.3 years (Zheng et al., 2011) and model results from the THC model (Zheng at al., 2015b) and THMC model with linear swelling (THMC-LS).

The THMC model, just like THC model, overestimates the measured calcium concentration across the entire bentonite barrier (Figure 4.27). In addition to the transport processes, the precipitation of dolomite and the dissolution of calcite also affect the concentration level of calcium. Eventually the model needs to delicately balance the pH, bicarbonate, calcium concentration, calcite dissolution, and dolomite precipitation to capture the concentrations of all of them.

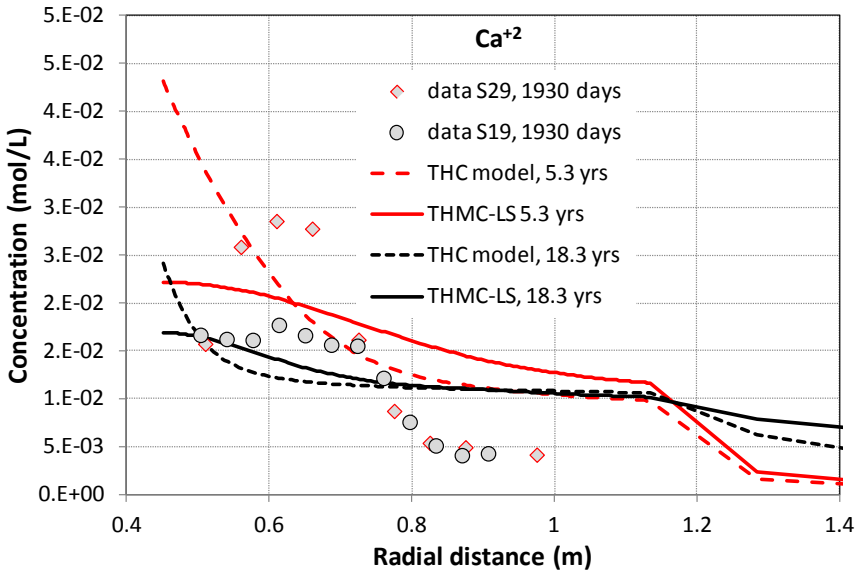

Figure 4.27. The concentration profile of calcium at 5.3 years (Zheng et al., 2011) and model results from the THC model (Zheng at al., 2015b) and THMC model with linear swelling (THMC-LS).

Zheng et al. (2015b) showed that magnesium is involved in the dissolution/precipitation of smectite, the precipitation of dolomite, and cation exchange, but eventually these reactions seem to cancel each other out, and magnesium concentration is largely controlled by the transport processes just like chloride. The

discrepancy between the THMC model and magnesium concentration data is similar to other cations (Figure 4.28).

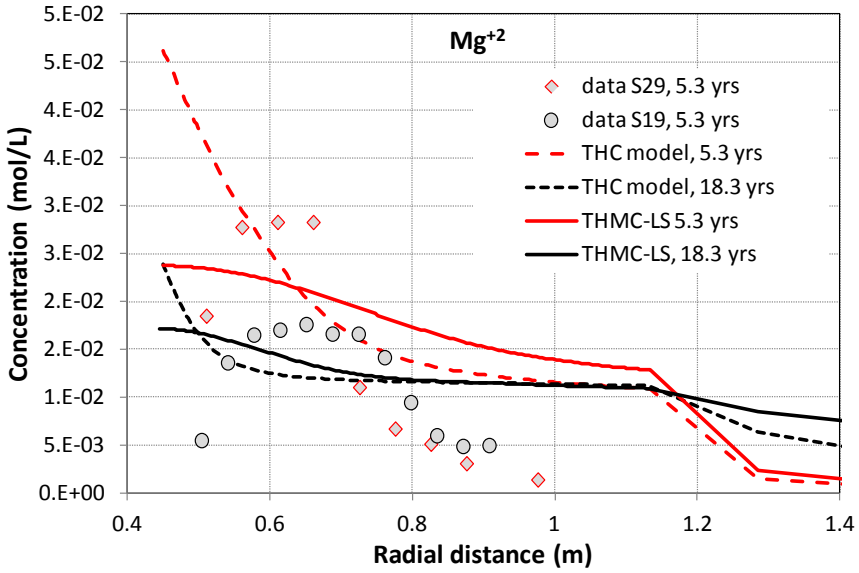

Figure 4.28. The concentration profile of magnesium at 5.3 years (Zheng et al., 2011) and model results from the THC model (Zheng at al., 2015b) and THMC model with linear swelling (THMC-LS).

The computed concentration of potassium from the THC model (Zheng et al., 2015b) that include chemical reactions is actually lower than that from a sensitivity run that did not consider any chemical reactions, suggesting that some reactions consume potassium in the pore water, which turned out to be the precipitation of illite. Although the THMC model overestimates slightly the potassium concentration near the granite, it seems to match the potassium concentration near the heater quite well.

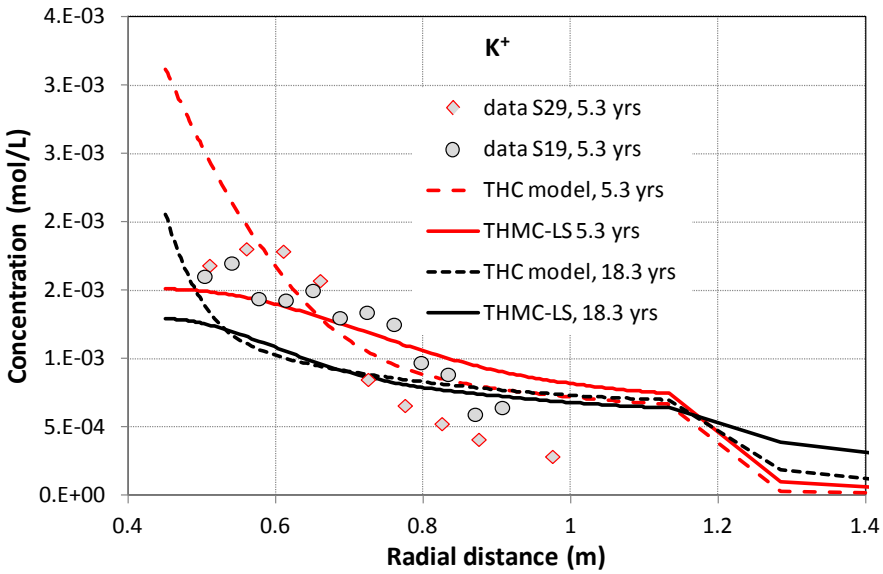

Figure 4.29. The concentration profile of potassium at 5.3 years (Zheng et al., 2011) and model results from the THC model (Zheng at al., 2015b) and THMC model with linear swelling (THMC-LS).

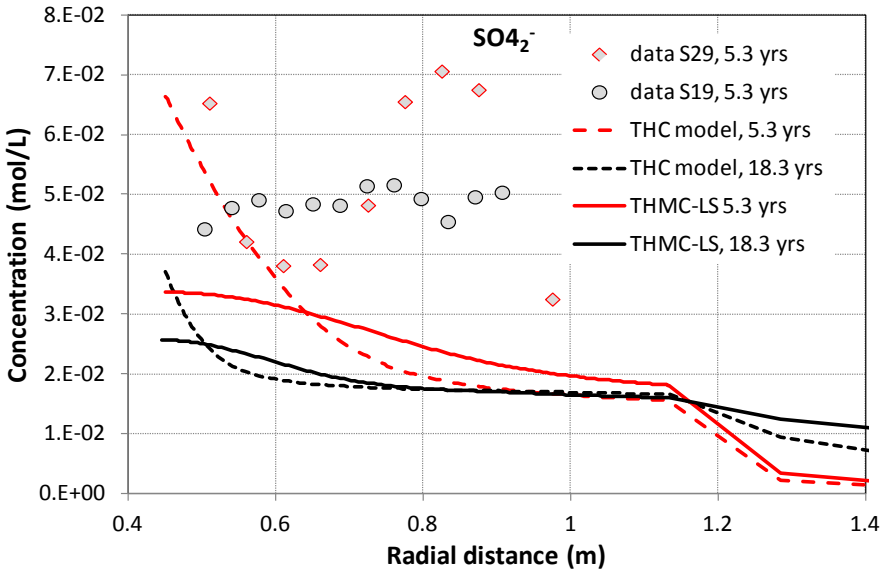

Figure 4.30. The concentration profile of sulfate at 1930 days (Zheng et al., 2011) and model results from the base model.

FEBEX bentonite contains a small amount of gypsum (ENRESA, 2000). But the amount is very small and gypsum is very soluble, so a small change in the water saturation may make gypsum disappear, which makes it debatable whether there is gypsum initially in the bentonite. The presence of gypsum had been one of the major uncertainties when the pore water compositions under *in situ* conditions were inferred from aqueous extract data (Zheng and Samper, 2008). Figure 4.30 shows the inferred data and model results. Unlike cations, the data for sulfate does not follow the trend of chloride, which indicated strong interference by chemical reactions. In the current model, no gypsum is present in the bentonite. Both the THC and THMC model results underestimate the data. Refinement of the current chemical model is warranted in the future.

It is usually very difficult to predict pH because it involves many reactions. For FEBEX bentonite, pH is mainly regulated by carbonate reactions involving calcite and dolomite and surface protonation reactions. Zheng et al. (2011) showed that surface protonation has strong pH buffering capacity and the model in this report confirms that observation. However, both the THC and THMC models still underestimate the measured pH slightly by 0.1-0.2 unit, which may be attributed to the uncertainties in the initial amount of calcite. Figure 4.32 shows the concentration profile of bicarbonate. Previous modeling work (e.g. Samper et al., 2008) showed that bicarbonate concentration is very sensitive to the alteration of calcite and dolomite and is coupled with pH changes. The current model does not consider the dissolution/exsolution of CO_2 gas, which may be a key reaction to explain the underestimation of pH and bicarbonate by the model. Also as mentioned above, inference processes using geochemical modeling were needed to obtain the chemical composition of pore water in bentonite under *in situ* conditions based on the measured concentrations by aqueous extract (Zheng et al., 2008a). However, during the aqueous extract, there was CO_2 exsolution that changed the inventory of total carbonate, which was difficult to capture accurately in the geochemical model that was used to infer the concentration under the *in situ* conditions (Zheng et al., 2008). This is another source of uncertainty regarding the pH and concentration of bicarbonate.

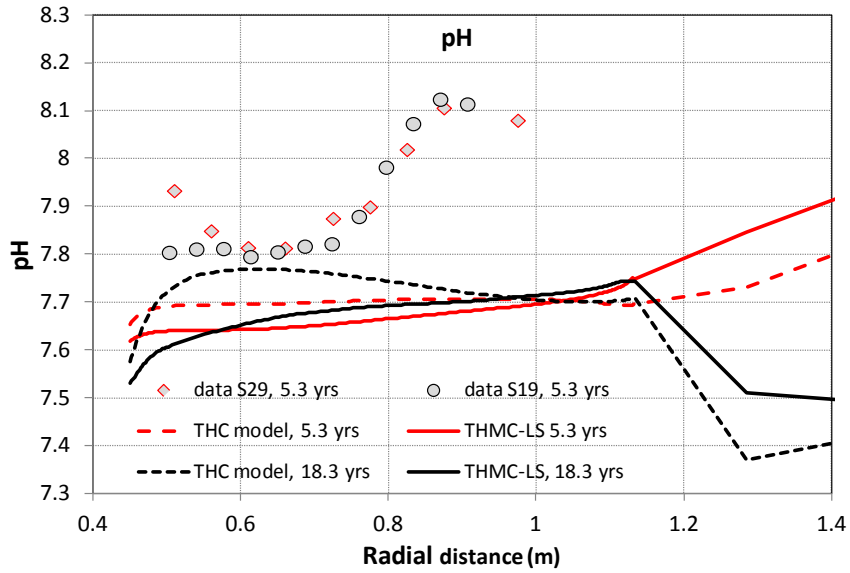

Figure 4.31. The profile of pH at 1930 days (Zheng et al., 2011) and model results from the base model.

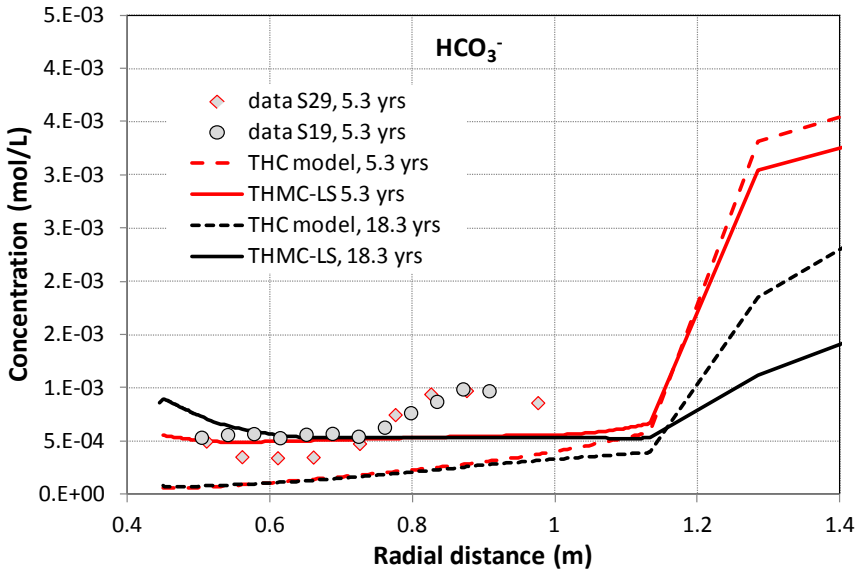

Figure 4.32. The concentration profile of bicarbonate at 1930 days (Zheng et al., 2011) and model results from the base model.

Regarding the evolution of concentration of major cations in pore water, after 18.3 years (Figures 4.25 to 4.32) the THMC model predicts lower concentrations across the entire bentonite barrier whereas the THC model predict lower concentration near the heater than that after 5.3 years, but concentrations near granite similar to the level of 5.3 years. Sulfate concentration will be further diluted as more water comes to saturate bentonite (Figure 4.30), but pH and bicarbonate at 18.3 years stay roughly the same level as at 5.3 years (Figures 4.31 and 4.32).

4.4.2 THMC model using BExM

Conceptually BExM divides the bentonite into a dual structure (Figure 4.33). Similar structural concept had been used by other modeler such as Bradbury and Baeyens (2003), Samper and Zheng (2008b) and Zheng and Samper (2015). Swelling take place predominantly in the micro-structure—water molecular enters into the inlayer space and cause an expansion of clay aggregates, and water flows occurs mainly through the macro-structure. The expansion of micro-structure compresses the space of macro-pore and therefore leads to a reduction in permeability. Such a reduction in permeability would be one of the major reasons that THMC can explain the water content data, which cannot be achieved by TH model. Figure 4.34 shows the measured water content at 5.3 years (dismantling of heater #1) and 18.3 years (dismantling of heater #2) and model results by the THMC model using linear swelling (THMC-LS) and BExM (THMC-BExM). Both models have similar water content results and match nicely the measured water content at 5.3 years. However, at 18.3 years, they deviate —THMC-BExM underestimates the water content data whereas the THMC-LS results match sufficiently the water content data. A close examination of the calculated spatial distribution of permeability (Figure 4.35) and porosity (Figure 4.36) at 5.3 years shows that THMC-BExM has lower permeability than THMC-LS but higher porosity than THMC-LS, which is why THMC-BExM and THMC-LS have similar water content results. At 18.3 years, THMC-BExM has similar total porosity to THMC-LS, but lower permeability THMC-LS, which explains why THMC-BExM computes lower water content than THMC-LS. Permeability and porosity changes will be further discussed in the next section.

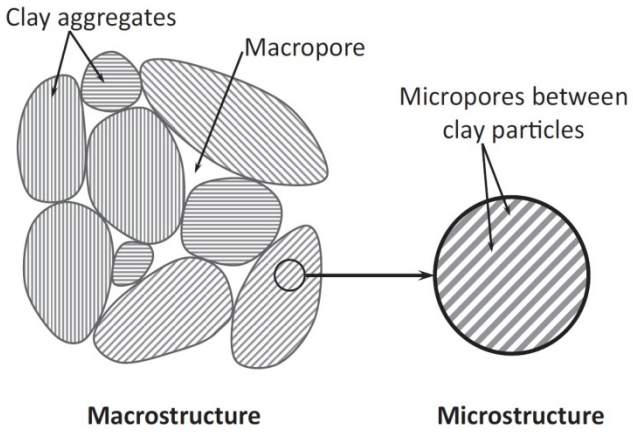

Figure 4.33. Schematic representation of the two structural levels considered in the dual structure BExM (Vilarrasa et al., 2015).

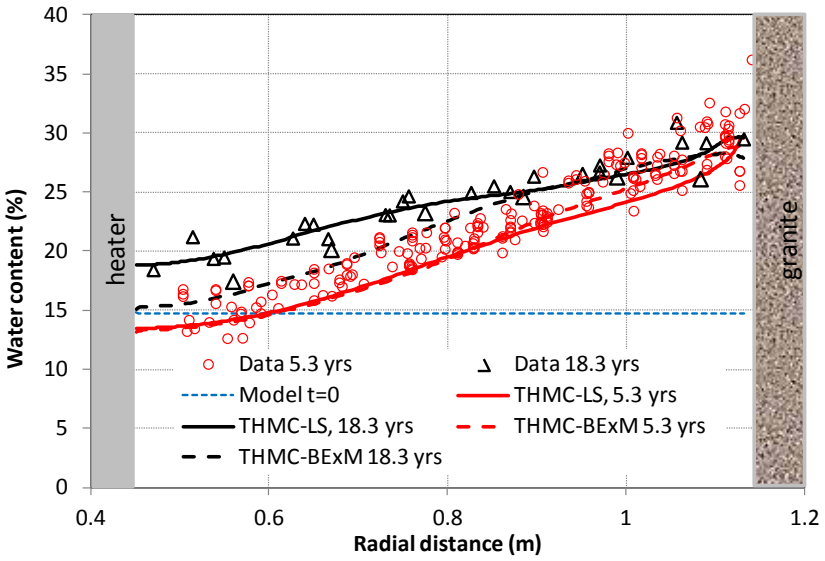

Figure 4.34. Measured water content at 5.3 years (dismantling of heater #1) and 18.3 years (dismantling of heater #2) and model results by the THMC model using linear swelling (THMC-LS) and BExM (THMC-BExM).

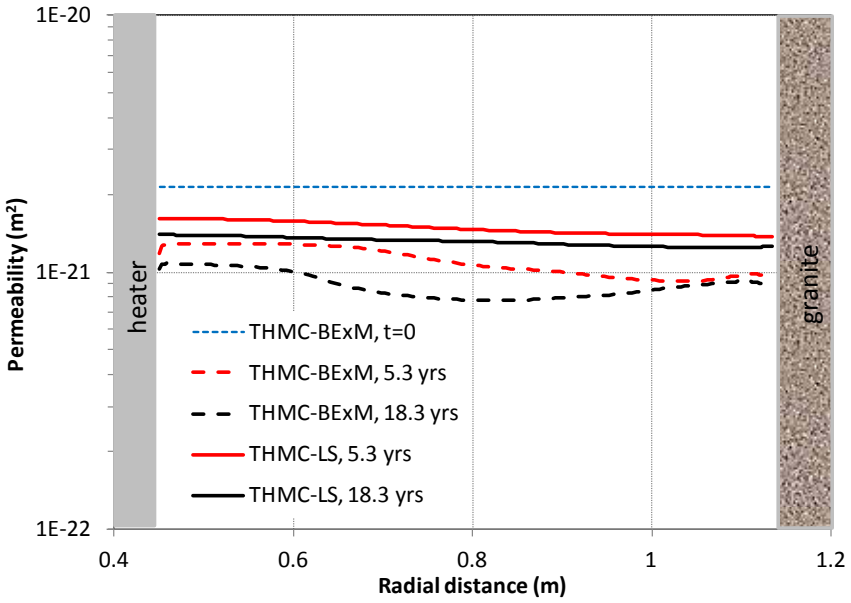

Figure 4.35. Spatial distribution of intrinsic permeability at time zero, 5.3 years (dismantling of heater #1) and 18.3 years (dismantling of heater #2) calculated by the THMC model using linear swelling (THMC-LS) and BExM (THMC-BExM).

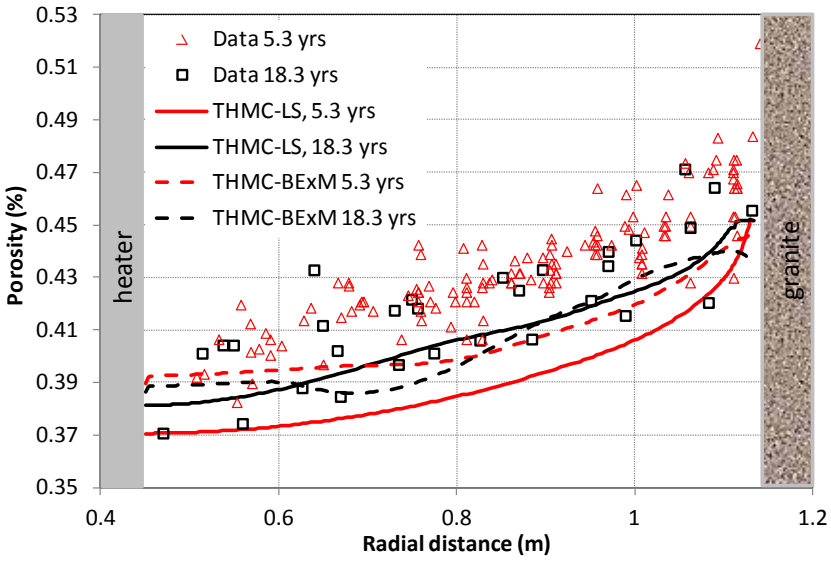

Figure 4.36. Measured porosity at 5.3 years (dismantling of heater #1) and 18.3 years (dismantling of heater #2) and calculated porosity by the THMC model using linear swelling (THMC-LS) and BExM (THMC-BExM).

Figure 4.37 shows the dry density data and model results, which have the following observations. First, the data is very scattered, which makes the interpretation difficult. A better measurement procedure might be needed. Second, although the THMC-LS model shows a decrease of dry density from 5.3 years to 18.3 years, observational data show no clear difference between 5.3 years and 18.3 years and neither do the model results by THMC-BExM. In BExM, as suction keeps decreasing upon the hydration of bentonite, the micro-structure experiences swelling, but the macro-structure, depending on the local stress state at a given time, could be compressed or expanded, which is why in THMC-BExM, dry densities at 18.3 years are not always lower than that at 5.3 years. On the contrary, THMC-LS uses a linear swelling model, i.e., swelling strain is merely a function of water saturation. As a result, increase in water saturation from 5.3 years to 18.3 years leads to more swelling and subsequently higher porosity and lower dry density. Simply from the goodness-of-fit the measured data dry density, it seems that THMC-BExM outperforms THMC-LS and likely reflects the reality.

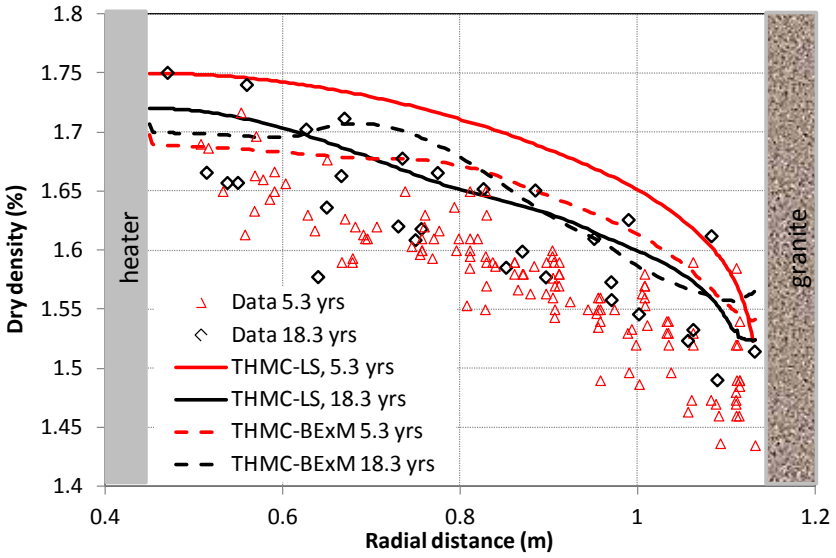

Figure 4.37. Measured dry density at 5.3 years (dismantling of heater #1) and 18.3 years (dismantling of heater #2) and model results by the THMC model using linear swelling (THMC-LS) and BExM (THMC-BExM).

There was about 70 days of cooling down period between the time that the heater #2 was switched off and bentonite samples were taken section by section due to operational reason. During this time period, temperature in the bentonite decreased to about 30 °C (Figure 4.38). This cooling off period, albeit seemingly very short compared with more than 18 years of operation of the test, has a significant impact on the spatial distribution of water content, as shown in Figure 4.39. Both THMC-LS and THMC-BExM show remarkable re-distribution of water content from 18.2 years to 18.3 years, which is featured by an increase in water content near the heater (roughly with a radial distance < 0.6 m) and a decrease in water content in the middle of bentonite barrier (radial distance from 0.6 to 0.9 m), indicating an moisture movement from the middle of the bentonite barrier towards the heater. Such a phenomenon might be caused by the deceased vapor diffusion upon the disappearance of thermal gradient, or the loss of thermal osmosis.

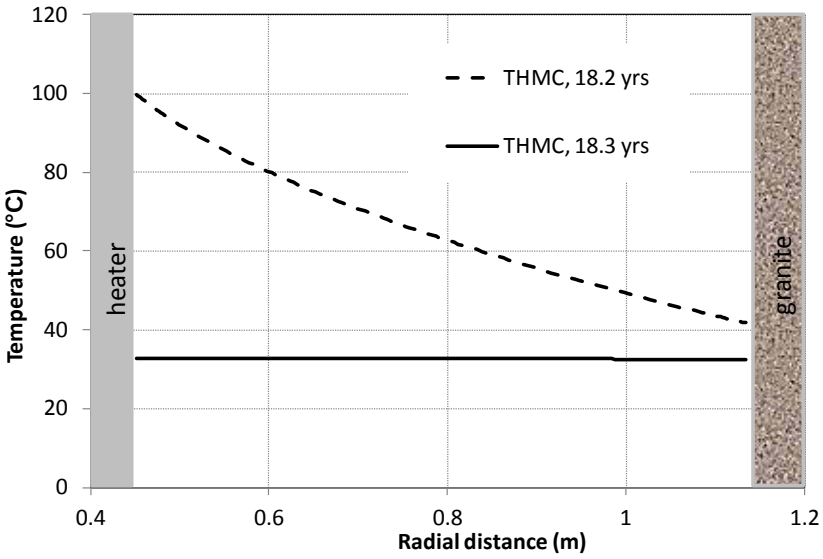

Figure 4.38. Calculated temperature at the time that heater #2 was switched off (18.2 years) and dismantling was conducted (18.3 years).

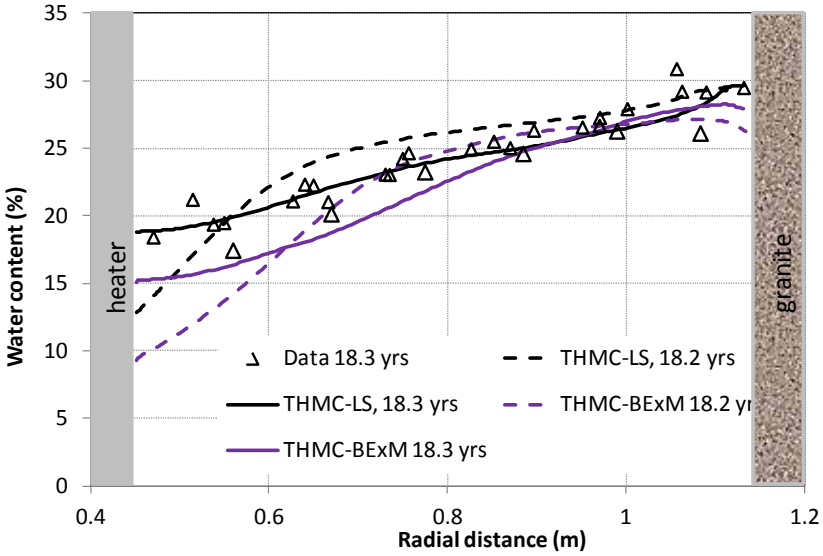

Figure 4.39.Measured dry density at 18.3 years (dismantling of heater #2) and model results by the THMC model using linear swelling (THMC-LS) and BExM (THMC-BExM) at the time that heater #2 was switched off (18.2 years) and dismantling was conducted (18.3 years).

Figures 4.40 to 43 depict the measured relative humidity and values computed with THMC-LS and THMC-BExM at four radial distances. THMC-BExM match nicely the relative humidity data near the heater (Figure 4.40) and outperforms the THMC-LS model, but underestimates slightly the data in the middle of the bentonite barrier (Figure 4.41) and underperforms slightly THMC-LS for the data in the middle of bentonite barrier. THMC-LS and THMC-BExM have similar calculated relative humidities at the outer rings of bentonite barrier and both of them match well with measured data.

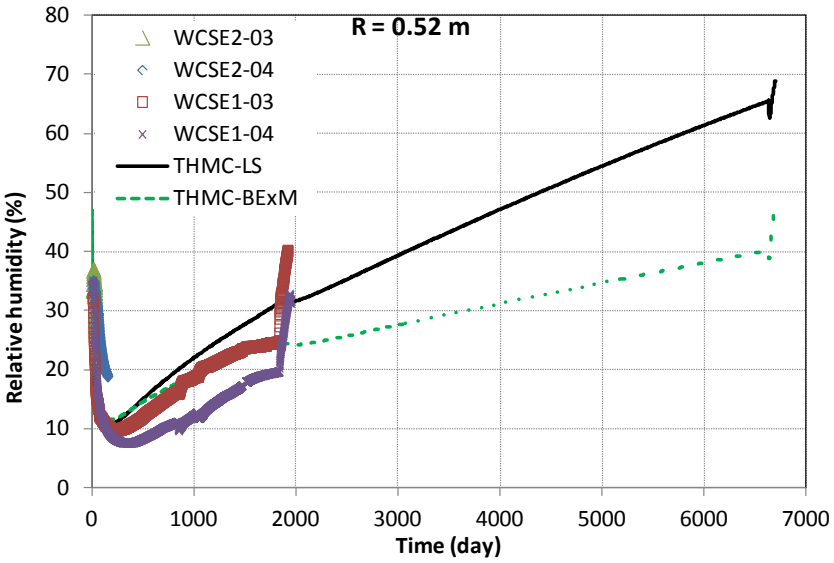

Figure 4.40. Measured relative humidity by sensors located at a radial distance of 0.52 m in sections E2 and E1 and model results from THMC model using linear swelling (THMC-LS) and BExM (THMC-BExM).

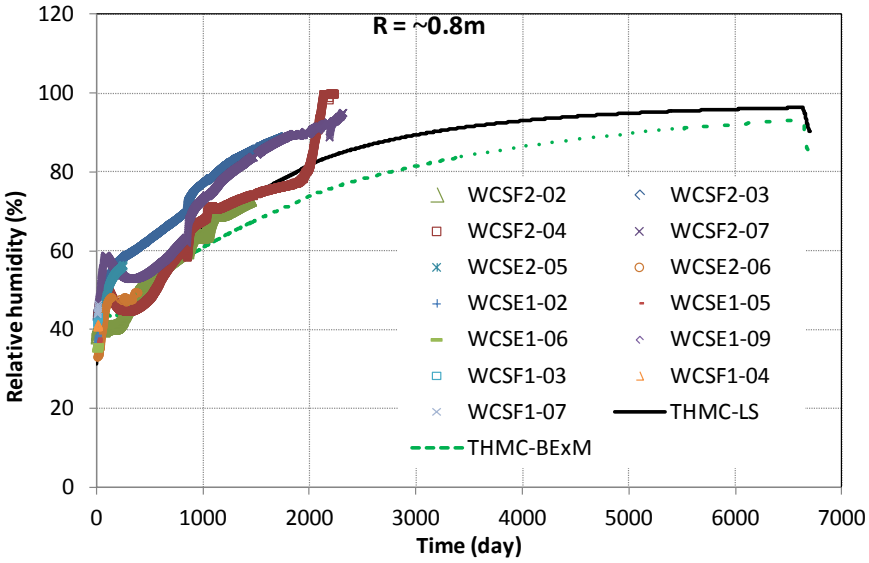

Figure 4.41. Measured relative humidity by sensors located at a radial distance of ~0.8 m in sections E1, E2, F1 and F2 and model results from THMC model using linear swelling (THMC-LS) and BExM (THMC-BExM).

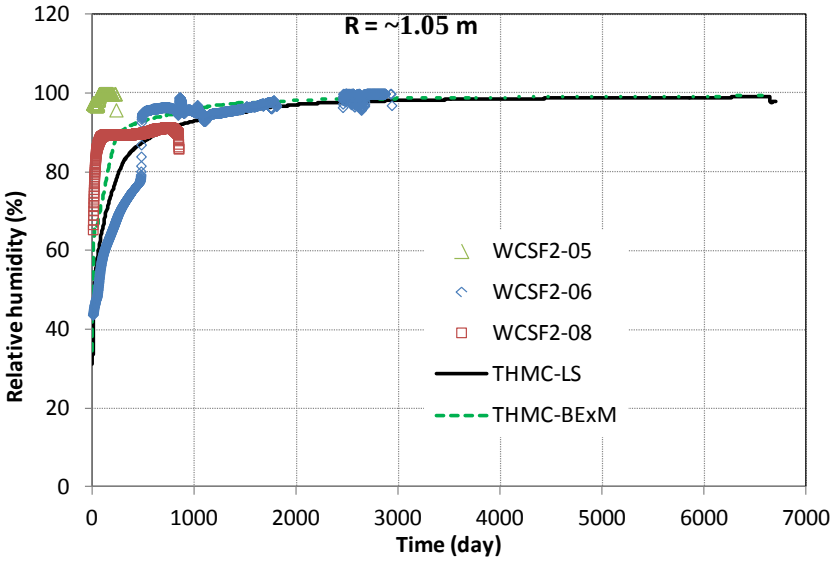

Figure 4.42. Measured relative humidity by sensors located at a radial distance of ~1.05 m in section F2 and model results from THMC model using linear swelling (THMC-LS) and BExM (THMC-BExM).

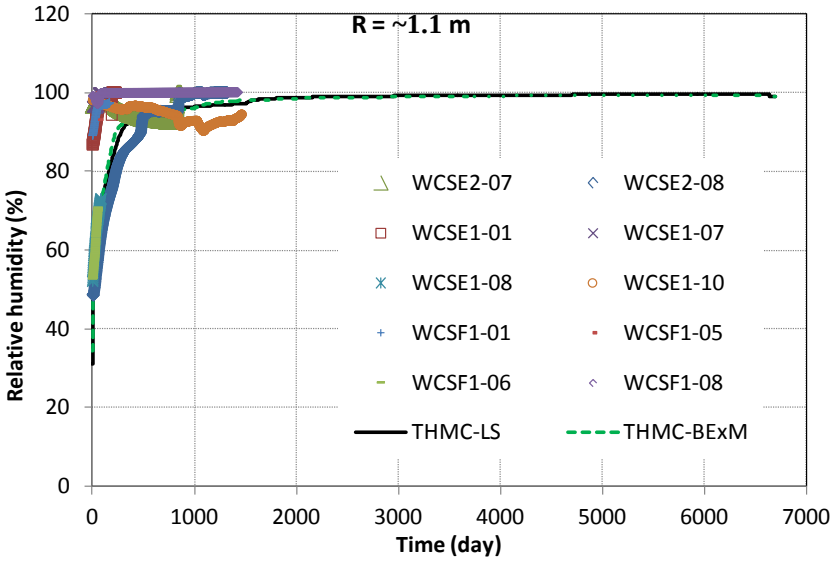

Figure 4.43. Measured relative humidity by sensors located at a radial distance of ~1.1 m in sections E1, E2 and F1 and model results from THMC model using linear swelling (THMC-LS) and BExM (THMC-BExM).

Figures 4.44 and 4.45 show the measured stress and model results by both THMC-LS and THMC-BExM. The expansion of bentonite gradually drives the stress to higher levels, but a rise in stress gradually slows down as the bentonite becomes fully saturated. BExM models that describe the swelling of bentonite more mechanistically, match better the stress increase in the early time than the linear swelling model that is known to be unable to describe the transient state of swelling.

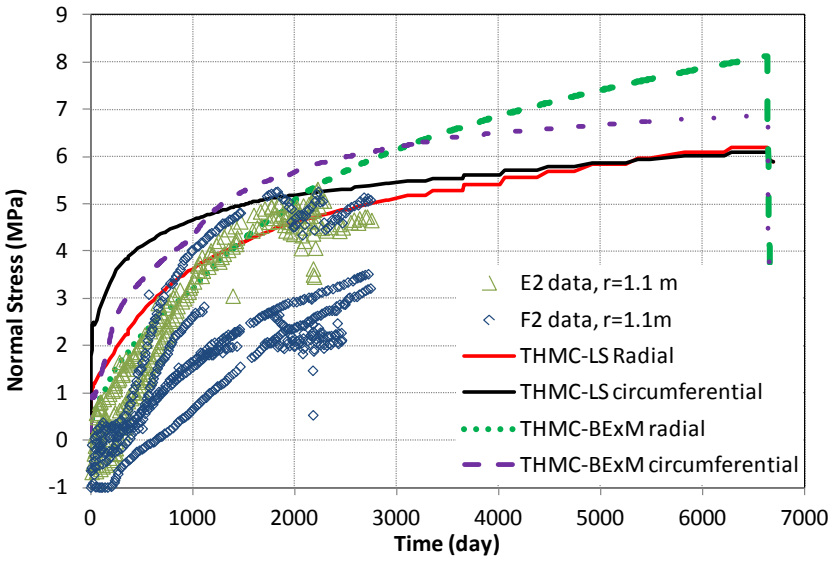

Figure 4.44. Measured stress by sensors located at radial distance of ~1.1 m in sections E2 and F2 and THMC model with linear swelling (THMC-LS).

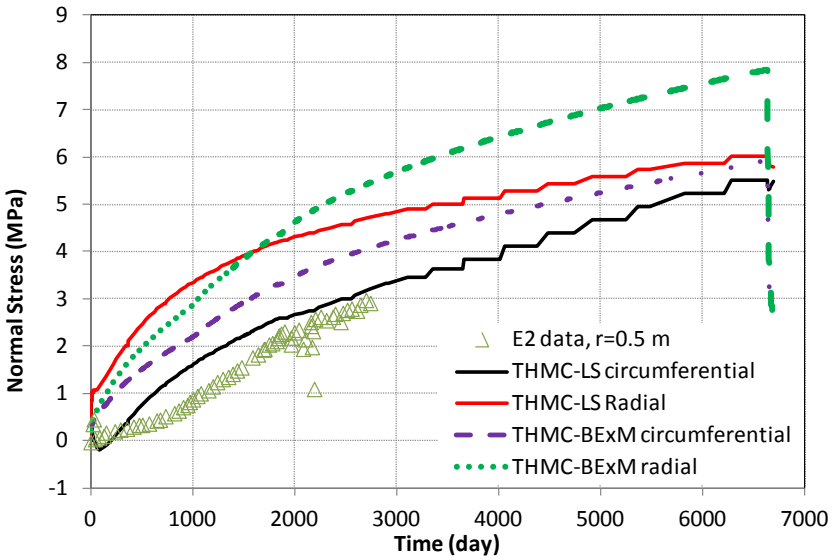

Figure 4.45. Measured stress by sensors located at a radial distance of ~0.5 m in section E2 and THMC model with linear swelling (THMC-LS).

In general, THMC-LS and THMC-BExM yield rather similar results in terms of water content, dry density, relative humidity and stress, despite the difference in calculated permeability and porosity. Considering uncertainties in the measured water content, dry density, relative humidity and stress data, both models seem to be sufficiently calibrated by the THM data and THMC-BExM maybe slightly better. However, as shown in Figure 4.47, THMC-BExM is facing the same problem the THMC-LSoverestimation of the chloride concentration near the granite and underestimation of its concentration near the heater. In fact, THMC-BExM is even worse than THMC-LS with its flatter spatial concentration profile. The fact that current THMC models, either using linear swelling or more complex BExM, reasonably match THM data but fail to explain the chemical data, indicate that the current THMC model

is flawed—either some critical coupling relationships were not correctly calibrated or some important processes are missing, which will be further discussed in the next section.

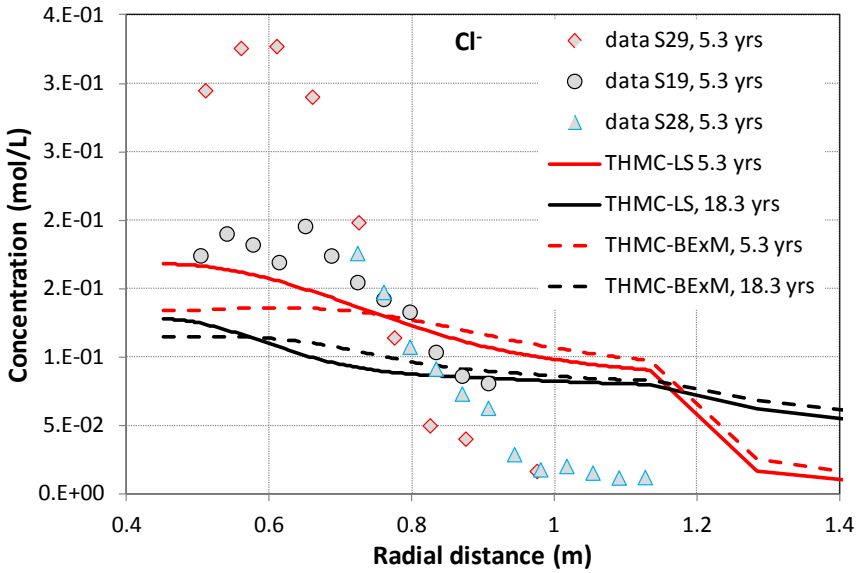

Figure 4.46. The concentration profile of chloride at 5.3 years (Zheng et al., 2011) and model results from the THMC model with linear swelling (THMC-LS) and BExM (THMC-BExM).

4.4.3 Effect of permeability change on chloride concentration

As discussed in Sections 4.4.1 and 4.4.2, the THMC models using either linear swelling (THMC-LS) or BExM (THMC-BExM) sufficiently match the THM data, but fail to match the concentration profile of chloride at 5.3 years. Chloride is a conservative species; its spatial distribution is controlled exclusively by advection and diffusion. In the THMC-LS and THMC-BExM model shown in Sections 3.4.1 and 3.4.2, the effective diffusion coefficient is 2E-9 m^2/s. In order to test if the match between the THMC model and chloride data can be improved by adjusting the diffusion coefficient, we conducted a sensitivity run in which the effective diffusion coefficient is reduced to 2E-10 m^2/s. As shown in Figure 4.48, the model with a lower diffusion coefficient significantly overestimates the concentration near the heater although it matches better the concentration near the bentonite/granite interface. More important, neither model is able to match the shape of concentration front (concentration profile from radial distance 0.7 m to 0.9 m). The sensitivity analysis shows that discrepancies between THMC model and chloride data cannot be resolved by adjusting diffusion, which means that advection is not properly calculated in the THMC models. Because advection is totally dependent on the water movement in the bentonite, in this section we re-visit the permeability change in the THMC model to see if we can solve the dilemma that THMC models match the THM data but not the chemical data.

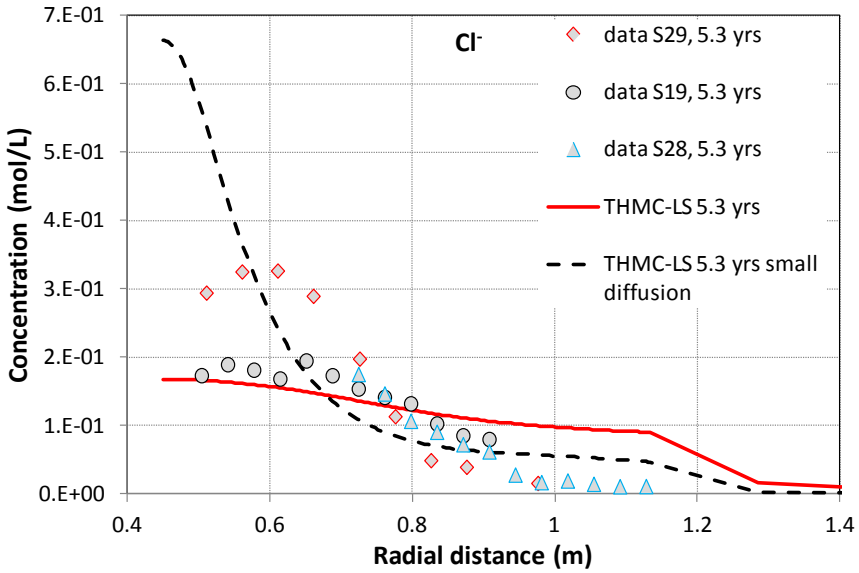

Figure 4.47. The concentration profile of chloride at 5.3 years (Zheng et al., 2011) and model results from the THMC model with linear swelling (THMC-LS) and a sensitivity run in which the effective diffusion coefficient is 2E-10 m^2/s.

For water flow in unsaturated medium, flux is related to pressure gradient via an effective permeability, which is the product of intrinsic permeability (k) (or saturated permeability, absolute permeability) and relative permeability (k_r). The relative permeability function of $k_r=S_l^3$ has been used for FEBEX bentonite (Zheng et al., 2011; Sánchez et al., 2012b; Kuhlman and Gaus, 2014), however, there are uncertainties in the relative permeability function (Table 4.11): different exponent values were obtained in different tests, ranging from 1.1 to 4.46. In two sensitivity runs shown in Figure 4.49, we used two relative permeability functions with exponent equal to 1.1 and 4, respectively. The concentration profile is flatter if the exponent in the relative permeability function is higher (e.g., equal to 4 in Figure 4.49) and steeper if the exponent in the relative permeability function is higher (e.g., equal to 1.1 in Figure 4.49), but adjusting the relative permeability function is not able match the shape of the concentration front.

Table 4.12. Exponent in relative permeability law obtained from different type of tests (ENRESA, 2000)

Test	Value of n, in $k_r = S_r^n$
Water infiltration in small teflon cells	4.64
Water infiltration in bentonite in contact with granite	3.50
Heat and water flow experiment 1	3.06
Heat and water flow experiment 2	1.10
Heat and water flow experiment 3	1.68

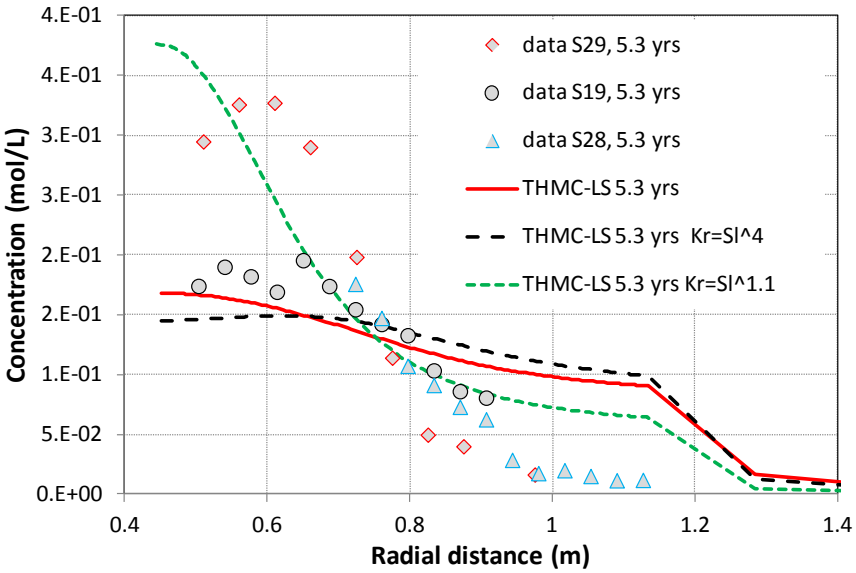

Figure 4.48. The concentration profile of chloride at 5.3 years (Zheng et al., 2011) and model results from the THMC model with linear swelling (THMC-LS) and sensitivity runs in which the exponent in the relative permeability functions are 4.4 and 1.1, respectively.

After failing to match the concentration profile by adjusting the diffusion coefficient and the relative permeability function, we checked the intrinsic permeability. Intrinsic permeability is usually measured under saturated condition and it is a function of total porosity (Figure 4.50) or dry density (Figure 4.51) for FEBEX bentonite. The data from Villar (2002) can be fitted with Equation 4.8:

$$k = \exp[19(\emptyset - 2.9) \quad 4.8$$

And the data from ENRESA (2000) can be fitted by Equation 4.9:

$$\log k = -2.96\rho_d - 8.57 \quad 4.9$$

Based on measured dry density 18.3 years (Figure 4.17), we can calculate the permeabilities across the bentonite barrier at 18.3 years based on Equations 4.8 and 4.9, which are shown in Figure 4.52. Also shown in Figure 4.52 are the permeabilities from THMC models using linear swelling (THMC-LS) or BExM (THMC-BExM). We can see the THMC models exhibit a different trend than the data — from granite toward the heater, the data show a gradual decrease whereas the models show a gradual increase. Although it is known that permeability values measured in the laboratory are different (typically smaller) than that revealed by large scale model due to a scaling effect, the fact that the model and data exhibit distinct spatial trends in Figure 4.52 clearly reveals that the permeability-porosity relationship used in THMC-BExM or permeability-stress relationship used in THMC-LS needs to be revised to match not only the THM data but also chemical data.

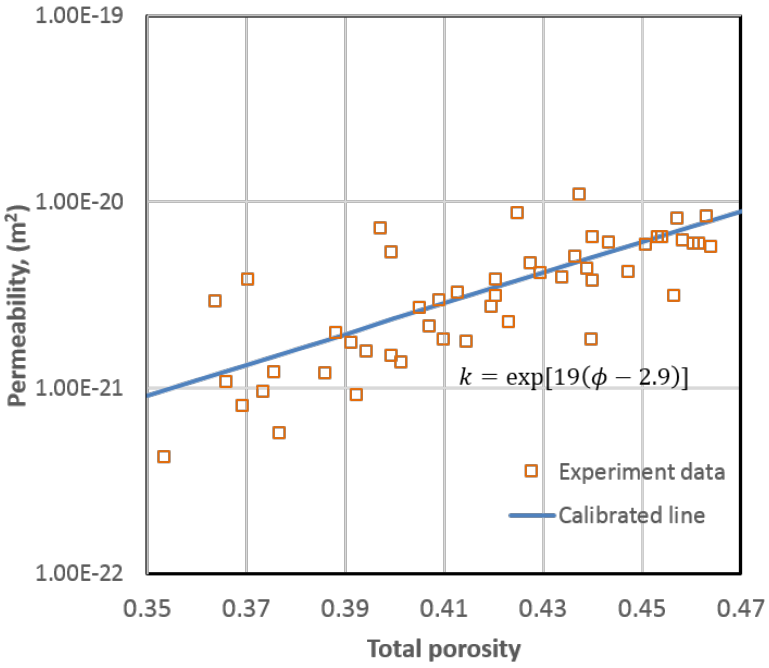

Figure 4.49. Intrinsic permeability as a function of total porosity (Villar, 2002)

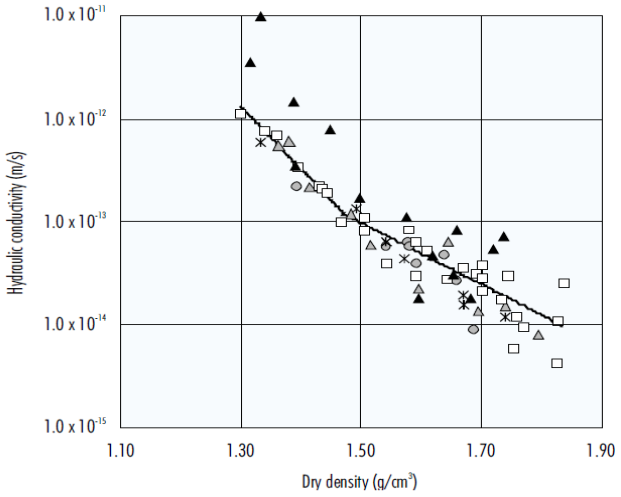

Figure 4.50. Intrinsic permeability as a function of dry density, which can be fitted with $\log k = -2.96\rho_d - 8.57$ **(ENRESA, 2000).**

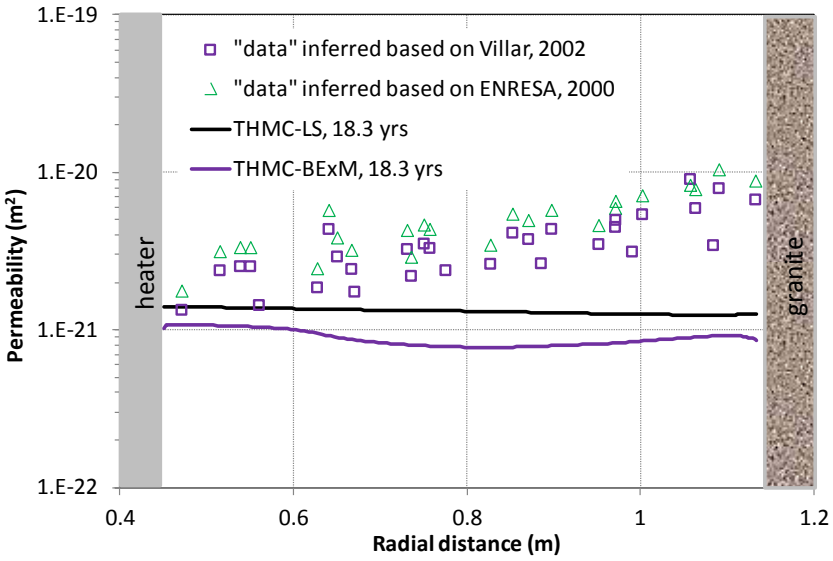

Figure 4.51. Intrinsic permeability calculated from dry density data based on Equation 4.7 ("data inferred based on Villar, 2002) and based on the Equation 4.8 (data inferred based on ENRESA, 2000) and the computed permeabilities from THMC-LS and THMC-BExM.

We therefore conducted a simulation using Equation 4.10 for permeability changes:

$$\log k = (-2.96\rho_d - 8.57)/\alpha \qquad 4.10$$

Equation 4.10 is modified from Equation 4.9 by adding a factor α of 2.45 to account for the scaling effect (difference in permeability between laboratory measured and field calibrated values). This simulation, named "Model B" in Figure 4.53, is based on the THMC-LS model presented in Section 3.4.1. It provides an overall decent match of chloride data at 5.3 years and especially at the concentration front. However, from the middle of the bentonite (radial distance of 0.7) towards the heater, the concentration data plateaus whereas the model results show a monotonic rise. Model B predicts very low concentrations in most parts of the bentonite barrier and very high concentrations close to heater after 18.3 years. Figure 4.54 shows the measured water content and results from "Model B". Although model B matches nicely the measured water content at 5.3 years, it overestimates the data at 18.3 years. In summary, using the revised function for permeability change as has been done in "Model B" leads to a better fit the chloride concentration data but a worse fit to the water content data. An additional process is probably needed for the model to match both THM and chemical data.

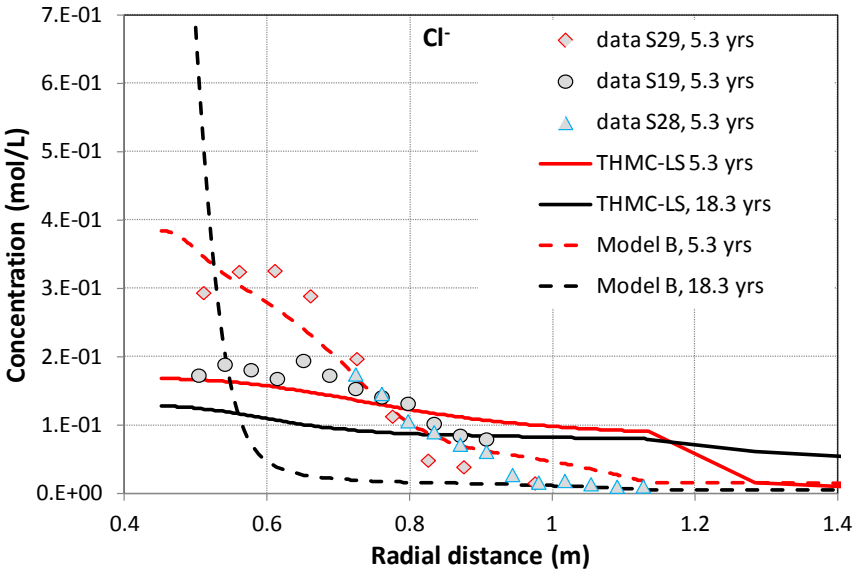

Figure 4.52. The concentration profile of chloride at 5.3 years (Zheng et al., 2011) and model results from the THMC model with linear swelling (THMC-LS) and sensitivity runs (model B) using the Equation 4.9 for permeability change.

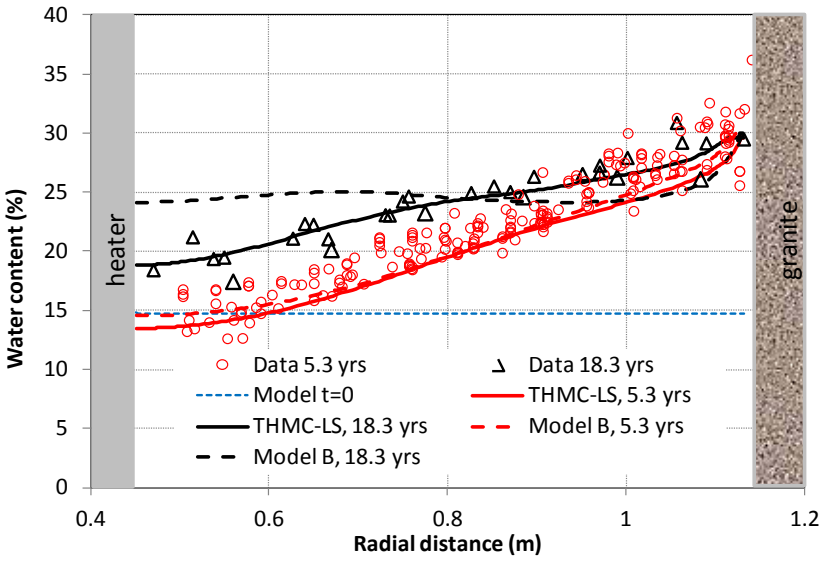

Figure 4.53. Measured water content at 5.3 years (dismantling of heater #1) and 18.3 years (dismantling of heater #2) and model results by the THMC model using linear swelling (THMC-LS) and Model B which is based on THMC-LS but using different function for permeability change.

4.5 QUANTITATIVE CHARACTERIZATION OF THE FRACTURE NETWORK IN THE FEBEX SAMPLES VIA SYNCHROTRON X-RAY MICROCT

4.5.1 Introduction

In a radioactive waste repository with bentonite backfilled engineered barrier system, bentonite barrier undergoes simultaneously heating and hydration. The hydration leads to swelling, which helps the bentonite to seal gaps and pre-existing micro-fractures, while the heating could lead to desiccation of bentonite and creates micro-fractures. How these two competitive processes play out in the long run is important for estimating the permeability change in bentonite. Theoretical and empirical relationships for permeability change have been tested in the models for the FEBEX *in situ* test. Although the comparison between model and THMC data has been very helpful in calibrating the "right" relationships (or key parameters for the relationships), uncertainties in other processes and interaction of coupled processes might results in non-unique sets of parameters that could lead to equal or similar reasonable fit between model and data. Checking the microstructure of the bentonite buffer will serve as additional evidence to delineate the right permeability change functions and increase the predictability of models. Bentonite samples were taken from the FEBEX *in situ* test after the dismantling of heater #2. In this section, we describe a series of synchrotron X-ray microCT (SXR-μCT) experiments to examine the microstructure of bentonite.

4.5.2 The technique

SXR-μCT has so far proven to be a very valuable tool for studying the fracture network of these samples. While some sample conservation and preparation issues might be present, the basically non-destructive aspect of the technique puts SXR-μCT at an advantage to other imaging methods such as scanning electron microscopy (SEM). In electron microscopy the sample is (usually) kept in vacuum under an electron beam, and in such conditions some dehydration is guaranteed to occur. But also measurements in environmental SEM's would still require a non-trivial sample preparation: the sample would need to be cut to create a flat surface for the analysis, and the surface would be of course the part of the sample most subject to artifacts due to cutting. The surface itself is also the part of the sample more prone to dehydration, given its immediate contact with the atmosphere. In addition to that, there is of course the issue of having to deal with 2D data. For all these reasons, we used XR-μCT to look at the interior of the sample, undisturbed as much as possible, in a non-destructive fashion. The collected data can be used for 3D visualization of the samples via software rendering, where operations such as virtual cuts are possible to investigate the interior of the sample, but the data can be used to characterize the microstructure of the sample in a quantitative fashion, using a variety of morphometric parameters (see e.g. Zandomeneghi et al., 2010). A quantitative characterization is especially important when looking at differences within a series of samples.

The experiments were carried out at the 8.3.2 beamline at the Advanced Light Source (ALS) at LBNL (MacDowell et al., 2012). The experiment consists of placing the sample on a rotating stage, and taking radiographs over 180 degrees of rotation, at given angular intervals. Software based on the concept of the filtered-back projection will provide as a result, starting from the radiographs, a virtual volume of the sample in the form of a stack of horizontal "slices" (e.g. Kak and Slaney, 1988).

In these experiments the samples were measured with monochromatic X-rays (34 keV), 650 ms of exposure time, collecting 2049 projections, with a continuous tomography and "local area" (sample larger than the field of view) setup. The advantage of using a sample larger than the field of view in this specific

context is important: the outer part of the sample is not actually measured, but that part of the sample is the one theoretically more subject to issues due to the sample preparation, so instead of performing a conventional tomographic measurement and then extensively croping the dataset, we decided to use this strategy to be able to acquire a larger usable dataset with each measurement. The resulting voxel size of these measurements was 3.22 μm and the usable datasets were cylinders of 1820 vx (= 5.86 mm) diameter and 500 vx (= 1.61 mm) height.

Two measurements at higher resolution (0.633 μm voxel size) were carried out as well. Higher resolution measurements were done to check the presence of smaller fractures, which would have been missed at the lower resolution. Still, this resolution only allows the measurement on a very small sample, raising serious issues about its representativeness, also given the heterogeneity of the material at that scale.

In addition to the static experiments, an *in-situ* experiment involving the heating of the sample to monitor the development of cracks had been also carried out. The sample was heated up to ~180 °C for 8 minutes, sealed (but vented) in an unconfined pressure state. This was carried out in order to both mimic a worst-case scenario (sudden heating), but also, and mostly, to check the mechanisms of crack nucleation and propagation under heating conditions typical of this material.

4.5.3 Sample selection and preparation

The samples were protected in vacuum-sealed bags that were delivered to LBNL from the source, until sampling for SXR-μCT took place. The sample was prepared by carefully cutting a ~1.5 cm piece from each of the bulk bentonite samples, making sure that the sample was not coming from the outer surface of the blocks. Just after cutting the sample, the fragments were immediately sealed in plastic wrap and aluminum foil to minimize as much as possible the loss of moisture, which would likely develop new cracks. Maximum care was paid not to expose the samples to air for any significant amount of time and not to generate new cracks in general. Smaller fragments (~4 mm) were chosen for higher resolution measurements. For the *in-situ* heating experiment, no plastic wrap was used.

The stability of the material over time was also further confirmed by the lack of appreciable motion artifacts in the collected datasets. This kind of artifact is very common in samples rich in highly hydrated clays or organic material measured in air.

From the selection of samples available, we decided to analyze two series:

1) The BD-48 series consists in two samples from section 48 around the heater (see Figure 4.6 for the position of section 48). We analyzed samples immediately adjacent to the heater (BD-48-3) and close to the host rock tunnel surface (BD-48-7). Section 48 is located right in the middle of theheater and underwent the strongest heating and the slowest hydration. Over the course of the test, the temperature at section 48 near the heater is around 100 °C and about 50 °C near the granite. Although water content and dry density were not measured for samples in section 48, water content and dry density measured for samples at section 49, which is next to section 48, can be used as a reliable reference of water content and dry density. Based on the data collected at the same radial distance from the central axis of gallery at section 49, sample BD-48-3 is likely to have a water content of 18-19% and a water saturation degree of 80%, whereas sample BD-48-7 is fully saturated with a water content of around 30%.

2) The BD-59 series includes samples from section 59 located near the end of the gallery and away from heater #2. Three samples from different positions were analyzed: close to the heater (BD-59-15), in the middle of the section (BD-59-8), and close to the host rock, in the outer rim (BD-

59-3). The temperatures at section 59 have always been low during the entire testing period, which is around 22 °C and has no spatial variation.

In Figure 4.54 (left) the localization of the samples has been highlighted on the schematics of the BD-59 section. The samples from BD-48 are shown to the right, with the position of the heater in that section colored in red.

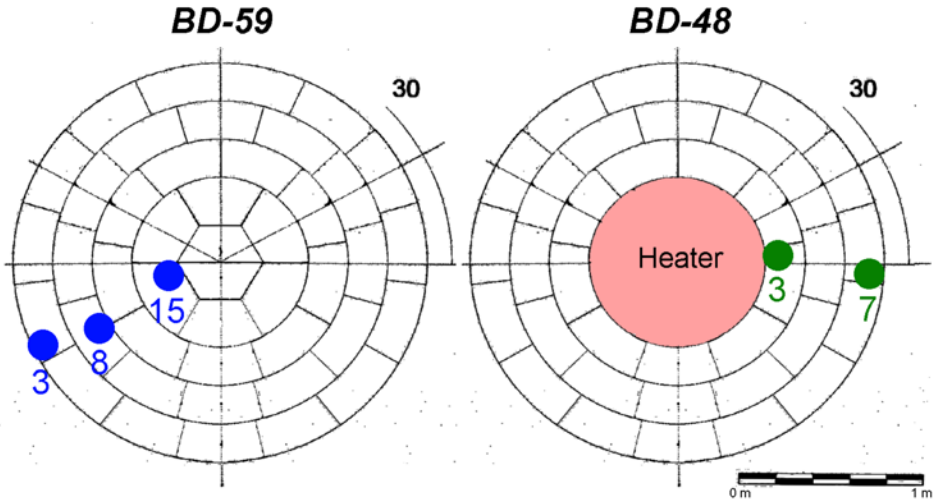

Figure 4.54. Location of the different samples: the series from the section outside the heater (section 59, sampling points in blue), and the series from the section with the heater (section 48, with measured sampling points marked in green) are shown within the pattern of the bentonite blocks.

4.5.4 Analysis strategy

The problem of fracturing in these samples has been addressed using different approaches aimed at different important issues. We can divide the work into three main parts:

1) Quantitative characterization of the fracture networks in the different samples: Which parameters can we use to describe the fracture networks in a quantitative fashion? Is the resolution vs. field of view ratio good enough for this characterization? Is there any appreciable heterogeneity among different samples?
2) Effect of dehydration: What is the effect of strong dehydration on the fracture network? Can we identify specific mechanisms of crack nucleation and propagation?
3) The effect of resolution: high resolution means the ability of finding smaller scale features such as micro- and nano- fractures. But it also means a much smaller volume investigated. What are we missing from the main measurements? Is this higher resolution really important from a practical point of view?

To answer the questions listed above we developed specific analysis strategies taking advantage of the experimental setup available at the X-ray imaging synchrotron beamline 8.3.2 at the ALS.

4.5.5 Results

Listed below are the results obtained addressing the three different main parts.

4.5.5.1 Quantification of the fracture network

The micro-structure of bentonite is represented by the fracture network in the sample and the quantification of the fracture network is the main topic for this research. We want to be able to associate a quantitative parameter to each sample such that we can understand the variation of the fracture network for samples at different locations. To reach this goal, we selected three points at different positions with respect the distance from the tunnel wall in section 59, which has no heater in the center, and two samples from section 48, which has a heater in the center. To monitor the variability of the fracture network in the same positions we have chosen three different samples for each position, and a total of 15 samples were analyzed.

The analysis of the tomographic datasets was carried out using an automated Fiji (Schindelin et al., 2012) script, minimizing human intervention and assuring that each sample was analyzed in the exact same way. The main target for the script was to obtain volumes where the medial axis of the fractures was labeled, in each point, with the local thickness (Dougherty and Kunzelmann, 2007), a value related to the aperture. The resulting volumes include all the information about the frequency and size distributions of the fracture network.

In the figures presented in this chapter, the sample names follow this structure: "SectionName"_"BlockNumber"_SampleNumber", so e.g., BD48_3_2 is the 2nd sample measured from the block #3 of the section BD-48.

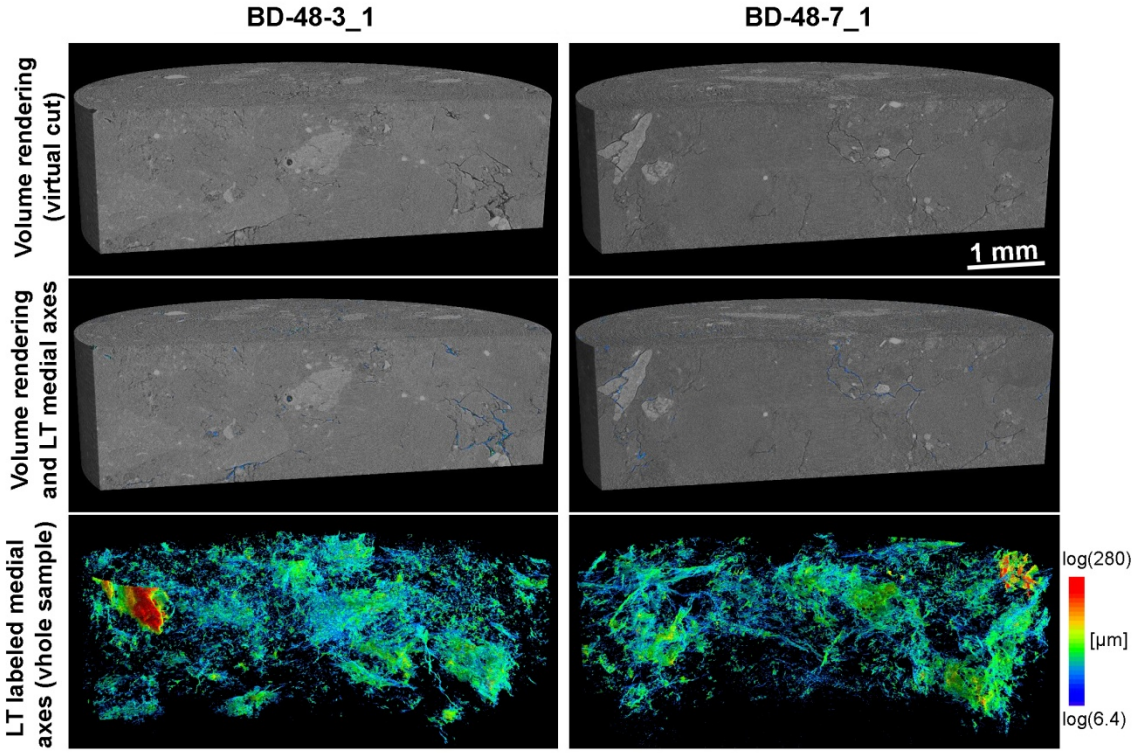

Figure 4.55. Graphical results of the microCTanalysis of two samples from section 48: BD-48-3 (near the heater) and BD-48-7 (near the granite).

From the results in Figure 4.56, we can appreciate that the samples are pervaded by a network of thin fractures, with sizes in the order of the few tens of microns. In the volume renderings we can see that the fractures are present in the clay matrix, some cut across larger crystalline particles (quartz, feldspar, etc.), and some fractures are located along the interfaces of the crystals with the clay-rich matrix. From this

observation it seems safe to assume that there are different mechanisms involved in the development of the fractures. In the middle of Figure 4.56, the superimposing of the medial axes of the fractures (labeled with the values of the local thickness -LT- in each voxel) serves as a check to confirm that the script finds all the fractures above the actual resolution, and the labeling with the LT values is correct.

In the lower sections, only the rendering of the labeled medial axes is shown. A color log scale for the aperture values has been chosen since the vast majority of the aperture values are small, so in a log scale it is easier to appreciate the small variations in aperture in the fracture network. This also serves as a comparison to the final plots where a log scale was chosen for the same reason.

The same approach was used to analyze the other 9 samples (3 for each position) from section 59, and the graphical results are shown in Figure 4.57.

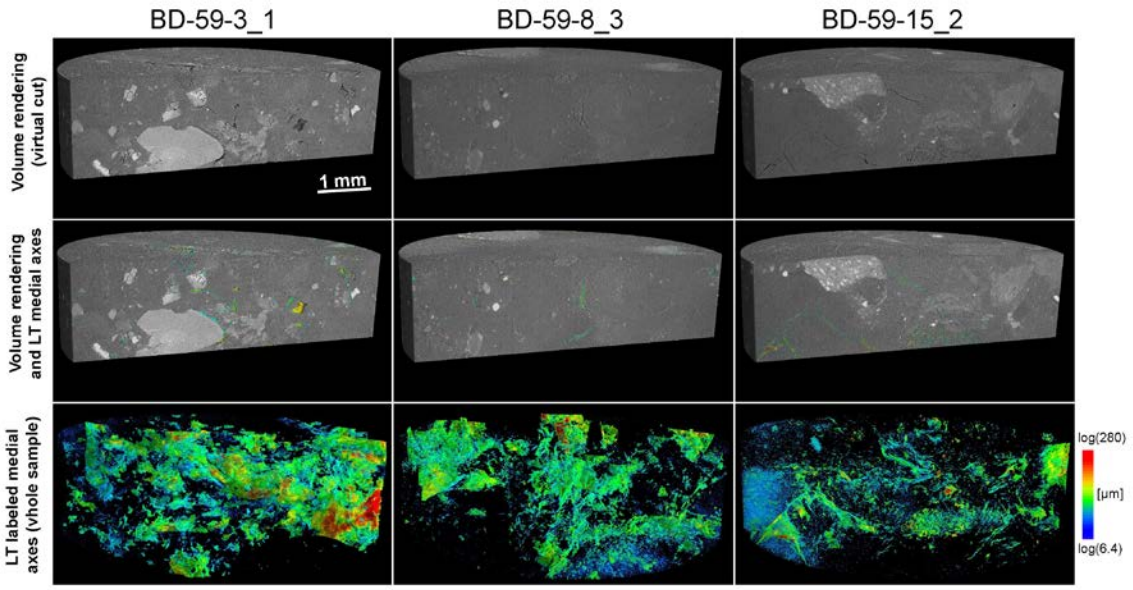

Figure 4.56. Graphical results of the analysis of two samples from the section 59: BD-59-3 sample (near the granite), BD-59-8 (half radius) and BD-59-15 (center). See Figure 4.55 for more precise sample location information.

Similarly with the observations in samples BD-48-3 and BD-48-7, the samples from section 59 present an extensive fine fracture network, with different kinds of fractures of (aggregate-matrix detaching, pure desiccation cracks of the clay matrix, etc.). It is also noteworthy to point out that there is a small amount of microporosity apparently not related to modifications in the microstructure of the material, but with the nature of the aggregate particles in the bentonite. An example is visible in the left side of the sample BD-59-15 in Figure 4.57.

More details about the characteristics of the fracture network can be seen in Figure 4.58, where a thin horizontal slice of a sample (from BD-59-3) is shown superimposed with a smaller volume of the fractures (as a white isosurface) to emphasize the structure and provide context for the fracture network. A zoom of a detail of the slice, but with the LT labeled medial axes is also shown to highlight the different kinds of fractures present. It is easy to see that fractures run inside broken aggregate particles (e.g., top right), and that they connect different aggregate particles, but thin fractures are also present in the clay matrix. From Figure 4.58 it is also possible to appreciate again that the calculation of the medial axes and the fracture aperture-related values seem to be correct.

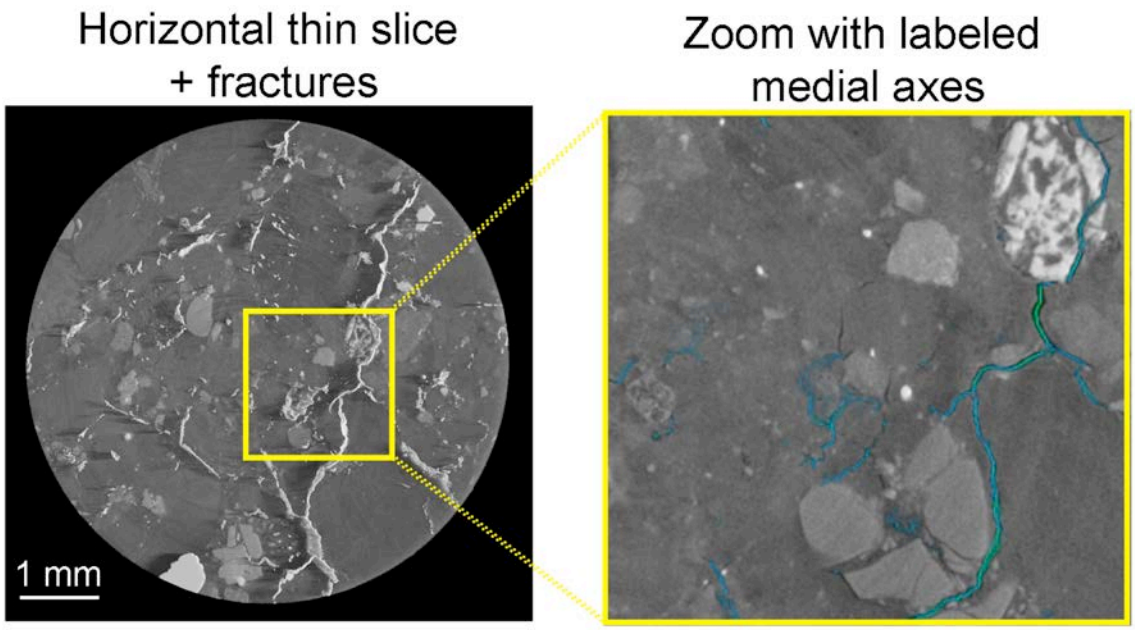

Figure 4.57. Highlighting different features of the fracture network in a sample from BD-59-3.

Having available 15 volumes, 3 for each point in the two sections, allowed us to carry out some analysis trying to characterize the networks in a more quantitative fashion. For each sample a frequency plot of apertures has been calculated, and the results are shown in Figure 4.59.

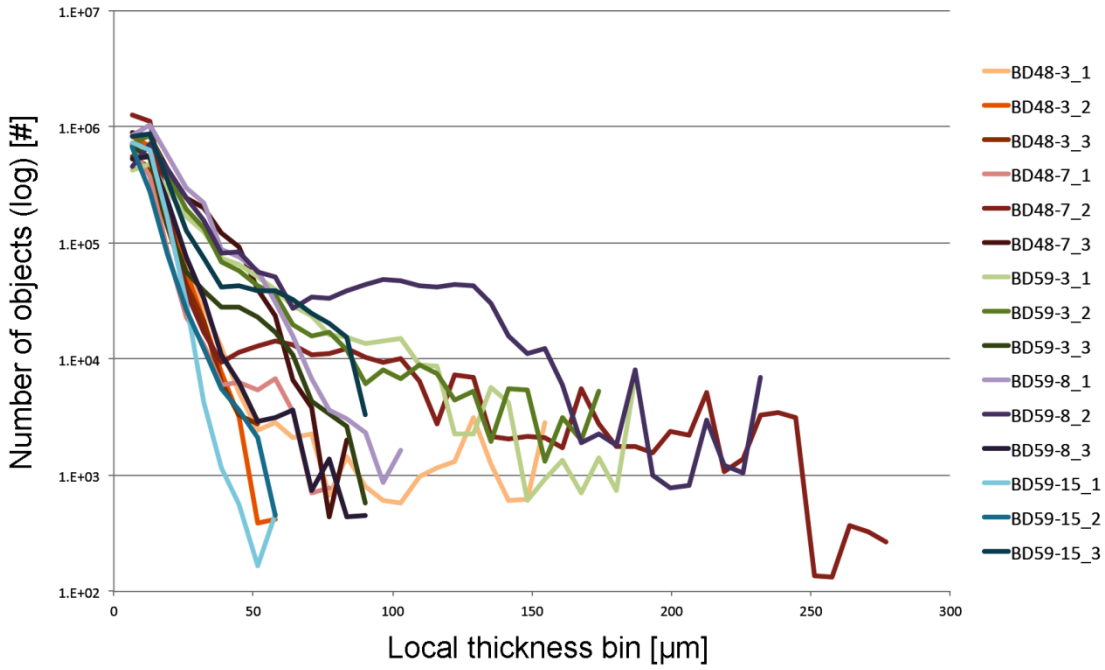

Figure 4.58. Local Thickness (LT) frequency plots (in absolute values) for all the 15 samples.

From Figure 4.59 it is possible to observe that at the largest LT values the samples are very different, in a seemingly chaotic fashion, but also the largest values of LT (i.e. large cracks) are very uncommon. The most interesting observation can be done in the range from 25 to 45 μm, where a bifurcation of the trends of the plots seems to be present. This is an interesting interval since for smaller than 25 μm size bins, the size starts to be too close to the resolution, and the morphometric parameters start to be less reliable. Below the 25 μm size the microporosity of a few aggregates also starts to be important and potentially impacts the reliability of the calculation (this issue is discussed in terms of reliability of the shape-preferred orientation morphometric analysis in Voltolini et al. 2011). The number of points in the medial axes of the fractures below the 45 μm size is also very large, making the analysis more reliable from a purely statistical point of view. Obtaining statistically reliable results would be more challenging for the larger fractures, with bins larger than 100 μm, for example.

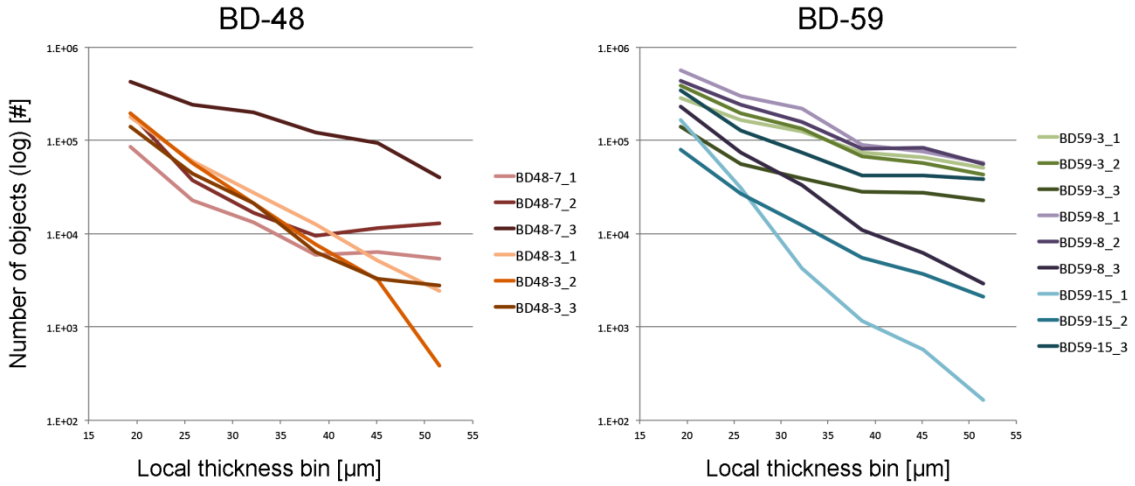

Figure 4.59. LT frequency plots in a smaller interval for the two different sections separated.

The fracture aperture distributions in this interval are roughly linear (in log scale), and a linear regression for each sample has been calculated. The slope of the fitted line (angular coefficient) provides direct information about the ratios of small vs. large fractures. For example, smaller values of the angular coefficient mean that a large amount (exponentially proportional) of microfractures are present in the sample, close to the resolution value of our measurements, while higher values highlight the presence of larger cracks.

To summarize the results, the average of the values of the 3 volumes (since measurements were done in triplicate: each position in the sections had 3 different samples measured) was calculated as well, so the values plotted refer to a total volume of ~ 130 mm^3, for each position sampled. As can be appreciated by the plots in Figures 4.6 and 4.7 the variability of the samples in the same block can be rather high. This calculation was done to see if there was any difference of the samples related to its position relative to the heater (section in the heater vs. section outside the heater), but also to see if there was any difference related to the distance from the wall of the tunnel. Differences in hydration values have been reported from *in situ* measurements during the tests, so these values could be related to different extent of fracturing.

The values below in Figure 4.60 show what seems to be a correlation of the angular coefficient relative to the distance to the granite contact, but the variability of the values is quite different from sample to sample, so while this trend shows some consistency, a much larger number of measurements should be carried out to fully validate this finding.

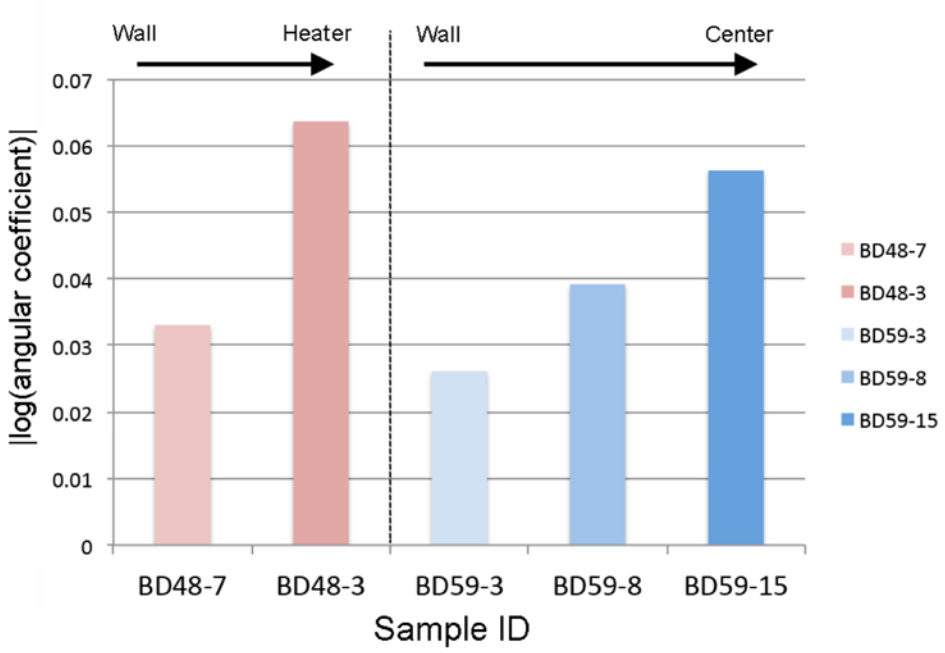

Figure 4.60. Angular coefficients (average of the 3 measured for each point) of the linear regressions of the plots shown in Figure 4.58.

Figure 4.60 shows that the |slope| of the linear regression curve increases with the distance from the wall, which seems to indicate that the samples closer to the wall tend to have a larger amount of large fractures compared to the samples close to the heater or to the center of the section. The sample close to the heater (BD-48-3) has the largest relative amount of the smallest microfractures of all the samples. This analysis seems to suggest that the slight decrease in humidity promotes the relative creation of smaller microfractures, while no evident trend is observable looking at the absolute values.

4.5.5.2 Dehydration-induced fracturing: SXR-µCT in situ heating

The most likely fracturing mechanism in these samples is likely due to the shrinkage caused by the loss of water. In the FEBEX *in situ* test, the bentonite near the heater underwent (see section 4.4.1.1) a fairly long time period (about 3000 days) of desaturation—relative humidity decreased from the initial 40% to 8% after 500 days and took about 2500 days to recover to the initial values, and then gradually got hydrated and reached an relative humidity about 80-90% by the end of test (about 6700 days). Questions raised include whether fractures are developed during the desaturation period and whether those fractures vanished after the moisture content in bentonite increases. The desaturation of bentonite near the heater in FEBEX *in situ* test or in a typical repository condition occurs in a confined condition and is accompanied by the rise of stress. Although it is extremely difficult to monitor the development of fractures under the same conditions, in this report, we have performed an *in situ* SXR-µCT measurement of a sample from BD-59-3 subject to heating at a relatively high temperature under an unconfined conditions, hopefully to shed light on the fracturing mechanism while we are fully aware the difference between the laboratory and field conditions. The sample was mounted, sealed in aluminum foil onto the rotating stage of the SXR-µCT beamline and a baseline scan was done. After the baseline scan, the sample was heated with a hot air blower to ~ 180 °C for 8 minutes. After the heating a final measurement of the sample was done again. The visual results are presented in Figure 4.61.

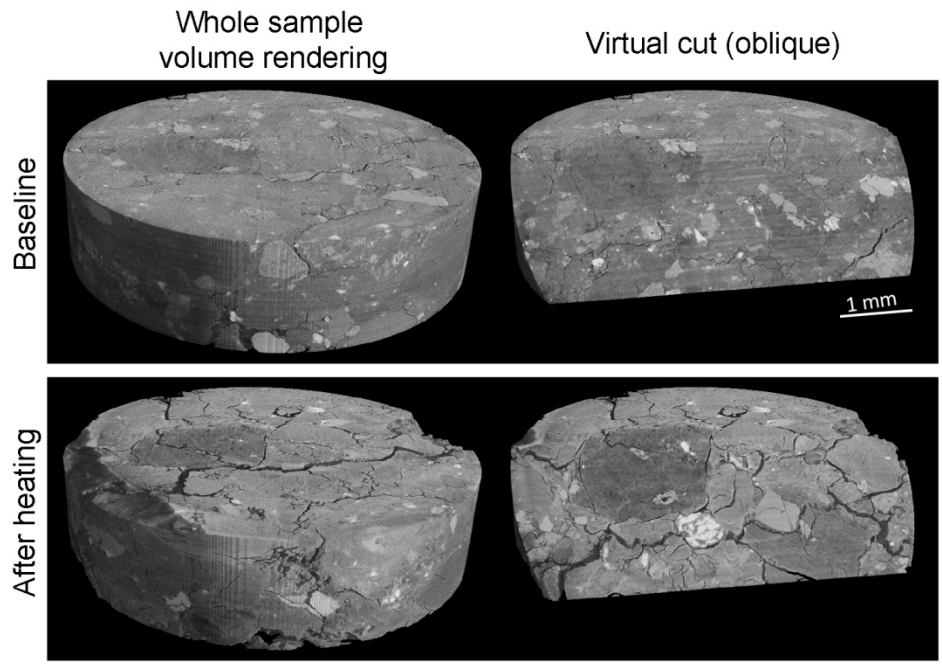

Figure 4.61. Sample from BD-59-3 before and after heating. A virtual cut of the sample is also shown to better appreciate the interior of the sample.

The results displayed in Figure 4.61 clearly show a dramatic increase in the number and size of the fractures. Different fracturing mechanisms can be observed here as well, with fractures connecting different aggregate particles, running along their interfaces, but through them as well. In addition to that, an extensive network of small fractures also develops in the clay-rich parts of the sample.

Although we have observed rapid development of fractures after heating it is noteworthy that such a case would be very unlikely in a real use case scenario, where a constant supply of moisture should be provided by the host rock, so that the migration of moisture would be limited by the surrounding material; and the confining stress of the bentonite barrier would make the development of fractures more difficult. Nevertheless such an experiment does give an insight of development of fractures in bentonite, i.e., fractures would be created along the interfaces of clay aggregates and through the aggregates as well.

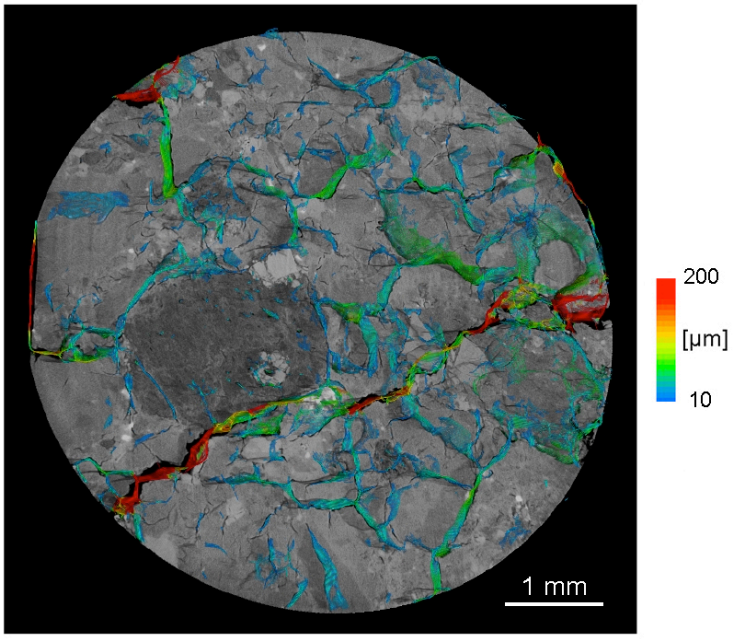

Figure 4.62. Thin horizontal slice of the sample BD-59-3 after heating. A thicker volume of the LT labeled medial axes of the fractures has been superimposed to highlight the topological features of the fractures network.

The development of the fracture network after heating is rather dramatic. As shown in Figure 4.62, samples after heating have much larger aperture values (the scale in this figure is linear, since there was no need to use a logarithmic scale as for the previous fracture network datasets) and a more pervasive fracture network was developed than what was observed in the sample before heating. Major fractures running across the whole sample are present, with a very large number of small fractures (see the blue values), which create a very dense network of connected fractures.

An analysis focusing on the quantitative comparison of the fracture networks before and after the heating process is still ongoing.

4.5.5.3 High resolution SXR-µCT

The analyses presented in Section 4.5.5.1 used a resolution of 3.22 µm, trying to balance the sample size and the imaging resolution, finding the best compromise between the smallest fractures we were able to detect, while trying to maximize the actual volume of the sample analyzed. The parameters measured show significant variability, but also some weak trends depending of the sample. Because measuring and analyzing very large numbers of volumes would be highly impractical due to the time required for both the measurement and the analysis, in section 4.5.5.1, we focused on checking fracture apertures distributions for various samples with duplicates using a resolution of 3.22 µm. However, such resolution may not allow us to detect nanoscale features, which are known to be important for clay-rich materials. All the imaging techniques, by their very nature, deal with the resolution vs. field of view issue: high-resolution means smaller volume, therefore the statistical meaningfulness rapidly decreases. On the other hand, large volumes analyzed at low resolution might miss some fundamental characteristics. In this context we have decided to carry out a measurement at much higher resolution (633 nm per voxel) on the sample BD48-7. Given the higher resolution the usable volume investigated is a ~1 mm large cylinder.

The main target is to see how much of the smaller features, below the resolution of the measurements described in Section 4.5.5.1, are missed using the lower resolution scans, and to check if those are important.

The graphical results are shown in Figure 4.63, where the segmented volume of the voids (fractures + micropores) has been highlighted in red.

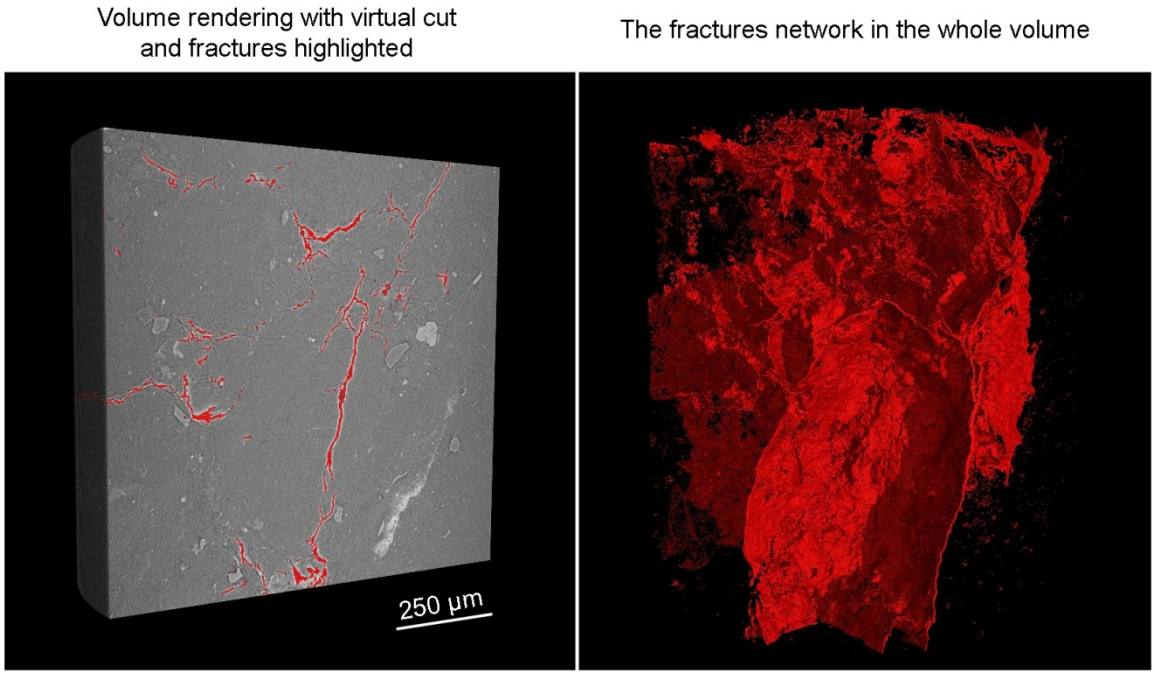

Figure 4.63. Results from the high-resolution SXR-µCT measurement on sample BD-48-7. The voids have been highlighted in red.

Figure 4.63 shows that the separation of the voids (fractures and micro- and nano-pores) looks correct. From a simple qualitative point of view it is possible to see that the amount of fractures with aperture values close to the resolution is relatively low. This observation, if confirmed by a quantitative analysis, would be very important since it would tell that very high-resolution measurements are not strictly necessary to obtain a comprehensive description of the fracture network. On the other hand, some features visible only at this resolution are present: more specifically nanoporosity present in some specific aggregate particles becomes visible, and measurable, at this resolution. Another important topic is the overall quality of the data used to obtain the quantitative description of the fracture network: being described by a much larger amount of voxels, the fractures in this sample are easier to analyze, and with greater accuracy, providing better quality results. In addition, having information at this scale would help in getting more accurate information about the connectivity. The resolution of the measurements in 4.5.5.1 has been proven good enough to obtain a sufficiently accurate description of the aperture distributions of the fractures in the sample, but the connectivity of fractures can be on smaller scales that even if their importance from a volumetric point of view is negligible, and while their detection may have limited utility for the purposes of many topological parameters aimed at the description of the framework, some physical properties, such as permeability, can be impacted by the presence of nanometric connections building a connected, and thus significantly more permeable, material. Hence, it is important to have high-resolution datasets in case permeability models are to be employed to model realistic hydraulic properties for these samples.

A comprehensive characterization of the fracture network in this volume, to compare it directly with a low-resolution volume from the same sample, is ongoing.

4.6 SUMMARY AND FUTURE WORK

4.6.1 Coupled THMC Modeling of FEBEX *in situ* Test

The FEBEX *in situ* test that lasted more than eighteen years is extremely valuable for validating the coupled THMC model and deepening our understanding of the evolution of the bentonite barrier over the course of heating and hydration. In the FEBEX-DP project, heater #2 was dismantled and extensive THMC characterization was conducted. LBNL/DOE joined the FEBEX-DP in FY15. The ultimate goal is to use THMC data from FEBEX-DP to validate THMC models and therefore enhance our understanding of coupled THMC processes in bentonite.

In FY15, TH model with Non-Darcian flow and the THC model were developed and sensitivity to key parameters was conducted. Model results showed that including Non-Darcian flow into the TH model led to a significant underestimation of the relative humidity data in the entire bentonite barrier. In FY16, the THC model was extended to THMC models and mechanical processes were simulated using both linear swelling model and dual structure BExM. The results from THMC models match reasonably the measured temporal evolution of temperature, relative humidity and stress at several compliance points in the bentonite barrier and the measured spatial distribution of water content and dry density at 5.3 years when the heater #1 was dismantled and at 18.3 years when the heater #2 was dismantled. However, the THMC models failed to explain the spatial profile of concentration at 5.3 years. The major findings from current modeling work are as follows:

- As expected, the THMC model outperformed the THC model in terms of matching measured THM data. Permeability and porosity changes due to mechanical process (swelling) were the key to matching all the THM data.
- The THMC model using complex double structure BExM (THMC-BExM) did not clearly outperform the THMC model using linear swelling model (THMC-LS) in terms of matching the measured data. THMC-BExM led to a slightly better fit of measured relative humidities and stress near the heater and a slightly worse fit to the measured water content and dry density at 18.3 years. Although BExM is a more mechanistic approach and describes structural details of bentonite (the micro- and macro-structure of bentonite), it failed to manifest its superiority to the simple linear swelling model, which is probably due to that the THM data including relative humidity, stress, dry density and water content are all macroscopic such that these data cannot delineate the more mechanistic BExM from a linear swelling model.
- Although the THMC models successfully matched the THM data, they failed to desirably match the measured concentration profile of conservative species (chloride) at 5.3 years and subsequently the concentration profile of reactive species. The concentration profiles of cations (calcium, potassium, magnesium and sodium) were largely shaped by transport processes despite that their concentration levels were affected by mineral dissolution/precipitation and cation exchange. The concentration profile of pH, bicarbonate and sulphate were largely determined by chemical reactions.
- Revising the function for permeability changes in the THMC model improved the goodness-of-fit to chloride concentration profile but deteriorated the fit to water content data. It seemed there was a dilemma that the THMC model cannot match both the THM and chemical data simultaneously, suggesting that additional processes might be needed in the conceptual model.

- The THMC model predicted that concentration levels of major cations and anions at 18.3 years when the heater #2 was dismantled would continue going down in most parts of the bentonite barrier except the area very close to the heater, where the concentration would go up, which will be compared with concentration data that are expected to be available by the end of 2016.
- In the remaining months of FY16 and FY17, the following work is planned:
- Thermal osmosis, a moisture movement driven by the thermal gradient, has already been incorporated in the simulator TOUGHREACT-FLAC3D. We will test if the THMC model with thermal osmosis can match both the THM data and the concentration profile of chloride.
- Once the THMC model is calibrated against THM data and measured concentration data at 5.3 years, it will be used to interpret the concentration data for 18.3 years that are expected to be available by the end of 2016.
- The chemical model will be fine-tuned, especially regarding redox condition evolution in the bentonite barrier and bentonite-canister interaction, and evolution of gases such CO_2, CH_4 and H_2.

Ultimately, after the THMC models for FEBEX *in situ* test are fully validated with data, they will used to explore THMC changes in the long run under higher temperature.

4.6.2 Quantitative characterization of the fracture network in the FEBEX samples

Although the comparison between model and THMC data has been very helpful in calibrating the "right" relationships (or key parameters for the relationships), uncertainties in other processes and interaction of coupled processes might results in non-unique sets of parameters that could lead to equal or similar reasonable fit between model and data. Checking the microstructure of the bentonite buffer will serve as additional evidence to delineate the right permeability change functions and increase the predictability of models. Bentonite samples were taken from the FEBEX *in situ* test after the dismantling of heater #2. In FY16, we have conducted a series of synchrotron X-ray microCT (SXR-μCT) examination of the microstructure of bentonite samples. The major accomplishments are as follows:

- A total of 5 samples from different locations were examined with three duplicates for each sample. Fracture networks for each sample were obtained and quantified. We found that the variability among duplicates from the same location in bentonite barrier is significant, mostly linked to the heterogeneity of the material. Nevertheless some weak correlation has been found: the ratio of large to small aperture fractures is larger from samples with higher water content (they are also close to the bentonite/granite interface). In other words, samples closer to the bentonite/granite interface tend to have a larger amount of large fractures, whereas samples close to the heater or to the center of the section tends to have larger amount of small fractures. While a truly statistically meaningful validation of this result is still needed, this correlation is clearly present in our sample survey. It is noteworthy that a larger amount of measurements would be experimentally impractical to carry out, and the quantitative analyses of 5 different samples with 3 duplicates for each sample that were accomplished in this report is already something not commonly found in the XR-μCT literature.
- XR-μCT imaging was also conducted for a sample at the "as is" state (the state that we received from the FEBEX *in situ* test) and a heated state. Comparison between the fracture network before and after heating showed heating completely modified the microstructure of the material, generating a pervasive network of fractures, both very large in size with a thick network of small ones especially in the clay aggregates of the sample, but whether this is due to the heating itself or moisture loss over the course of heating needs further study. While we are fully aware that the

sample was heated under different conditions than what would be expected in the field, such an exercise seems to emphasize the importance of keeping bentonite well hydrated to ensure a good sealing effect.

- During the experiment, we also addressed some important technical issues: (1) we have found *the best resolution vs. field of view compromise, and representativeness issues as well.* We have tried to maximize the analyzed volume while avoiding losing important details due to too low resolution. (2) *We have successfully developed a protocol/software for the analysis of the fracture network, focusing on the aperture value distributions.*

At this stage, the results suggest that SXR-μCT is an ideal tool for checking the micro-structure of clay-based backfill for nuclear waste repository, and providing some quantitative parameters to directly compare different samples. This opens new opportunities to advance the research in the bentonite barrier such as:

- *Testing the behavior of different candidate sealing materials before deploying them.* This includes advanced characterization (multi-technique, when needed) and *in situ* experiments. As an example, analyses could be conducted to check different clay vs. aggregate ratios, different type of clays, the use of surfactants / antiflocculants / interlayer exchangeable molecules / etc. to obtain clay aggregates with different mechanical properties and/or response to dehydration, or even completely different sealing materials. The ability of *in situ* heating also provides the unique opportunity to see directly the modification of the sample during the loss of moisture. XR-μCT can also be coupled with other XR scattering-based techniques when a precise correlation with the hydration state of the clay structure (wide-angle X-ray powder diffraction) or the size of the clay tactoids (small-angle X-ray scattering) needs to be directly correlated with the development of desiccation cracks (e.g. Suuronen et al. 2014).
- *Using the measured datasets to build predictive tools.*
  Besides the visualization and quantitative characterization of the sealing materials, SXR-μCT is also able to provide 3D volume datasets which can be used in a digital rock physics context: if the volume(s) obtained are meaningful, in terms of resolution vs. field of view, for measuring a given property, specific software able to calculate those properties (such as permeability, invasion of non-wetting fluids, diffusion, etc.) from the datasets are available or under development. This ability of calculating some physical properties of the samples following the SXR-μCT measurement would end the path that started from the scientific question and would result with a predictive tool available to the scientific community.

4.7 References

Alonso, E. E., J. Vaunat and A. Gens 1999. Modeling the mechanical behaviour of expansive clays. Engineering Geology 54: 173-183.

Bárcena, I., Fuentes-Cantillana, J.L. & García-Siñeriz, J.L. (2003). Dismantling of the Heater 1 at the FEBEX "in situ" test. Description of operations. Enresa Technical Report 9/2003.

Bear, J., (1972). Dynamics of fluids in porous media. American Elsevier Publishing Company Inc, New York. ISBN 0-486-65675-6.

Bradbury, B., Baeyens, B., (2003). Porewater chemistry in compacted resaturated MX-80 bentonite. Journal Contaminant Hydrology 61, 329–338.

Bradbury, M. H. and B. Baeyens (2005). Modelling the sorption of Mn(II), Co(II), Ni(II), Zn(II), Cd(II), Eu(III), Am(III), Sn(IV), Th(IV), Np(V) and U(VI) on montmorillonite: Linear free energy relationships and estimates of surface binding constants for some selected heavy metals and actinides. Geochimica et Cosmochimica Acta 69(4): 875-892.

Bradbury, M.H., Baeyens, B., (1998). A physicochemical characterisation and geochemical modelling approach for determining porewater chemistries in argillaceous rocks. Geochimica et Cosmochimica Acta 62, 783–795.

Castellanos, E., M. V. Villar, E. Romero, A. Lloret and A. Gens 2008. Chemical impact on the hydro-mechanical behaviour of high-density FEBEX bentonite. Physics and Chemistry of the Earth, Parts A/B/C 33, Supplement 1(0): S516-S526.

Chen, Y., Zhou, C., Jing, L., (2009). Modeling coupled THM processes of geological porous media with multiphase flow: theory and validation against laboratory and field scale experiments. Computers and Geotechnics 36 (8), 1308–1329.

Clifford K.H. and Webb S.W. (1996). A Review of Porous Media Enhanced Vapor-Phase Diffusion Mechanisms, Models, and Data – Does Enhanced Vapor-Phase Diffusion Exist? Sandia National Laboratories Albuquerque, NM. SAND96-1198

Cui YJ, Tang AM, Loiseau C, Delage P (2008). Determining the unsaturated hydraulic conductivity of a compacted sand-bentonite mixture under constant-volume and free-swell conditions. Physics and Chemistry of the Earth 33, S462-S471

Daucousse D. Lloret A. (2003) Results of “in situ” measurements of water content and dry density, Technical report, Polytechnic University of Catalonia, 70-UPC-L-5-012.

David C, Wong T-F, Zhu W, Zhang J. (1994) Laboratory measurement of compaction-induced permeability change in porous rocks: Implications for the generation and maintenance of pore pressure excess in the crust. Pure Appl. Geophys. 1994;143:425-456.

Detzner K. and Kober F. (2015) FEBEX-DP drilling and sampling report sections 32-34, Internal report, AN15-714, NAGRA.

Dougherty, R. and Kunzelmann, K.H., 2007. Computing local thickness of 3D structures with ImageJ. Microscopy and Microanalysis, 13(S02), pp.1678-1679.

ENRESA (2000). Full-scale engineered barriers experiment for a deep geological repository in crystalline host rock FEBEX Project, European Commission: 403.

ENRESA, (2006a). FEBEX: Updated final report. ENRESA Tech. Publ. PT 05-0/2006, 589 pp.

ENRESA, (2006b). FEBEX: Final THG modelling report. ENRESA Tech. Publ. PT 05-3/2006, 155 pp.

Fernández, A. M., B. Baeyens, M. Bradbury and P. Rivas (2004). Analysis of the porewater chemical composition of a Spanish compacted bentonite used in an engineered barrier. Physics and Chemistry of the Earth, Parts A/B/C 29(1): 105-118.

Fernández, A., Rivas, P., (2003). Task 141: post-mortem bentonite analysis. geochemical behaviour. CIEMAT/DIAE/54520/05/03, Internal Note 70-IMA-L-0-107 v0.

Fernández, A.M., Cuevas, J., Rivas, P. (2001). Pore water chemistry of the FEBEX bentonite. Mat. Res. Soc. Symp. Proc. 603, 573-588.

Fernández, A.M., Rivas, P., (2005). Pore water chemistry of saturated FEBEX bentonite compacted at different densities. In: Alonso, E.E., Ledesma, A. (Eds.), Advances in Understanding Engineered Clay Barriers. A.A Balkema Publishers, Leiden, The Netherlands, pp. 505–514.

Garcia-Sineriz, J.L., Abós, H., Martínez, V., De la Rosa, C., Mäder, U. and Kober, F. (2016): FEBEX-DP Dismantling of the heater 2 at the FEBEX "in situ" test. Nagra Arbeitsbericht NAB 16-011. p. 92

Ghabezloo S, Sulem J, Guédon S, Martineau F. Effective stress law for the permeability of a limestone. Int. J. Rock Mech. Min. Sci. 2009;46:297-306.

Huertas, F. B. de la Cruz, J. L. Fuentes-Cantillana, et al. (2005). Full-Scale Engineered Barriers Experiment for a Deep Geological Repository for High-Level Waste in Crystalline Host Rock – Phase II. EUR 21922

Itasca, (2009). FLAC3D, Fast Lagrangian Analysis of Continua in 3 Dimensions, Version 4.0, Minneapolis, Minnesota, Itasca Consulting Group.

Kak, A.C. and Slaney, M., 1988. Principles of computerized tomographic imaging (pp. 5-47). IEEE press.

Kwon O, Kronenberg AK, Gangi AF, Johnson B. Permeability of Wilcox shale and its effective pressure law. J. Geophys. Res.-Sol. Ea. 2001;106:19339-53.

Kuhlman U., Gaus I. (2014). THM Model validation modelling of selected WP2 experiments:Inverse Modelling of the FEBEX in situ test using iTOUGH2. DELIVERABLE-N°: D3.3-1, NAGRA.

LaManna, J. M. and S. G. Kandlikar 2011. Determination of effective water vapor diffusion coefficient in pemfc gas diffusion layers. International Journal of Hydrogen Energy 36(8): 5021-5029.

Liu, H.-H. and J. Birkholzer (2012). On the relationship between water flux and hydraulic gradient for unsaturated and saturated clay. Journal of Hydrology 475: 242-247.

Liu, H.H., J. Houseworth, J. Rutqvist, L. Zheng, D. Asahina, L. Li, V. Vilarrasa, F. Chen, S. Nakagawa, S. Finsterle, C. Doughty, T. Kneafsey and J. Birkholzer. (2013). Report on THMC modeling of the near field evolution of a generic clay repository: Model validation and demonstration, Lawrence Berkeley National Laboratory, August, 2013, FCRD-UFD-2013-0000244.

Lloret A, Villar MV, Sánchez M, Gens A, Pintado X, Alonso EE. Mechanical behaviour of heavily compacted bentonite under high suction changes. Géotechnique 2003; 53(1):27–40.

Lloret, A., Alonso, E.E., 1995. State surfaces for partially saturated soils, In proceedings of the International Conference on Soils Mechanics and Foundation Engineering, Balkema, pp. 557-562.´

MacDowell, A.A., Parkinson, D.Y., Haboub, A., Schaible, E., Nasiatka, J.R., Yee, C.A., Jameson, J.R., Ajo-Franklin, J.B., Brodersen, C.R. and McElrone, A.J., 2012, October. X-ray micro-tomography at the Advanced Light Source. In SPIE Optical Engineering+ Applications (pp. 850618-850618). International Society for Optics and Photonics.

Pruess, K., C. Oldenburg and G. Moridis (1999). TOUGH2 User's Guide, Version 2.0, Lawrence Berkeley National Laboratory, Berkeley, CA.

Pusch, R. and Madsen, F. T. (1995). Aspects on the illitization of the kinnekulle bentonites. Clays and Clay Minerals 43(3): 261-270.

Ramírez, S., J. Cuevas, R. Vigil and S. Leguey (2002). Hydrothermal alteration of "La Serrata" bentonite (Almeria, Spain) by alkaline solutions. Applied Clay Science 21(5–6): 257-269.

Rutqvist, J., Y. Ijiri and H. Yamamoto 2011. Implementation of the Barcelona Basic Model into TOUGH–FLAC for simulations of the geomechanical behavior of unsaturated soils. Computers & Geosciences 37(6): 751-762.

Rutqvist, J., Zheng, L., Chen, F., Liu, H.-H. and Birkholzer, J. (2013). Modeling of Coupled Thermo-Hydro-Mechanical Processes with Links to Geochemistry Associated with Bentonite-Backfilled Repository Tunnels in Clay Formations. Rock Mechanics and Rock Engineering: 1-20.

Sacchi, E., Michelot, J.L., Pitsch, H., Lalieux, P., Aranyossy, J.F., (2001). Extraction of water and solution from argillaceous rock for geochemical characterisation: methods, processes, and current understanding. Hydrogeology Journal 9, 17–33.

Samper, J., L. Zheng, A. M. Fernández and L. Montenegro (2008b). Inverse modeling of multicomponent reactive transport through single and dual porosity media. Journal of Contaminant Hydrology 98(3–4): 115-127.

Samper, J., L. Zheng, L. Montenegro, A. M. Fernández and P. Rivas (2008a). Coupled thermo-hydro-chemical models of compacted bentonite after FEBEX in situ test. Applied Geochemistry 23(5): 1186-1201.

Sánchez, M., A. Gens and L. Guimarães (2012a). Thermal–hydraulic–mechanical (THM) behaviour of a large-scale in situ heating experiment during cooling and dismantling. Canadian Geotechnical Journal 49(10): 1169-1195.

Sánchez, M., A. Gens and S. Olivella (2012b). THM analysis of a large-scale heating test incorporating material fabric changes. International Journal for Numerical and Analytical Methods in Geomechanics 36(4): 391-421.

Sánchez, M., A. Gens, L. J. D. N. Guimarães and S. Olivella (2005). A double structure generalized plasticity model for expansive materials. International Journal for numerical and analytical methods in geomechanics 29: 751-787.

Schindelin, J., Arganda-Carreras, I., Frise, E., Kaynig, V., Longair, M., Pietzsch, T., Preibisch, S., Rueden, C., Saalfeld, S., Schmid, B. and Tinevez, J.Y., 2012. Fiji: an open-source platform for biological-image analysis. Nature methods, 9(7), pp.676-682.

Siitari-Kauppi, M., Leskinen, A., Kelokaski, M., Togneri, L. Alonso, U., Missana, T., García - Gutiérrez, (2007). Physical Matrix Characterisation: Studies of Crystalline Rocks and Consolidated Clays by PMMA Method and Electron Microscopy as Support of Diffusion Analyses. CIEMAT Technical Report, 1127, December 2007.

Suuronen, J.P., Matusewicz, M., Olin, M. and Serimaa, R., 2014. X-ray studies on the nano-and microscale anisotropy in compacted clays: Comparison of bentonite and purified calcium montmorillonite. Applied Clay Science, 101, pp.401-408.

Van Genuchten, M. T. 1980. A closed-form equation for predicting the hydraulic conductivity of unsaturated soils. Soil science society of America journal 44(5): 892-898.

Vilarrasa, V., J. Rutqvist, L. B. Martin and J. Birkholzer 2015. Use of a Dual-Structure Constitutive Model for Predicting the Long-Term Behavior of an Expansive Clay Buffer in a Nuclear Waste Repository. International Journal of Geomechanics 0(0): D4015005.

Villar, M.V. 2002. Thermo-hydro-mechanical characterisation of a bentonite from Cabo de Gata: a study applied to the use of bentonite as sealing material in high-level radioactive waste repositories. ENRESA, Madrid. Technical Publication 01/2002.

Voltolini, M., Zandomeneghi, D., Mancini, L. and Polacci, M., 2011. Texture analysis of volcanic rock samples: quantitative study of crystals and vesicles shape preferred orientation from X-ray microtomography data. Journal of Volcanology and Geothermal Research, 202(1), pp.83-95.

Wolery, T. J., (1993). EQ3/6, A software package for geochemical modelling of aqueous systems,Version 7.2. Lawrence Livermore National Laboratory, USA.

Xu, T., E. Sonnenthal, N. Spycher and K. Pruess (2006). TOUGHREACT: A Simulation Program for Non-isothermal Multiphase Reactive Geochemical Transport in Variably Saturated Geologic Media. Computers and Geosciences 32: 145-165.

Xu, T., Spycher, N., Sonnenthal, E., Zhang, G., Zheng, L. and Pruess, K. (2011). TOUGHREACT Version 2.0: A simulator for subsurface reactive transport under non-isothermal multiphase flow conditions. Computers & Geosciences 37(6): 763-774.

Zandomeneghi, D., Voltolini, M., Mancini, L., Brun, F., Dreossi, D. and Polacci, M., 2010. Quantitative analysis of X-ray microtomography images of geomaterials: Application to volcanic rocks. Geosphere, 6(6), pp.793-804.

Zheng L., Rutqvist J. Kim, K. and Houseworth J. (2015b), Investigation of Coupled Processes and Impact of High Temperature Limits in Argillite Rock. FCRD-UFD-2015-000362, LBNL-187644.

Zheng, L. and J. Samper (2008). A coupled THMC model of FEBEX mock-up test. Physics and Chemistry of the Earth, Parts A/B/C 33, Supplement 1: S486-S498.

Zheng, L. and J. Samper (2015). Dual-continuum multicomponent reactive transport with nth-order solute transfer terms for structured porous media. Computational Geosciences 19(4): 709-726.

Zheng, L. Jonny Rutqvist, Carl Steefel, Kunhwi Kim, Fei Chen, Victor Vilarrasa, Seiji Nakagawa, Jiangtao Zheng, James Houseworth, Jens Birkholzer. (2014). Investigation of Coupled Processes and Impact of High Temperature Limits in Argillite Rock. FCRD-UFD-2014-000493, LBNL-6719E

Zheng, L., J. Rutqvist, J. T. Birkholzer and H.-H. Liu 2015a. On the impact of temperatures up to 200 °C in clay repositories with bentonite engineer barrier systems: A study with coupled thermal, hydrological, chemical, and mechanical modeling. Engineering Geology 197: 278-295.

Zheng, L., J. Samper and L. Montenegro (2008). Inverse hydrochemical models of aqueous extracts tests. Physics and Chemistry of the Earth, Parts A/B/C 33(14–16): 1009-1018.

Zheng, L., J. Samper and L. Montenegro (2011). A coupled THC model of the FEBEX in situ test with bentonite swelling and chemical and thermal osmosis. Journal of Contaminant Hydrology 126(1–2): 45-60.

Zheng, L., J. Samper, L. Montenegro and A. M. Fernández (2010). A coupled THMC model of a heating and hydration laboratory experiment in unsaturated compacted FEBEX bentonite. Journal of Hydrology 386(1–4): 80-94.

Zheng, L., Li, L., Rutqvist, J., Liu, H. and Birkholzer, J.T., (2012). Modeling Radionuclide Transport in Clays. Lawrence Berkeley National Laboratory. FCRD-URD-2012-000128

This page is intentionally left blank

5. DISCRETE FRACTURE NETWORK (DFN) APPROACH FOR THM DAMAGE MODELING IN ARGILLACEOUS ROCK

In this section, we present LBNL's activities related to development, testing, and applications of a discrete fracture network (DFN) approach for modeling THM induced damage and fracturing in argillaceous rocks. In argillaceous rocks, fractures are major factors that change hydrological and mechanical properties of the rock materials. Although clay-rich formations usually exhibit low intrinsic rock permeability with very limited fracture permeability, under certain conditions permeable fracture networks occur leading to the increase of rock permeability (Cosgrove, 2001; Bossart et al., 2004). Herein, two classes of fracturing processes are investigated: 1) fracture propagation induced by fluid overpressure; and 2) fracture-damage due to stress redistribution around an excavation in the excavation damage zone (EDZ).

The former class may involve rather vigorous hydro-mechanical interactions of fluid contents within clay-rich formations. In various scenarios of pressure change of fluid contents, limited fluid flow arises very slowly due to the low permeability of rock matrix. Consequently, the rock systems are not in pressure equilibrium, and the pressure conditions can trigger fault reactivation and hydraulic fracturing (Gonçalvès et al., 2004). Geologic evidence of natural fractures suggests that the Mercia Mudstone within the Bristol Channel Basin in the UK was subject to repeated episodes of natural hydraulic fracturing over its 250 million year history (Cosgrove, 2001). Also, fluid-driven fracturing processes are often addressed in many geo-engineering applications. For example, hydraulic fracturing and stimulation of fracture networks are utilized by the energy industry (e.g., shale gas extraction, enhanced geothermal systems) to increase permeability of geological formations (Freeman et al., 2011; Zimmermann and Reinicke, 2010). From the opposite perspective, related to underground storage of nuclear waste or CO_2, fracturing of the repository rock could be detrimental for geo-environmental issues due to increasing the risk of contaminant leakage (Bossart et al., 2004; Chiaramonte et al., 2008).

As the latter class, fractures in the EDZ have been routinely observed in clay-rock underground research laboratories (URLs) in Europe, including the Opalinus Clay at Mont Terri URL, Switzerland, Boom Clay at MOL in Belgium, and the Callovo-Oxfordian Clay at Bure in France (Volckaert et al., 2004). These fractures mainly form as a consequence of static and dynamic stress disturbance by excavation (Bossart et al., 2002). However, other effects, such as shrinkage caused by ventilation dry-out during the pre-closure phase, and thermal pressurization and gas evolution expected after closure, may also result in fracturing (Blümling et al., 2007). The EDZ not only exhibits fracturing along tunnel surfaces, but can contain fracture damage in thin zones (<~1 m) around drifts, which has been verified from measurements of permeability in that area (Bossart et al., 2004). The connectivity of fractures along a tunnel has been observed in the HG-A test at Mont Terri, Switzerland, where a test tunnel section, backfilled with sand and sealed by a packer, was saturated and a series of water injection tests were performed. In the test results, non-uniform pressure increases along the packer sleeve were monitored, which indicates preferential fluid flow paths formed by heterogeneous fracture damage around the excavation zone (Lanyon et al., 2009).

This report covers an overview of the modeling approach, including coupled THM processes in the simulation code and representation of mechanical anisotropy, in Sections 5.1. The simulation code combines TOUGH2 with the rigid-body-spring network (RBSN) model, which enables a discrete representation of fractures and fracture networks in rock formations. In Section 5.2, the TOUGH-RBSN code is validated against the laboratory experiments for hydraulic fracture propagation in rock-analogue samples and sensitivity analyses are conducted through qualitative comparisons of simulations results for which reservoir configurations are changed. Section 5.3 presents anisotropic failure characteristics in the simulations of uniaxial compression tests and a tunnel excavation process in the presence of discrete faults, in which the simulation results are compared with the theory and the field-test observations.

5.1 METHODOLOGY

5.1.1 Model discretization

The computational domain for both the TOUGH2 and RBSN calculations is tessellated using a Voronoi diagram (Okabe et al., 2000). The discretization process is carried out basically in three steps: 1) nodal point insertion; 2) Delaunay tessellation; and 3) Voronoi discretization. Within the domain, nodal points are positioned in regular or irregular formation. For random point generation, a minimum allowable distance l_{min} is used to define the desired nodal density of the unstructured grid. The Delaunay tessellation is conducted based on the nodal positions, where each Delaunay edge defines the nodal connection of the corresponding lattice element. Through the dual Voronoi tessellation, the spatial domain is collectively filled with discrete polyhedral cells that render the elemental volumes. More detailed procedure of the domain partitioning is presented elsewhere (Yip et al., 2005; Asahina and Bolander, 2011).

The Voronoi discretization is not only an effective method for partitioning a spatial domain, but is also an essential part of the RBSN model formulation. The Voronoi diagram serves to scale the element coefficients for the system equations. Also, the availability of sharing the same grid geometry for the TOUGH2 and RBSN models enables a tight coupling without any spatial interpolation of primary variables.

For the discrete fracture network (DFN) approach, fractures and such discontinuities are explicitly modeled within the Voronoi grid. Voronoi cells generally represent the matrix component in a geomaterial constitution, and pre-existing or newly generated fractures are placed on the Voronoi cell boundaries. The geometry of fracture networks (e.g., orientation, length, curvature) can be obtained by observational mapping data, computer-generated statistical reproductions, or mechanical simulation results. An example of the discretization procedure in 2D modeling involving a straight fracture is as follows:

i. Generate a Voronoi unstructured grid for the spatial domain.
ii. Overlay the reference fracture trajectory onto the grid.
iii. Test all connections of natural neighboring nodes to check if they cross the fracture. For example, compare connections ij and jk in Figure 5.1.
iv. The collection of the Voronoi cell boundaries corresponding to the nodal connections that cross the reference fracture (such as ij) forms discretized fractures.

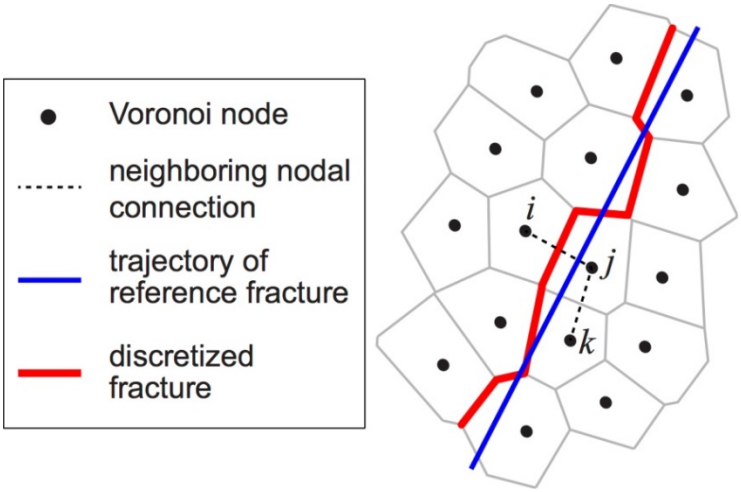

Figure 5.1. Fracture mapping and discretization within an unstructured Voronoi grid.

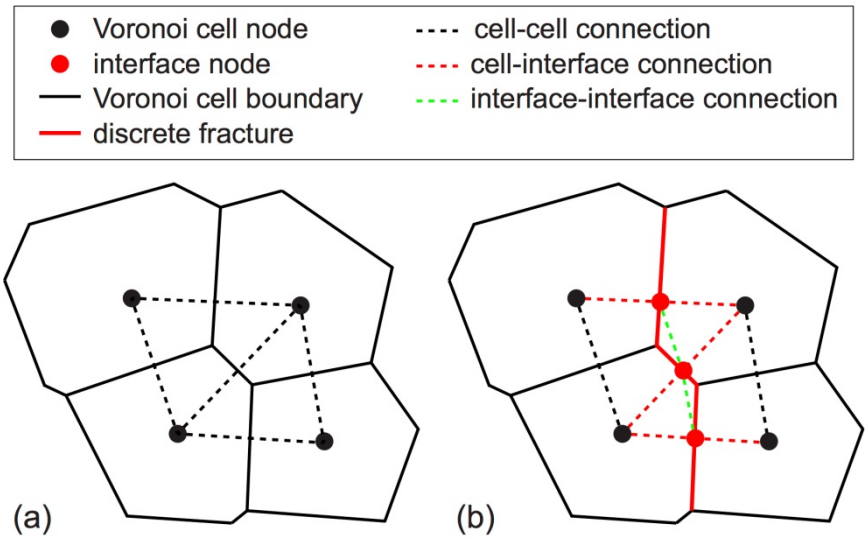

Figure 5.2. Introduction of interface nodes and additional connections for flow through discrete fractures: a) original Voronoi cell nodes and connections; and b) insertion of interface nodes and connections.

By repeating the above process for multiple fractures, a network of discrete fractures can be generated. This fracture discretization process is completely automated and can be easily extended to more complicated geometries in 3D modeling. However, the grid size should be carefully chosen to obtain a sufficiently accurate representation of the reference fracture. With a finer grid, the discretized fractures correspond more closely to the reference fracture, but the computational expense may be increased.

In the TOUGH2 simulations using a grid structure of the ordinary Voronoi discretization, flow and mass transfer are enacted only through the connections of the neighboring Voronoi nodes (called cell-cell connections in Figure 5.2 (a). However, if fracturing occurs within the matrix, substantial flow may arise through the fracture path. For the DFN approach, a modification of the grid structure is proposed, in which dynamic formation of flow channels along the fractures is facilitated by introducing additional interface nodes and the associated connections. As shown in Figure 5.2 (b), an interface node is inserted where the cell-cell connection intersects the Voronoi cell boundary. The original cell-cell connection is divided into two cell-interface (and vice versa) connections by the interface node. In addition, the connections between the interface nodes are established to activate flow channels in discrete fractures.

Fluid flow through fractures is assumed to conform with Darcy's law (Witherspoon et al., 1980), and hydrological properties (e.g., porosity and permeability) of a discrete fracture can be evaluated from the grid geometry and the fracture aperture width. The fracture aperture can be either assigned as a pre-existing fracture property or explicitly measured from the mechanical-damage computation of the RBSN model. A parallel-plate mode (Bear 1972) is applied to define fracture permeability, which is related to a hydraulic aperture within the validity of cubic law for Darcy flow.

5.1.2 Hydrological and mechanical coupling in TOUGH-RBSN

This section describes the linkage between the TOUGH2 simulator and the RBSN approach. The hydrological and mechanical codes are sequentially coupled to each other, where the general procedure is similar to that applied for the TOUGH-FLAC simulator (Rutqvist et al., 2002; Rutqvist, 2011). However, the TOUGH-RBSN coupling modules have been substantially modified to account for the fluid flow through discrete fractures.

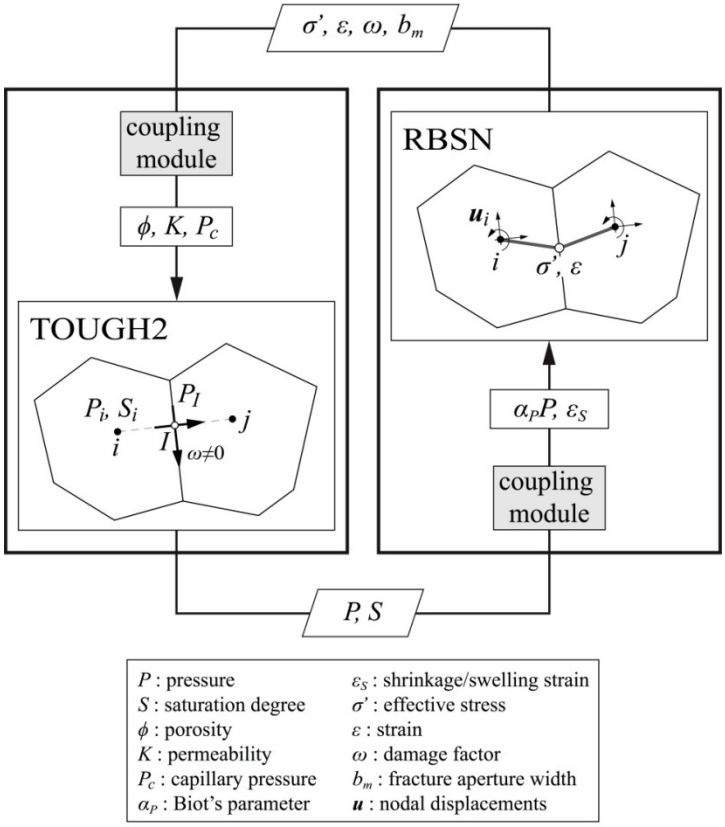

Figure 5.3. Flow diagram of the TOUGH-RBSN coupling procedure.

Figure 5.3 shows a schematic flow diagram of the coupling procedure between the TOUGH2 and RBSN codes. Coupling modules are implemented in each side of the modeling codes, by which material properties and mechanical boundary conditions are updated with the outputs of primary variables of physical quantities. As aforementioned, an advantage from sharing the same Voronoi grid geometry in the TOUGH-RBSN simulator is that the primary variables are highly correlated at the same nodal position and thus the data exchange between the two models is straightforward during the coupling procedure.

First, the TOUGH2 to RBSN link supplies pressure and degree of saturation to update the mechanical quantities. From the pore pressure P, the effective (grain-to-grain) stress $\sigma_n{}'$, applied to the normal spring of a lattice element, is calculated using Biot's theory (Biot and Willis 1957):

$$\sigma_n{}' = \sigma_n + \alpha_p P \tag{5.1}$$

where σ_n is the total normal stress obtained from overall loading, including external loads; α_p is Biot's effective stress parameter. Note that tensile stress is taken to be positive for the sign convention in this report. The effective stress in a lattice element ij can be calculated by averaging the pressure at nodes i and j, for which Equation (5.1) is transformed into an incremental form:

$$\Delta\sigma' = \Delta\sigma + \alpha_p(\Delta P_i + \Delta P_j)/2 \tag{5.2}$$

where ΔP_i and ΔP_j are the pressure increments at nodes i and j, respectively. If the element ij corresponds to an interface node I for the activated fluid flow through the fracture, the effective stress increment can be described as

$$\Delta\sigma' = \Delta\sigma + \alpha_p \Delta P_I \quad 5.3$$

where ΔP_I is the pressure increment at node I in the TOUGH2 model. Also, the shrinkage/swelling effect due to the local changes of liquid saturations can be taken into account:

$$\Delta\varepsilon_s = \alpha_s(\Delta S_i + \Delta S_j)/2 \quad 5.4$$

where ε_s is shrinkage/swelling strain; and α_s is the hydraulic shrinkage coefficient. If a poroelastic geomaterial is subjected to confinement conditions, the effective stress can be affected by the swelling/shrinking strain as

$$\Delta\sigma' = \Delta\varepsilon_s E \quad 5.5$$

where E is the Young's modulus.

Next, the RBSN to TOUGH2 link supplies the effective stress and the strain calculated in the lattice element to update the hydrological properties of the corresponding TOUGH2 grid blocks i and j. Porosity, permeability, and capillary pressure are generally related with the effective stress and strain values (Rutqvist and Tsang, 2002).

If fracturing occurs at element ij (i.e., $\omega \neq 0$), the associated fracture node I and additional connections are activated in the TOUGH2 model. The permeability of an individual fracture depends on the hydraulic aperture b_h (Witherspoon et al., 1980). According to a parallel-plate model, the fracture permeability is defined as $b_h^2/12$. The hydraulic aperture is coupled to the mechanical aperture b_m (Rutqvist et al., 1998, 2000):

$$b_h = b_{hr} + f b_m \quad 5.6$$

where b_{hr} is the residual hydraulic aperture and $f \leq 1.0$ is a dimensionless factor that accounts for the slowdown of flow in a natural rough fracture in comparison to the ideal case of parallel smooth fracture surfaces. However, herein f is set equal to unity for simplicity.

5.1.3 Implementation of mechanical anisotropy in the RBSN models

Most sedimentary and metamorphic rocks (e.g., shales and slates) have directional fabrics such as bedding, foliation, and flow structures, which result in anisotropic features in bulk-scale mechanical responses. For example, Opalinus Clay rocks exhibit transversely isotropic elastic properties, in which Young's modulus is greater in the direction parallel to bedding than normal to the bedding (Bossart, 2012). Anisotropic features may also be observed in failure responses. In this study, a novel scheme for geomechanical models is introduced to represent those anisotropic features without the need of cumbersome manipulation of the grid geometry to be aligned to the bedding fabric.

5.1.3.1 Anisotropy in elasticity

Figure 5.4 shows the arrangements of spring sets within a Voronoi grid and the corresponding lattice elements. A 2D description is provided herein for simplicity, but this scheme has been developed within 3D modeling framework. In the ordinary RBSN model, the spring sets are oriented to their individual local coordinates defined by the Voronoi diagram. However, in the new scheme, all the spring sets are aligned to the principal bedding direction. The spring coefficients are defined in global fabric coordinates, where two orthogonal *N*- and *P*-axes are normal and parallel to bedding, respectively. For a lattice element with the cross-section area A_{ij} and the element length h_{ij}, two translational spring coefficients k_N, k_P, and one rotational spring coefficient k_ϕ are calculated by using transversely isotropic Young's moduli related to the bedding direction:

$$k_N = E_N \frac{A_{ij}}{h_{ij}},\ k_P = E_P \frac{A_{ij}}{h_{ij}},\ k_\phi = E_N \frac{I_\phi}{h_{ij}} \tag{5.7}$$

where I_ϕ is the second moment of area of the element cross-section, and E_N and E_P are Young's moduli normal and parallel to bedding, respectively.

As seen in Figure 5.4, three distinct coordinate systems are considered for representation of kinematic quantities: global *X*-*Y* coordinates based on domain construction; local *x*-*y* coordinates for individual elements; and global *N*-*P* coordinates related to the orientation of fabric. For each spring set, the spring stiffness matrix is established in *N*-*P* coordinates:

$$\mathbf{k}_b = \begin{bmatrix} k_N & & \\ & k_P & \\ & & k_\phi \end{bmatrix} \tag{5.8}$$

Although the derivation is invariant to coordinate systems, it is more convenient for matrix formulation to represent and manipulate the stiffness quantities in local *x*-*y* coordinates rather than in global *N*-*P* coordinates. Thus the spring stiffness matrix, $\mathbf{k}_b$, is transformed to local *x*-*y* coordinates using following coordinate transformation (McGuire and Gallagher, 1979):

$$\mathbf{k}_s = \boldsymbol{\gamma}^T \mathbf{k}_b \boldsymbol{\gamma} \tag{5.9}$$

where $\boldsymbol{\gamma}$ is the 3×3 coordinate transformation matrix from local (*x*-*y*) to global fabric (*N*-*P*) coordinates:

$$\boldsymbol{\gamma} = \begin{bmatrix} Nx & Ny & 0 \\ Px & Py & 0 \\ 0 & 0 & 1 \end{bmatrix} \tag{5.10}$$

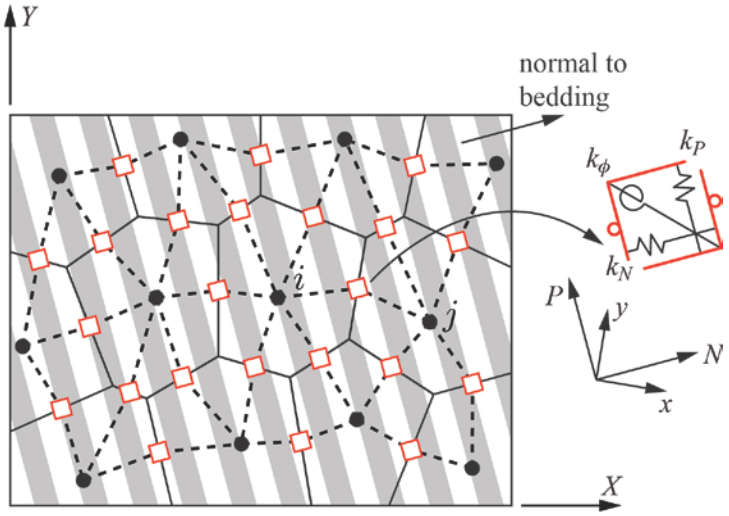

Figure 5.4. Arrangements of the spring sets in the identical lattice structure, where the spring coefficients comply with transversely isotropic elastic properties.

The first 2×2 entries in $\boldsymbol{\gamma}$ are the direction cosines between the bedding direction and the local coordinate axes. The element stiffness matrix, $\mathbf{k}_e$ (with respect to local x-y coordinates), is obtained by post- and pre-multiplication of $\mathbf{k}_s$ by the geometric transformation matrix that relates the generalized relative displacements at the spring set to the nodal displacements. Detailed formulation is presented elsewhere (Bolander and Saito, 1998; Berton and Bolander, 2006).

Finally, the element stiffness matrix is transformed to global coordinates:

$$\mathbf{K}_e = \boldsymbol{\Gamma}^T \mathbf{k}_e \boldsymbol{\Gamma} \tag{5.11}$$

where $\boldsymbol{\Gamma}$ is the coordinate transformation matrix from global domain *X*-*Y* to local *x*-*y* coordinates.

5.1.3.2 Stress tensor calculations and weak-plane failure model

Determination of local failure of a lattice element starts from evaluating the stress state based on the stress tensor calculation. The calculation of stress tensor at a Voronoi cell node is possible by considering the equilibrium conditions of the spring forces. Sets of the spring forces are applied at the boundaries surrounding a Voronoi cell (Figure 5.5 (a)), and nodal force components F_{nn}, F_{ns}, and F_{nt} can be calculated for an arbitrary section passing through the Voronoi cell node (Figure 5.5(b)) with its corresponding local *n*-*s*-*t* coordinates (Figure 5.5(c)), which satisfy the equilibrium condition with all the forces acting on the remaining cell boundaries. Moment contributions to equilibrium are not considered here. By dividing these force components by the cut-face area A_{cut}, whose normal direction is in *n*-axis, the corresponding stress components σ_{nn}, σ_{ns}, and σ_{nt} can be obtained:

$$\begin{aligned} \sigma_{nn} &= F_{nn}/A_{cut} \\ \sigma_{ns} &= F_{ns}/A_{cut} \\ \sigma_{nt} &= F_{nt}/A_{cut} \end{aligned} \tag{5.12}$$

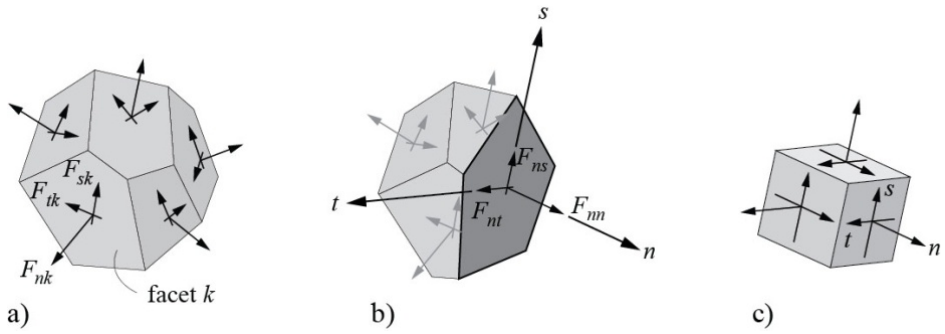

Figure 5.5. a) components of spring force local coordinates; b) a set of nodal forces satisfying the equilibrium; and c) complete stress tensor at Voronoi cell node (Adopted from Yip et al., 2005).

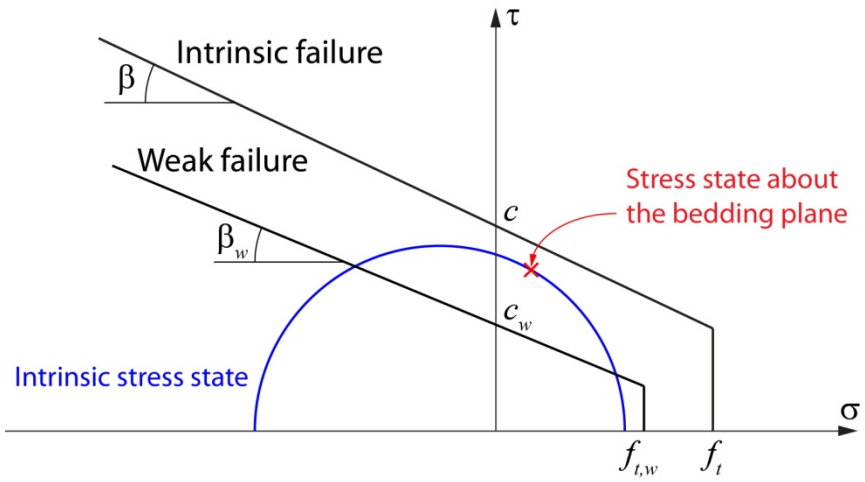

Figure 5.6. Weak-plane failure model with two different Mohr-Coulomb type criteria for intrinsic failure and weak failure.

By repeating this process for two other mutually perpendicular sections (Figure 5.5c), the full stress tensor is obtained:

$$\boldsymbol{\sigma} = \begin{bmatrix} \sigma_{nn} & \sigma_{ns} & \sigma_{nt} \\ & \sigma_{ss} & \sigma_{st} \\ Symm. & & \sigma_{tt} \end{bmatrix} \tag{5.13}$$

Consequently, the stress tensor of the inter-element is calculated by averaging the corresponding nodal stress tensor matrices:

$$\overline{\boldsymbol{\sigma}} = (\boldsymbol{\sigma}_i + \boldsymbol{\sigma}_j)/2 \tag{5.14}$$

where $\boldsymbol{\sigma}_i$ and $\boldsymbol{\sigma}_j$ are the stress tensors at the neighboring nodes *i* and *j*, respectively.

From the calculated $\overline{\boldsymbol{\sigma}}$, the Mohr circle of a lattice element can be drawn on the $\tau - \sigma$ coordinates, which will be assessed by Mohr-Coulomb type criteria to determine local failure as shown in Figure 5.6. Herein, the weak-plane model is used to represent strength anisotropy. The model assumes that the inherent strength is the same in all directions of a rock material, except for one set of parallel planes where the strength is lower. Since the bedding planes in sedimentary rocks may be planes of weakness, the model has a physical basis, and therefore it is quite important in spite of its simplicity. Two different sets of strength parameters are necessary to define the failure envelopes, which are explicitly available from typical laboratory test results. First, intrinsic strength parameters (cohesive strength c, friction angle β, and tension cut-off f_t) define a failure envelope that represents isotropic failure in all directions except the direction of bedding. If the stress state of a lattice element is such that the Mohr circle exceeds the envelope, the material will undergo failure like as it is an isotropic material, so called intrinsic failure. For the anisotropic failure on the bedding planes, the weak plane criterion is given by lower values of the cohesion c_w, friction angle β_w, and tensile strength $f_{t,w}$. The stress state about the bedding plane is represented as one point on the Mohr circle, which is compared with the weak plane criterion. If the stress point falls outside the envelope, failure will occur along the weak plane. Figure 5.6 demonstrates a determination of weak failure in which the stress state only violates the weak plane criterion.

5.2 Hydraulic Fracturing in Rock-Analogue Samples

5.2.1 Model description

The coupled HM modeling involves hydraulic fracture propagation in a laboratory experimental program which has been supported by the Assistant Secretary for Fossil Energy, Office of Natural Gas and Petroleum Technology, through the National Energy Technology Laboratory. The laboratory tests have been conducted using soda-lime glass blocks in which fractures are artificially generated to provide some analogy to fractured rock materials. A complex pre-existing fracture network is designed and fabricated within the specimens (Figure 5.7 (a)), for which a laser-engraving technique is utilized to generate defects (Stewart et al., 2012). The fracture formation is described as a planar cloud of thermally induced, isolated micro-cracks.

For model preparation, a 90 mm square domain with a 3.2 mm diameter borehole at the center is discretized, and the pre-existing fractures are replicated by mapping the designed pattern onto the unstructured grid, as described in Section 5.1.1. Figure 5.7 (b) depicts details of the fracture network modeled in the Voronoi grid. Mechanical properties of the glass material are set as follows: Young's modulus E=73.8 GPa, tensile strength f_t=11.3 MPa; cohesive strength c=8.5 MPa; and internal friction angle β=25° for the Mohr-Coulomb failure criterion. It is simply assumed that the glass material is impermeable, non-porous, and incompressible. Also, all the interface nodes, which represent fractures in the TOUGH2 simulation, are initially set to be impermeable. For an activated pre-existing fracture or a newly generated fracture, the corresponding interface node undergoes a permeability increase, which is calculated based on the hydraulic aperture as suggested by Equation (5.6).

The specimen is subjected to anisotropic confining stresses, σ_x: σ_y= 4.83:7.24 MPa, and water is injected into the borehole at a constant rate. Because the glass is prone to brittle fracturing, the injection rate should be carefully considered to induce observable fracture propagation. The injection rate is 3.8×10^{-5} cm^3/s per unit centimeter thickness, which is roughly estimated from the injection volume history in the actual tests.

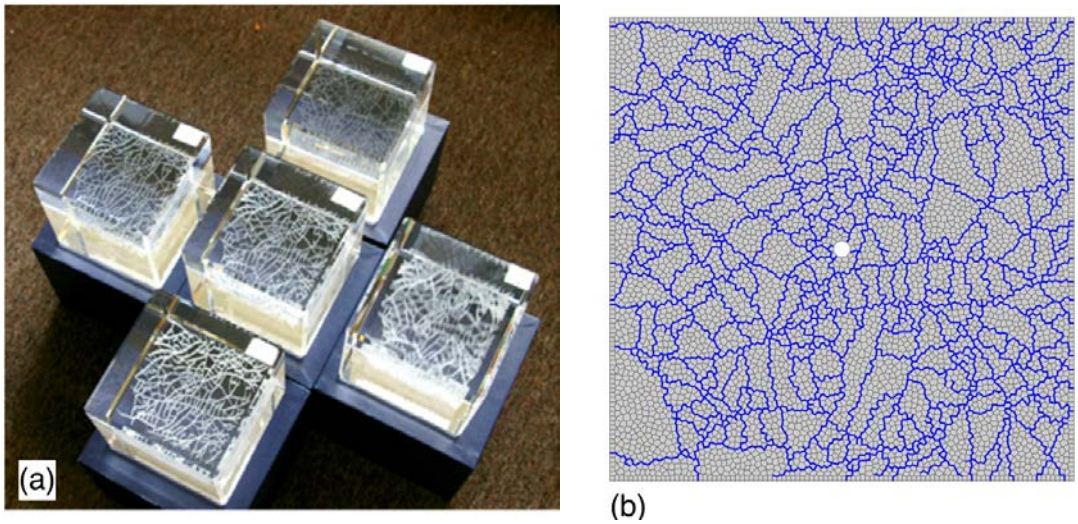

Figure 5.7. Physical and numerical representations of complex pre-existing fractures: a) 3D laser-engraved fractures in glass blocks with different opaqueness of their fracture network reflecting different mechanical properties of these fractures; and b) mapping of the fracture network onto an unstructured Voronoi grid.

5.2.2 Hydraulic fracture propagation in intact glass blocks

Hydraulic fracturing simulations are performed for intact glass blocks to determine other unknown parameters through a calibration process. By setting the mechanical properties of the pre-existing fracture elements same as those of the glass domain, the fractured glass block can convert into the intact glass block while preserving the grid geometry and modeling configurations described in Section 5.2.1. With the given injection rate, the compressibility of the borehole is adjusted to 5.0×10^{-9} Pa^{-1}. The injection pressure evolution is plotted in Figure 5.8, where the simulated pressurization rate, denoted by the slope of the ascending branch, is fitted to the experimental result for an intact borehole. The preset/calibrated hydrological properties are listed in Table 5.1.

Figure 5.9 shows snapshots of the fracture traces and the pressure distributions over time. The breakdown point is captured at time t_0, from which the time lapse during fracture propagation is counted as $\tau = t - t_0$. Two fracture branches stretch out from the borehole and propagate mainly in the direction parallel to the maximum confining stress. As the fractures advance, the injected fluid transfers into the empty space created by the fractures. The fracture paths reflect higher pressure contrasting to the surrounding glass matrix, and accordingly the injection pressure decreases at the borehole. Further fracture growth occurs at one branch reaching the upper boundary in two seconds. Such rapid and instantaneous fracture propagation makes it difficult to observe details of interactions between pre-existing fractures and hydraulic fractures in the experiments.

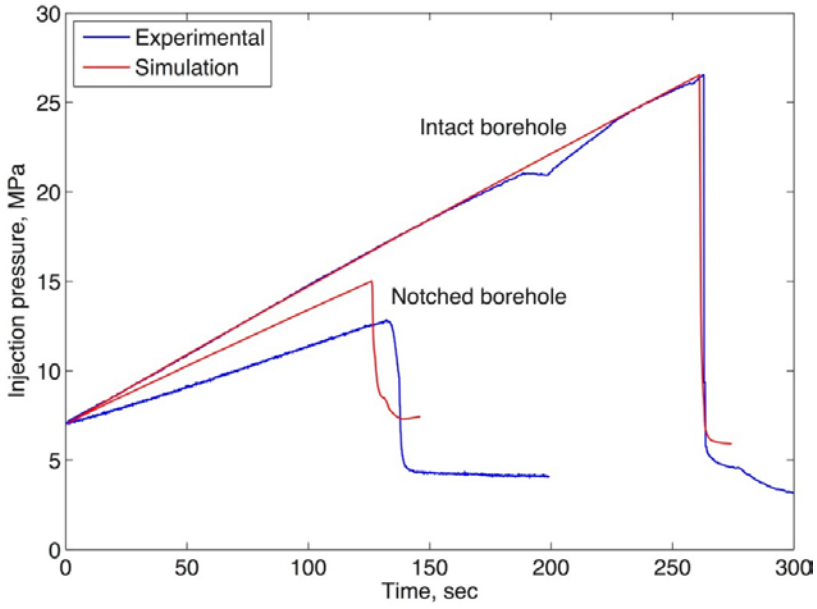

Figure 5.8. Injection pressure evolutions for hydraulic fracturing of intact glass blocks.

Table 5.1 Hydrological properties of glass, fracture, and borehole domains.

		Permeability (m^2)	*Porosity (-)*	*Compressibility (Pa^{-1})*
Glass		***0***	***0***	***0***
Fracture	***Pre-existing***	***0***	***0***	***0***
	Activated	$b_h^{12}/12^{\dagger}$	***0.8***	3.0×10^{-8}
Borehole		1.0×10^{-9}	***0.8***	5.0×10^{-9}

[†]The permeability of an activated fracture depends on the hydraulic aperture width, which is evaluated by Equation (5.6) with an assumption for the residual hydraulic aperture b_{hr}= 0.25 μm.

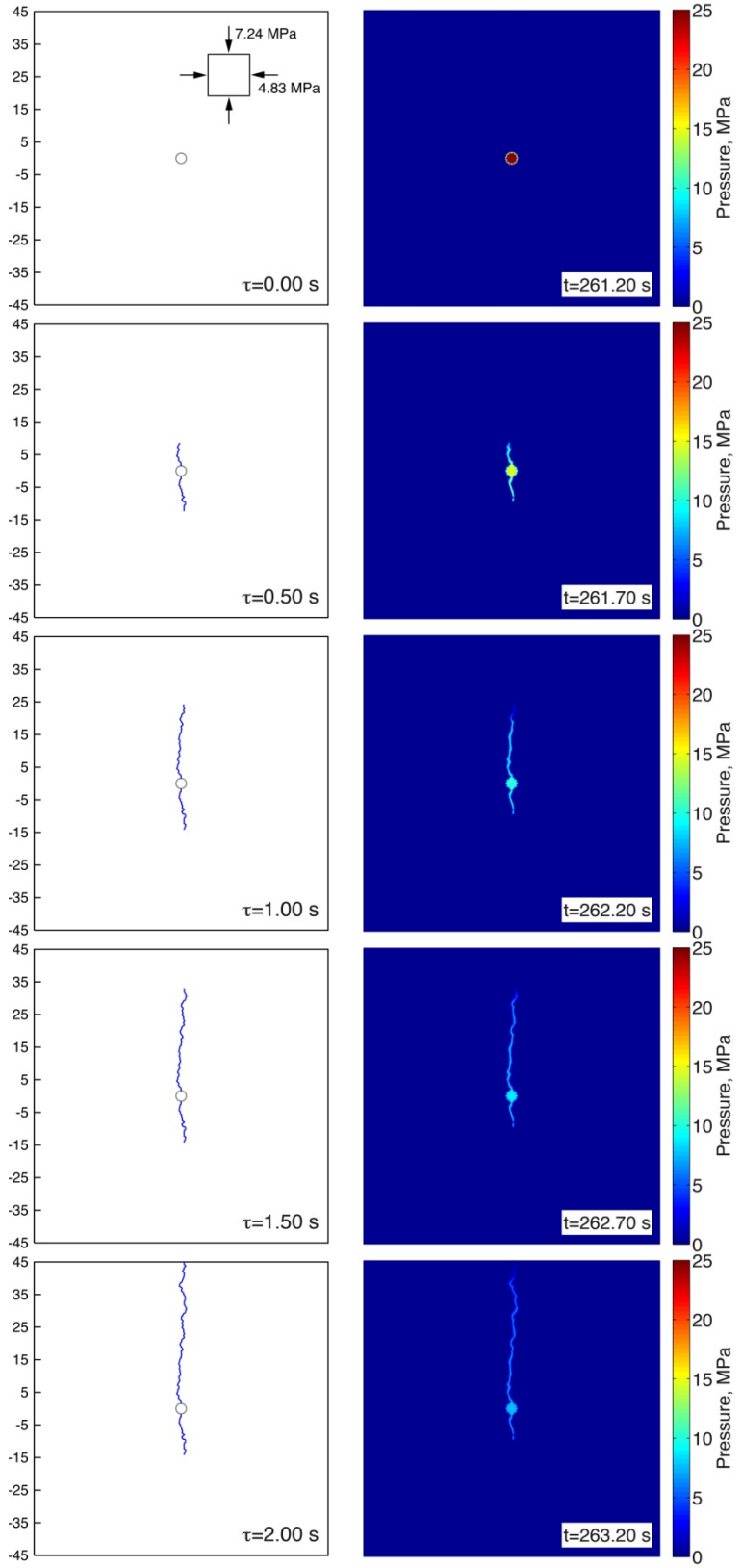

Figure 5.9. Snapshots of the fracture traces and the pressure distributions during fracture propagation from the intact borehole.

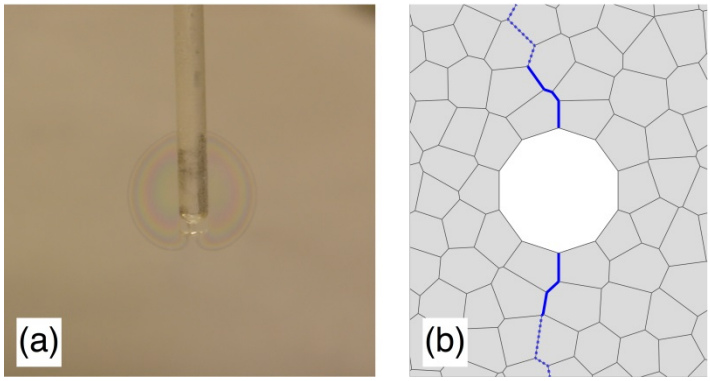

Figure 5.10. Introduction of initial notches around the borehole: a) pre-cracking of a test sample; and b) modeling of the notches by selecting fractured segments (illustrated by blue solid lines).

To stabilize the fracture growth, pre-cracks or notches are introduced around the borehole. Strain singularity and stress concentration arise at the crack tips (Rice, 1968), which is expected to advance the fracture initiation with a lower triggering pressure and thus provide a gradual fracture propagation. In the experimental program, a small flaw is generated by mechanically compressing a rubber plug at the bottom of the borehole. This method generates stable pre-cracks by pressurizing the borehole wall (Figure 5.10 (a)). The orientation of the flaw can be controlled to some degree by applying confining stresses to the specimen during the pressurization. In the numerical models, notches or other types of discontinuities (e.g., defects, fault planes, etc.) are represented by breaking/damaging the elements. From the resulting fracturing paths for the intact borehole presented in Figure 5.9, the fractured interface segments are manually picked to introduce the notches around the borehole (Figure 5.10 (b)), in which the mechanical resistance is completely removed in tension and small permeability and porosity are introduced.

The injection pressure evolution of the notched borehole is plotted and compared with that of the intact borehole in Figure 5.8. The injection pressure increases at a lower rate in the pre-peak region, which is attributed to infiltration of the injected fluid into the notches. The breakdown occurs at a lowered peak pressure as expected and the pressure is gradually released in the post-peak region, which implies slower fracture propagation with the notched borehole. Both the simulations and the laboratory tests demonstrate that the fracture growth is slower in the case of the notched borehole. However, a disagreement exists on the peak pressure and the pressurization rate between the simulation and experimental results. These quantitative discrepancies may be because it is difficult to precisely measure the length of the pre-cracks and therefore they may not be correctly represented in the model.

A comparison between Figures 5.9 and 5.11 explicitly explains the effects of the notched borehole on the rate of fracture growth. The fracturing speed is significantly reduced with the notched borehole, in which about 5 to 10 times longer period of time is taken for the same extent of fracture propagation. Moreover, a low level of the triggering and driving pressure evolves during the fracturing process with the notched borehole, and therefore the fracture is arrested after reaching a certain length (at τ=8.00 s) and then the fracture front proceeds very slowly while the fluid injection is continued at a constant rate.

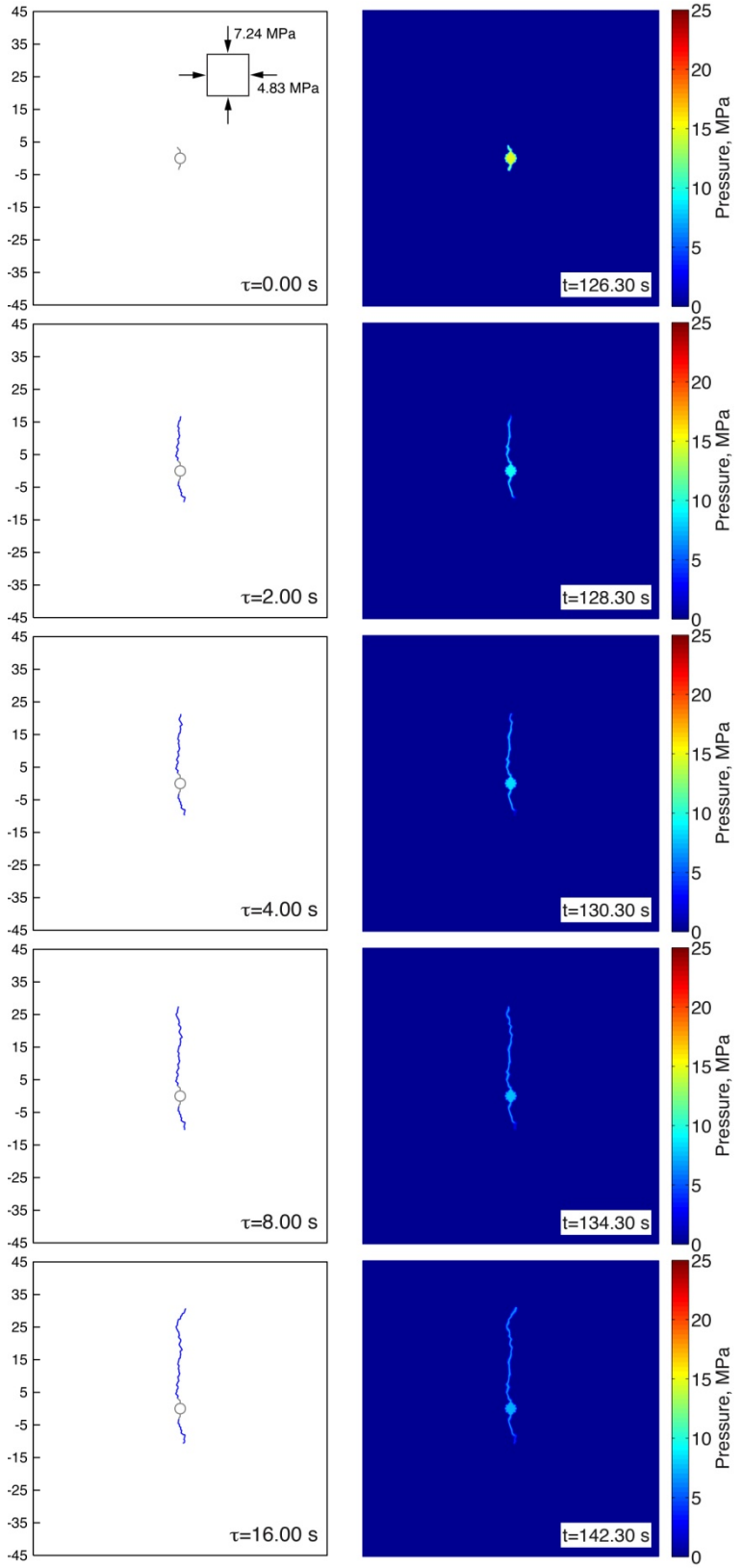

Figure 5.11. Snapshots of the fracture traces and the pressure distributions during fracture propagation from the notched borehole.

5.2.3 Hydraulic fracture propagation in a glass block containing pre-existing fractures

Within the same model description presented in Section 5.2.1, a fractured glass block is modeled by assigning weaker and more compliant mechanical properties to the lattice elements which correspond to the pre-existing fractures. The mechanical properties of the pre-existing fractures can be varied based on the expected weakening in accordance with the density of the etched micro-cracks in the test samples, which is reflected by the opaqueness of the fracture network in Figure 5.7 (a). For the simulation presented in this section, Young's modulus, the tensile strength, and the cohesive strength are initially reduced by half from those of the intact glass material, whereas the internal friction angle is retained. The notches around the borehole are modeled in the same way described in Section 5.2.2, but from the result of a preliminary simulation the fractured segments are taken at different locations mainly corresponding to the pre-existing fractures. Hydrological properties of the material domains conform to the values in Table 5.1. Note that the pre-existing fractures are assumed to be initially impermeable, thus they do not affect the hydrological behavior unless activated, whereas the notches are regarded as activated fractures (See Table 5.1).

The resulting fracture trace shows that the direction of hydraulic fracturing is influenced by a combination of the anisotropic stress condition and the degraded mechanical properties of the pre-existing fracture network (Figure 5.12 (a)). Two main fractures propagate from the borehole in the direction sub-parallel to the maximum confining stress with a slight perturbation due to the local heterogeneity of pre-existing fractures. The fracture branches mostly follow the activated pre-existing fractures (depicted by blue lines), and at some locations cut-throughs are made by newly generated fractures (depicted by red lines). The overall shape of the simulated fracture trace agrees well with the visualized hydraulic fracturing paths in the laboratory test, where a red fluorescent dye is mixed with the injected fluid for better visibility of fracturing paths (Figure 5.12 (b)).

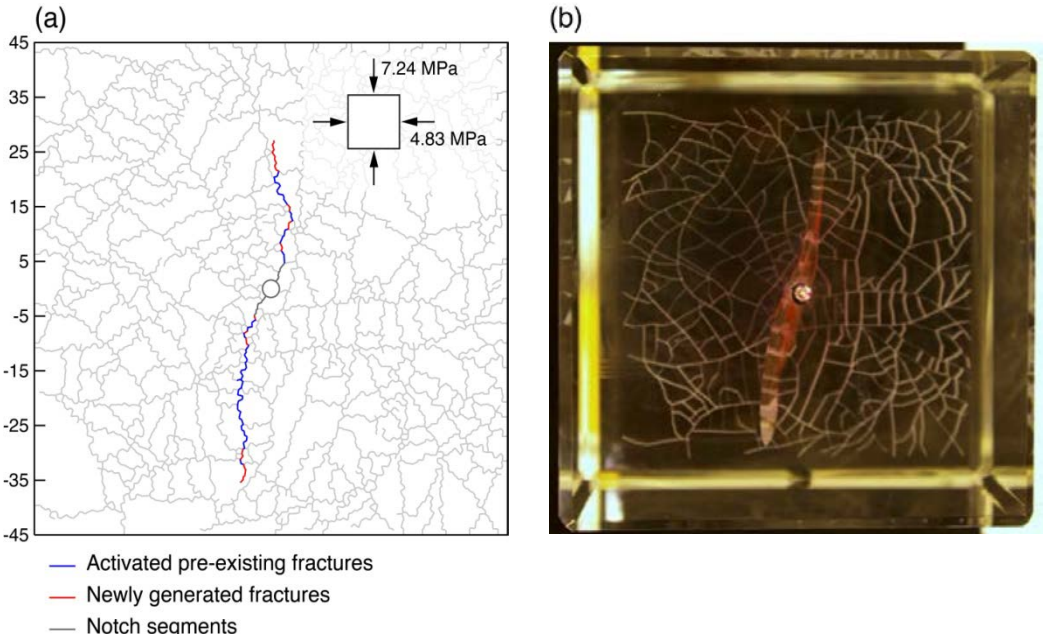

Figure 5.12. A comparison between a) the simulated fracture trace within the pre-existing fractures and b) the visualization of hydraulic fractures in the laboratory test.

5.3 SIMULATIONS OF DAMAGE AND FRACTURE IN OPALINUS CLAY ROCKS

5.3.1 Uniaxial compression tests

The modeling scheme proposed in Section 5.1.3 is verified through simulation of uniaxial compression tests for various orientations of bedding planes. Consider 2D configurations of a cylindrical core sample subjected to unconfined uniaxial compression, in which the loading direction forms an angle relative to the bedding plane, θ (see Figure 5.13). The simulations consider seven cases of the loading angle: $\theta = 0^{\circ}, 15^{\circ}, 30^{\circ}, 45^{\circ}, 60^{\circ}, 75^{\circ}, 90^{\circ}$. Boundary conditions are assigned at top and bottom layers of cells. Incremental loading is applied at the top layers by displacement control and the bottom layers are fixed. Herein the anisotropic mechanical properties of the rock material are adopted from the experimental results for the Opalinus Clay (Bossart, 2012), which are arranged in Table 5.2.

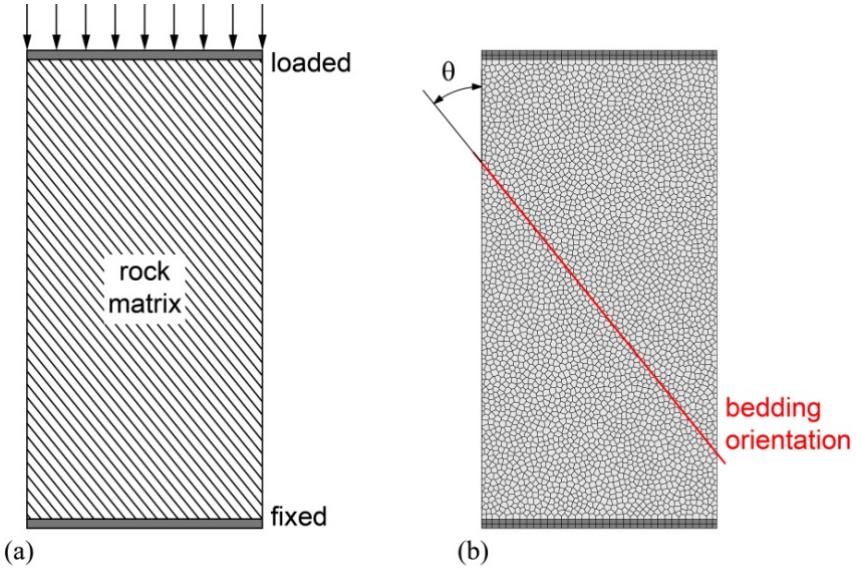

Figure 5.13. 2D specimen for uniaxial compression test: a) schematic drawing of the test program; and b) model discretization.

Table 5.2. Anisotropic mechanical properties of the Opalinus Clay (Bossart, 2012).

Mechanical properties	*Parallel to bedding*	*Normal to bedding*
Young's modulus (GPa)	*15.5*	*9.5*
Uniaxial tensile strength (MPa)	*2.0*	*1.0*
Cohesion (MPa)	*5.5*	*2.2*
Internal friction angle (degrees)	*25*	*25*

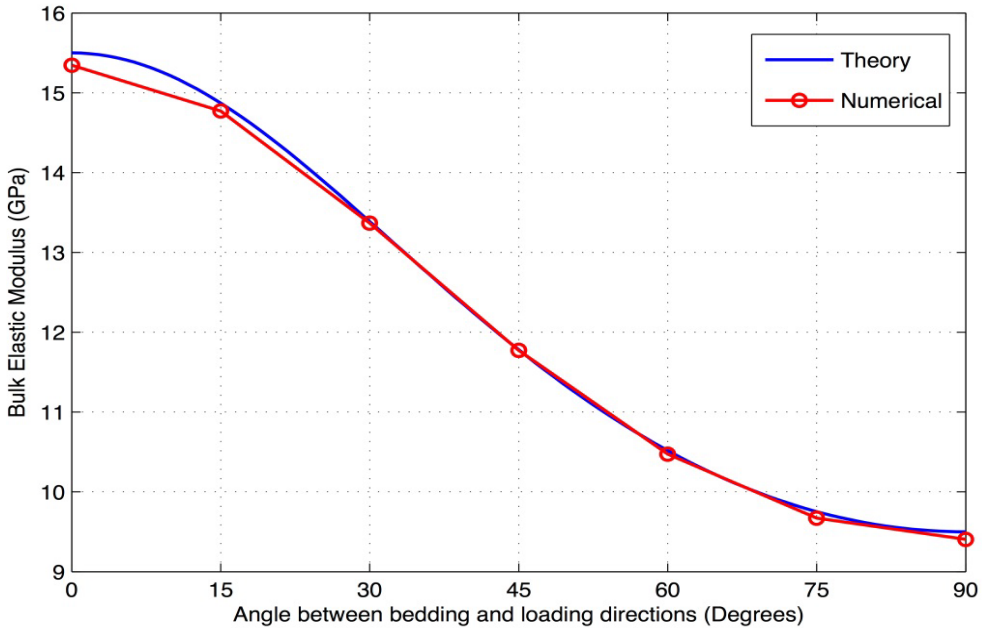

Figure 5.14. Variation of elastic modulus of Opalinus Clay with different loading angles.

The anisotropy of the elastic properties can be found in bulk elastic moduli. Theoretically, the bulk elastic modulus for loading angle θ is obtained by (Pariseau, 2006):

$$\frac{1}{E} = \frac{\cos^4\theta}{E_P} + \left(\frac{1}{G_{12}} - \frac{2\nu_{12}}{E_P}\right)\sin^2\theta\ \cos^2\theta + \frac{\sin^4\theta}{E_N} \qquad 5.15$$

where G_{12} is shear modulus and ν_{12} is Poisson ratio. An approximation of the relationship between shear modulus and Young's moduli for an anisotropic system with $\nu = 0$ is given as

$$G_{12} = 1/(\frac{1}{E_P} + \frac{1}{E_N}) \qquad 5.16$$

With this assumption for Equation (5.15), the theoretical variation in bulk elastic modulus is depicted in Figure 5.14. Simulated elastic moduli show a are in agreement with the theoretical evaluations.

For the weak-plane failure model proposed in Section 5.1.3.2, the two different failure criteria limit the maximal compressive principal stresses at their critical stress states, which can be theoretically derived with an assumption of unconfined loading configurations:

$$\sigma_1 = 2\frac{c\cos\beta}{1-\sin\beta} \qquad 5.17$$

for the intrinsic failure criterion (cohesion c, friction angle β) and

$$\sigma_{1,w} = 2\frac{c_w\cos\beta_w}{\sin 2\theta\cos\beta_w - (\cos 2\theta + 1)\sin\beta_w} \qquad 5.18$$

for the weak failure criterion (cohesion c_w, friction angle β_w, respectively. The minimum value between the two limit stresses is chosen to be uniaxial compressive strength for a specific loading angle θ. The Variation of the theoretical values as a function of loading angle is plotted in Figure 5.15. From the simulation results, peak stress values of the stress-strain response curves can be regarded as uniaxial compressive strengths. The simulated strengths are perfectly matched with the theoretical values.

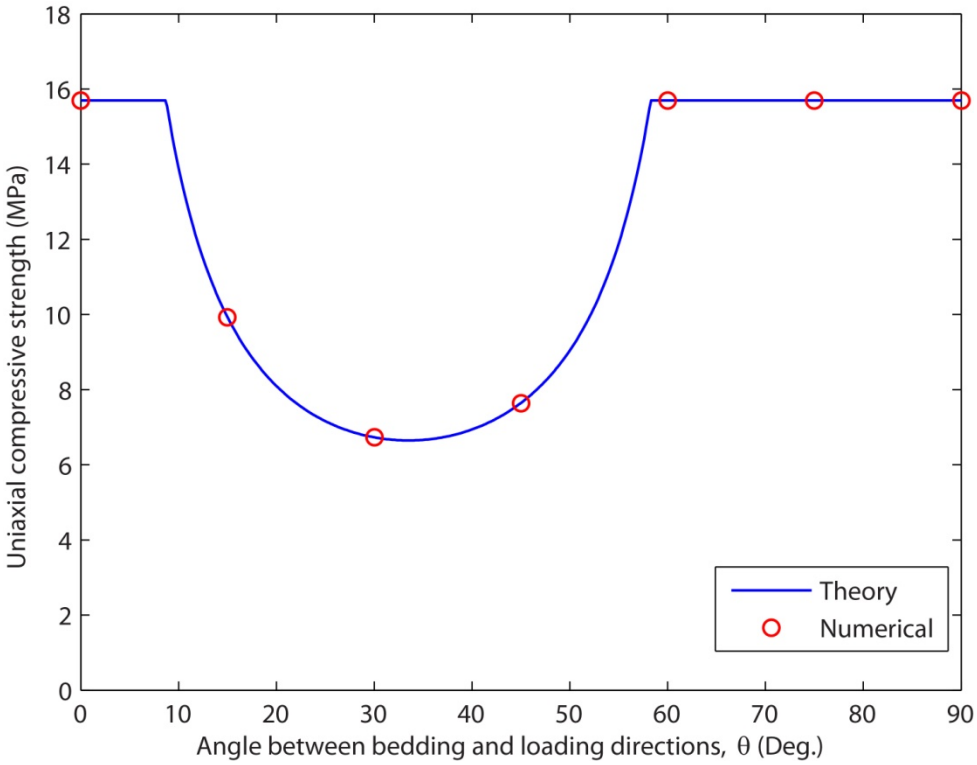

Figure 5.15. Variation of elastic modulus of Opalinus Clay with different loading angles.

5.3.2 EDZ formations in the HG-A microtunnel

This section presents the validity of the modeling scheme for anisotropic failure behavior observed in the field site, the HG-A microtunnel. The 1-m diameter microtunnel is located at the Mont Terri underground research laboratory (URL) near Saint-Ursanne, Switzerland. The rock of the test site is relatively homogeneous in meter-scale, but pronounced bedding was discovered at finer scales (Marschall et al., 2006). The rock formation is highly fractured with frequencies of 0.3 to 1 m, although the fracture permeability is not significant, which indicates that fractures are mostly closed under natural stress conditions (Marschall et al., 2006; 2008).

One main purpose of the HG-A test is to provide data on the geomechanical and hydrogeologic effects of the excavation damage zone (EDZ). Although the long-term physical features observed in the test are related to coupled hydro-mechanical processes, as an initial study, herein the problem is simplified by assuming a constant uniform pore pressure such that fracture damage is simulated using the mechanical modeling of the RBSN approach exclusively. This assumption is valid up until the point at which mechanical deformation occurs much more quickly than water flow processes in the rock formation, where mechanical equilibrium is held within a rapid (undrained) excavation (Liu et al., 2013).

Figure 5.16 (a) shows excavation damage of the microtunnel. Partial damage and exfoliations have occurred along the microtunnel wall, which are mainly attributed to the anisotropic strength characteristics of the rock. The relative weakness orthogonal to the bedding and the weakness near faults intercepting the tunnel, as depicted in Figure 5.16 (b), result in the non-uniform damage around the excavation wall.

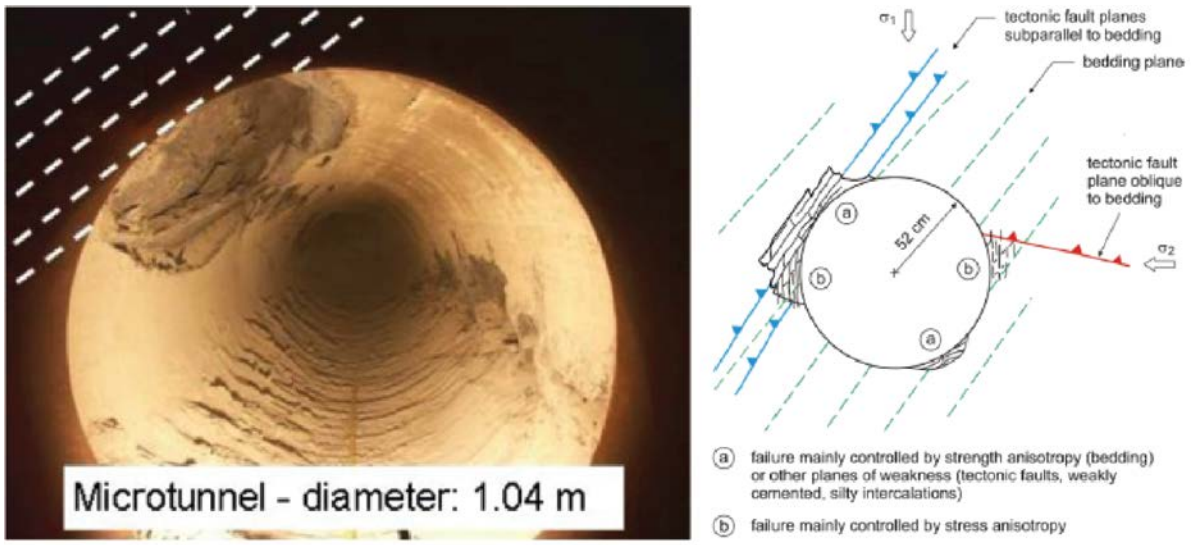

a) b)

Figure 5.16. a) Excavation damage viewing from the HG-A Niche towards back end (Marschall et al., 2006); and b) Conceptual diagram of the damage zone (Lanyon et al., 2009; Marschall et al., 2006).

This study is focused on investigating the effects of the faults on the failure characteristics. As shown in Figure 5.17, 2D computational domain with dimension of 10-m square is discretized with a gradual nodal density, where a circular subdomain for excavation is defined at the center. The bedding planes are assumed to be aligned at 45° from the horizontal axis similarly to the orientation of fabric shown in Figure 5.16 (b). The anisotropic elastic and strength properties of the rock matrix conform to the parameters listed in Table 5.2. The observed fault planes are precisely modeled into a grid (see Figure 5.17b), for which the weaker strength parameters are assigned: tensile strength $f_{t,f} = 0.5$ MPa; cohesion $c_f = 1.0$ MPa; and friction angle $\beta_f = 23°$.

Far-field confining stresses are applied at the boundary edges: 4.5 MPa in the horizontal direction and 6.5 MPa in the vertical direction (Martin and Lanyon, 2003), and the pore pressure of 1.5 MPa is applied over the domain at the initial stage. A one-step preliminary simulation is conducted to grasp the initial stress state for the given stress and pressure configurations, so the main simulation starts with the undeformed condition. An excavation process can be demonstrated by gradually reducing the elastic parameters, internal stress and pressure in the excavation zone over the loading steps. Herein, an exponential function is adopted, by which the values will be decreased to about 10^{-6} of the initial configurations after 100 loading steps.

Figure 5.18 presents the resulting failure patterns. Damage occurs mainly around the excavation zone, and more brisk failures are found at the tunnel wall where its tangent is sub-parallel to the bedding planes, which has been found in the field observations (Figure 5.16). The effects of fault planes on the failure patterns can be interpreted in comparison between Figures 5.18 (a) and 5.18 (b). The matrix domain is homogenous in the material composition, thus the failure pattern is quite symmetric without fault planes (Figure 5.18 (a)), which may be attributed to the anisotropic strength properties. However, in the presence of faults (Figure 5.18 (b)), distinct shear fracture develops along the fault planes, and then fractures grow from the fault planes. One kind of distinguishing characteristics in the fracture pattern with fault planes is that the fracture growth is limited by the fault planes. The resulting fracture pattern is not symmetric due to the stress contour perturbed by the fault planes.

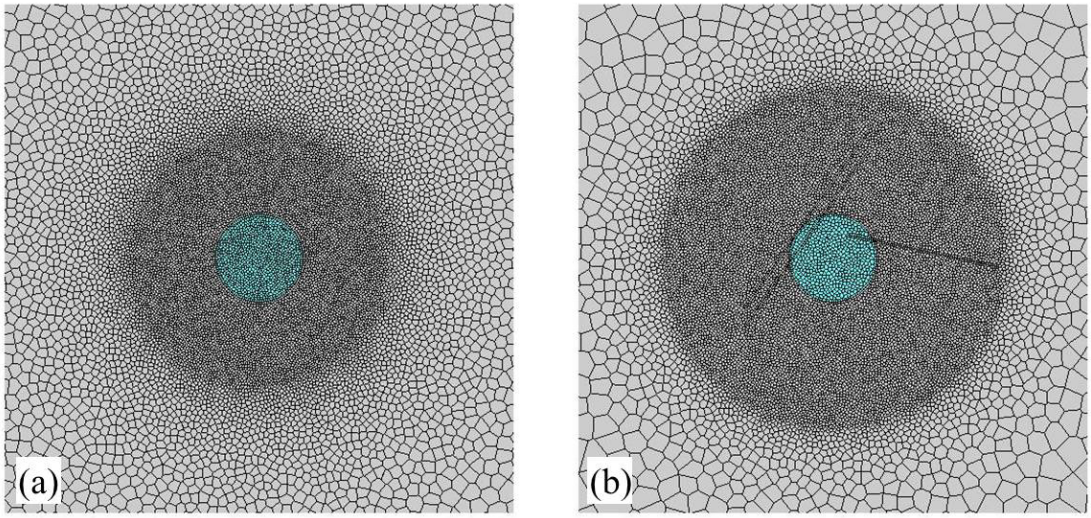

Figure 5.17. Discretizations of the computational domain for the HG-A test simulations: a) without fault planes; and b) with fault planes explicitly modeled into the grid.

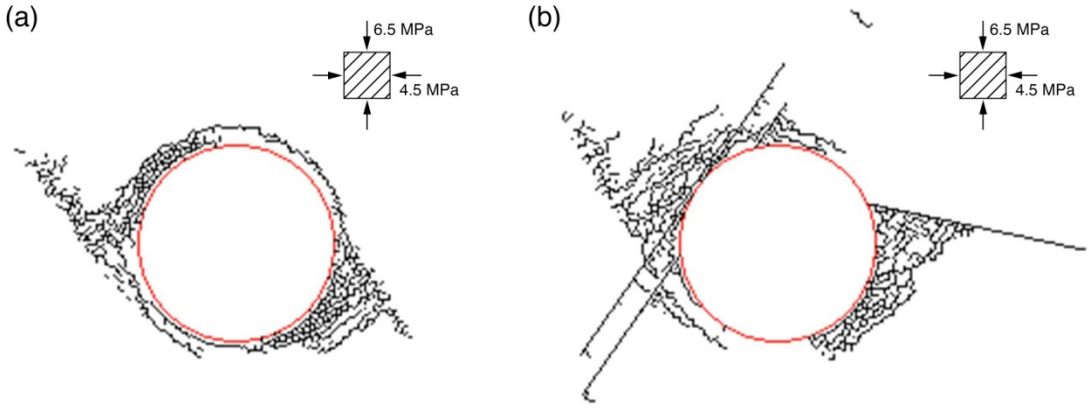

Figure 5.18. Resulting failure patterns around the tunnel excavation zone: a) without fault planes; and b) with fault planes.

5.4 DEVELOPMENT OF DYNAMIC SIMULATION CODE

In dynamic modeling of mechanical behavior, the motion of the system is governed by a differential equation based on Newton's second of law of motion. The particle-lattice model, considered in this work, consists of Voronoi cells with mass and inertial moments, which are interacting with their neighbors via spring connections constructed by the RBSN theory. Figure 5.19 shows a free-body diagram of a Voronoi cell subjected to external load applied at the node and local internal forces generated at the spring sets. Each cell has six nodal degrees of freedom in 3D global coordinates. Let us consider the external load vector $\mathbf{p}(p_X, p_Y, p_Z, \tau_X, \tau_Y, \tau_z)$ and a local internal force vector $\mathbf{f}_k(f_{nk}, f_{sk}, f_{tk}, m_{nk}, m_{sk}, m_{tk})$ for a Voronoi facet k. The rotational components of the internal spring force vector (i.e., m_{nk}, m_{sk}, m_{tk}) are omitted for visibility in Figure 5.19 (b). The internal spring force terms in the local coordinates are transformed into the global coordinates and assembled into a global vector **f**:

$$\mathbf{f} = \sum_{k=1}^{n} \mathbf{\Gamma}_k{}^T \mathbf{f}_k \qquad 5.19$$

where $\mathbf{\Gamma}_k$ is a 6×6 matrix for coordinate transformation from global *X*-*Y*-*Z* to local *n*-*s*-*t* for individual Voronoi facets.

The governing equation for nodal displacements and rotations varying with time can be constructed as

$$\mathbf{J}\ddot{\mathbf{u}} + \mathbf{f} = \mathbf{p}(t) \tag{5.20}$$

where $\ddot{\mathbf{u}}$ is a second derivative of displacement vector (i.e., acceleration). **J** is the inertia matrix containing mass and moment of inertia tensor of the Voronoi cell, which can be expressed with the corresponding sub-matrices **M** and **I**:

$$\mathbf{J} = \begin{bmatrix} \mathbf{M} & 0 \\ 0 & \mathbf{I} \end{bmatrix} = \begin{bmatrix} m & & & 0 & & \\ & m & & & & \\ & & m & & & \\ & & & I_{XX} & I_{XY} & I_{XZ} \\ & 0 & & I_{YX} & I_{YY} & I_{YZ} \\ & & & I_{ZX} & I_{ZY} & I_{ZZ} \end{bmatrix} \tag{5.21}$$

The mass and inertial moment terms are calculated from the geometrical properties of the Voronoi cell. The polyhedral cells are mostly in irregular shape so that it demands a generalized method to compute the volume, centroidal position, and inertia tensor of an arbitrary polyhedron. In the proposed method, a polyhedron can be treated as the combination of pyramids defined by the cell facets and the cell node, which are regarded as the pyramid bases and the apex, respectively. Consequently, the geometrical properties of the polyhedral cell can be easily computed by combining those of all pyramids. Construction of the inertia matrix is essential to calculate the acceleration vector:

$$\ddot{\mathbf{u}} = \mathbf{J}^{-1}[\mathbf{p} - \mathbf{f}] \tag{5.22}$$

Herein, the resultant acceleration is used to explicitly derive higher-order kinematic information (i.e., velocity and displacement). The solution in Equation (5.22) can be rewritten in the discretized form at time $t_{n+1} = (n+1)\Delta t$:

$$\ddot{\mathbf{u}}_{n+1} = \mathbf{J}^{-1}[\mathbf{p}_{n+1} - \mathbf{f}_{n+1}] \tag{5.23}$$

where the resultant internal force $\mathbf{f}_{n+1}$ applied to the spring sets is explicitly related to the nodal displacement $\mathbf{u}_{n+1}$, which is derived by integrating the known kinematic information up to time *n*:

$$\mathbf{u}_{n+1} = \mathbf{u}_n + \dot{\mathbf{u}}_n \Delta t + \frac{\ddot{\mathbf{u}}_n}{2}\Delta t^2 \tag{5.24}$$

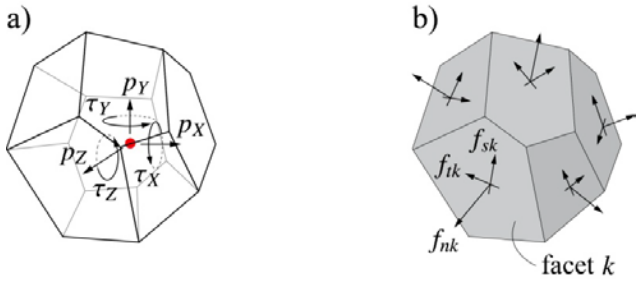

Figure 5.19. Free-body diagram of a Voronoi particle for dynamic equilibrium condition: a) external force terms; and b) internal forces corresponding to the RBSN spring forces.

Then, the unknown velocity $\dot{\mathbf{u}}_{n+1}$ is derived using the calculated $\ddot{\mathbf{u}}_{n+1}$:

$$\dot{\mathbf{u}}_{n+1} = \dot{\mathbf{u}}_n + \frac{\ddot{\mathbf{u}}_{n+1}+\ddot{\mathbf{u}}_n}{2}\Delta t \qquad 5.25$$

If there are velocity-dependent terms involved in the force calculation such as a damping force, the internal force $\mathbf{f}_{n+1}$ is not simply fixed until the velocity $\dot{\mathbf{u}}_{n+1}$ converges. For that case, an additional "predictor-corrector" iteration algorithm is necessary during these explicit time integrations.

As an ongoing development stage, the simulation code has been established with modern programming features (e.g., dynamic memory allocation, modularized program blocks) implemented in Fortran 90. New data structures will provide better computational efficiency and simple code management for extension and modification. Also, the calculation of the inertial tensor of an arbitrary polyhedron is included in the code. The Voronoi-based particles are the most fundamental elements for dynamic modeling, so it is crucial to obtain their geometrical properties for solving the governing ODEs. The solution phase is implemented using explicit time integration algorithms (e.g., velocity Verlet scheme), which will ease converting the serial computing to a parallelized version. High performance computation libraries, such as PETSc and Polymec, can be adopted for parallelization of the simulation code.

5.5 SUMMARY AND FUTURE WORK

In this work we are implementing an effective two-way coupling between the TOUGH2 simulator and the RBSN approach for the application of damage and fracturing in argillaceous rocks. In FY16 we have continued our work on modeling damage and deformation in anisotropic rock and around tunnels, but have also made substantial effort in simulation of fluid driven fracture propagation. The work on fluid driven fracture propagation forms the groundwork for another future application related to gas migration in bentonite and clay rocks. The simulator currently provides a discrete representation of hydrological (fluid flow through fracture networks) and mechanical (fracture initiation and propagation) responses. The permeability of an individual fracture is rigorously evaluated from the grid geometry and the fracture aperture width.

In addition to the TOUGH-RBSN linkage, an improvement in the RBSN modeling scheme has been achieved to extend the applicability of the model to general geomaterials that exhibit mechanical anisotropy. In a new approach, elastic spring coefficients and strength parameters are systematically formulated for individual lattice elements based on the bedding orientation, and a simple but efficient weak-plane failure model is adopted to represent the anisotropic fracture response with fabric-dependent strength parameters.

The TOUGH-RBSN code and the developed algorithms for fluid driven fracturing has been applied to predictive and interpretative simulations for hydraulic fracturing of the laboratory experiment samples. The hydraulic fractures reproduced in the simulations compare favorably to the experimental results with respect to the injection pressure evolutions and the resulting fracture paths. As for the mechanical anisotropy, uniaxial compression tests on Opalinus Clay have been simulated in order to demonstrate the validity of the new modeling scheme. Thereafter, updated simulations of EDZ formations for the Mont Terri HG-A microtunnel have been conducted. Qualitative comparisons show that the simulation results closely match field observations, in which non-uniform failure patterns attributed to the anisotropic mechanical characteristics form around the excavation zone and the presence of fault planes significantly influences the failure patterns.

In summary, in FY16 we have further developed TOUGH-RBSN with the goal of producing an efficient tool for understanding the variety of characteristics in THM processes in argillaceous rocks, including fracture damage and fluid driven fracture propagation. The series of simulations presented in this report

section demonstrate the current TOUGH-RBSN capabilities for modeling tightly coupled HM processes and the RBSN approach for mechanical anisotropy in elastic and fracture responses. For the ongoing development, a refinement could be made into the TOUGH-RBSN code to rigorously evaluate the change of fracture porosity as a response of the mechanical fracture aperture change, which will be addressed in future work. In addition, the ongoing work on the dynamic version and porting that version to high performance computing will provide an avenue for modeling larger scale problems, including 3D complex fracture geometry.

For FY17, recommended work is as follows:

- We plan to complete the dynamic simulation framework, and verification and validation of the simulation code will be provided through geomechanics examples including fracturing processes. Also, by high performance computing in the dynamic simulation code, our modeling capacities will be extended to full 3D large scale problems.
- More realistic simulations will be available by setting the fracture porosity dependent on the fracture aperture width in the TOUGH-RBSN coupling modules.
- Relating to the DECOVALEX-2019 task, TOUGH-RBSN code can be applied to the gas migration in bentonite clay, in which the clay material often dilates to create preferential flow pathways. We will attempt to demonstrate such preferential pathways using the discrete modeling approach.
- Swelling of a ductile/expanding shale matrix will be simulated to investigate the time-dependent deformation of the rock, including fracture closure/sealing, which significantly impacts on the hydrological properties of the rock material.

5.6 References

Asahina, D. and Bolander, J.E. 2011 Voronoi-based discretizations for fracture analysis of particulate materials, *Powder Technology*, 213, 92–99.

Bear, J. 1972 *Dynamics of Fluids in Porous Media*, Elsevier, New York, New York.

Berton, S. and Bolander, J.E. 2006 Crack band model of fracture in irregular lattices, *Computer Methods in Applied Mechanics and Engineering*, 195, 7172–7181.

Biot, M.A. and Willis, D.G. 1957 The elastic coefficients of the theory of consolidation, *Journal of Applied Mechanics*, 24, 594–601.

Blümling, P., Bernier, F., Lebon, P., and Martin, C.D. 2007 The excavation damaged zone in clay formations time-dependent behaviour and influence on performance assessment, *Physics and Chemistry of the Earth*, 32, 588–599.

Bolander, J.E. and Saito, S. 1998 Fracture analyses using spring networks with random geometry, *Eng. Fract. Mech.*, 61, 569–91.

Bossart, P. 2012 Characteristics of the Opalinus Clay at Mont Terri, http://www.montterri.ch/internet/montterri/en/home/geology/key_characteristics.parsys.49924.DownloadFile.tmp/characteristicsofopa.pdf.

Bossart, P., Meier, P.M., Moeri, A., Trick, T., and Mayor, J.C. 2002 Geological and hydraulic characterisation of the excavation disturbed zone in the Opalinus Clay of the Mont Terri Rock Laboratory, *Engineering Geology*, 66(1–2), 19–38.

Bossart, P., Meier, P.M., Moeri, A., Trick, T., and Mayor, J.-C. 2004 Structural and hydrogeological characterisation of the excavation-disturbed zone in the Opalinus Clay (Mont Terri Project, Switzerland), *Applied Clay Science*, 26, 429–448.

Chiaramonte, L., Zoback, M.D., Friedmann, J., and Stamp, V. 2008 Seal integrity and feasibility of CO_2 sequestration in the Teapot Dome EOR pilot: geomechanical site characterization, *Environ. Geol.*, 54, 1667–1675.

Cosgrove, J.W. (2001) Hydraulic Fracturing during the Formation and Deformation of a Basin: A Factor in the Dewatering of Low-Permeability Sediments, *AAPG Bulletin*, 85(4), 737–748.

Freeman, C.M., Moridis, G.J., and Blasingame, T.A. (2011) A numerical study of microscale flow behavior in tight gas and shale gas reservoir systems, *Transport in porous media*, 90(1), 253–268.

Gonçalvès, J., Violette, S., and Wendling, J. (2004) Analytical and Numerical Solutions for Alternative Overpressuring Processes: Application to the Callovo-Oxfordian Sedimentary Sequence in the Paris Basin, France, *Journal of Geophysical Research*, 109, 14.

Lanyon, G.W., Marschall, P., Trick,T., de La Vaissière, R., Shao, H. and Leung, H. (2009) Hydromechanical evolution and self-sealing of damage zones around a microtunnel in a claystone formation of the Swiss Jura Mountains, *ARMA*, 09-152.

Liu, H.H., Houseworth, J., Rutqvist, J., Zheng, L., Asahina, D., Li, L., Vilarrasa, V., Chen, F., Nakagawa, S., Finsterle, S., Doughty, C., Kneafsey, T. and Birkholzer, J. (2013) Report on *THMC modeling of the near field evolution of a generic clay repository: Model validation and demonstration*, (FCRD-UFD-2013-000244), U.S. DOE Used Fuel Disposition Campaign.

Marschall, P., Distinguin, M., Shao, H., Bossart, P., Enachescu, C. and Trick, T. (2006) Creation and evolution of damage zones around a microtunnel in a claystone formation of the Swiss Jura Mountains, *Society of Petroleum Engineers*, SPE-98537-PP.

Marschall, P., Trick, T., Lanyon, G.W., Delay, J. and Shao, H. (2008) Hydro-mechanical evolution of damaged zones around a microtunnel in a claystone formation of the Swiss Jura Mountains, *ARMA*, 08-193.

Martin, C.D. and Lanyon, G.W. (2003) Measurement of in-situ stress in weak rocks at Mont Terri Rock Laboratory, Switzerland, *International Journal of Rock Mechanics & Mining Sciences*, 40, 1077–1088.

McGuire, W. and Gallagher, R.H. (1979) *Matrix Structural Analysis*, John Wiley & Sons, New York.

Okabe, A., Boots, B., Sugihara, K., and Chiu, S.N. (2000) *Spatial Tessellations: Concepts and Applications of Voronoi Diagrams*, 2nd ed., Wiley, NYC, 696 pages.

Pariseau, W.G. (2006) *Design Analysis in Rock Mechanics*, Taylor & Francis, London, UK.

Rice, J.R. (1968) A path independent integral and the approximate analysis of strain concentration by notches and cracks, *Journal of Applied Mechanics*, 35 (2), 379–386.

Rutqvist, J. (2011) Status of the TOUGH–FLAC simulator and recent applications related to coupled fluid flow and crustal deformations, *Computers & Geosciences*, 37(6), 739–750.

Rutqvist, J. and Tsang, C.-F. (2002) A study of caprock hydromechanical changes associated with CO_2-injection into a brine formation, *Environmental Geology*, 42, 296–305.

Rutqvist, J., Noorishad, J., Tsang, C.-F., and Stephansson, O. (1998) Determination of fracture storativity in hard rocks using high-pressure injection testing, *Water Resources Research*, 34 (10), 2551–2560.

Rutqvist, J., Tsang, C.-F., and Stephansson, O. (2000) Uncertainty in the maximum principal stress estimated from hydraulic fracturing measurements due to the presence of the induced fracture, *International Journal of Rock Mechanics and Mining Sciences*, 37, 107–120.

Rutqvist, J., Wu, Y.-S., Tsang, C.-F., and Bodvarsson, G. (2002) A modeling approach for analysis of coupled multiphase fluid flow, heat transfer and deformation in fractured porous rock, *International Journal of Rock Mechanics & Mining Sciences*, 39, 429–442.

Stewart, R.R., Dyaur, N., Omoboya, B., de Figueiredo, J.J.S., Willis, M., and Sil, S. (2012) Physical modeling of anisotropic domains: Ultrasonic imaging of laser-etched fractures in glass, *Geophysics*, 78(1), D11-D19.

Volckaert, G., Bernier, F., Sillen, X., Van Geet, M., Mayor, J.-C., Göbel, I., Blümling, P., Frieg, B., and Su, K. (2004) Similarities and differences in the behaviour of plastic and indurated clays, *The Management and Disposal of Radioactive Waste: Euradwaste '04*, Luxembourg.

Witherspoon, P. A., Wang, J. S. Y., Iwai, K., and Gale, J. E. (1980) Validity of cubic law for fluid flow in a deformable rock fracture, *Water Resources Research*, 16, 1016–1024.

Yip, M., Mohle, J., and Bolander, J. (2005) Automated modeling of three-dimensional structural components using irregular lattices, *Computer-Aided Civil and Infrastructure Engineering*, 20, 393–407.

Zimmermann, G., and Reinicke, A. (2010) Hydraulic stimulation of a deep sandstone reservoir to develop an Enhanced Geothermal System: Laboratory and field experiments, *Geothermics*, 39(1), 70–77.

6. SUMMARY

(1) THM modeling: FE heater test and DECOVALEX (Section 2)

UFD and LBNL greatly benefit from participating in these international activities for developing expertise and testing advanced models for coupled THM processes to be used for predicting long-term THM evolution of a multibarrier nuclear waste repository system, involving backfilled emplacement tunnels in argillite host formations. In FY16, we have been able to successfully complete the DECOVALEX-2015 modeling associated with the Mont Terri HE-E experiment and Horonobe EBS experiment, and for the first time been able to analyze field data from the largest ongoing underground heater test in the worlds; the Mont Terri FE experiment. The main accomplishments in FY16 include the improvement of the implementation and efficiency of the Barcelona Expansive Model (BExM) in TOUGH-FLAC as well as the interpretative modeling of field data from all the three underground heater experiments included in LBNL's international commitments on heater experiments.

The interpretative analyses of heater experiments, as well as the evaluation of the outcome of predictive modeling have confirmed that temperature and moisture evolution can be predicted with confidence. Related to the evolution of moisture content and buffer resaturation some questions remain related to the thermally driven diffusion, how strong this process is and why we observe some apparent inconsistencies between the modeling of different experiments; we observed some difference in moisture evolution between the Mont Terri HE-E and FE experiments that should be studied further.

Related to the mechanical evolution of the buffer, it is well known this is more complex as it depends on a number of processes such as swelling, pore pressure and thermal expansion that in turn depends on the evolution of saturation, temperature, pressure and 3D geometrical mechanical confinement effects. No mechanical measurements were conducted in the buffer for the HE-E experiment, whereas the stress in the buffer has not yet been developed very much in the case of the Horonobe EBS experiment and Mont Terri FE experiment. The stress in the buffer will take years to develop and this should be modeled in the future, especially related to the Mont Terri FE experiment which is comprehensively monitored regarding mechanical changes in both buffer and host rock.

In the remaining months of FY16 and FY17, the following activities are recommended:

- We plan to continue our work on participating in major international underground heating experiments, by continuing modeling of the Mont Terri FE experiment as one of the international modeling teams and starting on a new modeling tasks in the new DECOVALE-2019 project. These commitments in the new DECOVALEX-2019 project will replace our previous commitments related to the Mont Terri HE-E and Horonobe EBS experiments in the DECOVALEX-2015, which has been completed.
- The DECOVALEX-2019 tasks to be started in FY17 are denoted Task A and Task E in the new DECOVALEX-2019 project. Task A is related to gas migration in bentonite, and TOUGH-FLAC with dual-structure model is one of the approach that will be tested. Task E is related to upscaling of modeling results from small scale to one-to-one scale based in heater test data in Callovo-Oxfordian claystone (COx) at MHM underground research laboratory in France. This will be a perfect task for our development and application of the model capabilities we have developed and tested over the last few years within the UFD Campaign. Upscaling is an important issue for the repository design and safety calculation. The question is how to go from sample to a repository scale? This task will include modeling at difference scales, from laboratory scale to field scale heater experiments and all the way to repository scale.
- The FY17 work on the Mont Terri FE experiment will be focused on modeling of the mechanical evolution of the buffer and host rock, including the application of the BExM model at a large scale. It will be a great opportunity to apply and test the BExM at the larger scale on the FE

experiment, in particular because one the other international modeling teams is the University of Catalonia group in Barcelona, Spain that is the origin of the BExM model and they will apply BExM for the modeling of the Mont Terri FE experiment, but using a different numerical simulator. At the same time we will continue to validate and gain experiences in the use of the BExM.

- In addition to these tasks related to underground heater experiments, in FY17 we intend to study a few important technical issues that arose from the DECOVALEX-2015 work on HE-E and Horonobe experiments. The first, is related to the strength of thermally driven diffusion which did not seem consistent between different experiments, such as the HE-E and FE experiments. We will investigate different options of enhanced thermal diffusion which may resolve the small deviation between modeling and measurements of the evolution of relative humidity the buffer as observed for the HE-E experiment. The second is related to the small inconsistencies we observed in the early time stress evolution at the Horonobe EBS experiment. We now have longer term measurement data from the experiment and using this we plan to try different constitutive mechanical models, such as BBM instead of simple swelling, to investigate whether a more consistent mechanical behavior can be modeled.
- Finally, the implementation and application of a continuum damage model for the evolution of the excavation disturbed zone is another needed addition to the current model for the calculating the evolution of permeability along with damage as well as sealing and healing. Different approaches can be tested, including continuum damage models considering fracture evolution implicitly. Such a model can be benchmarked against discrete fracture modeling of damage zone fractures using TOUGH-RBSN. The goal is to build a pragmatic continuum model that can be validated against field experiments such as sealing experiments conducted in underground research laboratories.

(2) Investigation of the impacts of high temperature limits with THMC modeling (Section 3)

Coupled THMC modeling have used to evaluate the chemical alteration and associated mechanical changes in a generic repository to consider the interaction between EBS bentonite and the NS clay formation. Two main scenarios were developed for comparison: a “high T” case in which the temperature near the waste package can reach about 200 ^{o}C and a “low T” scenario in which the temperature peaks at about 100 ^{o}C. The coupling between chemical and mechanical processes is the key part of THMC model that allow us to evaluate the impact of chemical changes on mechanical behavior. In FY16, THMC models utilize dual structure (BExM) (Sánchez et al., 2005) to link mechanical process with chemistry, allowing us to simultaneously incorporate the effects of exchangeable cations, ionic strength of pore water and abundance of swelling clay on the swelling stress of bentonite. In addition, the corrosion of steel canister was considered in the chemical model to evaluate whether the iron-bentonite interaction would aggravate the negative impact on swelling stress through the formation of Fe bearing clay minerals.

Coupled THMC models using BExM were developed for a generic case using FEBEX bentonite as EBS and Opalinus clay as NS. The following observations have been concluded from the model results:

- The chemical changes as a whole reduce both total stress and effective/net stress in the bentonite buffer except the positions near the confinement rocks in the “high T” cases. However, the difference between the result computed with C-M coupling and the result without C-M coupling is very small (less than 0.5 MPa).
- Three chemical changes, including the change in the volume fraction of smectite, change in exchanged cations, and ionic strength, contribute distinctively to the stress evolution in bentonite. In current model, dissolution of smectite leads to decrease in the volume fraction of smectite which decrease the stress; because the enrichment of exchanged sodium in the interlayer, the change in exchanged cations cause the increase in stress; the infiltration of more concentrated

water from clay formation to EBS bentonite leads to the increase in osmotic suction and subsequently lowers the stress. The relative importance of these three effects varies temporally and spatially and between cases ("high T" versus "low T"), and the combination of these three effects determines whether chemical change enhances or suppresses the stress.

- The effect of chemical change on stress is very sensitive to the parameters related to the chemical-mechanical coupling.
- In comparison with the THMC that used extended linear swelling model (Zheng et al., 2015), THMC model using BExM showed much less chemical effect on stress. The first reason is that exchanged cations which was not able to be taken into account by extended linear swelling model, is now considered in BExM. For FEBEX bentonite, change in exchanged cations has positive effect on the stress, which cancel out the negative effect due to the change of ionic strength (via osmotic sunction) and consequently the chemical change overall has much less effect on stress in THMC model using BExM, than that in the THMC that used extended linear swelling model. The second reason is that the chemical-mechanical coupling via BExM, the dissolution of smectite was factored in directly via the volume fraction of smectite by modifying the bulk modulus for micro-structure, but in BExM, bulk modulus is a function of stress and change significantly in the model, the bulk modulus changes by smectite dissolution was overshadowed by the stress change.
- Interaction between corroded steel canister and bentonite was taken into account in a THMC model for FEBEX bentonite using extended linear swelling. The corrosion process was simplified and the model focused on the possibility of forming Fe bearing clay minerals. Based on literature survey, we included vermiculite, berthierine, saponite as the potential Fe-clay mineral forming in the model, but none of them is formed. However, including Fe-bentonite interaction leads to slightly more precipitation of chlorite and dissolution of smectite, which drives down the swelling stress reduction slightly. As far as the dissolution of smectite and swelling stress reduction is concerned, including Fe-bentonite interaction does not seem to be very important.

The current coupled THMC model greatly improves our understanding of the coupled processes contributing to chemical and mechanical alteration in EBS bentonites and NS argillite formations and answers questions regarding the thermal limit of EBS bentonite in clay repository. However, more questions remain to be answered regarding the THMC alteration of bentonites and clay formations under high temperature. Further refinement of current models and improvements for the TOUREACT-FLAC3D simulator are needed in the future. In the remaining months of FY16 and FY17 the following activities are proposed:

- The current dual-structure model contains some limitations based on its physical assumptions. Moreover, the number of parameters for BExM is much more than other mechanical models, which increases the difficulty to calibrate the model for specific materials. The model needs to be simplified to improve its numerical robustness and to apply easily to different materials.
- The THMC model using BExM will be utilized in more numerical analysis with other buffer material such as Kunigel-VI bentonite. In current model, THMC model using BExM was only conducted for FEBEX bentonite because BExM had been calibrated for FEBEX bentonite and its concept fit better bentonite with high smectite content. However, the applicability of BExM for bentonite with low smectite content such as Kunigel-VI bentonite need to be tested and how chemical-mechanical coupling via BExM work out for Kunigel-VI need to be evaluated.
- The geochemical model for the Fe-bentonite interaction will be refined and calibrated against data. In the current model, no significant iron-related bentonite alteration was found despite some laboratory and field studies have shown formation of iron-clay minerals. The geochemical conceptual model and thermodynamic data base are the key to raise our confidence on the model.

In FY17, the geochemical model for Fe-bentonite interaction will be tested from data obtained in an eighteen years' *in situ* test and then simulations with higher temperature and long time will be conducted.

- Current models show precipitation of silicate minerals during illitization, which could result in the cementation of bentonite and subsequently lead to change in the mechanical properties of bentonite. Although the formation of silicate minerals is only about 3-4%, the change of mechanical properties as result of cementation needs to be quantified before we can safely conclude that silicate cementation won't significantly affect the mechanical properties.

(3) Understanding the THMC evolution of bentonite in FEBEX-DP— Coupled THMC modeling and examination of the structure of bentonite (Section 4)

Coupled THMC modeling

The FEBEX *in situ* test whichlasted more than eighteen years is extremely valuable for validating the coupled THMC model and deepening our understanding of the evolution of the bentonite barrier over the course of heating and hydration. In the FEBEX-DP project, heater #2 was dismantled and extensive THMC characterization was conducted. In FY16, the THC model was extended to THMC models and mechanical processes were simulated using both linear swelling model and dual structure BExM. The results from THMC models match reasonably the measured temporal evolution of temperature, relative humidity and stress at several compliance points in the bentonite barrier and the measured spatial distribution of water content and dry density at 5.3 years when the heater #1 was dismantled and at 18.3 years when the heater #2 was dismantled. However, the THMC models failed to explain the spatial profile of concentration at 5.3 years. The major findings from current modeling work are as follows:

- As expected, the THMC model outperformed the THC model in terms of matching measured THM data. Permeability and porosity changes due to mechanical process (swelling) were the key to match all the THM data.
- The THMC model using complex double structure BExM (THMC-BExM) did not clearly outperform the THMC model using linear swelling model (THMC-LS) in terms of matching the measured data. THMC-BExM led to a slightly better fit of measured relative humidities and stress near the heater and a slightly worse fit to the measured water content and dry density at 18.3 years. Although BExM is a more mechanistic approach and describes structural details of bentonite (the micro- and macro-structure of bentonite), it failed to manifest its superiority to the simple linear swelling model, which is probably due to that the THM data including relative humidity, stress, dry density and water content are all macroscopic such that these data cannot delineate the more mechanistic BExM from a linear swelling model.
- Although the THMC models successfully matched the THM data, they failed to desirably match the measured concentration profile of conservative species (chloride) at 5.3 years and subsequently the concentration profile of reactive species. The concentration profiles of cations (calcium, potassium, magnesium and sodium) were largely shaped by transport processes despite that their concentration levels were affected by mineral dissolution/precipitation and cation exchange. The concentration profile of pH, bicarbonate and sulphate were largely determined by chemical reactions.
- Revising the function for permeability changes in the THMC model improved the goodness-of-fit to chloride concentration profile but deteriorated the fit to water content data. It seemed there was a dilemma that the THMC model cannot match both the THM and chemical data simultaneously, suggesting that additional processes might be needed in the conceptual model.
- The THMC model predicted that concentration levels of major cations and anions at 18.3 years when the heater #2 was dismantled would continue going down in most parts of the bentonite

barrier except the area very close to the heater, where the concentration would go up, which will be compared with concentration data that are expected to be available by the end of 2016.

In the remaining months of FY16 and FY17, the following work is planned:

- Thermal osmosis, a moisture movement driven by the thermal gradient, has already been incorporated in the simulator TOUGHREACT-FLAC3D. We will test if the THMC model with thermal osmosis can match both the THM data and the concentration profile of chloride.
- Once the THMC model is calibrated against THM data and measured concentration data at 5.3 years, it will be used to interpret the concentration data for 18.3 years that are expected to be available by the end of 2016.
- The chemical model will be fine tuned, especially regarding redox condition evolution in the bentonite barrier and bentonite-canister interaction, and evolution of gases such CO_2, CH_4, and H_2.
- Ultimately, after the THMC models for FEBEX *in situ* test are fully validated with data, they will used to explore THMC changes in the long run under higher temperature.

Quantitative characterization of the fracture network in the FEBEX samples

Although the comparison between model and THMC data has been very helpful in calibrating the "right" relationships (or key parameters for the relationships), uncertainties in other processes and interaction of coupled processes might results in non-unique sets of parameters that could lead to equal or similar reasonable fit between model and data. Checking the microstructure of the bentonite buffer will serve as additional evidence to delineate the right permeability change functions and increase the predictability of models. Bentonite samples were taken from the FEBEX *in situ* test after the dismantling of heater #2. In FY16, we have conducted a series of synchrotron X-ray microCT (SXR-μCT) examination of the microstructure of bentonite samples. The major accomplishments are as follows:

- A total of five samples from different locations were examined with three duplicates for each sample. Fracture networks for each sample were obtained and quantified. We found the variability among duplicates from the same location in bentonite barrier is significant, mostly linked to the heterogeneity of the material. Nevertheless some weak correlation has been found: samples closer to the bentonite/granite interface tend to have a larger amount of large fractures, whereas samples close to the heater or to the center of the section tends to have larger amount of small fractures. While a truly statistically meaningful validation of this result is still needed, this correlation is clearly present in our sample survey.
- During the experiment, we also addressed some important technical issues: (1) we have found the best resolution vs. field of view compromise. (2) We have successfully developed a protocol/software for the analysis of the fracture network, focusing on the aperture value distributions.

In the remaining months of FY16 and FY17, the following experimental work is planned :

- (SXR-μCT) examination will be conducted for more samples at different locations to overcome the heterogeneity and find statistically defensible relationship between microstructure and physical parameters such as water content.
- The measured datasets will be used to build predictive tools. Besides the visualization and quantitative characterization of bentonite, SXR-μCT is also able to provide 3D volume datasets which can be used in a digital rock physics context: if the volume(s) obtained are meaningful, in terms of resolution vs. field of view, for measuring a given property, specific software able to

calculate those properties (such as permeability, invasion of non-wetting fluids, diffusion, etc.) from the datasets are available.

(4) Discrete Fracture Network (DFN) Approach for THM Damage Modeling in Argillaceous Rock (Section 5)

In FY16 we further developed TOUGH-RBSN with the goal of producing an efficient tool for understanding the variety of characteristics in THM processes in argillaceous rocks, including fracture damage and fluid driven fracture propagation. The series of simulations presented in this report section demonstrate the current TOUGH-RBSN capabilities for modeling tightly coupled HM processes and the RBSN approach for mechanical anisotropy in elastic and fracture responses. For the ongoing development, a refinement could be made into the TOUGH-RBSN code to rigorously evaluate the change of fracture porosity as a response of the mechanical fracture aperture change, which will be addressed in future work. In addition, the ongoing work on the dynamic version and porting that version to high performance computing will provide an avenue for modeling larger scale problems, including 3D complex fracture geometry.

The TOUGH-RBSN code and the developed algorithms for fluid driven fracturing have been applied to predictive and interpretative simulations for hydraulic fracturing of the laboratory experiment samples. The hydraulic fractures reproduced in the simulations compare favorably to the experimental results with respect to the injection pressure evolutions and the resulting fracture paths. As for the mechanical anisotropy, uniaxial compression tests on Opalinus Clay have been simulated in order to demonstrate the validity of the new modeling scheme. Thereafter, updated simulations of EDZ formations for the Mont Terri HG-A microtunnel have been conducted. Qualitative comparisons show that the simulation results closely match field observations, in which non-uniform failure patterns attributed to the anisotropic mechanical characteristics form around the excavation zone and the presence of fault planes significantly influences the failure patterns. For FY17, recommended work is as follows:

- We plan to complete the dynamic simulation framework, and verification and validation of the simulation code will be provided through geomechanics examples including fracturing processes. Also, by high performance computing in the dynamic simulation code, our modeling capacities will be extended to fully 3D large scale problems.
- More realistic simulations will be available by setting the fracture porosity dependent on the fracture aperture width in the TOUGH-RBSN coupling modules.
- Relating to the DECOVALEX-2019 task, TOUGH-RBSN code can be applied to the gas migration in bentonite clay, in which the clay material often dilates to create preferential flow pathways. We will attempt to demonstrate such preferential pathways using the discrete modeling approach.
- Swelling of a ductile/expanding shale matrix will be simulated to investigate the time-dependent deformation of the rock, including fracture closure/sealing, which significantly impacts on the hydrological properties of the rock material.

7. ACKNOWLEDGEMENTS

Funding for this work was provided by the Used Fuel Disposition Campaign, Office of Nuclear Energy, of the U.S. Department of Energy under Contract Number DE-AC02-05CH11231 with Lawrence Berkeley National Laboratory.